Episodic Development of Fault-Zone Architecture Investigated Using Small Displacement Strike-Slip Faults

Eliza S. Nemser

A dissertation submitted in partial fulfillment of the
requirements for the degree of

Doctor of Philosophy

University of Washington

2009

Program Authorized to Offer Degree:
Earth and Space Sciences

University of Washington
Graduate School

This is to certify that I have examined this copy of a doctoral dissertation by

Eliza S. Nemser

and have found that it is complete and satisfactory in all respects,
and that any and all revisions required by the final
examining committee have been made.

Chair of the Supervisory Committee:

Darrel S. Cowan

Darrel S. Cowan

Reading Committee:

Darrel S. Cowan

Darrel S. Cowan

Thomas S. Pratt

Thomas Pratt

Trenton Cladouhos

Trenton Cladouhos

Date: March 13, 2009

In presenting this dissertation in partial fulfillment of the requirements for the doctoral degree at the University of Washington, I agree that the Library shall make its copies freely available for inspection. I further agree that extensive copying of the dissertation is allowable only for scholarly purposes, consistent with "fair use" as prescribed in the U.S. Copyright Law. Requests for copying or reproduction of this dissertation may be referred to ProQuest Information and Learning, 300 North Zeeb Road, Ann Arbor, MI 48106-1346, 1-800-521-0600, to whom the author has granted "the right to reproduce and sell (a) copies of the manuscript in microform and/or (b) printed copies of the manuscript made from microform."

Signature Eliza S. Nemser

Date March 13, 2009

University of Washington

Abstract

Episodic Development of Fault-Zone Architecture Investigated Using Small Displacement Strike-Slip Faults

Eliza S. Nemser

Chair of the Supervisory Committee:
Professor Darrel S. Cowan
Earth and Space Sciences

Fault-zone architecture records valuable information about fault mechanics and imposes a structural influence on petrophysical and geophysical properties within fault zones. In this study, fault perpendicular and downdip variations in fault-related deformation are evaluated using cross-sectional exposures of small displacement strike-slip faults. The selected faults originated as dilational fractures in laumontite-cemented Pliocene sandstones and represent subsidiary deformation associated with the San Jacinto fault zone in the western Salton Trough region of southern California. The geometry of damage-zone deformation within these small displacement fault zones resembles a structural mesh, with cemented and open extensional fractures that are polymodal and mutually abutting. Integrated field and microstructural data provide evidence of episodic dilational fracturing, fluid flow, and cataclasis associated with phases of seismic activity. Spatial variability in petrophysical behavior is observed at multiple scales within the fault zones and results from the heterogeneity of host rocks, the irregular distribution of intergranular cement, and the variable distribution and localized effects of deformation features associated with alternating cycles of dilation, cementation, and cataclasis.

The paleo-damage zone model is introduced to account for observed fault-parallel damage-zone domains and provides a framework to evaluate contrasting models for the chronological and spatial pattern of damage-zone deformation. Step-wise decreases in fracture density with increasing perpendicular distance from the fault cores define relatively sharp domain boundaries that indicate the outer extent of deformation associated with unique slip events. The number of slip events on each fault exceeds the number of domains, and it is likely that the domain architecture was established early in the slip histories and preserved during subsequent events. Two of the fault zones exhibit downdip segmentation at the outcrop scale: vertically restricted, steeply dipping fault segments step over along mechanically weak stratigraphic units that accommodate bedding-parallel slip. Similar stepover geometries are observed within relocated seismicity data from the southern San Jacinto fault zone; this correspondence suggests that downdip segmentation may be common within strike-slip fault zones over a wide range of scales.

TABLE OF CONTENTS

LIST OF FIGURES

Figure Number Page

LIST OF TABLES

Table Number Page

ACKNOWLEDGEMENTS

I am deeply grateful to my supervisor, Darrel Cowan, who gave me the independence and confidence to develop my own research ideas and write my own grant proposals. My ownership over this project has been a continual source of motivation and Darrel has contributed essential insight, guidance, and mentoring. Darrel is my co-author on the publication that describes the downdip segmentation of strike-slip faults detailed in Chapter 5; we thank Michele Cooke and John Walsh for constructive reviews on an earlier version of that publication. My other committee members, Tom Pratt, Trenton Cladouhos and Paul Bodin, provided thought-provoking discussion and valuable feedback on various drafts of this dissertation. Eric Flodin at Chevron supplied the funding for the petrophysical analysis and critical comments on drafts of Chapter 4; Eric is my co-author on the publication that describes the petrophysical results presented in Chapter 4. Elizabeth Barnett, Rex McLachlin and Matt Quann were stellar field assistants at Borrego Mountain. Anren Li, Rob Knipe, and Russell Davies at Rock Deformation Research Ltd provided funding, resources for SEM analysis, and helpful feedback on an early draft of the microstructural analysis presented in Chapter 3. I thank Paula Matano for preparing my friable and challenging samples for analysis on the microprobe, and Scott Kuehner who was very helpful during the microprobe work. GeoSystems LLP performed the XRD analysis; sample preparation and all other petrophysical tests were performed by PTS Laboratories, Inc. George Jefferson from Anza-Borrego Desert State Park facilitated the permitting and was an important resource during fieldwork.

I am extremely appreciative of the USGS fellowship that supported me for most of the duration of this project and Tom Pratt's sponsorship and persistent efforts on my behalf. Don Medwedeff was an inspiring mentor during my 3-month hiatus from this research as an intern at Chevron, and later contracted me to lead corporate field trips at Borrego Mountain; these contracts were an important component of my research funding. This research was also funded by grants awarded by the Geological Society of America, the American Association of Petroleum Geologists, and grants and fellowships awarded by the Earth and Space Sciences Department at the UW.

I cannot imagine having accomplished this goal without the incredible patience and unwavering support of my husband, Matt Quann, who helped me maintain balance and perspective. My parents have also been a constant and vital source of moral support.

Introduction

Fault damage zones include deformation surrounding the fault core that results from slip on the fault and decays in density as a function of distance from the core (Chester et al., 1993; Chester and Chester, 1998; Sibson, 2003; Biegel and Sammis, 2004; Kim et al., 2004). The internal architecture of damage zones is typically defined by fault-parallel domains that may have distinct geological, geophysical, and petrophysical properties (Schulz and Evans, 2000; Li and Vernon, 2001; Sayed, 2001; Spudich and Olsen, 2001; Wilson et al., 2003). Detailed analysis of damage-zone deformation within exhumed fault zones provides valuable information about the mechanics of faulting (Chester et al., 1993; Evans and Chester, 1995; Billi et al., 2003; Faulkner et al., 2003; Wibberley and Shimamoto, 2003; Wilson et al., 2003) and the spatial variability of fluid-flow properties across fault zones (Caine et al., 1996; Evans et al., 1997; Fisher and Knipe, 1998).

The focus of this study is an investigation of fault-zone evolution along small displacement (<5 m) strike-slip faults at Borrego Mountain, in the western Salton Trough region of southern California. The faults of interest are exposed within the Pliocene West Butte Conglomerate, a laumontite-cemented lithic arenite. These faults represent subsidiary deformation related to the Coyote Creek segment of the southern San Jacinto fault zone; the San Jacinto fault zone is part of a much larger system of active seismogenic strike-slip faults related to the plate-boundary San Andreas fault system. Small displacement faults with relatively less damage-zone complexity represent the early phases of deformation along larger faults and offer an increased potential for correlating deformation features with individual slip events. In this work, field observations are integrated with microstructural and petrophysical analysis to test current models that address the temporal and spatial evolution of fault-related deformation and the associated permeability structure.

Chapter 1 of this manuscript, *Regional Tectonic and Stratigraphic Setting: the Western Salton Trough*, presents a review of published work on the regional tectonic and

stratigraphic history of the western Salton Trough region of southern California, USA. This background information places the Borrego Mountain study area into a broader context. The regional setting provides a framework for the detailed investigations of fault-zone development that are the focus of this study.

Chapter 2, *Late Tertiary–Quaternary Stratigraphy and Structural History of Borrego Mountain*, describes the local stratigraphy and structural history of Borrego Mountain, in Anza-Borrego Desert State Park near Borrego Springs, California. Previous studies in the vicinity of Borrego Mountain provide a comprehensive geological framework for the detailed structural analysis of small displacement faults that represent subsidiary deformation associated with the Coyote Creek fault. This chapter begins with a summary of recent investigations into the stratigraphy and structure of the Borrego Mountain area (e.g., Steely, 2003; Steely, 2006), and the earthquake history of the Coyote Creek fault. Chapter 2 also includes a discussion of the heat flow and geothermal gradient at Borrego Mountain, and estimates of the sedimentary overburden at the study areas during the initiation of faulting.

The history of deformation and fluid flow along the small displacement faults is detailed in Chapter 3, *Structural Evolution and Damage-Zone Development Along Small Displacement Strike-Slip Faults Adjacent to the Southern San Jacinto Fault Zone, Borrego Mountain, California, USA*. The temporal and spatial accumulation of fault-related damage is evaluated in the context of the 'paleo-damage zone' model, a new conceptual model for damage-zone evolution that specifically addresses the development of distinct fault-parallel domains. An original methodology for the analysis of two-dimensional fracture data is also introduced and used to delineate the damage-zone domains. Mesoscopic and microstructural observations of deformation within the damage-zone domains reveal the chronology of repeating cycles of dilation, fluid flow, and cataclasis throughout fault-zone evolution. Within the paleo-damage zone model, is possible to assess how the damage-zone domains record the earthquake history of each fault zone, and specifically how the number of observed domains

relates to the number of slip events hosted on each fault. The role of fluid flow within the seismic cycle is also discussed.

Chapter 4, *Heterogeneous Petrophysical Properties of Fault Zones Formed Along Joints in Laumontite-Cemented Sandstone,* describes the structural influence of damage-zone domains on the petrophysical properties of these small displacement faults. Petrophysical analysis of small displacement (subseismic) fault zones is critical in hydrocarbon exploration as subseismic faults are typically abundant in the vicinity of larger, geophysically resolvable faults and may significantly influence fluid flow within a faulted reservoir (Heath et al., 1994; Shipton et al., 2002). Previously published work on fluid flow in faulted sandstones primarily addresses deformation band-style fault zones. Fault zones that develop by the shearing of joints in the absence of deformation bands have distinct behavior and heretofore have only been documented in uncemented, well-sorted sandstones. The fault zones exposed within the poorly sorted West Butte Conglomerate at Borrego Mountain are characterized by pervasive intergranular laumontite cement and abundant cemented fractures that give rise to heterogeneous and complex flow properties.

Chapter 5, *Downdip Segmentation of Strike-Slip Fault Zones in the Brittle Crust*, presents field and seismological evidence that segmentation of strike-slip faults in the downdip direction (previously undocumented) may in fact be common at a variety of scales. The heterogeneous stratigraphy exposed in exhumed fault zones at Borrego Mountain reveals the influence of mechanical stratigraphy on the kinematics of strike-slip faulting. Steep fault segments are laterally offset along shallowly inclined mechanical boundaries within relatively weak strata. Stepover geometries occur in these fault zones and bedding-parallel shear is the mechanism of strain accommodation within the weaker units. Previously published work has addressed the downdip segmentation of normal faults, thrust faults, and fractures, and the along-strike segmentation of strike-slip faults. The original model described in this chapter is based on new field data, cross-sections of relocated crustal seismicity along the southern San

Jacinto fault zone, and original interpretations. This model may lead to the reinterpretation of fault geometry and kinematics in many strike-slip fault zones and an improvement in seismic hazard assessments of strike-slip fault zones.

Chapter 1: Regional Tectonic and Stratigraphic Setting: the Western Salton Trough

1.1 Tectonic Evolution of the Salton Trough Region, Southern California: ~30 Ma–Present

1.1.1 Tectonic History of the Salton Trough Region: ~30 Ma to the Pliocene

The Salton Trough in southern California is a structurally controlled basin that lies along the Pacific-North American plate boundary at the northwestern extension of the Gulf of California (Figure 1.1A).

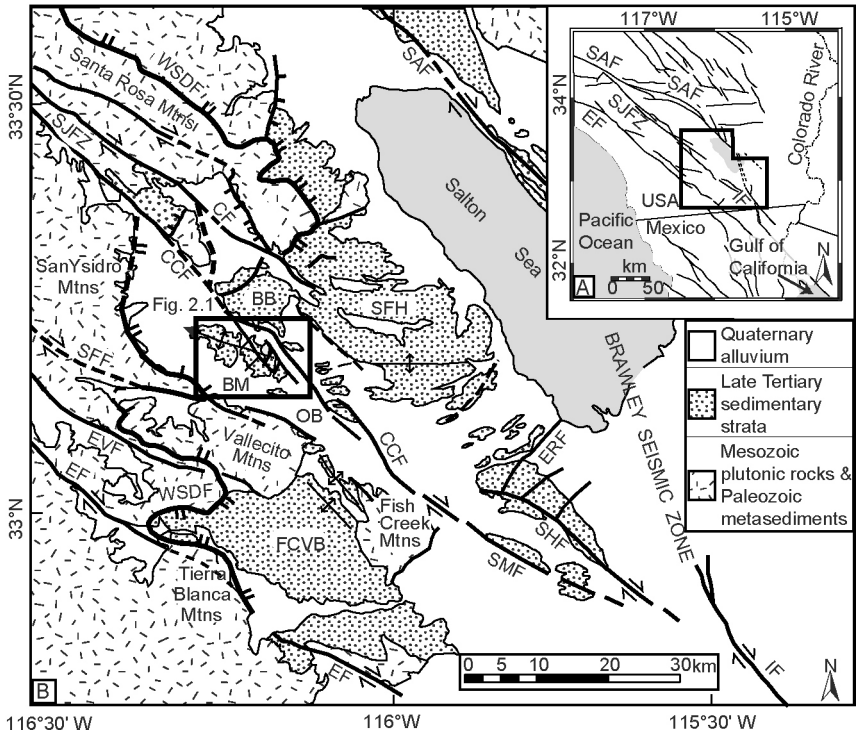

Figure 1.1. (A) (Inset) Fault map of Southern California (modified from Lutz et al., 2006). (B) Generalized geologic map of the western Salton Trough (modified from Lutz et al., 2006). Borrego Mountain is shown in detail in Figure 2.1. *BB*, Borrego Badlands; *BM*, Borrego Mountain; *CCF*, Coyote Creek fault; *CF*, Clark fault; *EF*, Elsinore fault; *ERF*, Elmore Ranch fault; *EVF*, Earthquake Valley fault*; FCVB*, Fish Creek–Vallecito basin; *IF*, Imperial fault; *OB*, Ocotillo Badlands; *SAF*, San Andreas fault; *SFF*, San Felipe fault; *SFH*, San Felipe Hills; *SHF*, Superstition Hills fault; *SJFZ*, San Jacinto fault zone; *SMF*, Superstition Mountain fault; *WSDF*, West Salton detachment fault.

The modern tectonic setting of the Salton Trough region is the result of a major tectonic reorganization of this region at ~30 Ma. At this time, the easterly migrating

East Pacific Rise spreading ridge reached the subduction zone at the western boundary of the North American Plate, leading to the inception of a transform boundary (Atwater, 1970, 1989). As the plate boundary continued to migrate east, parts of the North American continent were transferred to the Pacific plate. The new transform boundary grew in length as the Mendocino triple junction migrated to the northwest (Atwater and Stock, 1998).

At ~12 Ma, the Rivera triple junction jumped to the southeast, extending the transform boundary along the western edge of Baja California (Spencer and Normark, 1989; Lonsdale, 1991). At ~6 Ma, the transtensive Pacific-North American plate boundary rapidly relocated to the eastern side of Baja California and extension localized in the modern Gulf of California (Oskin et al., 2001). This event caused a major marine incursion in the Gulf of California that flooded the Salton Trough (Oskin et al., 2001; Oskin and Stock, 2003b). The current configuration of the ~1,200 km long San Andreas fault system was established at this time, linking the Mendocino fracture zone and the Cascadia subduction zone in northern California to the spreading center in the Gulf of California (Figure 1.1A).

1.1.2 Pliocene Tectonic History of the Western Salton Trough

A plethora of recent work in the western Salton Trough has addressed the complex late Tertiary–Quaternary tectonic evolution of this region (e.g., Dorsey, 2002; Dorsey and Janecke, 2002; Axen et al., 2004; Janecke et al., 2004; Steely et al., 2004a; Steely et al., 2004b; Dorsey et al., 2005; Housen et al., 2005; Janecke et al., 2005; Kairouz, 2005; Kirby et al., 2005; Kirby, 2005; Lutz, 2005; Shirvell et al., 2005; Steely et al., 2005b; Lutz et al., 2006; Steely, 2006; Dorsey et al., 2007; Kirby et al., 2007). From ~6 Ma to the early Pleistocene, basin subsidence in the western Salton Trough was caused by a combination of: (1) crustal extension and transtension along the dextral-oblique, east- to northeast-dipping West Salton detachment fault zone that bounds the west side of the basin; and (2) dextral slip on the San Andreas fault that bounds the north and northeast sides of the basin (Figure 1.1) (Dibblee, 1984, 1996; Axen and Fletcher,

1998; Axen et al., 2004; Steely, 2006). A transition from this period of crustal extension and transtension to the modern dextral strike-slip and transpressional environment occurred during the Late Pliocene or Early Pleistocene (Dorsey and Roering, 2006; Lutz et al., 2006). Recent stratigraphic and sedimentary investigations document a major structural reorganization in the southwestern Salton Trough at ~1.1 Ma that likely corresponds with this shift from detachment faulting to dextral strike-slip faulting (Lutz et al., 2006; Kirby et al., 2007).

1.1.2.1 West Salton Detachment Fault Zone

The West Salton detachment fault zone (WSDF) is the northern segment of a ~250 km long system of detachment faults that extends south from the Salton Trough to Baja California (Figure 1.1) (Axen and Fletcher, 1998). Slip along the northwest-striking, 15° to 40° east-dipping WSDF initiated during the latest Miocene, and accommodated the extensional component of plate motion along the oblique Pacific-North American plate boundary (Axen and Fletcher, 1998; Dorsey and Janecke, 2002). A wrench-style tectonic model is consistent with east-west extension adjacent to a northwest-striking strike-slip fault (Christie-Blick and Biddle, 1985; Axen et al., 2004; Steely, 2006). The presence of oblique striae on the detachment fault and multiple fault-parallel growth anticlines in the hanging-wall suggest that the WSDF also had a significant strike-slip component (Steely et al., 2004b). Slip on the detachment fault continued through the Pliocene and likely ceased with the initiation of slip along the dextral strike-slip San Jacinto and San Felipe fault zones in the early Pleistocene (Axen and Fletcher, 1998; Lutz et al., 2006; Kirby et al., 2007).

Fabrics of the WSDF overprint and are spatially associated with the eastern Peninsular Ranges mylonite zone, a mid- to late-Cretaceous, moderately east-dipping (30° to 60°) reverse-sense shear zone that extends from Palm Springs to Baja California in the Peninsular Ranges batholith (Sharp et al., 1979; Engel and Schultejann, 1984; Simpson, 1984a; Todd et al., 1988; George and Dokka, 1994). The Santa Rosa mylonite zone is the ~100 km long northern portion of the eastern Peninsular Ranges

mylonite zone and extends along the eastern Peninsular Ranges from Palm Springs to Yaqui Ridge in the southwestern Salton Trough (Sharp et al., 1979; Engel and Schultejann, 1984; Simpson, 1984b; Axen and Fletcher, 1998; Kairouz, 2005; Steely, 2006). In places, the WSDF reactivates fabrics of the Santa Rosa mylonite zone; along shallower-dipping portions of the WSDF, the younger extensional fault offsets the steeper Santa Rosa mylonite zone (Erskine and Wenk, 1985; Axen and Fletcher, 1998).

1.1.3 Tectonic History of the Western Salton Trough: Pleistocene to the Present

Geodetic measurements indicate that the Pacific plate is currently traveling northwest relative to the North American plate at ~50 mm/yr; most of this plate motion is accommodated along the San Andreas fault system (DeMets et al., 1994; Antonelis et al., 1999). The plate boundary is particularly complex in southern California, where plate motion is distributed along a suite of northwest-striking, subparallel, right-lateral strike-slip faults that occupy a ~200 km wide swath near the coast; the primary onshore faults include the San Andreas, San Jacinto, Imperial, and Elsinore faults. South of the Transverse Ranges, 20–25% of the plate motion is accommodated along the 250 km long San Jacinto fault zone that branches off from the San Andreas fault in the eastern San Gabriel Mountains and merges with the Imperial fault in the southeast (Figure 1.1) (Sharp, 1967; DeMets et al., 1994). The Borrego Mountain study area is adjacent to the Coyote Creek fault of the San Jacinto fault zone, and the tectonic history of Borrego Mountain has been dominated by slip along the San Jacinto fault zone from early Pleistocene to the present (Figure 1.1).

1.1.3.1 San Jacinto Fault Zone

The seismically active San Jacinto fault zone (SJFZ) has the third highest slip rate of any fault in southern California (after the San Andreas and Imperial faults) and has a recurrence interval of ~10 years for M ≅ 6 earthquakes (Hutton et al., 1991). The SJFZ is highly segmented; the segments (from north to south) include the Claremont, Casa Loma, Clark, Coyote Creek, Superstition Hills, and Superstition Mountains faults

(Sharp, 1967, 1975; Sanders, 1989; Sanders and Magistrale, 1997). The highly complex, discontinuous nature of the SJFZ may reflect its youthfulness and the influence of preexisting crustal structure (Langenheim et al., 2004). The average slip rate along the SJFZ is ~10–12 mm/yr (Sharp, 1981; Rockwell et al., 1990a; Wesnousky et al., 1991; Kendrick et al., 1994; Bennett et al., 1996), although the different segments of the SJFZ have widely variant slip rates; estimates range from ~1 mm/yr along the Superstition Hills segment (Hudnut and Sieh, 1989; Petersen and Wesnousky, 1994) to ~20 mm/yr along the Claremont segment (Kendrick et al., 2002). The total dextral offset along the SJFZ varies from ~21 km to ~30 km with an apparent decrease in slip to the southeast (Sharp, 1967; Bartholomew, 1970; Hill, 1984; Revenaugh, 1998; Dorsey, 2002). Estimates of the age of slip initiation on the SJFZ range from 2.4 to 1.0 Ma based on stratigraphic, structural and paleoseismic studies (Sharp, 1981; Rockwell et al., 1990a; Morton and Matti, 1993; Dorsey, 2002; Kendrick et al., 2002; Lutz et al., 2006).

The subparallel Clark and Coyote Creek segments of the SJFZ are active in the southwestern Salton Trough (Figure 1.1). Total offset along the Coyote Creek and Clark segments is 6 and 15 km, respectively (a total of 21 km of displacement along the SJFZ in this region), based on the separation of the Late Cretaceous mylonite (Sharp, 1967; Dorsey and Janecke, 2002). The Coyote Creek segment has a slip rate of ~5 mm/yr and the Clark segment has a slip rate of ~10 mm/yr, although there is evidence along both segments that more offset can be observed in the crystalline basement than in the Late Cenozoic basin fill deposits; this discrepancy has also been proposed along other strike-slip faults (Fialko et al., 2005; Janecke et al., 2005). For example, at Borrego Mountain, offset of a marker bed within the Pliocene Diablo Formation indicates 1–2 km of right separation across the Coyote Creek fault zone, whereas gravity data from the San Felipe Anticline show ~4.1 km of offset along crystalline rocks in the core; this latter estimate is consistent with ~4.0 km of separation of crystalline rocks along the Coyote Creek fault west of Coyote Mountain (Janecke et al., 2005).

1.2 Western Salton Trough Regional Stratigraphy

The record of upper Miocene to Pleistocene sedimentation and deformation in the western Salton Trough can be observed in two distinct subbasins: the Fish Creek–Vallecito basin in the south, and the San Felipe–Borrego basin in the north that includes the San Felipe Hills, the Borrego Badlands, and Borrego Mountain (Figure 1.1) (Kerr and Kidwell, 1991; Winker and Kidwell, 1996; Axen and Fletcher, 1998; Dorsey et al., 2005; Dorsey and Roering, 2006). These subbasins originally belonged to one large supradetachment basin in the hanging wall of the WSDF, and were separated by the development of the San Felipe fault zone at ~1.1 Ma (Figure 1.1) (Kirby, 2005; Steely et al., 2005a; Steely, 2006; Kirby et al., 2007). The Tertiary sequence rests on basement rocks that include Late Cretaceous plutonic rocks of the Peninsular Ranges Batholith, older metasedimentary rocks, and the Santa Rosa Mylonite zone that records Late Cretaceous thrusting (Figure 1.2) (Dibblee, 1984; Simpson, 1984a).

1.2.1 Miocene Split Mountain Group

The oldest Tertiary formations within the western Salton Trough are the sandstones and conglomerates of the Red Rock Formation and the overlying ~14–22 Ma Alverson Volcanics, both of the Miocene Split Mountain Group (Figure 1.2) (Ruisaard, 1979; Kerr and Kidwell, 1991; Winker and Kidwell, 1996). The Split Mountain group also includes coarse-grained deposits of the Elephant Trees Formation, the base of which is ~8.1 Ma and may represent the earliest record of extension or transtension in this region (Dorsey et al., 2007). The Elephant Trees Formation is overlain by debris flows and sturzstom deposits (Rightmer and Abbott, 1996).

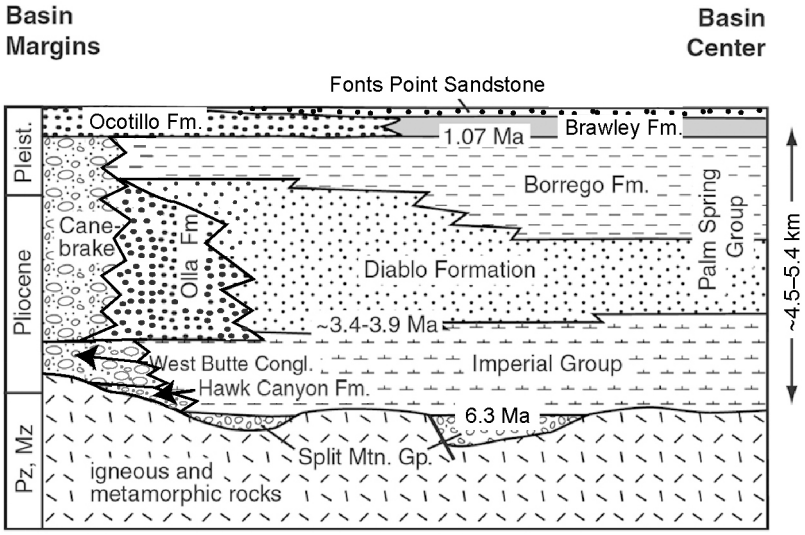

Figure 1.2. Stratigraphy of the San Felipe-Borrego basin in the western Salton Trough (modified from Lutz et al., 2006).

1.2.2 Pliocene Imperial Group

The transition between the Split Mountain Group and the overlying Pliocene Imperial Group is stratigraphically complex, with abrupt facies changes and local thickening of deposits (Figure 1.2) (Winker, 1987; Dorsey, 2005). A thick, discontinuous gypsum deposit known as the Fish Creek Gypsum lies at this boundary; the origin of this gypsum is uncertain and disputed in the literature (Dean, 1988; Dean et al., 1990; Jefferson and Peterson, 1998). The ~6.3 Ma base of the Imperial Group includes a thick and widespread marine section that is interpreted as evidence of the large-scale marine incursion into the Salton Trough that resulted from the shift of the transform boundary into the Gulf of California (Dibblee, 1984; Kerr and Kidwell, 1991; Winker and Kidwell, 1996; Oskin et al., 2001; Oskin and Stock, 2003a; Dorsey et al., 2007). The Imperial Group also contains a megabreccia unit that may represent large-scale basin reorganization (Dean, 1988; Dean et al., 1990; Kerr and Kidwell, 1991; Winker and Kidwell, 1996). Several workers have postulated that this reorganization may correspond with the transition from high-angle normal faulting to low-angle detachment faulting along the WSDF (Dorsey and Janecke, 2002; Winker and Kidwell, 2002).

1.2.3 Pliocene Palm Spring Group

The Pliocene deposits of the Imperial Group and overlying Palm Spring Group include thick marine and nonmarine accumulations that record rapid subsidence due to extension along the WSDF (Figure 1.2) (Axen and Fletcher, 1998). During the early Pliocene, the Salton Trough and northern Gulf of California were linked along the Imperial seaway during a major marine transgression (Winker and Kidwell, 1996). The Imperial Group comprises a coarsening-upward sequence of sediments derived from the ancestral Colorado River and reflects the gradual shallowing of the basin due to sedimentation (Janecke et al., 2005).

The Diablo Formation of the Palm Spring Group includes ancestral Colorado River-derived sediments that were deposited in a large fluvial-deltaic system. The Canebrake Conglomerate and Olla Formation represent the coarse-grained lateral equivalent and contain sediments derived from local basement uplifts that were deposited in an alluvial setting (Kerr and Kidwell, 1991; Dibblee, 1996; Winker and Kidwell, 1996). The Borrego Formation includes non-marine lacustrine sediments that were deposited once the Colorado River delta isolated the Salton Trough from the Gulf of California (Winker and Kidwell, 1986; Kerr and Kidwell, 1991; Dibblee, 1996; Winker and Kidwell, 1996). The Borrego Formation may represent the final stages of regional transtension associated with slip on the WSDF (Dorsey et al., 2004; Kairouz, 2005; Steely, 2006).

1.2.4 Pleistocene Ocotillo/Brawley Formations

The early to middle Pleistocene Ocotillo Formation and the laterally equivalent finer-grained Brawley Formation are separated from the underlying syndetachment sequence by a contact that varies from conformable to an angular unconformity (Figure 1.2) (Dibblee, 1984; Kerr and Kidwell, 1991; Winker and Kidwell, 1996; Lutz et al., 2006; Kirby et al., 2007). The transition from the Borrego Formation to the Ocotillo and Brawley Formations represents a significant and abrupt change in sedimentary and depositional environment that has been correlated with the deactivation of the WSDF,

the growth of the San Felipe anticline, and the initiation of dextral and oblique-slip faulting at ~1.1 Ma (Dorsey, 2002; Lutz et al., 2006; Steely, 2006; Kirby et al., 2007).

1.2.5 Pleistocene Fonts Point Sandstone

The Fonts Point Sandstone is a thin and laterally extensive alluvial deposit that overlies the Ocotillo Formation in the Borrego Badlands (Dibblee, 1984; Kerr and Kidwell, 1991; Winker and Kidwell, 1996; Lutz et al., 2006; Kirby et al., 2007). The contact between the Fonts Point Sandstone and the Ocotillo Formation varies from conformable to an angular unconformity; the conformable base of the Fonts Point Sandstone has been dated at ca. 0.6 Ma (Dibblee, 1984; Kerr and Kidwell, 1991; Winker and Kidwell, 1996; Lutz et al., 2006; Kirby et al., 2007). The transition from the Ocotillo Formation to the Fonts Point Sandstone correlates with the propagation of the Coyote Creek fault southeast to the Borrego Badlands, the initiation of the Inspiration Point fault, and the onset of uplift in the Borrego Badlands and the San Felipe Hills; these events represent a significant structural reorganization of the SJFZ in this region at ca. 0.6 Ma (Lutz et al., 2006; Kirby et al., 2007).

Chapter 2: Late Tertiary–Quaternary Stratigraphy and Structural History of Borrego Mountain

Late Miocene and younger sedimentary rocks exposed at Borrego Mountain in the western Salton Trough region of southern California were deposited in the upper plate of the WSDF in a fluvial-deltaic environment between the ancestral Colorado River and the Gulf of California (Dibblee, 1954; Morley, 1963; Woodard, 1963; Hoover, 1965; Reitz, 1977; Winker, 1987; Winker and Kidwell, 1996; Axen and Fletcher, 1998; Steely, 2006). These strata were initially deformed and uplifted during anticlinal folding in the hanging-wall of the WSDF and subsequently in the current transpressive regime along the Coyote Creek segment of the southern San Jacinto fault.

2.1 Tertiary Stratigraphy at Borrego Mountain

Late Miocene to Pleistocene strata of the San Felipe-Borrego sub-basin are exposed at Borrego Mountain due to folding along the Borrego Mountain anticline and uplift in the vicinity of a restraining bend along the Coyote Creek strand of the SJFZ (Figure 2.1) (Steely, 2003; Steely, 2006).

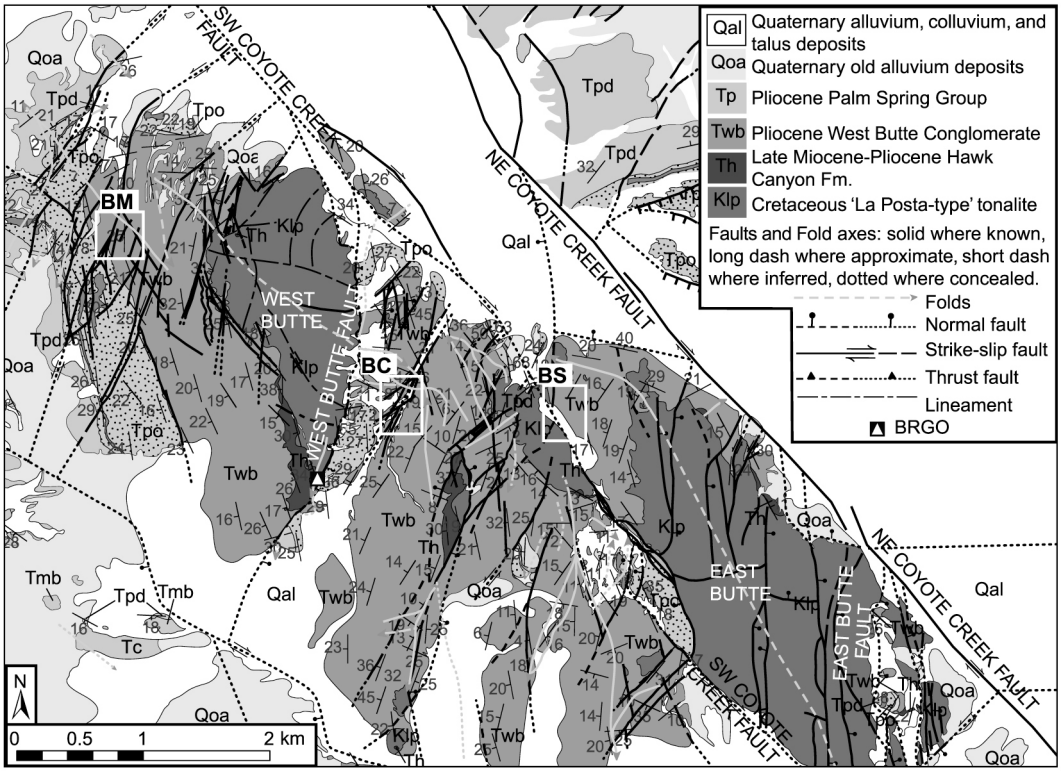

Figure 2.1. Geology of the Borrego Mountain area (modified from Steely, 2006); location is shown on Figure 1.1. Study areas are indicated with white boxes; *BM*, Borrego Mountain Wash; *BC*, Butte Canyon Wash; *BS*, Blow Sand Wash.

At Borrego Mountain, the late Miocene to Pliocene Imperial Group, Pliocene Palm Spring Group, Plio-Pleistocene Borrego Formation, and Quaternary Ocotillo and Brawley formations have a combined thickness of ~4.5–5.4 km (Figure 1.2) (Dibblee, 1954; Morley, 1963; Reitz, 1977; Dibblee, 1984, 1996; Dorsey, 2005; Kirby, 2005; Lutz, 2005; Steely, 2006). The Hawk Canyon formation and West Butte Conglomerate of the Imperial Group provide a minimum age for initial slip on the WSDF because they contain clasts that record footwall exhumation (Steely, 2006). Isopach maps reveal substantial variation in the thickness of the Hawk Canyon Formation, the West Butte Conglomerate, and the Olla Formation at Borrego Mountain; these units were folded syndepositionally along the northwest-trending Borrego Mountain anticline during slip on the WSDF (Figure 2.2) (Steely, 2006).

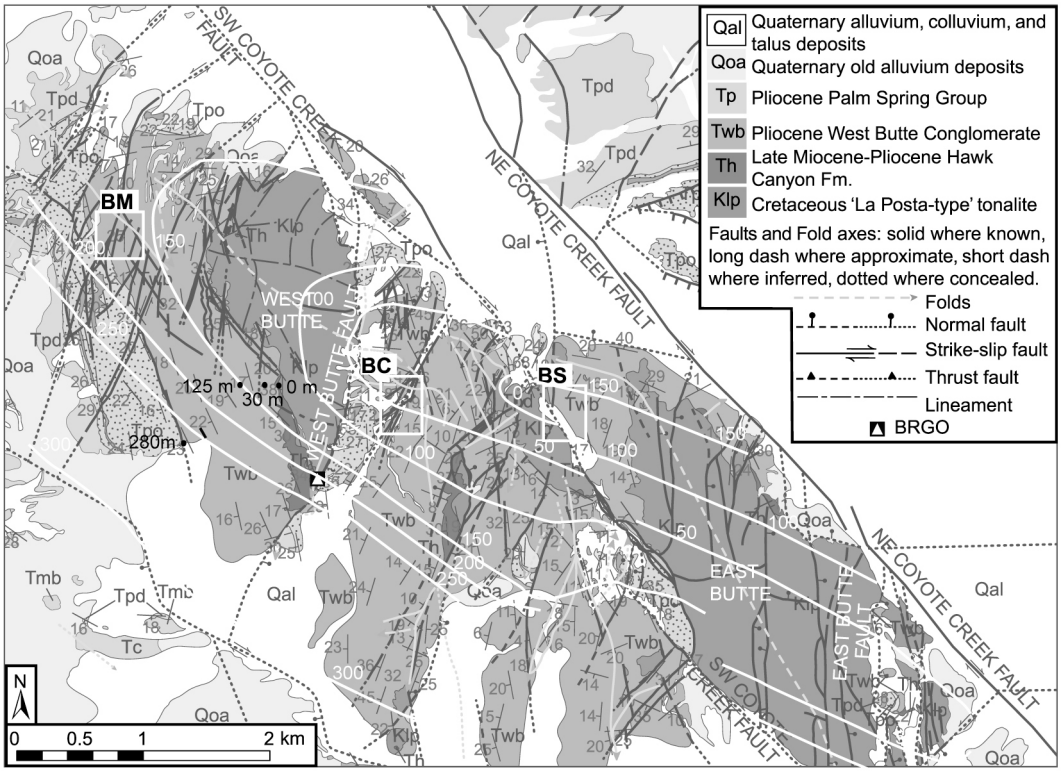

Figure 2.2. Geologic map of Borrego Mountain showing an isopach map of the West Butte Conglomerate (location is shown on Figure 1.1). Numbered black points in the vicinity of West Butte represent locations along the traverse where the complete stratigraphic section was measured by Steely (2006). Underlying geologic map from Steely (2006), isopach thicknesses, dashed where speculative, modified from Steely (2006). Study areas *BM,* Borrego Mountain Wash, *BC,* Butte Canyon Wash, and *BS*, Blow Sand Wash outlined with white boxes.

2.1.1 Pliocene Imperial Group at Borrego Mountain: Hawk Canyon Formation and West Butte Conglomerate

The base of the Imperial Group at Borrego Mountain consists of the late Miocene to Pliocene Hawk Canyon Formation; the basal, locally derived grus (lower member) of the Hawk Canyon Formation rests nonconformably on the basement tonalite (Figure 1.2). The lower member is overlain by locally derived marginal marine mudstones (middle member) and fluvial or alluvial sandstone and mudstones derived from the footwall and damage zone of the WSDF to the south-southeast of Borrego Mountain (upper member) (Herzig et al., 1995; Steely, 2006). The Hawk Canyon Formation is 0–80 m thick in the Borrego Mountain area and correlates with the marine deposits of the Imperial Group near Squaw Peak and Shell Reef (Steely, 2006).

A low-angle unconformity to disconformity separates the Hawk Canyon Formation from the overlying conglomeratic sandstones of the Pliocene West Butte Conglomerate (Figure 1.2). These conglomeratic sandstones were originally correlated with the Pliocene-Pleistocene Canebrake Conglomerate of the Palm Spring Group (Dibblee, 1954; Morley, 1963) but were recently reclassified as the West Butte Conglomerate of the Imperial Group based on a detailed analysis of clast lithologies (Steely, 2006). Clasts in the sandy conglomerate and conglomeratic sandstone of the West Butte Conglomerate are similar to those in the upper member of the Hawk Canyon Formation, and include chloritically and hematitically altered clasts that were likely derived from the footwall and damage zone of the WSDF and transported north-northeast to the Borrego Mountain area (Steely, 2006). The depositional environment is interpreted as an alluvial fan or part of a bajada (Steely, 2006). The West Butte Conglomerate has been interpreted as the fluvial equivalent to the marine Pliocene Imperial Group exposed at Squaw Peak (Steely, 2006). The thickness of the West Butte Conglomerate ranges from 0 to a maximum of 280 m at the proposed type locality southwest of West Butte and southeast of Borrego Mountain Wash where Steely (2006) constructed a measured section (Figure 2.2).

2.1.2 Pliocene Palm Spring Group at Borrego Mountain: Olla and Diablo Formations

At Borrego Mountain, the West Butte Conglomerate is conformably overlain by fluvial deposits of the Olla Formation that range from 38–120 m in thickness and form the base of the Palm Spring Group (Figure 1.2) (Dibblee, 1984; Winker, 1987; Steely, 2006). Clast compositions in the Olla Formation are similar to the West Butte Conglomerate and likely represent a similar south-southwest source (Steely, 2006). The West Butte conglomerate fines upward into the overlying Olla Formation; this boundary is defined as the stratigraphic level at which a more sandy conglomerate becomes subordinate to a coarse sandstone (Steely, 2006). The Colorado River-derived sandstones and mudstones of the Diablo Formation rest on the Olla Formation and

have been interpreted as deposits of the subaerial Colorado River delta plain (Winker and Kidwell, 1996).

2.1.3 Estimates of Sedimentary Overburden at Field Localities

The seven faults investigated in this study are northwest- and northeast- striking, steeply dipping strike-slip faults exposed within the West Butte Conglomerate. These faults are located in three different washes at Borrego Mountain: Borrego Mountain Wash (faults BM1, BM2, BM3), Butte Canyon Wash (faults BC1, BC3), and Blow Sand Wash (faults BS1, BS2). The total combined thickness of the overburden (estimated maximum depth of burial) of the faults in this study at the inception of faulting ranges from 2750–2770 m (at faults BC3, BC1, BS1 and BS2) to ~2870 m (at faults BM1, BM2, and BM3). These values have been determined using an estimate of the total combined thickness of the sedimentary overburden at each fault locality after the deposition of the Ocotillo/Brawley Formation at ca. 0.6 Ma. The combined thickness of the formations stratigraphically above the Olla Formation at Borrego Mountain, including the younger members of the Palm Spring Group (the Tertiary Diablo formation and Quaternary Borrego Formation) and other Quaternary units (including the Ocotillo/Brawley Formation) has not been quantified in the literature. However, in the absence of data on the thickness of these units at Borrego Mountain, estimated thicknesses of these units in the nearby San Felipe Hills and Borrego Badlands can be used as an approximation. The Diablo Formation is >550 m thick west of the Borrego Mountain study area (Morley, 1963; Dorsey et al., 2004; Steely, 2006). The Borrego Formation is 1600–1800 thick in the San Felipe Hills and Borrego Badlands (Dibblee, 1984; Kirby, 2005; Lutz et al., 2006). The Ocotillo and Brawley Formations are ~450 m thick in the Ocotillo Badlands, ~500 m in the Borrego Badlands, and ~480 m thick in the eastern San Felipe Hills (Kirby, 2005; Lutz et al., 2006). Adopting a thickness of 1700 m for the Borrego Formation, 475 m for the Ocotillo and Brawley Formations, and 550 m for the Diablo Formation, the total overburden thickness at each site can be calculated as the sum of 2725 m, the site-

specific depositional thickness of the Olla Formation, and the site-specific thickness of eroded West Butte Conglomerate.

The total depositional thickness of the West Butte Conglomerate and overlying Olla Formation at each site can be determined using isopach maps compiled by Steely (2006) (Figure 2.2). The Olla Formation is completely eroded away at each site; the thickness of eroded West Butte Conglomerate at the sites of faults in the Borrego Mountain Wash and Butte Canyon Wash study areas can be estimated by projecting the exposed west-dipping contact between the Olla Formation and the West Butte Conglomerate above the mapped faults.

At the mapped location of fault BM2, projecting the west-dipping contact indicates that the total thickness of the overlying Olla Formation, eroded away at the outcrop, was ~53 m; the total thickness of the now partially eroded West Butte Conglomerate at this site was ~173 m, with ~97 m eroded away. The estimated combined maximum overburden thickness of the West Butte Conglomerate and Olla Formation at this location was ~150 m. At the location of nearby faults BM1 and BM3, the West Butte Conglomerate and Olla Formations were ~178 m and ~58 m thick respectively, with ~81 m of the West Butte Conglomerate eroded away; the combined maximum overburden thickness of these units at BM1 and BM3 is ~139 m.

At fault BC3 the West Butte Conglomerate and Olla Formations were ~31 and ~25 m thick, respectively; at fault BC1, the West Butte Conglomerate and Olla Formations were ~45 and ~35, respectively. However, projecting the dipping contact exposed to the west of the exposures of BC3 and BC1 indicates that ~71 m of the West Butte Conglomerate is missing at fault BC3 and ~129 m is missing at fault BC1. These inconsistencies suggest that the assumption of a planar contact is invalid. In these instances, a conservative estimate of the combined maximum overburden thickness of these formations at BC3 and BC1 is ~25 m and ~35 m; it is likely that the exposures of these faults are nearly at the top of the West Butte Conglomerate section.

The thickness of eroded West Butte Conglomerate above the faults in the Blow Sand Wash study area can be inferred by projecting the contact between the tonalite and the West Butte Conglomerate (east of the Coyote Creek fault) below the field sites. Using an average dip of 16º west for the West Butte Conglomerate and the assumption that the contact between the tonalite and the West Butte Conglomerate is a (locally) planar boundary, the contact should be ~120 m below the present surface at faults BS1 and BS2. However, the isopach map suggests that the West Butte Conglomerate was only ~120 m thick at this location and >10 m is exposed. Therefore, this section is likely near the top of the West Butte Conglomerate and only subject to an overburden thickness imposed by the Olla Formation (~45 m) and younger units.

The Butte Canyon and Blow Sand Wash faults are located near the core of the Borrego Mountain anticline where there were thinner accumulations of the West Butte Conglomerate and Olla Formation, whereas the faults in Borrego Mountain Wash are located on the flank of the anticline where these formations were thicker. However, these discrepancies give rise to differences in burial depths of ~100 m that are not sufficient to significantly affect the deformation mechanisms or the fluid chemistry.

2.1.4 Heat Flow and Geothermal Gradient at Borrego Mountain

Seismicity data and seismogenic thickness estimates for the San Jacinto fault zone indicate a shallowing of the maximum depth of seismicity from 19 km at the Anza segment in the north to 10–11 km at the Superstition Mountain and Superstition Hills segments in the south; this shallowing trend correlates with an increase in heat flow as the fault nears the Salton Trough (Doser and Kanamori, 1986; Sanders, 1987; Nazareth and Hauksson, 2004). It is noteworthy that a particularly high rate of change in seismogenic thickness occurs along the Coyote Creek segment; the thickness decreases 6 km over 41 km (an ~8˚ dip) relative to 2–3˚ dips in seismogenic thickness in the adjacent segments (Nazareth and Hauksson, 2004).

The southeastern portion of the Coyote Creek segment near Borrego Mountain has a seismogenic thickness of ~10 km. The present-day geothermal anomaly associated

with the active Salton Sea geothermal field is limited to the southeastern portion of the Salton Sea, although low-temperature geothermal springs and wells throughout the region indicate that geothermal activity is widespread; a cluster of these features occurs southeast of Borrego Mountain. Heat flow measurements in the Salton Sea region (from the U.S. Geological Survey heat flow database; http://earthquake.usgs.gov/heatflow/Maps/116-33.html) document high heat flow (>100 mW/m^2) in the vicinity of the Salton Sea. A borehole at Borrego Mountain (BRGO), located in tonalite along the West Butte fault near the junction of Hawk Canyon and Butte Canyon at an elevation of 192 m (Figure 2.1), penetrated 91 m and recorded a high heat flow of 195 mW/m^2 (Lachenbruch et al., 1985). Using a reasonable value of thermal conductivity in tonalite of 3.0 W/mK at 50˚C (Clauser and Huenges, 1995), the geothermal gradient at this point may be as high as 65˚C/km.

The close spatial correspondence between the San Jacinto fault and active geothermal activity in the Imperial Valley affects the mechanics of faulting (Hill et al., 1975). Observations and numerical models indicate that regions with high heat flow and fluid activity are associated with earthquake swarms, diffuse patterns of seismicity, a shallow base of the seismogenic zone, and fewer aftershocks (Ben-Zion and Lyakhovsky, 2006). The high level of swarm activity in the Salton Trough has been attributed to high geothermal gradients and earthquake triggering by aseismic creep and/or by fluid flow events (Lohman and McGuire, 2007).

2.2 Structural History of Borrego Mountain

The Borrego Mountain area contains exceptional exposures of extensive deformation associated with slip along the West Salton detachment fault zone (WSDF) and slip on the Coyote Creek fault of the southern San Jacinto fault zone (SJFZ) (Figure 1.1). The structural history of Borrego Mountain was influenced by activity along the WSDF from the latest Miocene to the early Pleistocene, and slip along multiple strands of the dextral Coyote Creek fault from early Pleistocene to the present. Steely (2003) interpreted the multiple generations of faults and folds at Borrego Mountain as the

result of three distinct episodes of Late Cenozoic deformation: (1) extension on the WSDF; (2) an early phase of transtensive strike-slip activity on the SJFZ; and (3) ongoing transpressive deformation along the SJFZ beginning at ca. 0.6 Ma (Lutz et al., 2006; Kirby et al., 2007). The initial stage of transtensive deformation along the SJFZ has been correlated with large extensional stepovers within the fault zone, including a north-striking fault east of Coyote Mountain that connects the Clark and Coyote Creek faults (Figure 1.1) (Bartholomew, 1968, 1970; Dorsey, 2002; Steely, 2003). This transtensive phase of deformation may be characterized at Borrego Mountain by the north-striking normal faults that are particularly prevalent around East Butte (Figure 2.1).

With the exception of some normal faults that appear to be confined to the tonalite, the majority of faulting at Borrego Mountain affects the Pliocene West Butte Conglomerate and therefore must be Pliocene or younger (Figure 2.1). There have been several significant historical earthquakes along the northeast strand of the Coyote Creek fault adjacent to Borrego Mountain. Sparse seismicity throughout the Borrego Mountain area suggests that at least some of these secondary structures are both seismogenic and currently active. A map and discussion of the historical seismicity of this region is included in Chapter 5. There is a distinct dearth of seismicity recorded from 1981—2005 at Borrego Mountain relative to the surrounding regions within a comparable distance from the Coyote Creek fault. This relative lack of seismicity at Borrego Mountain may be related to the exposed basement rocks and significantly thinner package of sediments than in the surrounding areas.

Uplift at Borrego Mountain has been attributed to deformation associated with a restraining bend in the Coyote Creek fault (Steely, 2006). However, there is a distinct absence of thrust and reverse faults that typically characterize pop-up structures (e.g., McClay and Bonora, 2001) at Borrego Mountain, and abundant evidence for extensional deformation. The nearby Ocotillo Badlands are in a similar location relative to a different restraining bend along the Coyote Creek fault to the east, and

deformation is primarily contractional in the Ocotillo Badlands. The compressional folds at Borrego Mountain are interpreted to be hanging-wall deformation associated with oblique slip on the WSFD and therefore predate the Coyote Creek fault. The northwest-striking faults examined in this study originated as dilatant fractures and are oriented nearly parallel to the predicted orientation for subsidiary extensional features based on a dextral strain ellipse model. Analog models of restraining bends along strike-slip faults predict that the deformation should be concentrated at the bend (McClay and Bonora, 2001). In contrast, other workers have shown on the basis of field observations that whereas deformation along dilational bends is generally concentrated in the bend, deformation associated with restraining bends involves distributed strike-slip faulting over a broad region (Das and Scholz, 1981; Sibson, 1986).

2.2.1 Borrego Mountain Folds

The main fold in the Borrego Mountain area is the northwest-trending Borrego Mountain anticline. There are several other northwest- and north-trending folds throughout the area (Figure 2.1).

2.2.1.1 Borrego Mountain Anticline

The Borrego Mountain anticline (Figure 1.1) is a northwest-trending feature that corresponds with a gravity high that continues to the northwest but not to the southeast (Steely, 2006). This basement-cored structure is interpreted as a growth anticline that developed in the hanging wall of the WSDF. Significant variation in the thickness of the Hawk Canyon Formation, the West Butte Conglomerate (Figure 2.2), and the Olla Formation indicate that the anticline was active at the surface throughout the Pliocene (Steely, 2006). Gravity data suggest that the Borrego Mountain anticline and the east-west-trending San Felipe Hills anticline may be continuous at depth; the Borrego Mountain anticline may have originally formed as an east-west trending fold that has since been rotated into its current position (Steely, 2006; Kirby et al., 2007). Most of

the folding at Borrego Mountain has a northwest trend and may be associated with the Borrego Mountain anticline.

2.2.1.2 Other Folds at Borrego Mountain

There are several north-trending, south-plunging folds near Middle Butte within a region that is bounded to the west by the West Butte fault and to the east by the southwest strand of the Coyote Creek fault (Figure 2.1) (Steely, 2003). These folds may be related to the set of north-striking normal faults at Borrego Mountain that includes East Butte fault, West Butte fault, and a suite of faults in the tonalite basement at East Butte.

2.2.2 Borrego Mountain Faults

Northwest of Borrego Mountain, the Coyote Creek segment of the San Jacinto fault passes through a restraining bend and divides into two distinct strands (Figure 1.1). The northeast strand of the Coyote Creek fault bounds the northeast side of East Butte; the southwest strand separates and offsets Middle Butte and East Butte. In addition to the main strands of the Coyote Creek fault, there are many faults throughout the Borrego Mountain area. The subsidiary faults can be divided into four main sets: (1) north-northeast- and east-northeast-striking, steeply dipping, strike-slip to oblique-slip faults; (2) northwest-striking, steeply dipping, strike-slip to oblique-slip faults; (3) north-striking normal faults; and (4) east-striking normal faults (Figure 2.1).

2.2.2.1 Coyote Creek Fault

The 80 km long Coyote Creek segment of the SJFZ that traverses through Borrego Mountain has been the subject of numerous geodetic, seismological, and paleoseismological investigations (Clark, 1972; Sanders, 1989; Rockwell et al., 1990a; Rockwell et al., 1990b; Petersen et al., 1991; Magistrale, 2002). The northwest portion of the Coyote Creek fault zone may have hosted slip as early as ~1.0 Ma (Dorsey, 2002). However, several lines of evidence suggest that the Coyote Creek fault did not propagate southeast to the Borrego Badlands until ca. 0.6 Ma: (1) west of the Borrego

Badlands, folding along the San Felipe anticline on both sides of the Coyote Creek fault predates the deposition of the ca. 0.6 Ma Fonts Point sandstone but affects older units; folding had likely ceased before the Coyote Creek fault was established in this area (Lutz et al., 2006); (2) coarse-grained facies of the Ocotillo Formation conformably overlie lacustrine facies near the Borrego Badlands; this transition suggests that there was a significant structural reorganization of the SJFZ in this region at ca. 0.6 Ma (Lutz et al., 2006); (3) stratigraphic evidence suggests that initiation of the northeast-striking Inspiration Point fault and associated folds that caused uplift of the Borrego Badlands and the San Felipe Hills also correlates with the initial deposition of the Fonts Point sandstone at ca. 0.6 Ma (Lutz et al., 2006; Kirby et al., 2007). The Coyote Creek fault may have propagated ~5 km southeast of the Borrego Badlands to Borrego Mountain at this time or possibly sometime thereafter; this timing has not yet been constrained (Steely, 2003).

There is evidence for 5–6 km of slip along the Coyote Creek fault northwest of Borrego Mountain (Sharp, 1967; Dorsey, 2002), although it is unclear how this slip is partitioned along the strands of the Coyote Creek fault that pass through the Borrego Mountain area. Restoration of the depositional contact between the tonalite and the West Butte Conglomerate on Middle Butte with the same contact on East Butte indicates a minimum of ~1.6 km of dextral separation along the southwest strand of the Coyote Creek fault through Borrego Mountain (Figure 2.1) (Steely, 2003). It is difficult to determine the amount of displacement on the northeast strand of the Coyote Creek fault due to a lack of piercing points (Steely, 2003). The northeast and southwest strands of the Coyote Creek fault offset all other faults in the area. There is abundant evidence of Holocene activity on the northeast strand of the Coyote Creek fault at Borrego Mountain, including the 1968 M_w 6.5 Borrego Mountain earthquake. It is possible that slip along the Coyote Creek fault has been transferred from the southwest strand to the northeast strand (Steely, 2003).

Earthquake History on the Coyote Creek Fault

The 1968 M_w 6.5 Borrego Mountain earthquake occurred at 8 km depth and ruptured ~33 km of the San Jacinto fault zone (Clark, 1972). The surface break consisted of three rupture strands separated by antidilational and dilational jogs. The rupture caused up to 38 cm of mostly right-lateral motion on the northern strand; some vertical, down-to-the-northeast, motion was also observed (Allen et al., 1968; Clark, 1972; Sharp and Clark, 1972). The northern rupture strand (adjacent to Borrego Mountain) had the largest initial surface offset, relatively few aftershocks, and little afterslip; the southern strand hosted more aftershocks (Allen and Nordquist, 1972; Clark, 1972; Burdick and Mellman, 1976; Sibson, 1986). Afterslip has been documented along the central and south strands and is spatially coincident with the thick package of sediment adjacent to these strands (Burford, 1972). Dense concentrations of aftershocks occurred adjacent to the jogs between the segments (Das and Scholz, 1981; Sibson, 1986).

A 3 km step separates the Coyote Creek fault from the Superstition Mountain fault. At Carrizo Wash there is paleoseismic evidence for 8 surface rupturing events along the northernmost Superstition Mountain fault, all of which predate the A.D. 1680 Lake Cahuilla high stand deposits but have occurred in the past 1100 years (Ragona et al., 2003; Verdugo et al., 2005). Correlation between the paleoseismic histories of the Superstition Mountain fault and the southern Coyote Creek fault suggests that in most large earthquakes (~2 m of slip per event) that initiated along the Superstition Mountain fault, the southern segment of the Coyote Creek fault also ruptured (Gurrola and Rockwell, 1996; Ragona et al., 2001; Ragona et al., 2003; Verdugo et al., 2005). In contrast, the central Coyote Creek fault has ruptured repeatedly during the past 300 years in '1968-type events' (30–50 cm of slip), with 1.4 m of cumulative slip after A.D. 1680; most of these ruptures did not propagate onto the Superstition Mountain fault (Pollard and Rockwell, 1995; Ragona et al., 2003; Verdugo et al., 2005). A trench site located within the southern break of the Coyote Creek fault revealed evidence for up to 11 events; only two of these (including 1968) ruptured the site after A.D. 1600 (Ragona et al., 2003). These data suggest that only some of the frequent 1968-type

central Coyote Creek fault events rupture the southern segment of the Coyote Creek fault, whereas nearly all of the Superstition Mountain fault events rupture this segment. The southern Coyote Creek fault apparently behaves as an extension of the Superstition Mountain fault and has a distinct rupture history from the northern and central strands (Orgil et al., 2001; Ragona et al., 2001).

The 1987 M_w 6.2 Elmore Ranch and M_w 6.6 Superstition Hills events occurred within 12 hours of each other ~20 km to the south of Borrego Mountain and ruptured both the Superstition Hills fault and a cross fault. These earthquakes produced triggered slip along the Coyote Creek segment, including surface ruptures along the central break (Hudnut and Clark, 1989; Hudnut and Sieh, 1989).

2.2.2.2 Subsidiary Faults at Borrego Mountain

In addition to the northwest-striking strands of the Coyote Creek fault, there are several other sets of faults throughout Borrego Mountain. Two major sets of normal faults include north-striking, east-dipping faults and east-striking, north-dipping faults (Figure 2.1). Two prominent sets of steeply dipping strike-slip faults include northeast- and northwest-striking faults.

North- and East-Striking Normal Faults

There are two prominent sets of normal faults at Borrego Mountain: (1) north-striking, moderately east-dipping normal faults (including the West Butte and East Butte faults); and (2) east-striking, steeply-to-moderately north-dipping normal faults. The north-striking, east-dipping, West Butte fault separates the eastern edge of West Butte from Middle Butte, juxtaposes Palm Spring Group against tonalite, and shows evidence of ~550 m of dip-slip displacement (~370 m of dextral separation) (Figure 2.1) (Steely, 2006). Several smaller north-striking normal faults occur within the hanging-wall of the West Butte fault; these faults are deformed by northwest-trending folds (Steely, 2003). The east side of East Butte is bound by the East Butte fault, a normal fault with ~400 m of displacement (~270 m of dextral separation) that also juxtaposes Palm Spring Group against tonalite (Figure 2.1) (Steely, 2006). There are many large north-

striking normal faults within East Butte. The east-striking normal faults are confined to the basement tonalite on East Butte (although an east-striking lineament in the tonalite of West Butte may also indicate a fault from this set) and generally appear to predate faulting along the north-striking normal faults.

Northeast- and Northwest-Striking, Steeply Dipping Faults

Northeast- and northwest-striking, sub-vertical strike-slip faults are exposed throughout Borrego Mountain. The northeast-striking faults generally have smaller offsets, although several northeast-striking faults along the northeast side of East Butte have caused ~360 m of left-lateral displacement of the contact between the basement tonalite and the West Butte Conglomerate (Figure 2.1) (Steely, 2003). It is difficult to determine the sense and amount of offset along faults that do not juxtapose different lithologies, due to a lack of marker beds (Steely, 2003). There is no systematic relationship between the relative timing of slip on the northwest- and northeast-striking strike-slip faults; there are instances where northwest-striking faults offset northeast-striking faults, instances where the reverse is true, and instances where northwest-and northeast-striking faults appear to intersect with no apparent offset of either fault (Steely, 2003). Steeply dipping faults with both northwest- and northeast-striking orientations appear to offset the normal faults on Borrego Mountain, with the exception of the West Butte and East Butte faults, which are only clearly displaced along strands of the Coyote Creek fault (Figure 2.1).

Chapter 3: Structural Evolution and Damage-Zone Development Along Small Displacement Strike-Slip Faults Adjacent to the Southern San Jacinto Fault Zone, Borrego Mountain, California, USA

3.1 Summary

Fault damage zones are commonly organized into fault-parallel domains. The paleo-damage zone model introduced herein posits that damage-zone deformation represents the accumulation of deformation from multiple paleo-damage zones that were each associated with unique slip events on a fault; distinct fault-parallel damage-zone domains are a result of the superimposition of paleo-damage zones with variable widths. This model provides a framework to evaluate contrasting models for the chronological and spatial development of damage zones. Integrated field and microstructural observations indicate that small displacement strike-slip faults within laumontite-cemented sandstones adjacent to the San Jacinto fault zone in the western Salton Trough region originated as dilational fractures and exhibit evidence of episodic fracturing, fluid flow, and cataclasis. The geometry of the damage-zone deformation resembles a structural mesh, with polymodal fracture patterns. Step-wise decreases in fracture density with increasing perpendicular distance from the fault cores define relatively sharp domain boundaries. However, the spatial extents of various deformation features are not coincident with these boundaries. The number of earthquakes hosted on each fault exceeds the number of structural domains. Based on the extensive evidence for fracture reactivation, it is inferred that damage-zone architecture was established early in the slip history of each fault, possibly during the first few events, and preserved during subsequent slip events. These small displacement fault zones contain a record of episodic seismic activity that may be related to earthquake swarms.

3.2 Introduction

In many fault zones, the fault core accommodates the majority of slip along principal slip surface(s) and the core is embedded within a zone of host rock that has sustained

significant fault-related deformation, termed the “damage zone” (Chester et al., 1993; Chester and Chester, 1998; Sibson, 2003; Biegel and Sammis, 2004). Damage zones may be tabular (relatively uniform in width), wedge-shaped (wider towards the surface of the earth), or irregular in shape, and typically contain a wide array of mesoscopic and microscopic deformation features, including open fractures, cemented fractures (veins), and secondary faults (Ben-Zion and Sammis, 2003; Kim et al., 2004). The density of deformation within fault damage zones generally decreases with perpendicular distance from the fault core; the outer extent of the damage zone is defined by where the density of deformation is equivalent to the average regional (background) level of deformation in the surrounding host rock (Chester, 1995). Damage-zone deformation has been shown to result from fault slip at a range of velocities, including quasistatic velocities that are slow enough that no energy is radiated (Cowie and Scholz, 1992b), and seismic velocities on the order of 0.1–1.0 meters/second (Poliakov et al., 2002). During earthquake slip events, a portion of the released energy is partitioned into fracture energy, which is responsible for off-fault deformation within the damage zone (Kanamori, 2004; Chester et al., 2005).

Damage zones contain a valuable record of fault slip history, as deformation is generated or reactivated within damage zones during each fault slip event. Many workers have recognized that damage zones have a complex internal structure, and different fault-parallel domains may be delineated on the basis of geological observations (e.g., petrological differences, variation in microfracture density and/or orientation), and seismological observations (e.g., velocity structure, trapped waves) (Schulz and Evans, 2000; Li and Vernon, 2001; Sayed, 2001; Spudich and Olsen, 2001; Wilson et al., 2003). Damage-zone architecture affects fault mechanics (e.g., Ben-Zion and Sammis, 2003), the propagation of seismic waves (Ben-Zion et al., 2003), and fault-zone fluid flow and fault sealing behavior (Caine et al., 1996; Evans et al., 1997; Fisher and Knipe, 1998).

If structural elements in the damage zone are created or reactivated during each fault slip event, it is useful to introduce the term "paleo-damage zone" to describe damage that was active during a unique previous slip event. The manifestation of a fault damage zone at any point in time is the cumulative picture of deformation from multiple paleo-damage zones that were each associated with unique slip events on the fault (Figure 3.1). Distinct fault-parallel damage-zone domains may be a result of variable paleo-damage zone width throughout the history of fault development; each domain can be correlated with one or more paleo-damage zone(s), or slip event(s) (Figure 3.1).

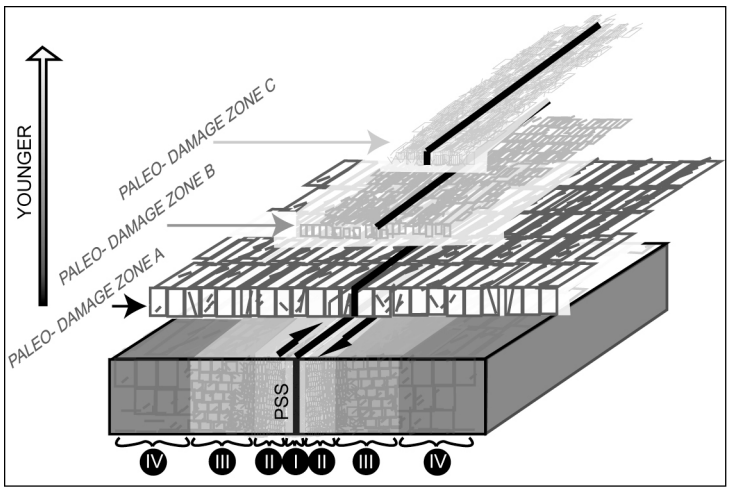

Figure 3.1. Schematic illustration of a fault zone that has accumulated damage during three distinct slip events, each event has a corresponding paleo-damage zone. The paleo-damage zones depict the extent of the actively deforming zone associated with each event. The overprint of multiple paleo-damage zones with variable widths results in a complex composite damage zone that appears to be organized into distinct fault-parallel domains, indicated with different shades of gray and Roman numerals.

The paleo-damage zone model does not include a description of how the density of deformation within each paleo-damage zone varies with perpendicular distance from the fault core. However, an inherent assumption in this model is that the density of deformation associated with an individual slip event decays with perpendicular distance from the fault core along some continuous function, or possibly remains constant over the width of the paleo-damage zone. A premise of the paleo-damage zone model is that an individual slip event is not expected to generate step-wise decreases in

deformation density with perpendicular distance from the fault core. Therefore, step-wise changes in the density of damage-zone deformation must represent the collective signature of multiple slip events that produced deformation with variable spatial extents. The paleo-damage zone theory provides a framework to evaluate different theoretical models that describe how the spatial distribution of damage changes over time.

Many field-based investigations of exhumed strike-slip faults describe damage-zone deformation along large displacement faults, including the Punchbowl and San Gabriel faults in southern California (Chester et al., 1993), the Carboneras fault in southeastern Spain (Faulkner et al., 2003), and the Median Tectonic Line in southwest Japan (Wibberley and Shimamoto, 2003). These mature fault zones have hosted a large number—perhaps thousands—of slip events, and complex deformation within their damage zones reflects the superimposition of many cycles of deformation and healing. Ideally, the most instructive way to explore fundamental relationships between the mechanical processes that operate along faults and the resultant structural architecture is to correlate deformation features within the damage zone with individual slip events. Towards this end, it is advantageous to study small displacement faults that have hosted relatively few slip events and have less damage-zone complexity. The detailed characterization of damage-zone architecture along small faults provides an opportunity to investigate the early phases of fault-zone development. This study examines the spatio-temporal development of damage-zone deformation along small displacement strike-slip faults at Borrego Mountain, adjacent to the seismogenic San Jacinto fault zone in southern California (Figure 3.2). Fracture density analysis is used in combination with field observations to determine the dimensions of distinct damage-zone domains. Integrated field and microstructural observations are used to reconstruct the temporal and spatial evolution of damage-zone deformation and to determine whether the observed damage-zone domains were established early or late during fault history.

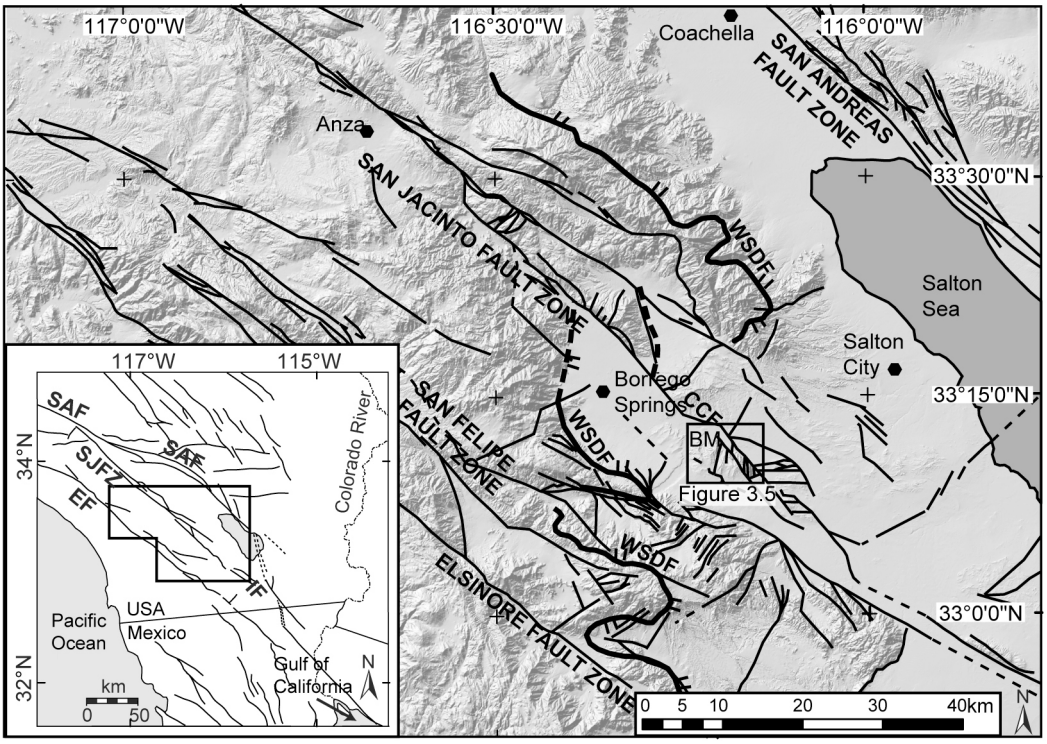

Figure 3.2. Regional map of the Salton Trough shows major cities, the surface traces of major Quaternary fault zones, and the *WSDF*, West Salton detachment fault, overlain on a DEM (modified from Steely, 2006). *BM,* Borrego Mountain, is shown in detail in Figure 3.4. Inset: Fault map of Southern California (modified from Lutz et al., 2006). *EF*, Elsinore fault; *IF*, Imperial fault; *SAF*, San Andreas fault; *SJFZ*, San Jacinto fault zone.

3.3 Mechanical Models of Damage Accumulation

Two important published models for fault-zone development, the process-zone model and the slip-localization model, provide explanations for the accumulation of fault-related damage. Although neither of these models specifically addresses the development of distinct damage-zone domains, the models make contrasting predictions about whether damage-zone architecture is established during the early or late stages of fault slip history.

3.3.1 Process-Zone Model

The process-zone model is based on linear elastic fracture mechanics, which has traditionally been used to describe fracture and fault growth by tip propagation. Vermilye and Scholz (1998) used cohesive-zone theory (a modified version of linear

elastic fracture mechanics) to demonstrate that quasistatic fault growth involves distributed fracturing in the region surrounding the tip of a propagating fault, the "process zone" (Dugdale, 1960; Cowie and Scholz, 1992b). Damage zones are interpreted as inactive process zones that remain along the border of faults during subsequent phases of growth. Several workers have used field and experimental data to determine scaling relationships between the width of process zones and the length of faults (Cowie and Scholz, 1992a; Scholz et al., 1993; Anders and Wiltschko, 1994; Vermilye, 1996; Shipton et al., 1997; Vermilye and Scholz, 1998; Janssen et al., 2001; Shipton and Cowie, 2003). The process-zone model predicts that with increasing fault length, the process zone increases in width, and therefore the paleo-damage zone associated with the most recent growth event likely overprints previous paleo-damage zones. In the field manifestation of this configuration, the youngest deformation in the damage zone would be located on the outside, farthest from the fault core (Figure 3.3A). The process-zone model is consistent with damage zones continually accruing deformation and damage-zone architecture evolving throughout fault history.

3.3.2 Slip-Localization Model

The slip-localization model is based on the observation that fault slip generally becomes increasingly localized on discrete surfaces with continuous displacement along large displacement faults, and faults at various scales that develop along preexisting weaknesses (Ben-Zion and Sammis, 2003; Sibson, 2003). Detailed observations of structural architecture along the large displacement San Gabriel, Kern Canyon, and Punchbowl faults reveal a relatively narrow (<2 m wide) fault core that is indicative of a strain-weakening rheology characterized by strain localization and strength reduction (Chester et al., 1993; Evans and Chester, 1995; Chester and Chester, 1998; Schulz and Evans, 2000). Martel et al. (1988) observed a similar structural architecture and evidence of slip localization along faults with up to 150 m of slip in the Sierra Nevada that developed along preexisting cooling joints. Deformation-band faults in aeolian sandstones in the Colorado Plateau region are also thought to have

evolved by the establishment of a throughgoing slip surface along preexisting deformation bands (e.g., Shipton and Cowie, 2003). The apparent localization of slip within a narrow fault core along faults with varying amounts of displacement suggests that slip localization may occur at a very early stage of fault development, and the damage zone contains relict deformation from the incipient phases of fault growth (Ben-Zion and Sammis, 2003). The process of slip localization is compatible with the prediction that the oldest record of deformation in the damage zone should be located at the outermost extent of the damage zone (Wilson et al., 2003) (Figure 3.3B).

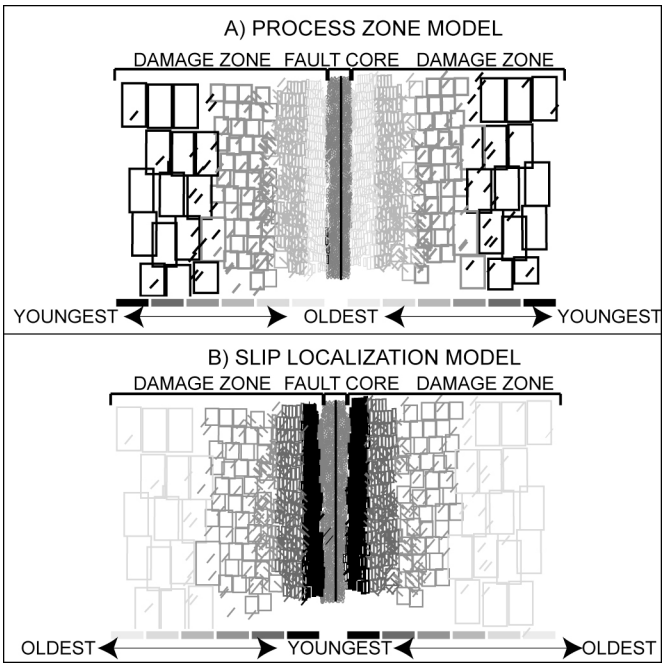

Figure 3.3. Schematic depiction of contrasting models for the temporal accumulation of damage (darker shades are used to represent younger damage). (A) In the process-zone model, the width of the damage zone increases over time. (B) In the slip-localization model, the width of the damage zone decreases over time.

These different models for damage accumulation provide a context in which to analyze the spatial and temporal development of the damage zone. The process-zone model predicts that damage-zone architecture continually evolves and widens with increasing fault length and displacement (Figure 3.3A). In contrast, the slip-localization model predicts that damage-zone architecture is established early in the fault history and represents relict deformation from the early stages of fault growth. In this study, the

record of damage-zone deformation along small displacement faults will be evaluated in the context of the paleo-damage zone model to determine whether damage-zone architecture was established early or late in the history of the faults. The paleo-damage zone model also affords an investigation of how the number of observed domains relates to the number of slip events along the faults.

3.4 Tectonic and Geologic Setting

Recent work in the western Salton Trough region of southern California has addressed the complex late Tertiary–Quaternary tectonic evolution of this region and provides a comprehensive geological framework for the detailed structural analysis of faults at Borrego Mountain (Figure 3.2) (e.g., Dorsey, 2002; Dorsey and Janecke, 2002; Lutz and Dorsey, 2003; Janecke et al., 2004; Steely et al., 2004a; Steely et al., 2004b; Dorsey et al., 2005; Housen et al., 2005; Janecke et al., 2005; Kairouz, 2005; Kirby, 2005; Lutz, 2005; Shirvell et al., 2005; Steely et al., 2005b; Dorsey and Roering, 2006; Lutz et al., 2006; Steely, 2006; Dorsey et al., 2007; Kirby et al., 2007). Late Tertiary sedimentary strata at Borrego Mountain were deposited in a fluvial-deltaic environment between the ancestral Colorado River and the Gulf of California (Dibblee, 1954; Morley, 1963; Woodard, 1963; Hoover, 1965; Winker and Kidwell, 1996; Axen and Fletcher, 1998; Steely, 2006). These strata contain a record of syndepositional deformation along the northwest-striking oblique-slip West Salton detachment fault from ca. 6 Ma until slip initiated along the dextral strike-slip San Jacinto fault zone at ca. 1.1 Ma (Axen and Fletcher, 1998; Lutz et al., 2006; Kirby et al., 2007).

Abundant youthful strike-slip and oblique-slip faults at Borrego Mountain represent subsidiary deformation associated with a restraining bend in the Coyote Creek segment of the southern San Jacinto fault zone to the northwest (Figures 3.2 and 3.4) (Steely, 2006). Excellent exposures of faults at Borrego Mountain provide an opportunity to examine damage-zone evolution along small displacement (<5 m) faults that are associated with a mature, seismogenic fault zone and are reasonably inferred to have been seismically active.

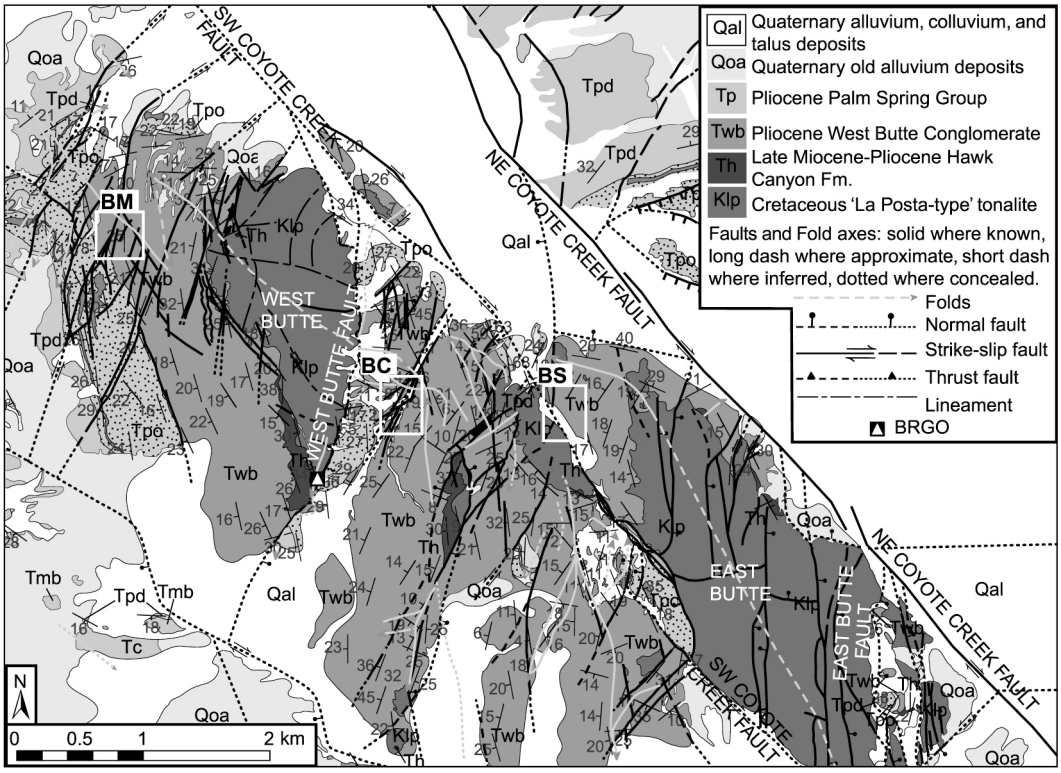

Figure 3.4. Geology of the Borrego Mountain area (modified from Steely, 2006); location is shown on Figure 3.2. Study areas are indicated with white boxes; *BM*, Borrego Mountain Wash; *BC*, Butte Canyon Wash; *BS*, Blow Sand Wash.

Ongoing deformation in the current transpressive regime along the Coyote Creek fault probably commenced at ca. 0.6 Ma at the latitude of Borrego Mountain as the fault propagated southeast (Lutz et al., 2006; Kirby et al., 2007); this estimate provides a maximum age for the subsidiary faults described in this study.

3.4.1 West Butte Conglomerate

The faults selected for detailed analysis in this study are exposed within the conglomeratic, laumontite-cemented, poorly to very poorly sorted sandstones of the Pliocene West Butte Conglomerate (Figure 3.5).

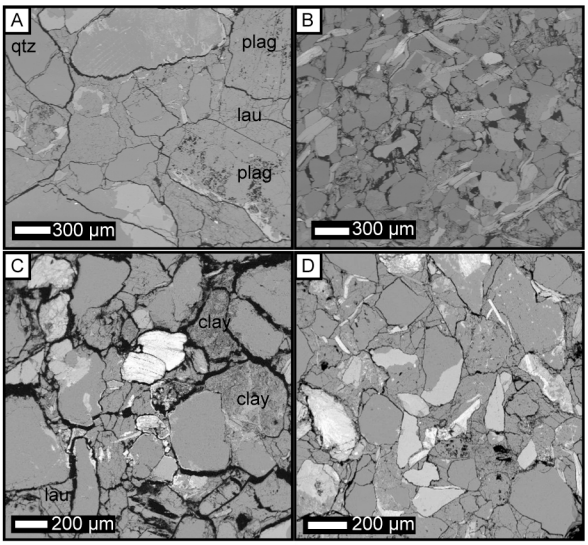

Figure 3.5. BSE photomicrographs of unaltered host rock from faults (A) BM2, (B) BS1, (C) BC3, and (D) BM1; *qtz*, quartz; *plag*, plagioclase; *lau*, laumontite; *clay*, detrital clay. (A) Partially dissolved plagioclase grains retain unaltered primary shapes. (B) Aligned micas in the host rock indicate that minor mechanical compaction predated laumontite cementation. (C) Host rock contains laumontite cement and a high proportion of detrital clay. (D) Host rock contains laumontite cement and partially dissolved feldspars.

The West Butte Conglomerate has been interpreted as alluvial fan or bajada deposits that represent the fluvial equivalent of the marine Pliocene Imperial Group; lithic clasts were derived from the footwall and damage zone of the West Salton detachment fault (Steely, 2006). The West Butte Conglomerate was folded syndepositionally along the northwest-trending Borrego Mountain anticline during slip on the West Salton detachment fault and is 0–280 m thick at Borrego Mountain (Steely, 2006). The estimated maximum burial depth of the faults in this study was ~3.0 km since the inception of faulting (see Section 2.1.3); this calculation is based on isopach maps of the West Butte Conglomerate and overlying Olla Formation (Steely, 2006), and other published data on the stratigraphic thicknesses of younger strata (Morley, 1963; Steely, 2006).

3.4.2 Field Localities

Ideally, the complete extent of fault-related deformation may be identified if the exposure of a fault zone is nearly orthogonal to the fault strike and the damage zone is exposed on both sides of the fault core and flanked by exposed host rock with

'background' levels of deformation. Two scenarios commonly interfere with this ideal situation: (1) erosion or cover may limit the exposure, and (2) deformation associated with adjacent faults can make it difficult to isolate the deformation related to the fault of interest. The seven small displacement strike-slip faults in this study were carefully selected from a large population of faults exposed at Borrego Mountain in an effort to minimize these complications.

The selected faults are exposed along three different washes at Borrego Mountain (fault locations are provided in Table 3.1): faults BM1, BM2 and BM3 from Borrego Mountain Wash (BM, Figure 3.4), faults BC1 and BC3 from Butte Canyon Wash (BC, Figure 3.4), and faults BS1 and BS2 from Blow Sand Wash (BS, Figure 3.4). The three study areas were mapped using aerial photo interpretations and field observations to provide local contexts for the detailed analysis of the selected faults (Figure 3.6).

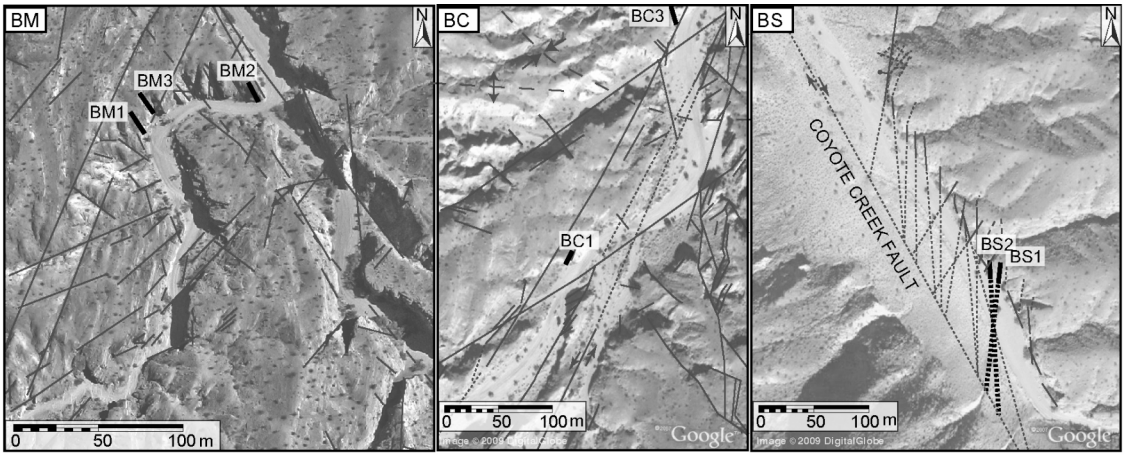

Figure 3.6. Fault maps of the study areas, *BM*, Borrego Mountain Wash; *BC*, Butte Canyon Wash; *BS*, Blow Sand Wash. Aerial photos (BM courtesy of Kelly McCague; BC, BS from Google Earth) were used as base maps to document the many smaller faults within the study areas. Faults, solid black lines (dotted where inferred) were mapped based on aerial photo interpretation and field checking; fold axes, dashed, from Steely (2006). Faults BM1, BM3, BM2, BC1, BC3, BS1 and BS2, shown as thick black lines, were selected for detailed analysis in this study.

Field observations indicate that the majority of the faults in these study areas are strike-slip, although some are oblique-slip with a dominantly strike-slip component of displacement. Multiple slip surfaces with variably oriented striae are present within many of these fault zones and provide evidence that slip occurred in different

directions. It is difficult to determine the dominant slip direction and total amount of displacement along the majority of these faults due to a lack of exposure of potential offset markers in map view.

3.4.3 Sheared Joints

Two distinct categories of faulting mechanisms have been documented in sandstones: deformation band faulting and shearing along joints (open fractures) (Aydin et al., 2006, and references therein). The damage zones of deformation band faults are dominantly composed of deformation bands (tabular bands of shear and volumetric deformation), whereas the shearing of joints produces joints, sheared joints, fragmented rock and fault gouge (Davatzes and Aydin, 2003). The contrasting styles of deformation may be distinguished on the basis of the dominant deformation features in the fault damage zones and from observations of nearby deformation zones that lack throughgoing slip surfaces, as these likely represent the deformation states that preceded faulting (Myers and Aydin, 2004). In the Borrego Mountain area, there are open and cemented fractures (with associated deformation and chemical alteration) throughout the region, only some of which are associated with throughgoing slip surfaces. Laumontite veins are commonly surrounded by bleached zones and are more abundant in close proximity to faults. Because the fault zones described in this study are flanked by open and cemented fractures with no displacement, it is reasonable to infer that they initiated as similar dilatant fractures (Figure 3.7). However, the clear increase in the density of deformation closer to the examined faults indicates that the majority of damage-zone deformation developed as a result of fault slip and not as a precursor to faulting. Furthermore, no deformation bands are observed in the field. Therefore, these faults are best described as sheared joints.

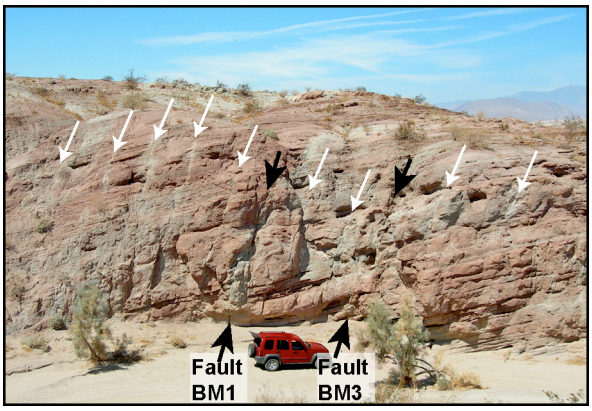

Figure 3.7. Photograph includes faults BM1 and BM3 (black arrows) and surrounding deformation, which consists of open and cemented fractures. White arrows highlight prominent altered fractures. The green alteration of the red sandstone is a result of laumontite precipitation.

There is substantial evidence of downdip segmentation within strike-slip fault zones at Borrego Mountain: vertically restricted steep fault segments are linked along bedding-parallel slip planes localized in mechanically weak stratigraphic units (see Chapter 5 or Nemser and Cowan (2009, *in press*) for a discussion of downdip segmentation). Observed stepover geometries provide additional evidence that these faults likely originated as extensional fractures: several authors have proposed that faults with stepovers may have inherited their segmented geometry from preexisting joint configurations (Crider and Peacock, 2004; Myers and Aydin, 2004).

3.4.3.1 Borrego Mountain and Butte Canyon Washes

The study areas along Borrego Mountain Wash and Butte Canyon Wash are within complex zones of faulting at the intersection of major NW-, NNE-, and ENE-striking strike-slip to oblique-slip faults (Figure 3.6). These three main sets of faults occur at a variety of scales; faults from each of these sets appear as lineaments on high-resolution aerial photos (Figure 3.6). Selected faults BM1, BM3, BM2, and BC3 belong to the set of NW-striking faults; fault BC1 belongs to the set of NNE-striking faults. The NNE-striking set of faults includes the longest faults in both study areas. In Borrego Mountain Wash, the ENE-striking faults are shortest and the NW-striking faults are

intermediate in length, whereas the opposite is the case in the vicinity of Butte Canyon Wash.

The Riedel shear zone model for simple shear provides a structural framework for the analysis of subsidiary structures in complex shear zones (Figure 3.8). Experimental work suggests that the (synthetic) R shear fractures and the (antithetic) R' shear fractures typically form first as conjugate faults to the direction of imposed maximum compression, at angles of about $\phi/2$ and $90^{\circ}-\phi/2$ to the main fault, respectively, where ϕ is the angle of internal friction (Riedel, 1929; Tchalenko, 1970; Logan et al., 1979; Katz et al., 2004). The P and Y faults form later with an increase in shear strain.

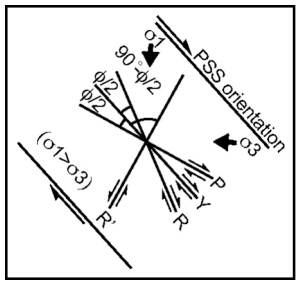

Figure 3.8. Schematic illustration of the Riedel shear model for dextral simple shear; the PSS orientation has been rotated parallel to the Coyote Creek fault to facilitate the comparison. This model is based on the assumption that the Coulomb failure criterion is valid. σ_1, maximum principal stress σ_3, minimum principal stress; ϕ, angle of internal friction (modified from Flodin and Aydin, 2004).

In the context of this model, the three major NNE-striking, sinistral strike-slip faults that extend from the southwest strand of the Coyote Creek fault to another (unnamed) NW-striking dextral strike-slip fault southwest of Borrego Mountain in the vicinity of Borrego Mountain Wash are consistent with the antithetical slip sense and orientation of R' structures (Figure 3.4). The northernmost portions of these sinistral faults may have been rotated out of their original orientation by drag along the southwest strand of the Coyote Creek fault. The smaller-scale NNE-striking faults in the Butte Canyon Wash study area are subparallel and apparently related to these major NNE- striking faults. The West Butte fault that bounds the east side of West Butte is also subparallel to the three major sinistral faults and may have initiated as an R' structure with left-lateral slip and subsequently been reactivated as a normal fault (Figure 3.4).

3.4.3.2 Blow Sand Wash

The study area along Blow Sand Wash includes two sets of *en-echelon*, steeply dipping oblique-slip faults (NNW-striking and NNE-striking) immediately adjacent to the southwest strand of the Coyote Creek fault (Figure 3.6). The traces of faults BS1, BS2, and other NNW-striking faults along Blow Sand Wash are oriented ~30° clockwise from the mapped trace of the southwest Coyote Creek fault (the fault intersections are obscured because the Coyote Creek fault is covered in Blow Sand Wash) (Figure 3.6). The second set of *en-echelon* faults is NNE-striking and oriented ~60° to the Coyote Creek fault. These conjugate fault sets likely represent horsetail and splay fractures associated with the propagation of the Coyote Creek fault through Borrego Mountain.

3.5 Methodology

3.5.1 Fault Maps

A 1-meter reference grid was placed over each fault zone using a horizontal hand leveler and a plumb bob. High-resolution photographs were acquired parallel to the strike of the dominant principal slip surface within each fault zone, with substantial (~40%) overlap between adjacent photos. High-resolution photomosaics were composed and rectified for each fault zone using the Stitcher Express 2.0 panorama creation software and used as base maps for detailed fault maps that include all mesoscopic structural elements (Figure 3.9).

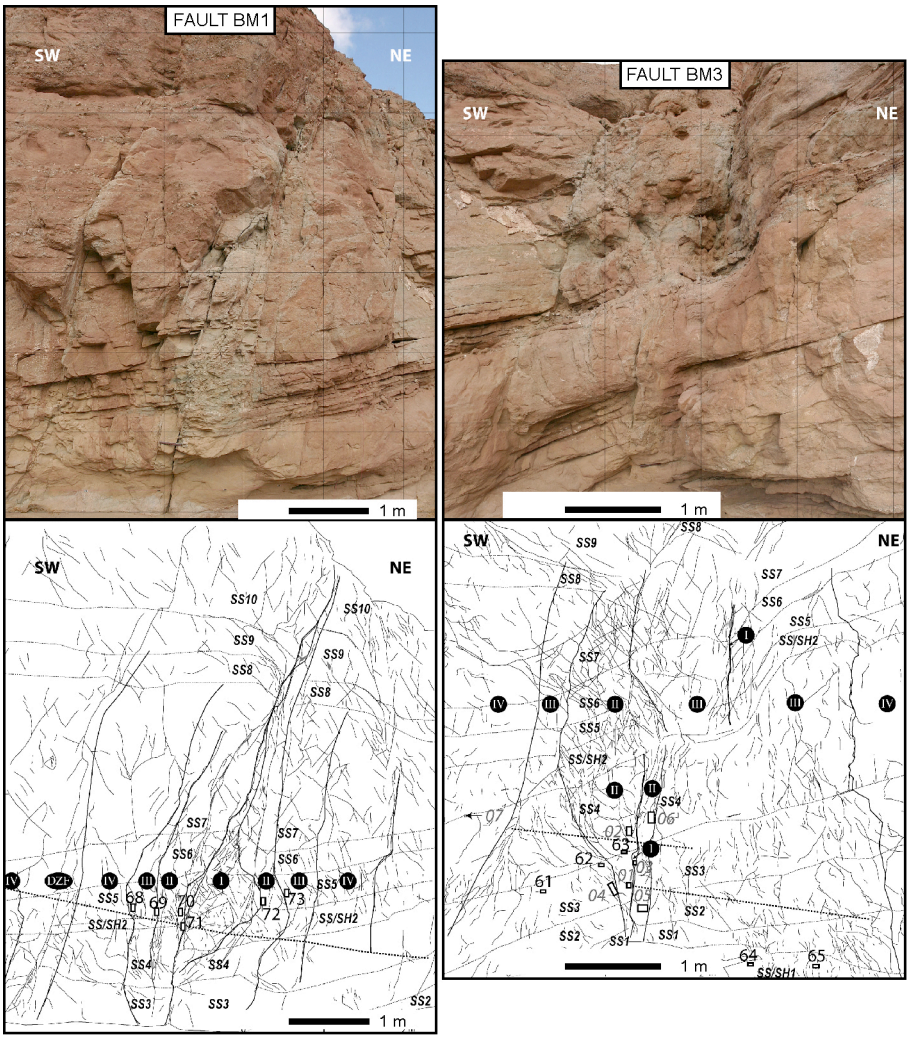

Figure 3.9. (Top) Cross-sectional photomosaics of faults; view in each photo is parallel to the fault strike, grid size is 1 m. (Bottom) Outcrop maps showing fault-related deformation (black solid lines indicate faults, veins and fractures; gray fill is used to represent veins that are >0.5 cm wide), stratigraphy (dashed black lines mark the stratigraphic boundaries; *SS#* indicate different stratigraphic units, *SS*, sandstone, *SH*, shale, *SS/SH*, interbedded sandstone and shale), and fault-zone domains (solid black lines mark the boundaries between domains; Roman numerals indicate different domains). Thick black dashed (fault-perpendicular) lines represent the locations of the scanlines. Also shown is the distribution of samples collected from each fault zone for microstructural analysis; italicized sample numbers for faults BM3, BC1, BC3, and BS1 indicate samples that were collected for petrophysical analysis, these results are in Chapter 4.

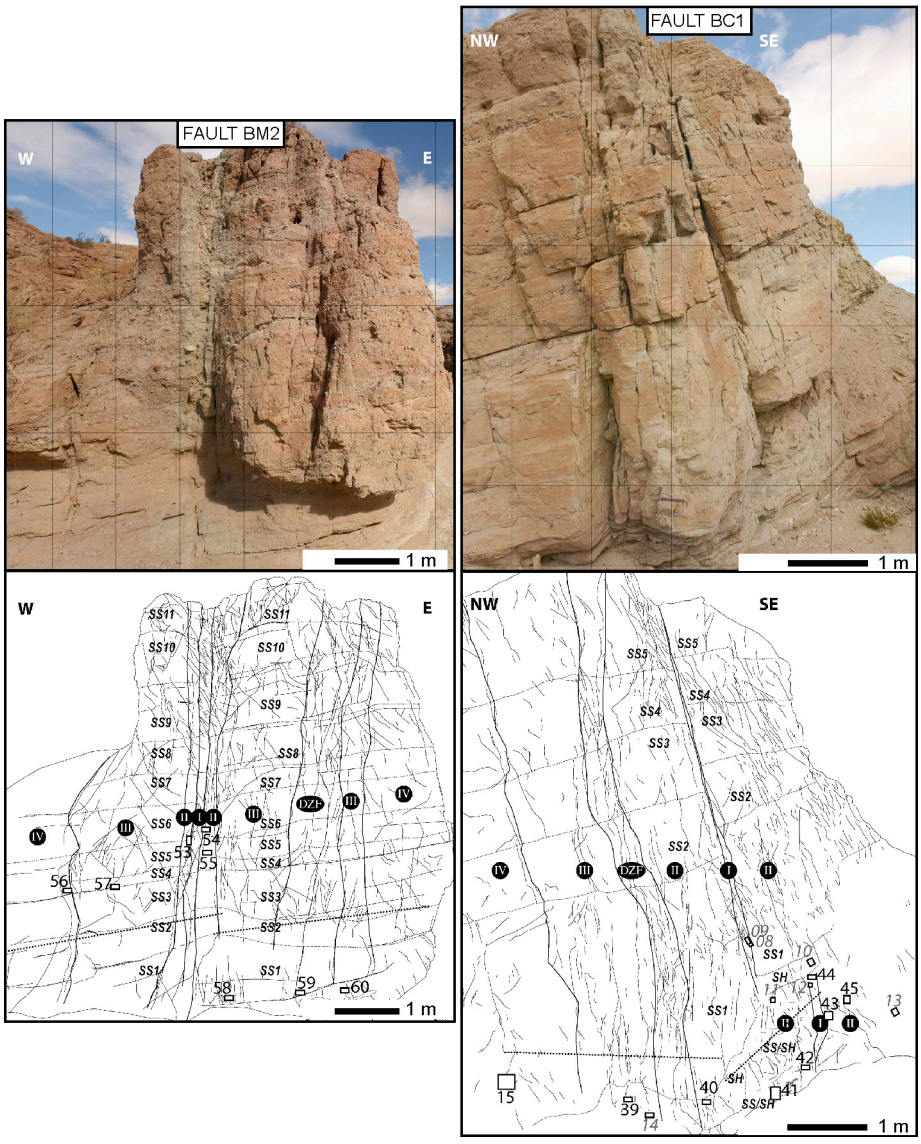

Figure 3.9. Continued.

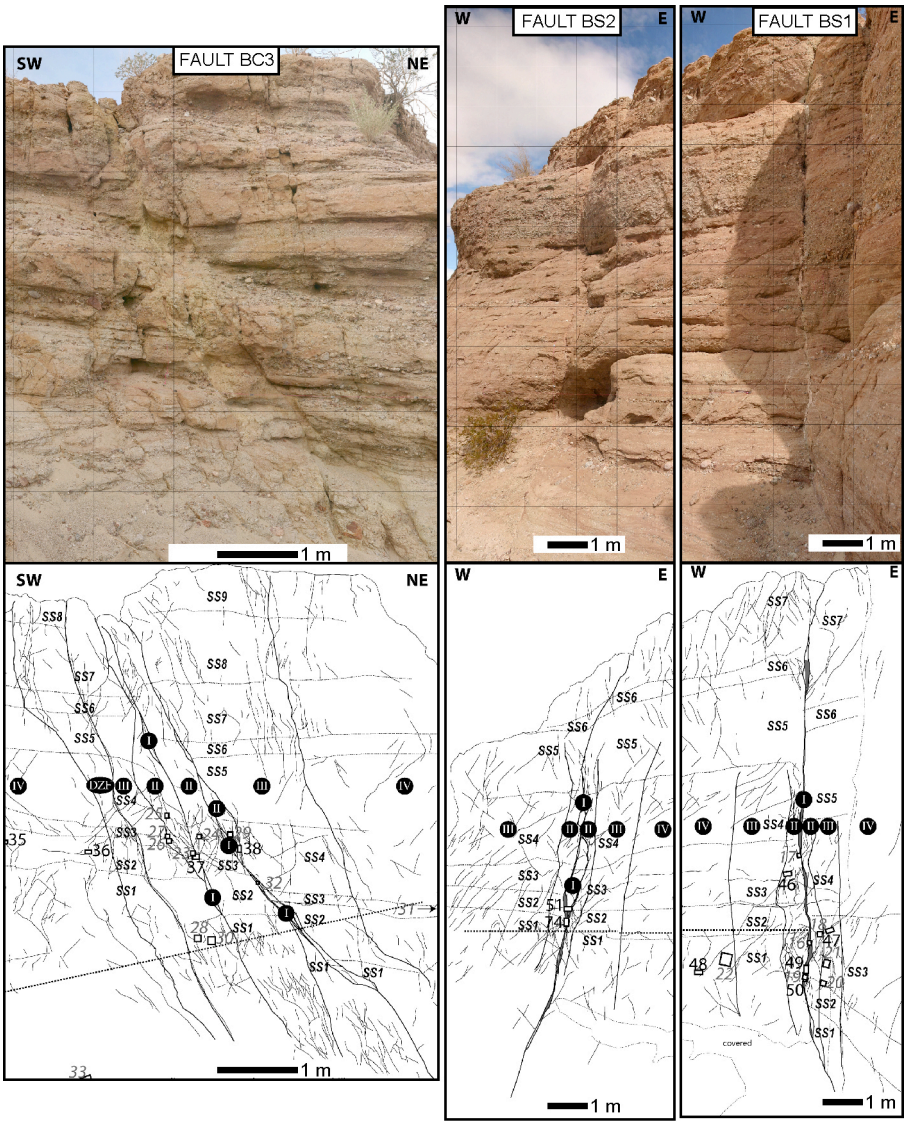

Figure 3.9. Continued.

3.5.2 Scanline Data

Fault-perpendicular variations in the density of deformation elements were recorded along representative scanlines oriented perpendicular to the strike of each fault zone (Figure 3.9). A scanline is a traverse with a defined orientation along which data are systematically documented; this technique is widely used and considered to be an effective and efficient method of extracting representative fracture data from a deformed volume of material (Priest and Hudson, 1981; LaPointe and Hudson, 1985).

Data obtained along each scanline includes the types of structural features present (e.g., open fractures, veins, minor faults), the spatial position, orientation, and dimensions of each feature, the morphology of the discontinuity surfaces, and all cross-cutting and abutting relationships. All features were recorded with centimeter-scale precision; the minimum threshold for the length of measured discontinuities is 6 cm.

3.5.3 Microstructural Analysis

Five to eight representative oriented samples of host and fault rock were collected along fault-perpendicular transects across each fault zone for microstructural analyses; the locations of these samples are shown in Figure 3.9. To the extent that it was possible, samples were collected at regular intervals, from each damage-zone domain, and from within the same unit to reduce the effects of petrophysical differences induced by mechanical stratigraphy. Samples were cut perpendicular to the fault plane and parallel to the slip direction. Previous work has demonstrated that this orientation provides maximum visibility for fault-related microfractures (Engelder, 1974), and that measurements made on slides of this orientation produce a good representation of measurements made by combining data from all three perpendicular orientations (Vermilye and Scholz, 1998, 1999).

Backscattered electron (BSE) image analysis in conjunction with energy dispersive x-ray analysis (EDAX) was conducted using a scanning electron microscope (SEM) and an electron microprobe to determine host rock, fault rock, and cement mineralogy, the style and spatial distribution of microstructures, and to discern the relative ages of the features that display cross-cutting relationships. Cross-cutting relationships preserve critical information about the relative timing between the different generations of damage; microstructural analysis can reveal cross-cutting configurations that are difficult to distinguish at an outcrop scale (Schulz and Evans, 2000). SEM-based cathodoluminescence (CL) microscopy is commonly used to image subtle compositional differences in cements and thereby reveal structural relationships between multiple generations of cements that are not apparent using other analytical

methods (Reed et al., 2002). In this study, CL microscopy was used to determine the composition and extent of overgrowth cements for samples from faults BM2 and BS1. Because quartz overgrowth was determined to be minimal, CL analysis was not conducted on samples from other fault zones.

3.6 Results

3.6.1 Host Rock Composition

The detrital mineralogy of the matrix is dominated by quartz, plagioclase, and k-feldspar, with subordinate amounts of mica (muscovite and biotite), rock fragments, detrital clay, and minor heavy minerals such as pyrite and apatite. Typically, there is less than 5% detrital clay in the sandstones; high clay content (up to 40%) is observed in rare clay-rich layers. This mineralogy is indicative of a lithic arenite of non-marine origin (Dott, 1964); the presence of feldspars, rock fragments, and mica grains that are not altered to clays indicates that the sandstone is immature and was deposited proximal to the source. Laumontite, a calcium-zeolite ($CaAl_2Si_4O_{12} \bullet 4H_2O$), occurs throughout the West Butte Conglomerate in veins and as intergranular cement. Detailed results from laser particle size and XRD analysis of samples from faults BM3, BC1, BC3, and BS1 are presented in Chapter 4, which focuses on the petrophysical variability within the fault zones.

3.6.1.1 Diagenetic Features

The main diagenetic processes to affect the mineralogy and petrophysical properties of the sandstones were precipitation of pervasive intergranular laumontite cement, feldspar dissolution, and some mechanical compaction (Figure 3.10). Other diagenetic phases present in lesser amounts are calcite cement, quartz overgrowth, and rare siderite cement (Figure 3.10). XRD analyses indicate that the abundance of laumontite cement in some undeformed sandstones can reach up to 18% of rock volume (see Chapter 4); the high minus-cement porosity suggests that the laumontite started to precipitate during the early diagenetic stage of shallow burial before substantial

compaction. It is inferred that the intergranular laumontite cement predates the establishment of the fault zones examined in this study based on the high minus-cement porosity and the lack of a correlation between proximity to the fault cores and the abundance of intergranular laumontite cement observed within undeformed ('host') portions of samples.

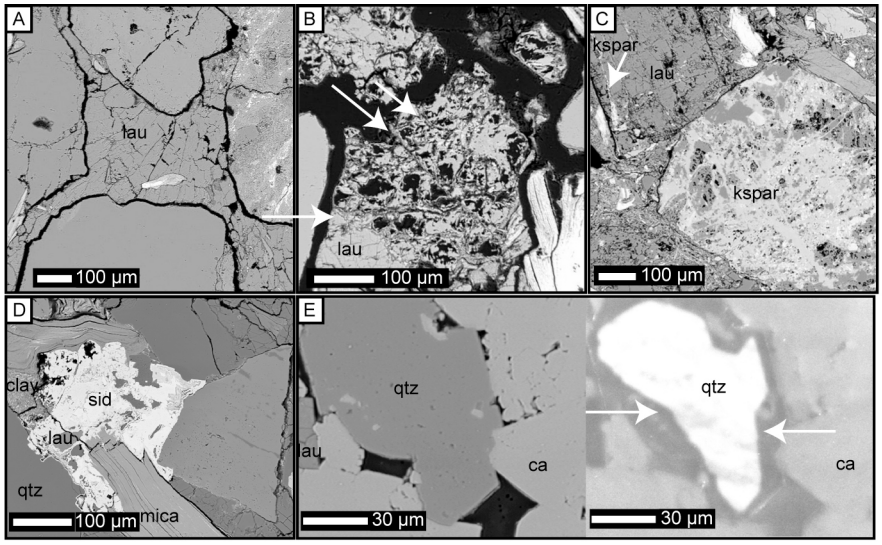

Figure 3.10. BSE photomicrographs of diagenetic features; *ca*, calcite; *clay*, detrital clay; *kspar*, k-feldspar; *lau*, laumontite; *qtz*, quartz; *sid*, siderite. (A) Host rock from fault BM1 contains pervasive intergranular laumontite cement. (B) Laumontite cement within a dissolved feldspar from fault BC3; note the preserved dissolution pathways (arrows). (C) Dissolved feldspar from fault BM1 is filled with laumontite, streaks of k-feldspar remain. The adjacent feldspar grain is dominantly k-feldspar and mostly undissolved. (D) Rare siderite cement from fault BM2 surrounds laumontite grains and postdates laumontite cementation. (E) Quartz grain surrounded by calcite cement from fault BM2; the CL image on the right reveals that quartz overgrowth (dark perimeter around the quartz grain, shown with arrows) predates the calcite cementation.

Bent and broken mica grains provide the only evidence for minor mechanical compaction after laumontite cementation. The distribution of intergranular calcite cement is highly variable throughout the fault zones and within individual samples. Rare instances of quartz overgrowth were observed in samples from faults BS1 and BM2 (Figure 3.10). Clay rim coatings around quartz grains commonly prohibited the growth of quartz cement around the perimeter of the grains; in these cases cementation is confined to the internal part of the grain. The amount of quartz overgrowth is limited due to early pervasive laumontite cementation.

Laumontite Precipitation

Pervasive authigenic intergranular laumontite cement is present within the matrix of all samples (including host rock, damage zone, and fault rock samples) of the West Butte Conglomerate examined in this study. Laumontite occurs as prismatic crystals that commonly display microfractures along cleavage planes (Figure 3.10A). Laumontite cement is common in immature sandstones that contain feldspars and rock fragments (Moore et al., 2001), and in sandstones derived from volcanic rocks (Boles and Coombs, 1977; Remy, 1994). Laumontite cement observed along major steeply dipping crustal and transform faults, including the San Andreas, Punchbowl, San Gabriel, and Sierra Madre faults, is interpreted as a product of circulating hydrothermal fluids associated with fault-related fluid flow (McCulloh and Stewart, 1982; Evans and Chester, 1995; Chester and Chester, 1998; Schulz and Evans, 1998). The occurrence of laumontite in the West Butte Conglomerate at Borrego Mountain is likely a result of hydrothermal fluids associated with flow along the Coyote Creek fault. Microprobe analysis of the trace element chemistry of both the intergranular laumontite cement and the laumontite cement that occurs in veins suggests that they were formed in the presence of hydrothermal fluids with similar composition.

Although zeolite formation is more strongly controlled by temperature conditions than lithostatic pressure (Zen and Thompson, 1974; Ghent, 1979), laumontite can form under a wide range of temperatures in volcaniclastic sandstones, from 50–300ºC (Surdam and Boles, 1979). The estimated maximum burial depth of the faults in this study (~3.0 km) (see Section 2.1.3) is consistent with the depth of laumontite mineralization in the Cajon Pass drillhole near the San Andreas fault (2.5–3.5 km) (Vincent and Ehlig, 1988). Temperatures between 140–190ºC have been suggested for zeolite mineralization along both the San Andreas and San Gabriel faults, where the geothermal gradient is 50°C/km (Anderson et al., 1980; Vincent and Ehlig, 1988); the geothermal gradient at Borrego Mountain may presently be as high as 65˚C/km (see Section 2.1.4). Given an average burial depth of 3.0 km and a geothermal gradient between 50°C/km and 65°C/km for the Borrego Mountain area, the circulating

hydrothermal fluids that were responsible for laumontite precipitation along the faults in this study may have reached temperatures of ~150°–~195°C.

Feldspars are an important precursor material for zeolite minerals in clastic sedimentary rocks (Bernet et al., 1997). All of the samples that were examined contain partially to completely dissolved feldspar grains, some with unaltered primary shapes, and some with authigenic laumontite cement within the secondary pores (Figures 3.10B and 3.10C). Laumontization by the alteration of plagioclase may proceed according to a direct *in-situ* reaction, or in two steps, with albitization followed by laumontization (Boles and Coombs, 1977; Boles, 1982; Blenkinsop and Sibson, 1992). The presence of secondary microporosity within many dissolved feldspar grains suggests that two separate reactions occurred: the differential dissolution of Ca-rich (anorthic) plagioclase (albitization) was followed by the precipitation of laumontite in pore spaces from hydrothermal fluid enriched in Ca^{+2} (laumontization).

3.6.2 Domain Characterization

Damage-zone domains contain the record of different generations of deformation (paleo-damage zones) that were active during unique slip events. Mapping fault-zone domains is essential for determining the minimum number, dimensions, and relative ages of paleo-damage zones. There are multiple ways to characterize damage-zone domains; for instance, Schulz and Evans (1998) compare the relative extents of distinct deformation-related signatures along the Punchbowl fault, including geochemical alteration, macroscopic, and microscopic deformation. For the purposes of this study, the fault zones were divided into fault-parallel domains based on relatively abrupt changes in the density and style of deformation across the damage zone with distance from the fault core. Preliminary domain designations were made in the field on the basis of a visual assessment of fault-perpendicular variations in mesoscopic damage density; the domain boundaries were subsequently revised according to results from a fracture analysis, described in the following section (Figure 3.9). The following conventions were used to define damage-zone domains: (1) Domain I is reserved for

the fault core(s). (2) Domain boundaries must be subparallel to the principal slip surface, although they need not be planar or continuous. (3) Domain boundaries may follow a discontinuity, a boundary defined by chemical alteration, a boundary where bedding becomes less distinct due to deformation, or a boundary where the average spacing of damage elements changes abruptly. (4) A discontinuity that is coincident with a boundary belongs to the higher-order bounding domain. (5) Domain definitions must be consistent across the dataset. (6) Domains need not be sequential (III,II,I,II,III), and can be nested, for example (III,II,I,II,I,II,IV). (7) The outermost domains should include the most distal deformation features associated with the fault, and the fracture density within the outermost domain should be elevated above background levels of deformation. (8) Prominent, throughgoing secondary faults within the damage zone ('damage zone faults', or 'DZFs') that are surrounded by enhanced deformation that interferes with the systematic decrease in the density of deformation away from the fault core define distinct domains.

3.6.2.1 Fracture Analysis

Numerous approaches may be used to quantify changes in the density of deformation with perpendicular distance from the fault core. Fracture index values may be calculated from one-dimensional scanline data by measuring the number of discontinuities per unit length of scanline (Narr and Suppe, 1991; Engelder et al., 1997), or from fracture maps (Escuder Viruete et al., 2001). The latter, more comprehensive method was employed in this study because of the exceptional cross-sectional exposures at Borrego Mountain. Fracture index values were derived from digital vector-based fracture maps using the image analysis software 'ImageJ64'. Digitized maps of the deformation within each fault zone were converted to binary (pixel values of 0=white and 255=black) and rotated such that the faults are parallel to a vertical reference line. The maps were trimmed in order to exclude excess white space from the analysis. Column-averaged profile plots were generated where the x-axes correspond with the horizontal distance in meters through each fault zone and the

y-axes represent the vertically averaged pixel intensity (mean of all binary values) sampled in parallel 0.45 cm wide vertical columns across each fault zone (Figure 3.11).

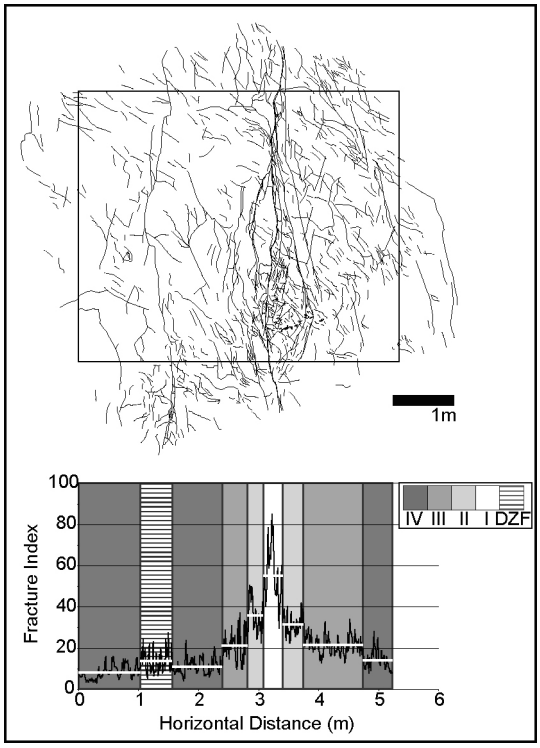

Figure 3.11. Binary digitized deformation map for fault BM1 (rotated such that the principal slip surface is parallel to a vertical reference line), shown with the average deformation density profile plot (black line graph) generated using the image analysis software ImageJ64. The fault map was trimmed along the black box (shown) to exclude excess white space from the analysis. The x-axis is the horizontal distance through the fault zone (m) and the y-axis represents the vertically averaged pixel intensity (mean of all binary values) sampled in parallel 0.45 cm wide vertical columns across the fault zone. White horizontal bars indicate the mean fracture index value for each domain; domains are indicated with shades of gray.

The fracture density plots are domainal in character and domain boundaries correspond with sharp changes in the fracture index. A mean fracture index value was calculated for each damage-zone domain within each fault zone. Each domain is characterized by a mean fracture index that is distinct from the value calculated for adjacent domains. Although the domain boundaries are irregular (not linear) in nature, the domain boundaries defined by the fracture analysis provide a useful approximation of the domain widths. Domain widths and associated mean fracture indices are summarized in Table 3.1.

Table 3.1. Summary of fault-zone domain widths. Domains are listed from left to right through each fault zone, widths are in meters; mean fracture indices are in brackets. UTM coordinates of each fault zone are provided in brackets. *BM3 T* and *BM3 B* refer to the top and bottom, respectively, of fault BM3.

Fault	DIV	DZIII	DZF	DIV	DZIII	DZII	FC	DZII	DZIII	FC	DZII	DZF	DZIII	DZIV	Total DZ Width
BM1 [572,658 m E; 3,673,495 m N]	1.03 [8.2]		0.53 [13.7]	0.83 [11.0]	0.42 [21.0]	0.26 [35.8]	0.33 [55.0]	0.34 [31.4]					1.00 [21.6]	0.48 [14.1]	5.22
BM3 T [572,665 m E; 3,673,507 m N]	2.17 [18.7]				0.32 [35.3]	0.87 [52.4]			0.59 [25.5]	0.07 [61.6]			1.37 [21.4]	0.59 [8.8]	5.99
BM3 B [same as BM3 T]	1.75 [13.6]				0.82 [29.3]	0.63 [34.5]	0.13 [65.2]	0.15 [33.5]					2.36 [26.5]	0.14 [15.1]	5.99
BM2 [572,730 m E; 3,673,508 m N]	0.17 [10.2]				0.72 [18.5]	0.09 [32.7]	0.24 [55.1]	0.40 [33.4]	1.00 [14.8]			0.73 [25.0]	0.59 [15.7]	0.30 [8.8]	4.25
BC1 [574,888 m E; 3,672,085 m N]	1.61 [6.8]	1.23 [14.9]	0.23 [40.8]			0.88 [19.8]	0.20 [48.1]	0.37 [22.8]		0.15 [35.0]	0.48 [24.2]		0.28 [13.6]		5.43
BC3 [574,969 m E; 3,672,301 m N]	1.34 [11.0]		0.15 [31.7]		0.41 [20.0]	0.25 [32.9]	0.09 [41.9]	0.19 [24.1]		0.15 [46.3]	0.30 [21.4]		1.34 [14.9]	1.26 [6.1]	5.48
BS1 [576,205 m E; 3,671,935 m N]	1.83 [4.9]				1.20 [6.4]	0.44 [15.7]	0.19 [35.9]	0.32 [9.5]					0.71 [7.3]	0.09 [6.3]	4.77
BS2 [576,199 m E; 3,671,938 m N]					2.39 [9.3]	0.32 [24.6]	0.18 [46.4]	0.20 [26.5]					2.02 [5.4]	0.36 [2.1]	5.46

There is excellent agreement between the location and configuration of the domain boundaries defined using the fracture analysis and those identified on the basis of field observations (Figure 3.11). Figure 3.12 shows generalized transects through each fault zone using average values for the width of each domain.

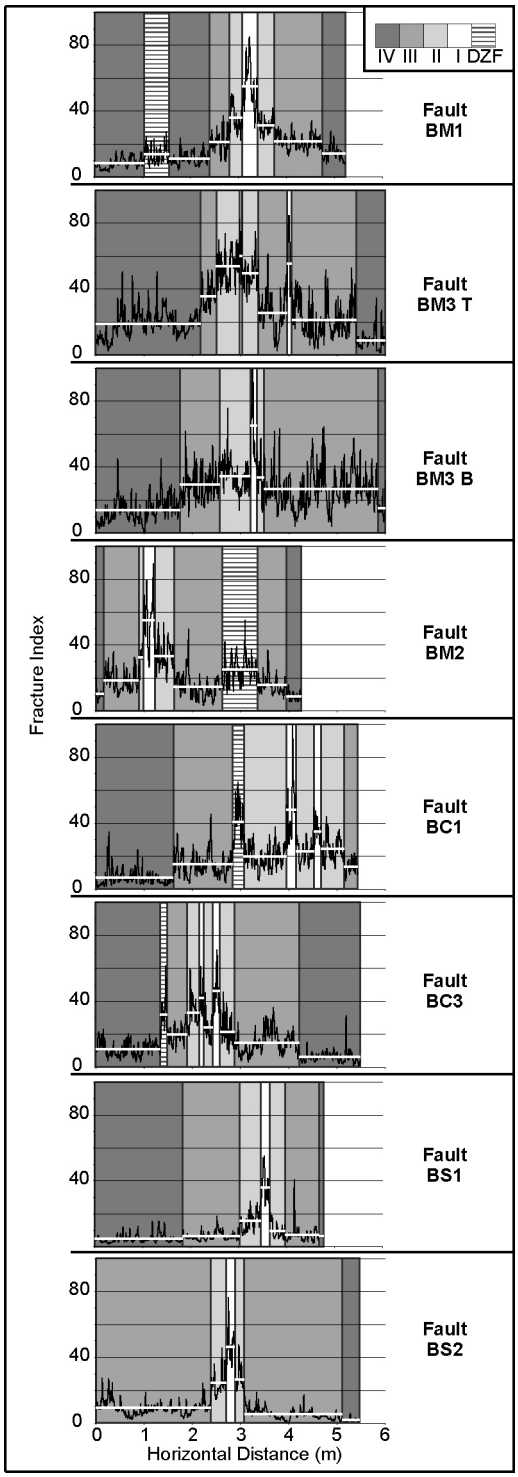

Figure 3.12. Comparison between generalized fault architecture of all fault zones. *BM3 T* and *BM3 B* refer to the top and bottom, respectively, of fault BM3.

The values for total damage-zone width provided in Table 3.1 must be considered approximate because it is difficult to delineate the outer extent of the damage zones due to limitations of the exposures and interactions with adjacent structures. The fault zones are generally symmetrical about the cores, with the exceptions of faults with limited exposure on one side of the damage zone (BS1 and BC1), faults with a damage zone fault (DZF), and faults with exposed bedding-parallel slip. Generally, on the scale of the entire damage zones, the density of deformation decreases with distance from the fault core on both sides. The presence of a DZF coincides with elevated levels of deformation and is only observed on one side of faults BM1, BM2, BC1, and BC3. These DZFs may represent incipient faults. Bedding parallel slip is observed within mechanically weak units in fault zones BC1 and BM3; distinct fault cores and associated damage zones can be identified stratigraphically above and below these units. For fault BM3, because the bedding-parallel slip occurs in the middle of the outcrop, the top and bottom of the fault zone are considered separately (Figures 3.9 and 3.12). In the context of the paleo-damage zone model, each domain represents the signature of at least one paleo-damage zone. The domain dimensions are used to infer the dimensions of individual paleo-damage zones and are analyzed in conjunction with data on the relative timing of deformation to determine whether the domains were established early or late in the history of each fault zone.

3.6.3 Displacement and Shear Strain

It is challenging to estimate total fault displacement on these predominantly strike-slip faults due to a lack of exposure of potential offset markers in map view. In the absence of reliable offset markers, published scaling relations between fault displacement and fault dimensions may be used to estimate total fault slip. Whereas many published studies propose scaling relations between fault length and displacement (e.g., Cowie and Scholz, 1992a; Schlische et al., 1996, and references therein), only a few studies explicitly investigate the scaling between fault-zone width and displacement (Vermilye and Scholz, 1998; Beach et al., 1999; Fossen and Hesthammer, 2000; Shipton and

Cowie, 2001). However, these relationships pertain to deformation-band faulted sandstones, and scaling relationships between damage-zone width and fault displacement are dependent on host rock porosity (Shipton and Cowie, 2001), and by inference, faulting mechanism. In contrast with primary faults, faulted joints do not follow linear displacement-length scaling relations, although they fall within the wide range of displacement/length ratios (0.001–1) reported in global datasets (Wilkins et al., 2001). Although it may not be possible to calculate a meaningful value of fault displacement based on the widths of the fault zones in this dataset, in view of the presumed correspondence between damage-zone width and fault displacement, it is possible to infer that the displacements are of similar magnitude across the dataset, because total fault-zone widths are comparable (Table 3.1).

3.6.4 Deformation Features

Deformation features identified within the fault zones include cataclastic fault rocks, laumontite-, calcite-, gypsum-, and halite-cemented fractures, and open fractures. Table 3.2 summarizes all distinct deformation features and their spatial extent within each fault zone based on a careful field inspection of each exposure and microstructural observations.

Table 3.2. Summary of deformation features present and their spatial distribution within each fault zone. *LV*, laumontite vein; *CV*, calcite vein, *GV*, gypsum vein; *HV*, halite vein; *CF*, cataclastic fault rock; *OF*, open fracture; '<' used to denote 'younger than'. *I, II, III, IV, DZF* are used to indicate the domains where each feature is observed, *ALL* represents all damage-zone domains.

	Deformation Features						
Fault	**LV**	**CV**	**GV**	**HV**	**CF**	**OF**	**Relative Timing**
BM1		I, II, DZF	ALL		I, II, III, DZF	ALL	GV<CV; OF<all
BM3		ALL	ALL	II	I	ALL	GV<CV; OF<all
BM2		ALL	ALL		I, DZF	ALL	GV<CV; CF<CV; 2+ gen CV; OF<all
BC1	I, II, III	I, II, III	I, II, III		I	ALL	CF<LV; CF<GV; GV<LV; GV<CF; GV<CV; 2+ gen GV; OF<all
BC3		ALL			I	ALL	OF<all
BS1	ALL	ALL	I, II, III		I	ALL	LV<CF; CF<CV; CV<LV; GV<CV; 2+ gen LV; OF<all
BS2	I, II, III	I, II, III	I, II, III		I	ALL	LV<CF; CF<LV; GV<CV; 2+ gen LV; OF<all

Tabular zones of cataclastic fault rock were identified in samples from each fault zone examined during this study (Figure 3.13). Microscopic observations confirm that the cataclastic fault rocks formed by deformation-induced grain fracturing and frictional sliding (Figure 3.13). The moderate grain-size reduction in the cataclastic fault rocks is consistent with the observed small displacements and suggests that these fault rocks were generated in lithified sediments under moderate effective stress conditions (~10–15 MPa), which could equate to intermediate burial depths (~1.0–1.5 km) under hydrostatic conditions. Some observed instances of cataclastic fault rock are associated with porosity collapse (Figures 3.13C and 3.13D) whereas other cataclastic fault rocks are associated with dilation and have enhanced porosity relative to the surrounding host rock (Figures 3.13A, 3.13B, 3.13E, 3.13F and 3.13G).

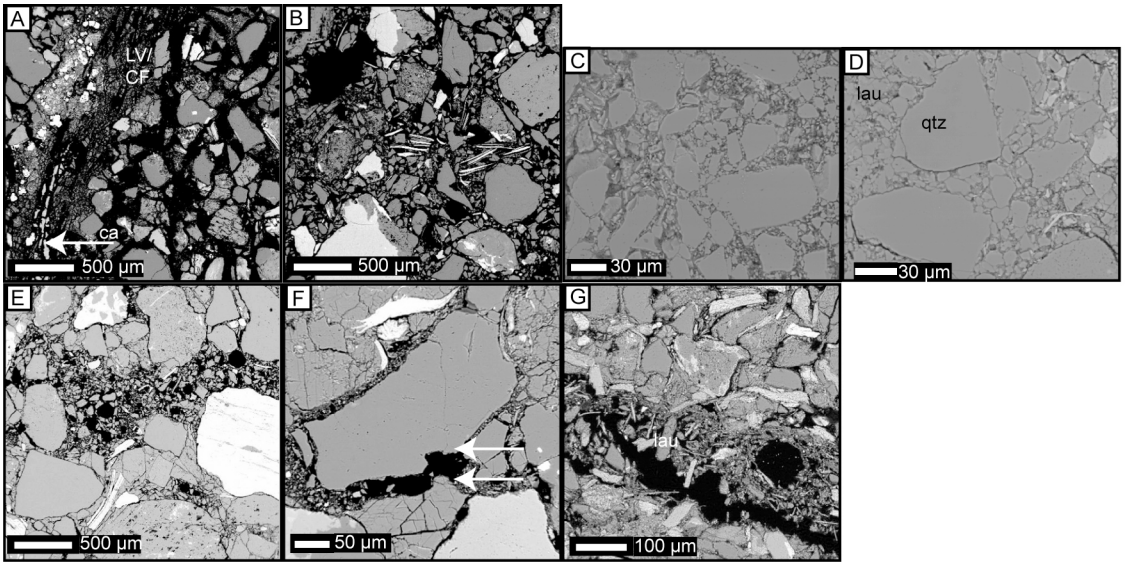

Figure 3.13. BSE photomicrographs of cataclastic fault rock from faults (A) BC1, (B) BC3, (C) BS1, (D) BM2, (E), (F) BM1, (G) BM3; *lau*, laumontite; *qtz*, quartz. (A) Faulted laumontite (*LV/CF*) and calcite vein (*ca*, arrow) is porous and highly fractured. Adjacent host rock is also porous and fractured. (B) Higher-porosity cataclastic fault rock contains fragmented laumontite cement. (C) Detail of cataclastic fault rock. (D) Cataclastic fault rock with moderate grain size reduction includes broken laumontite, indicates that cataclasis postdates at least one phase of laumontite cementation. (E) Tabular region of cataclastic fault rock. (F) Laumontite cement and detrital grain, previously attached, have been separated (arrows) and cataclastic fault rock has flowed in between. (G) Cataclastic fault rock contains laumontite and is dilatant.

Cemented fractures are also observed in all fault zones and contain authigenic cements that precipitated from fluids as they flowed through dilatant fracture networks.

Cemented fractures are commonly associated with crack-seal textures that indicate episodic mode I (opening-mode) fracturing and cementation; in the more complex veins there is evidence for up to ten cementation events (Figure 3.14). Although laumontite, calcite, gypsum, and halite cements are observed within veins, laumontite is the dominant fracture cement present in the samples from faults BC1, BS1, and BS2; calcite-cemented fractures are observed in all fault zones (Table 3.2).

Figure 3.14. Photograph of a complex vein from the damage zone of fault BC1. The vein shows evidence for episodic dilation and cementation; deposits from ten distinct cementation events can be observed macroscopically.

Microfracturing refers to the incipient breaking of grains, which is different from the cataclasis or crushing of grains into aggregate smaller pieces. The majority of detrital grains examined from faulted sandstones at Borrego Mountain are unfractured, and where grain fracturing is present, fractures are confined to individual grains. Some open transgranular and grain-boundary fractures also occur. Note that some wide fractures that follow grain boundaries are artificial, introduced during sample preparation. To assess the relationship between the density of microfracturing and proximity to the fault cores, BSE image montages (at 66X magnification) were assembled along representative transects perpendicular to the fault plane for samples collected from faults BS1 and BM2. Microfractures were counted within detrital quartz

and feldspar grains with long axes equal to or greater than 150 μm; fractured grains were calculated as a percentage of the total number of detrital quartz and feldspar grains above that size threshold (Figure 3.15).

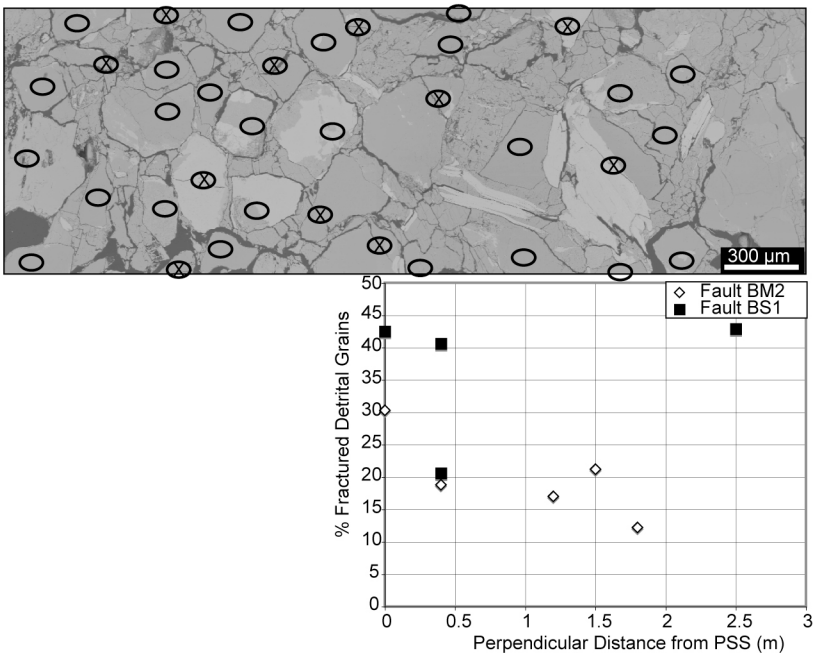

Figure 3.15. (A) An example of a section from a montage of BSE photomicrographs from fault BS1, sample 47. Detrital grains with long axes >150μm are marked as fractured (ovals with an '*X*') or intact (open ovals). (B) Chart shows a decrease in the percentage of fractured grains as a function of perpendicular distance from the principal slip surface for samples from faults BM3 and BS1.

Only fractures that intersect grain boundaries were included in the tally. In general, samples closer to each fault have a higher percentage of fractured grains (Figure 3.15). In fault BM2, sample #59, 1.5 meters from the fault, contains a higher percentage of fractured grains, likely related to deformation associated with the damage zone fault (DZF) (Figure 3.9). In fault BS1, sample #48, 2.5 meters from the fault, contains an extremely high percentage (42.9%) of fractured grains; this sample includes a laumontite vein, and enhanced grain fracturing likely accompanied dilation and fluid flow.

3.6.4.1 Relative Timing of Deformation Features

Cemented fractures are typically spatially coincident with cataclastic fault rock and open fractures, and valuable data on the relative timing of different deformation features can be gleaned from microstructural relationships (Figure 3.16).

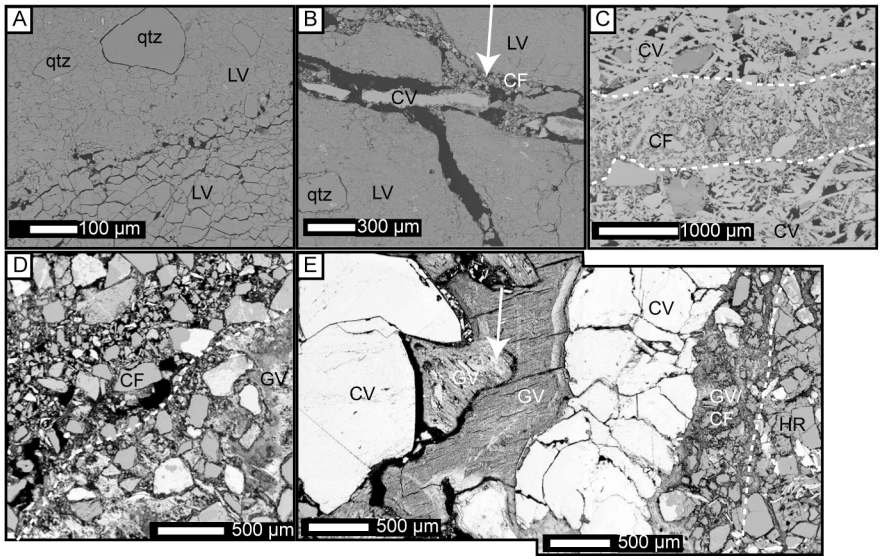

Figure 3.16. BSE photomicrographs of veins from faults (A) BS1, (B) BS1, (C) BM2, (D) BC1, and (E) BC1. (A) A thick laumontite vein (*LV*) has two distinct textures (indicating >1 cementation event) and entrained detrital quartz grains (*qtz*, arrows). (B) Late-stage fracture within a laumontite vein is partially filled with calcite cement; cataclastic fault rock in the fracture (*CF*, arrow) postdates the laumontite vein and predates the calcite vein (*CV*). (C) Cataclastic fault rock within a calcite vein postdates calcite cementation and is predominantly composed of calcite. (D) Gypsum vein (*GV*) is adjacent to cataclastic fault rock. (E) Two calcite veins, gypsum vein, and cataclastic fault rock are parallel; host rock (*HR*) at far right. Different generations of gypsum cement are recorded in variable growth textures.

The relative timing of deformation features as determined by field and microstructural analysis is summarized in Table 3.2. Intergranular laumontite cement is the earliest diagenetic event and predates both quartz overgrowth and siderite cement; all diagenetic features predate all deformation features (Figure 3.10). Laumontite veins predate all other vein types and some thicker veins include different textures, an indication that there have been multiple phases of dilation and mineralization (Figure 3.16A). Calcite cement commonly postdates laumontite veins (Figure 3.16B); precipitation of calcite cement that postdates and is spatially associated with zeolite cement has been reported in a number of settings (Orange et al., 1993; Prior et al.,

1995; Bernet et al., 1997; Neuhoff et al., 2000). Different textures of calcite are observed, even within the same vein, providing evidence for multiple generations of calcite cementation. Gypsum veins postdate laumontite and calcite veins and are predominantly present in bedding-parallel and bedding-perpendicular orientations; multiple generations of gypsum cementation are also observed (Figure 3.16E). Halite precipitation, observed only in samples from fault BM3, appears to be the latest cementation event. There is evidence for temporal alternation between cementation events and cataclastic faulting; some veins predate cataclastic fault rocks and some veins of each composition also postdate cataclastic fault rock development (Figures 3.13 and 3.16). Open (unfilled) fractures postdate all cataclastic faulting and cementation events and represent a late dilational phase. Whereas some open fractures developed during sample preparation, these are large and cut across the entire sample, and are thus readily distinguishable from deformation-induced open fractures.

3.6.5 Fracture Orientations

Structural data collected along fault-perpendicular scanlines across each fault zone are summarized in stereonet plots in Figure 3.17; these plots were created using Stereonet software (Allmendinger, 2002). For each fault, the data are plotted in the frame of reference of the cross-section: equal-area lower-hemisphere projections where the hemispheres project back into each outcrop. The corresponding view directions are horizontal and perpendicular to the azimuth of each exposure (and nearly parallel to the strike of each fault because fault-perpendicular exposures were a precondition for fault selection).

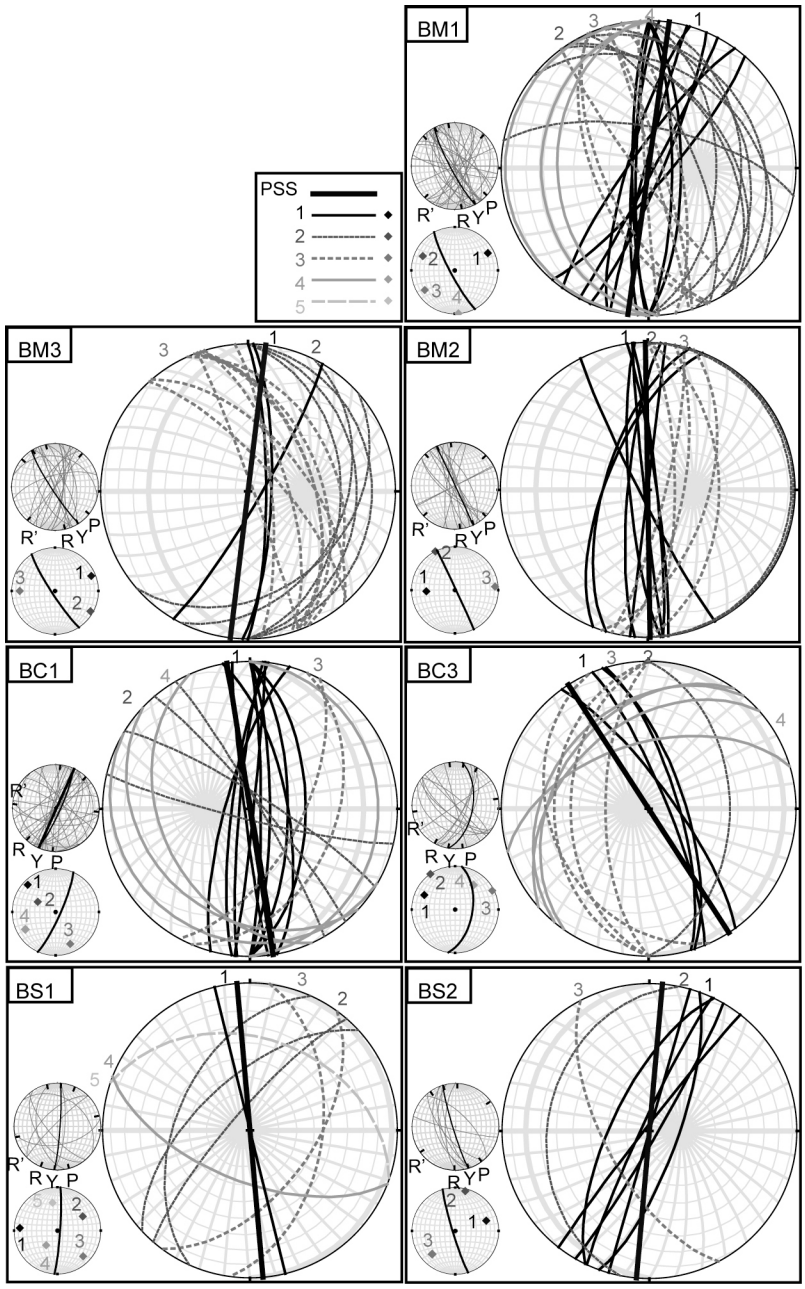

Figure 3.17. Equal-area stereographic projections of structural features measured along fault-perpendicular scanlines across all fault zones (scanline locations are indicated on Figure 3.9). The data are plotted in the frame of reference of each respective fault zone cross-section; each view direction is horizontal and perpendicular to the azimuth of the exposure (parallel to the strike of the principal slip surface). The result is an equal-area lower-hemisphere projection where the hemisphere projects back into the outcrop. The orientations of fractures are shown as great circles (*1–5* represent different principal fracture sets with common orientations); the thick black great circles represent the principal slip surfaces. Inset (upper) shows for reference the same data in an equal-area lower-hemisphere projection where the hemisphere projects down into the earth; markers indicate the expected orientations of subsidiary fractures based on the Riedel model for simple shear. Inset (lower) is also in a standard equal-area lower-hemisphere projection, and shows the poles to the fracture planes for each distinct principal fracture set.

Because the view direction varies for each fault zone, the data are also presented in a standard lower-hemisphere projection to normalize the frame of reference among the fault zones and facilitate comparisons (Figure 3.17, insets). For reference, the expected orientations of subsidiary shears based on the Riedel shear model are also indicated on Figure 3.17. These orientations are based on an adopted value of 38° for the angle of internal friction of the laumontite-cemented sandstones. This value was calculated using 0.77 as the coefficient of friction of laumontite, the mean of experimentally derived values attained at 30 MPa and 100 MPa under both dry and saturated conditions (Morrow and Byerlee, 1991).

Within each fault zone, three to five sets of fractures were observed along the scanlines; for each fault zone, those fractures that are subparallel to the main principal slip surface are designated as set 1. The Terzaghi correction (to correct for a sampling bias against features that are nearly parallel to the exposures) (Terzaghi, 1965) was not applied to these data, and it is likely that features in exposure-parallel orientations have been under-sampled. The dominant fracture sets were captured along each scanline, although it is possible that each scanline, though positioned to be representative, did not adequately sample all sets. There are fractures consistent with the orientations of R structures in all fault zones except fault BS1, but overall, the orientations of the fracture sets within each fault zone are not consistent with the Riedel shear zone model (Figure 3.17).

Although the damage-zone domains are clearly defined by spatial variations in the density of fracturing, there is no apparent spatial pattern between the differently oriented fracture sets. Damage-zone domains are not characterized by distinct preferred fracture orientation(s); fractures from each set are observed within all damage-zone domains of each fault zone. Mutually abutting relationships are observed among nearly all fracture sets within each fault zone. Abutting relationships are typically used to discern the relative ages of joints (e.g., Twiss and Moores, 1992; Cruikshank and

Aydin, 1995). However, in the case of mutually abutting relationships, it is not feasible to conclusively deduce the temporal relationships between different sets of fractures.

3.7 Discussion

3.7.1 Deformational Histories of Faults

The microstructural data show evidence of multiple episodes of fluid flow alternating with fault slip and the development of cataclastic fault rock. The deformation features observed within these fault zones formed at different times during the burial and structural evolution of the West Butte Conglomerate. Integrating the diagenetic and deformation histories can establish the sequence of fault-zone development. The precise number of events is difficult to constrain, but the observations of relative timing suggests the following chronology of events:

(1) An early phase of hydrothermal fluid flow probably associated with the Coyote Creek fault zone caused pervasive intergranular laumontite cementation of the host rock at shallow burial depth, prior to the development of the fault zones examined in this study. (2) Quartz overgrowth and siderite cement precipitated at ~90°C, prior to exhumation and deformation. (3) Multiple episodes of dilational fracturing and subsequent or contemporaneous hydrothermal fluid flow caused the precipitation of laumontite veins with several generations of cement. (4) Subsequent displacement occurred within discrete shear zones with moderate grain size reduction due to cataclastic deformation at moderate mean effective stress conditions (i.e. 10–15 MPa) during intermediate burial (1.0–1.5 km). (5) Additional dilational fracturing and fluid flow resulted in laumontite vein formation along cataclastic fault rocks. (6) Later phases of fluid flow along dilational fractures led to the precipitation of multiple generations of calcite vein cement. (7) At least one cataclastic faulting event occurred after calcite vein cementation, with some fault rocks localized within preexisting calcite veins. (8) Another episode of fracturing and calcite cementation occurred after the faulting of older calcite veins. (9) Subsequent dilational events were followed by (or contemporaneous with) the precipitation of gypsum cement; some gypsum veins

are localized parallel to and within preexisting calcite veins. Gypsum cementation probably occurred at temperatures of <50°C, under near-surface conditions. (10) The latest observed cataclastic faulting event occurred after gypsum cementation. (11) Late-stage halite precipitation postdates all other cementation events; halite was likely deposited by meteoric fluids. (12) A final stage of dilational fracturing opened (unfilled) fractures that postdate all cementation events.

3.7.2 Timing and Orientation of Fracture Development

The current prevailing conceptual model for the evolution of fault zones in sandstones that form along joints is based on field observations of faults in the Aztec Sandstone in the Valley of Fire State Park, Nevada (Flodin and Aydin, 2004; Myers and Aydin, 2004); and has been successfully simulated using finite element models (Lunn et al., 2008). According to this model, shearing along joints gives rise to splay fracturing, and three primary joint orientations develop, including the ultimate fault zone orientation and the original joint orientations (Figure 3.18).

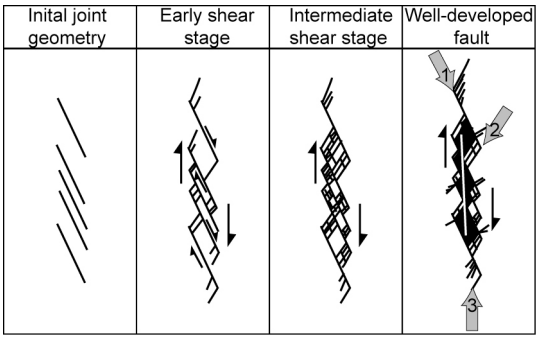

Figure 3.18. Published conceptual model for the evolution of faults by the shearing of joints (right-stepping, right-lateral, dilational geometry), modified from Myers and Aydin (2004). Arrows labeled 1–3 indicate the principal fracture orientations predicted by this model.

A fundamental feature of these geometries is the interconnectedness of the joint patterns; all of the joints in the splay hierarchy are linked, and the majority of them are connected to the fault core. Flodin and Aydin (2004) demonstrated that this model is inconsistent with the Riedel shear model with respect to both the chronology of splay fracture development and the orientations of these features. The geometry of

deformation features within fault zones at Borrego Mountain does not conform to either the sheared joints or the Riedel shear model. Specifically, the sheared joints model does not predict the damage-zone deformation that is observed within the fault zones at Borrego Mountain, the majority of which is discontinuous along the plane of exposure. It is important to note that the sheared joints model is valid for strike-slip faults in map view and dip-slip faults in cross-section (Myers and Aydin, 2004), so may not be directly applicable to the cross-sectional exposures of strike-slip faults at Borrego Mountain.

The mutually abutting relationships observed between nearly all fracture sets within each fault zone at Borrego Mountain suggests that either (1) fractures in different orientations formed contemporaneously, or (2) deformation events that activated differently oriented fracture sets alternated through time, possibly due to cyclical stress changes. Whereas in the traditional view, joints with different orientations formed under different stress states, recent field and theoretical work indicates that polymodal fault and fracture patterns can develop in a single stress field (Blenkinsop, 2008, and references therein). Mechanical models predict significant variation in maximum compressive stress directions and magnitudes along nonplanar faults due to local stress concentrations that result from irregularities along the fault, particularly where the fault has a relatively low coefficient of friction (Saucier et al., 1992; Chester and Fletcher, 1997; Chester and Chester, 2000). Faulkner (2006) demonstrated on the basis of field data, laboratory studies, and numerical modeling that remotely applied stresses are rotated within fault damage zones due to substantial changes in bulk elastic properties as a function of micro- and macrofracture density; these results are scale-invariant.

Hill (1977) and Sibson (1996) have proposed that fluid-driven deformation can produce variably oriented faults and fractures that link to form a “structural mesh”. Blenkinsop (2008) demonstrated that within structural meshes, at least some faults do not contain the intermediate principal stress direction σ_2; in such cases the lines of intersection between faults and related extensional fractures is not constrained to be

perpendicular to the fault slip direction and fractures may instead intersect faults along lines with a wide range of orientations (0°–90° from the direction of maximum resolved shear stress). The multiple distinct extensional fracture sets with mutually abutting relationships and variable orientations relative to the fault principal slip surfaces within the Borrego Mountain fault zones is consistent with heterogeneous stress distributions due to local variability in stresses and the structural mesh model. It is also noteworthy that structural meshes tend to be associated with small displacement faults (Sibson, 1996).

3.7.3 Paleo-Damage Zones at Borrego Mountain

In Figure 3.19, a summary of the alternating cycles of jointing, fluid flow and cementation, and cataclastic slip throughout the evolution of fault BS1 is presented in the context of the paleo-damage zone model.

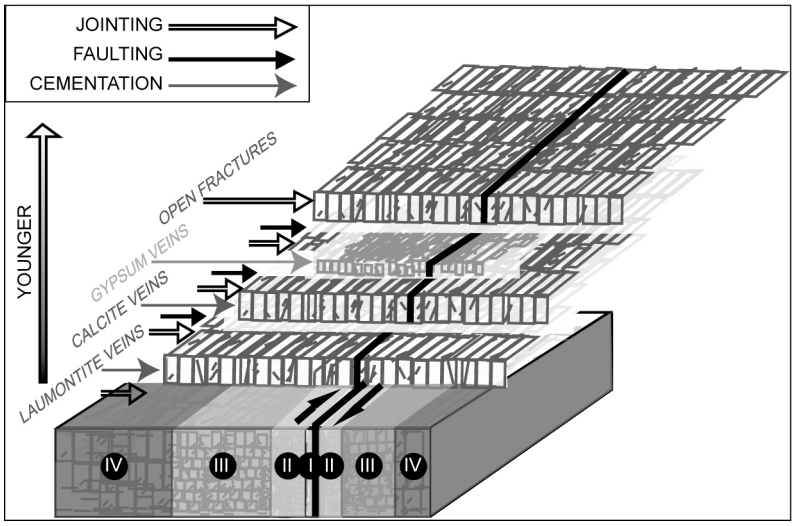

Figure 3.19. Schematic summary of the paleo-damage zone history of fault BS1. The various deformation elements are arranged chronologically and paleo-damage zone widths represent the spatial extent of each feature within the plane of observation.

The step-wise variations in deformation density within these fault zones is a compelling indication that the domain boundaries that they define are mechanically meaningful and represent the cumulative deformation from multiple slip events. If the

paleo-damage zone model is valid, the domain boundaries delineate the outer extents of paleo-damage zones associated with unique deformation events. The underlying assumption is that the density of deformation associated with a single event should decay with perpendicular distance from the fault core along a smooth, continuous function (or possibly remain constant over the width of the paleo-damage zone). A key finding of this study is that the spatial extents of various deformation elements (veins, etc.) are not coincident with the domain boundaries defined by the fracture density analysis (Figure 3.19). Schulz and Evans (1998) similarly noted a lack of spatial coincidence among the extents of distinct damage-zone signatures (e.g., geochemical alteration, macroscopic, and microscopic deformation) within the damage zone of the Punchbowl fault. A caveat to this result is the possibility that the spatial extents of specific vein cements within the planes of observation do not adequately represent the farthest distance of each feature from the fault cores. There are two reasonable explanations for the observation that the different vein cements are not apparently confined by the domain boundaries. Because the distance that fluids can travel within a fault zone perpendicular to the fault core is primarily a function of local fluid pressures and the permeability at the time of fluid flow, it is possible that (1) fluids routinely leak beyond the actively deforming zone or, (2) fluids may not have adequate pressure and/or permeability to reach the outer extent of the actively deforming region during a given event.

Because the deformation elements are not spatially restricted to the damage-zone domains, the timing relationships inferred from cross-cutting relationships between these features cannot be used to reconcile the relative ages of the different domains. However, there are three possible scenarios that relate the number of observed damage-zone domains to the number of earthquake events on each fault. (1) The number of earthquakes is equivalent to the observed number of domains; each domain represents the signature of one earthquake. (2) The number of earthquakes exceeds the number of domains, and the damage-zone architecture was established late in the slip history; the domains represent the signature from the last few events. (3) The number of

earthquakes exceeds the number of domains, and the damage-zone architecture was established early in the slip history and preserved during subsequent events.

The first option is inconsistent with observations from this study; three damage-zone domains were observed along each fault zone (not including the fault cores and DZF domains), and there is evidence for >3 slip events. The extensive evidence for episodic fracture reactivation observed in this study underscores the low probability that the fault architecture was established late in the slip history and therefore renders the second option unlikely. The favored interpretation is that in each case the number of earthquakes exceeds the number of domains, and the damage-zone architecture was established early—possibly during the first several events—and preserved.

The preservation of early damage-zone architecture indicates that either the signature of the domains was not overprinted during subsequent events or was continually accentuated. The architecture would not be overprinted if subsequent events mostly reactivated existing fractures rather than breaking fresh rock, or if extreme slip localization concentrated later deformation within the core and inner damage zone. The former explanation may be consistent with the process-zone model, and the latter explanation is consistent with the slip-localization model. Because of the observation that individual fractures within the damage zones have been reactivated up to ten times, it is unlikely that slip localization caused the cessation of distributed deformation throughout the damage zone once the domains were established. Therefore, the preferred explanation is that damage-zone architecture was established early in the slip history and preserved during subsequent events that mostly reactivated preexisting fractures within the damage zones, independent of the dimensions of subsequent paleo-damage zones. This scenario is consistent with the process-zone model if the paleo-damage zones grew sequentially larger, though the relative ages of the variably sized paleo-damage zones cannot be resolved in this study. It is also possible that the damage-zone architecture is repeatedly accentuated during subsequent characteristic-type events that have similarly sized paleo-damage zones.

3.7.4 The Role of Fluids in the Seismic Cycle

Alteration products such as dissolved feldspars, intergranular laumontite cement, and veins provide extensive evidence of fluid flow and fluid-rock interaction within the majority of the fault zones at Borrego Mountain (Figures 3.10, 3.14, and 3.16). Consistent with other observations of fault-related fluid-rock interactions along strike-slip faults in this region, syntectonic reactions were dominated by feldspar dissolution and laumontite precipitation (Evans and Chester, 1995). At both mesoscopic and microscopic scales, complex veins are spatially associated with cataclastic fault rock, and include different minerals and multiple generations of cement (Figure 3.16). Fault BC3 is the exception, characterized by a relative lack of veins and dry cataclasis within the fault core (Table 3.2). In experimental tests, dry cataclasis is associated with rate-weakening behavior (Dieterich, 1979; Tullis, 1988), whereas fluid-assisted deformation is associated with reduced frictional strength and rate strengthening behavior (Evans and Chester, 1995). Crack-seal textures indicate episodic dilation and fracture cementation that implies high fluid pressures. Reactivated cataclasites with different compositions provide evidence for cycles of shear strength recovery and hydrothermal fluid flow (Streit, 1997). The presence of crack-seal textures and reactivated cataclasites with different compositions suggests that faulting and vein filling were not contemporaneous and that the rate of deformation was not limited by the alteration reaction rates (Blenkinsop and Sibson, 1992).

The spatial association between crack-seal textures and reactivated cataclasites indicates that episodic fluid flow events may have been related to rupture events (Sibson, 1990; Chester et al., 1993; Petit et al., 1999). Elevated pore fluid pressures decrease the confining pressure and may cause fault slip under low resolved shear stress (Rice, 1992; Chester et al., 1993; Evans and Chester, 1995). Despite the results of experimental tests of the frictional properties of laumontite that indicate a high coefficient of friction (0.66–0.84) (Morrow and Byerlee, 1991), fluid-assisted deformation may be weaker (Evans and Chester, 1995). High fluid pressure has been identified as an important weakening mechanism in the seismic cycle. In the

dilatancy/fluid-diffusion (or 'seismic pumping') model presented by Scholz et al. (1973) and Sibson et al. (1975), the mechanics of faulting is inextricably linked with fluid migration. According to this model, increasing shear stress prior to faulting results in dilation within the surrounding region, manifested as open fractures normal to the least principal compressive stress. The increased porosity and permeability causes a decrease in fluid pressure within the dilatant zone and an increase in the normal stress across the fault. The decrease in fluid pressure causes an influx of fluids; elevated fluid pressures associated with fluid flow pulses lead to cementation and veining. As the fluid pressure increases, normal stress decreases, and shear failure occurs when the shear stress overcomes the shear strength. Finally, the stress drop associated with faulting allows cracks in the dilatant zone to collapse as fluids flow out of the dilatant region. Fluid flow through structural meshes is associated with earthquake swarm activity (Hill, 1977; Sibson, 1996); a high level of swarm activity has been recorded in the Salton Trough region and has been attributed to high geothermal gradients and triggering by aseismic creep and/or by fluid flow events (Lohman and McGuire, 2007). By analogy with other documented examples of structural meshes that have hosted earthquake swarms and in light of the proximity of the active geothermal area at the south end of the Salton Sea, it is reasonable to speculate that earthquake swarms may have produced the deformation observed at Borrego Mountain.

3.7.5 Evolution of Fault Permeability

Faults can form conduits or barriers to fluid flow (Caine et al., 1996), and in low-permeability rocks, fault and fracture geometry may exert the primary control on fluid flow. Assessments of static permeability address the spatial distribution of permeability, but do not capture changes in the plumbing of the fault system over time. During fault development, a complex history of fault-zone fluid flow is characterized by spatial and temporal variations in fault-zone permeability. Field observations and

microscale analyses can be analyzed in the context of the paleo-damage zone model to reconstruct the temporal and spatial evolution of fault-zone permeability.

Sibson (1996) notes the transitory nature of permeability within structural meshes, and it is likely that there have been substantial changes in the permeability of these fault zones over time as a result of the alternation between dilational fracturing, fluid flow, and cataclasis. The deformational history of the faults indicates that the major changes in the petrophysical characteristics of the fault zones were associated with the following events: (1) The precipitation of pervasive intergranular laumontite cement in the host rock caused a significant widespread reduction in porosity and permeability. (2) Multiple cycles of dilation, pulses of fluid flow in dilational fractures, and cataclasis were characterized by increases in permeability followed by local decreases in permeability due to mineral precipitation, fracture cementation and cataclastic grain size reduction. (3) Dissolution of detrital feldspar grains caused increased secondary microporosity. (4) The most recent dilational phase, characterized by open fractures, caused an increase in permeability that postdates cementation events. More detailed treatment of petrophysical variations within these fault zones can be found in Chapter 4.

Evans and Chester (1995) documented variation in the nature and extent of fluid-rock interactions along strike of large displacement strike-slip fault, and interpreted the variability as a result of differences in the presence and activity of fluids during deformation. Veins confined to the damage zones (within meters of the fault cores) provide evidence of at least meter-scale transport of fluids perpendicular to the fault cores. However, due to limitations in the map-view exposures of these fault zones, it is not possible to constrain how far fluids traveled along the fault cores. The differences in the amount of fluids present at fault BC3 in contrast with the other faults in this study may be attributed to the influence of the faults on the conductivity of the fluids on a regional scale (variations in the permeability structure of the Coyote Creek fault system) and/or on a local scale (permeability variations due to fault-zone architecture).

Permeability differences at both scales can give rise to differences in the quantity and chemistry of fluids (Evans et al., 1997) and to different fluid pressure regimes (Byerlee, 1993). Interestingly, fault BC3 is closest to fault BC1, which has the most extensive evidence of a complex fluid flow history of all fault zones in this dataset (Table 3.2). There are other differences between the fault zones, for instance fault BM2 shows evidence of more phases of hydrothermal fluid flow after the pervasive laumontite cementation in the host rock and prior to cataclastic failure than fault BS1. This difference may be a function of the distance from each fault to the main Coyote Creek fault; fault BS1 formed directly adjacent to the southwest strand of the Coyote Creek fault, whereas fault BM2 formed within a zone of complex subsidiary faulting (Figures 3.4 and 3.6). An alternative hypothesis is that faults with a more complex history of fluid flow may have a longer evolutionary history.

3.8 Conclusions

The paleo-damage zone model is derived from the common observation that damage zones are organized into fault-parallel domains. This model provides a framework to deconstruct fault-related damage into deformation associated with unique slip events and can be used to evaluate models and test hypotheses for the mechanical evolution of fault zones. Small displacement strike-slip faults at Borrego Mountain in the western Salton Trough region originated as dilational fractures and exhibit evidence of episodic fracturing, fluid flow, and cataclasis. Dissolved feldspars, intergranular laumontite cement, and veins with different compositions provide evidence of extensive fluid flow and fluid-rock interaction. Damage-zone architecture is generally symmetrical about the fault cores in the absence of exposed downdip segmentation or prominent secondary damage zone faults.

Step-wise variations in fracture density across the damage zones define relatively sharp domain boundaries that are interpreted as the outer extent of actively deforming zones (‘paleo-damage zones’) associated with individual slip events. The number of slip events on each fault exceeds the number of damage-zone domains. Cross-cutting

relationships between open fractures, cemented fractures and cataclastic fault rocks reveal valuable information about the chronology of deformation within these fault zones; however, because these features are not confined to damage-zone domains, this information cannot be used to infer the relative ages of different paleo-damage zones. Based on the abundant evidence for fracture reactivation, the damage-zone architecture was likely established early, and may represent the signature of deformation from the first few slip events. Subsequent slip events primarily reactivated preexisting fractures rather than breaking fresh rock, thereby preserving the damage-zone architecture. Multiple distinct extensional fracture sets with mutually abutting relationships are present throughout each fault zone. The geometry of damage-zone deformation along these faults resembles a Hill-type structural mesh of faults and dilational fractures (Hill, 1977; Sibson, 1996) and may result from heterogeneous stress distributions due to local variability in stresses or fluid-driven deformation, as in the structural mesh model. On the basis of the proximity of Borrego Mountain to the San Jacinto fault zone and a geothermally active region, and by analogy with evidence of episodic faulting and fluid flow in other regions with high heat flow, it is reasonable to infer that the deformation observed at Borrego Mountain was associated with seismic activity, possibly earthquake swarms.

Chapter 4: Heterogeneous Petrophysical Properties of Fault Zones Formed Along Joints in Laumontite-Cemented Sandstone

4.1 Summary

The petrophysical properties of faulted sandstones are strongly dependent on sediment composition, cementation history, and deformation mechanisms. This chapter presents petrophysical data from four small displacement strike-slip fault zones that evolved by shearing along joints within well-cemented, impure sandstones in the vicinity of the Coyote Creek segment of the San Jacinto fault zone in the western Salton Trough, southern California. Pervasive intergranular laumontite cement formed as a product of the *in-situ* alteration of plagioclase early in the diagenetic history of these fault zones. Although the density of mesoscopic deformation decreases throughout each fault damage zone in a systematic domainal fashion with increasing distance from the fault core, spatial variability in petrophysical behavior is observed within each domain, within individual core plugs, and at the microscale. Deformation features include laumontite-, gypsum-, and calcite-cemented dilational fractures and open fractures that locally act as barriers and conduits for fluid flow. Fault rocks are primarily composed of cement, open fractures, and tabular regions of cataclasis, and have increased porosity and reduced permeability relative to the host rocks. Secondary microporosity occurs within dissolved plagioclase grains and dilatant cataclastic fault rocks. Heterogeneous and unpredictable petrophysical properties within the fault zones result from the variability in host rock properties, the irregular distribution of intergranular cement, and the variable distribution and localized effects of deformation features associated with alternating cycles of dilation, cementation, and cataclasis throughout the history of faulting.

4.2 Introduction

The architectural elements of fault zones represent complex structural and lithological heterogeneities that cause spatial variability in petrophysical properties (Caine et al., 1996; Evans et al., 1997; Fisher and Knipe, 1998). The tendency of different

components of fault zones to act as fluid flow conduits or barriers is critical to fault seal analysis and hydrocarbon exploration. Subseismic (small displacement) faults can have a significant influence on flow within a reservoir, and outcrop-scale analysis of these faults is essential to assess their impact on fluid-flow behavior (Heath et al., 1994; Shipton et al., 2002). Recent work has clarified two categories of failure structures in sandstones: (1) tabular zones of shear or volumetric deformation, "deformation bands", and (2) sharp displacement discontinuities that arise from shear or volumetric deformation of fractures (Aydin et al., 2006, and references therein). These contrasting modes of deformation produce different deformation features that have distinct effects on the petrophysical properties of faulted rock (Davatzes and Aydin, 2003; Myers and Aydin, 2004; Aydin et al., 2006). Due to the prevalence of faulted sandstone reservoirs, analog studies are important for characterizing the impact of various deformation mechanisms on the petrophysical evolution of fault zones in sandstones.

Many factors affect the style of deformation in sandstones, including host rock porosity, clay content, confining pressure, and bulk strain (Antonellini et al., 1994). Deformation bands typically form in host rocks with a porosity >~15% (Antonellini and Aydin, 1994). Davatzes et al. (2005) demonstrated that local variations in stress state along a fault can give rise to deformation band formation under conditions of higher mean stress and more compressive least compressive principal stress, whereas regions of lower mean stresses and more tensile least compressive stresses favor the development of sheared joints. The petrophysical properties of deformation band-style fault rocks have been the subject of many published studies (e.g., Antonellini and Aydin, 1994; Main et al., 2000; Aydin et al., 2006). The flow properties of sandstones that are exclusively deformed by shearing across joints have only previously been described for faults in the Aztec Sandstone in Nevada, a poorly cemented to uncemented, subarkose to quartz arenite (Myers, 1999; Jourde et al., 2002; Flodin et al., 2005).

This chapter describes petrophysical data from four different small displacement strike-slip fault zones at Borrego Mountain, in southern California (Figure 4.1). The structural evolution of these fault zones is described in detail in Chapter 3.

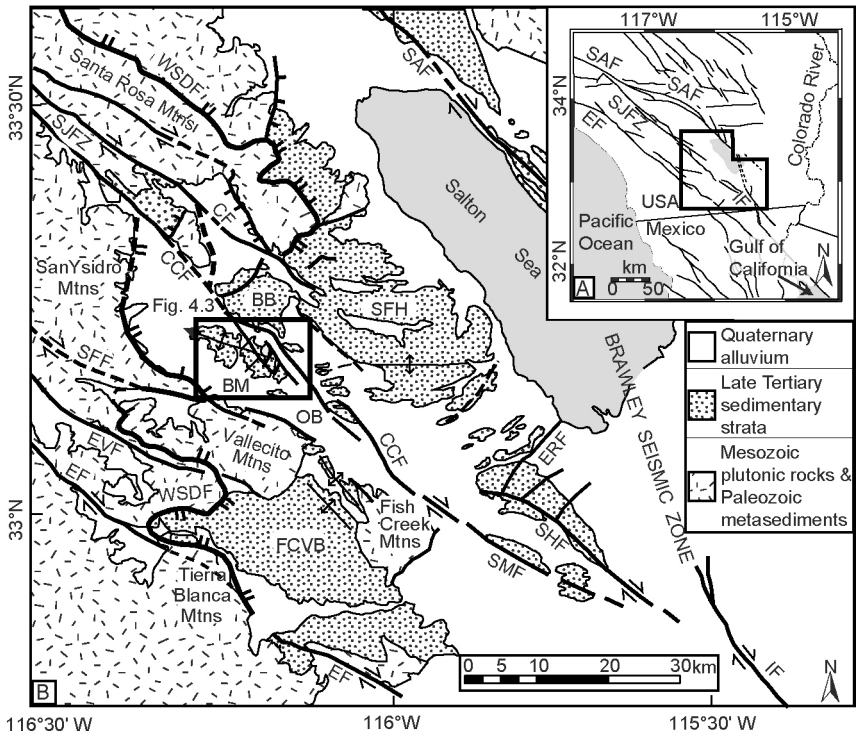

Figure 4.1. (A) (Inset) Fault map of Southern California (modified from Lutz et al., 2006). (B) Generalized geologic map of the western Salton Trough (modified from Lutz et al., 2006). Borrego Mountain is shown in detail in Figure 4.3. *BB*, Borrego Badlands; *BM*, Borrego Mountain; *CCF*, Coyote Creek fault; *CF*, Clark fault; *EF*, Elsinore fault; *ERF*, Elmore Ranch fault; *EVF*, Earthquake Valley fault*; FCVB*, Fish Creek–Vallecito basin; *IF*, Imperial fault; *OB*, Ocotillo Badlands; *SAF*, San Andreas fault; *SFF*, San Felipe fault; *SFH*, San Felipe Hills; *SHF*, Superstition Hills fault; *SJFZ*, San Jacinto fault zone; *SMF*, Superstition Mountain fault; *WSDF*, West Salton detachment fault.

Structural analysis indicates that these faults evolved by shearing along joints, although fault-zone evolution is not consistent with published models for the evolution of sheared joints that predict splay fracturing with interconnected joints in the damage zone that are linked to the fault core (see Section 3.7.3) (e.g., Myers and Aydin, 2004; Davatzes et al., 2005; Lunn et al., 2008). In contrast, the damage-zone deformation within these fault zones at Borrego Mountain generally appears to be more dispersed and discontinuous, with discrete damage elements that are not directly connected to the fault core.

The faults described in this study are exposed within the Pliocene West Butte Conglomerate, a poorly to very poorly sorted, cemented lithic arenite with measured host rock porosities that range between 12–19% (Figure 4.2) (Dott, 1964).

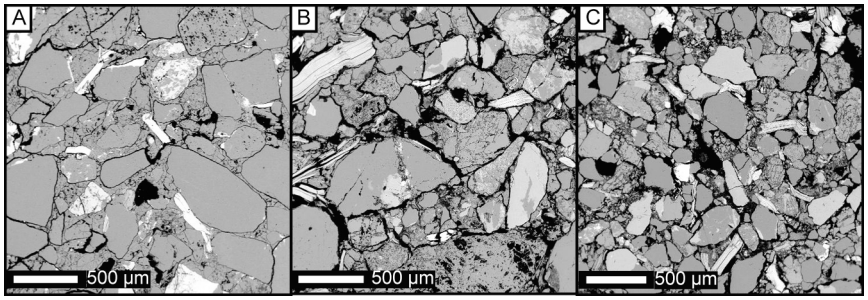

Figure 4.2. Photomicrographs of host rocks from faults (A) BM3, (B) BC3, and (C) BC1. Note the poor sorting, the variable amount of intergranular laumontite cement, and the abundance of detrital feldspars and micas.

Cementation products include pervasive but heterogeneously distributed intergranular laumontite cement and laumontite-, gypsum-, and calcite-cemented dilational fractures. Laumontite ($CaAl_2Si_4O_{12} \bullet 4H_2O$) is a Ca-zeolite, which is one of ~20 species of zeolite minerals that have been observed in sedimentary rocks (Hay and Sheppard, 2001). Laumontite cementation has been reported along major crustal and transform faults including the San Andreas, Punchbowl, San Gabriel, and Sierra Madre faults. In these settings, laumontite cement has been interpreted as a product of hydrothermal fluid-rock interaction (McCulloh and Stewart, 1982; Vincent and Ehlig, 1988; Evans and Chester, 1995; Chester and Chester, 1998; Schulz and Evans, 1998). Laumontite cement can have a major impact on porosity and permeability behavior (James and Silver, 1988; Yanagimoto and Iijima, 2003). Feldspars are an important precursor material for zeolites in clastic sedimentary rocks (Bernet et al., 1997), and microstructural analysis indicates that partially to completely dissolved detrital feldspar grains occur throughout the selected Borrego Mountain fault zones (see Section 3.6.1). This chapter describes the variability in the *in-situ* petrophysical properties of the fault zones in the context of detailed fault-zone architecture. Based on these results, the implications for predicting the fluid-flow properties of laumontite-cemented faulted sandstones are discussed.

4.3 Geologic Setting

The Borrego Mountain study area is adjacent to the Coyote Creek fault of the San Jacinto fault zone in the western Salton Trough region of southern California (Figure 4.1). The Salton Trough is a structurally controlled basin that lies along the Pacific-North American plate boundary at the northwestern extension of the Gulf of California (Figure 4.1A). The northwest-striking West Salton detachment fault accommodated basin subsidence in the Salton Trough from the latest Miocene (ca. 6 Ma) until slip initiated along the dextral strike-slip San Jacinto fault zone in the early Pleistocene (ca. 1.1 Ma) (Axen and Fletcher, 1998; Lutz et al., 2006; Kirby et al., 2007). Late Tertiary sedimentary strata exposed at Borrego Mountain were deposited in the upper plate of the West Salton detachment fault in a fluvial-deltaic environment between the ancestral Colorado River and the Gulf of California (Dibblee, 1954; Morley, 1963; Woodard, 1963; Hoover, 1965; Reitz, 1977; Winker, 1987; Winker and Kidwell, 1996; Axen and Fletcher, 1998; Steely, 2006). The Pliocene West Butte Conglomerate was folded syndepositionally along the northwest-trending Borrego Mountain anticline during slip on the West Salton detachment fault and has been interpreted as alluvial fan or bajada deposits (Steely, 2006).

The four small displacement strike-slip faults examined in this study are exposed along three different washes at Borrego Mountain: Borrego Mountain Wash (fault BM3), Butte Canyon Wash (faults BC1 and BC3), and Blow Sand Wash (fault BS1) (Figure 4.3).

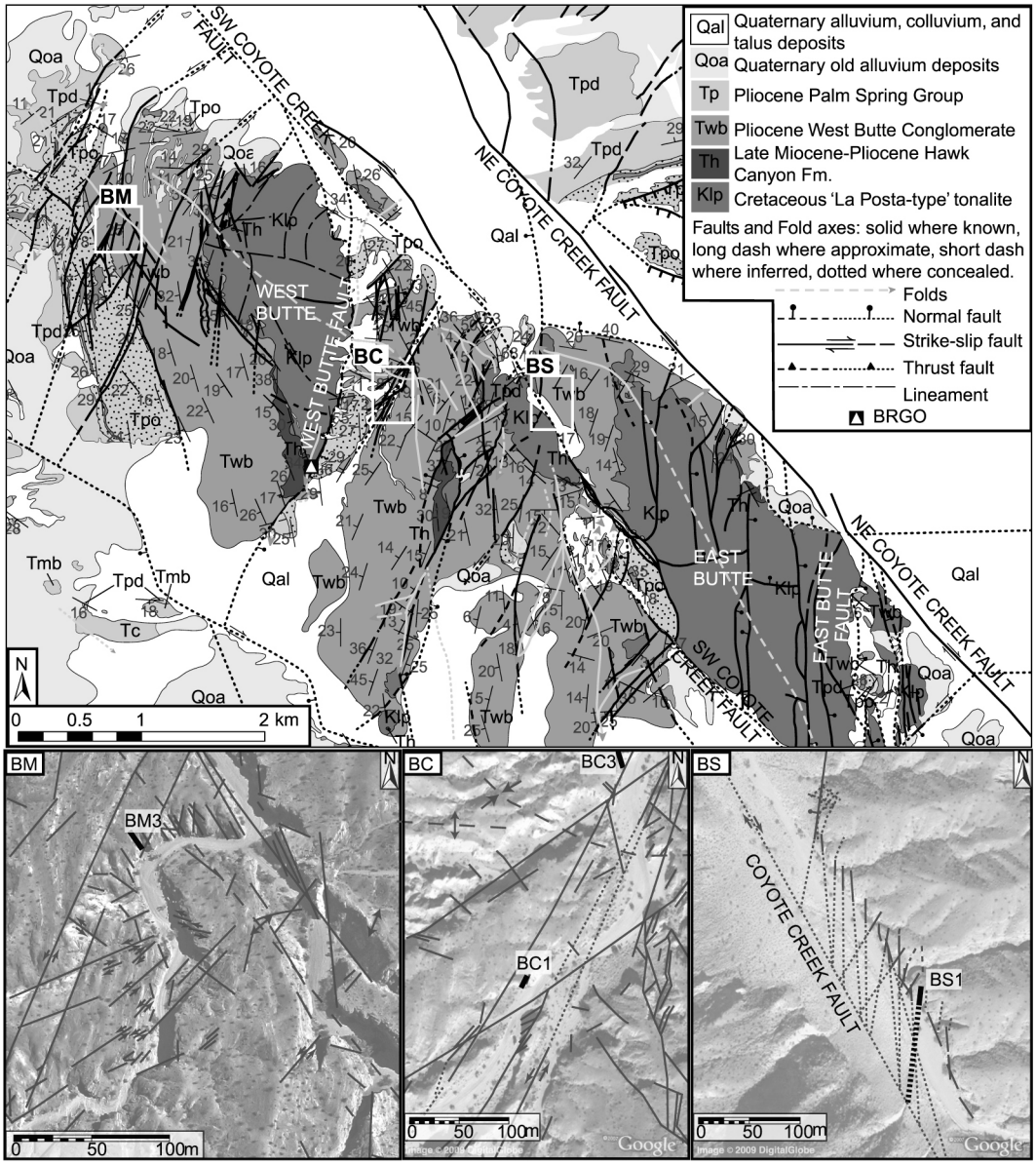

Figure 4.3. Geology of the Borrego Mountain area (modified from Steely, 2006). Study areas are indicated with white boxes; *BM*, Borrego Mountain Wash; *BC*, Butte Canyon Wash; *BS*, Blow Sand Wash. Insets: Aerial photos (BM courtesy of Kelly McCague; BC, BS from Google Earth) of the study areas were used as base maps to document the many smaller faults in the vicinity of the selected faults. Faults BM3, BC1, BC3, and BS1, shown with thick black lines, were selected for detailed petrophysical analysis. Arrows reflect slip senses determined from aerial photo interpretation of displaced strata, where possible. White triangle marks the location of station BRGO, where a heat flow measurement was taken just southwest of the Butte Canyon Wash study area, along the West Butte fault (Lachenbruch et al., 1985).

These faults belong to a larger population of strike-slip and oblique-slip faults at Borrego Mountain that represent subsidiary deformation associated with a restraining

bend in the Coyote Creek fault northwest of Borrego Mountain (Figures 4.1 and 4.3) (Steely, 2006). Slip along the Coyote Creek fault initiated in the vicinity of Borrego Mountain at ca. 0.6 Ma (Lutz et al., 2006; Kirby et al., 2007). The selected faults have an estimated maximum stratigraphic burial depth of ~3.0 km (see Section 2.1.3). In the vicinity of the Salton Trough, the San Jacinto fault zone is strongly affected by high heat flow in the region. The geothermal gradient at Borrego Mountain may be as high as 65˚C/km (see Section 2.1.4); this calculation is based on a heat flow measurement along the West Butte fault (station BRGO) (Figure 4.3) (Lachenbruch et al., 1985).

Faults BM3, BC1, BC3, and BS1 are well exposed, relatively isolated, accessible, and are reasonably inferred to have been seismogenic (see Chapter 3). It is challenging to estimate total fault displacement on these predominantly strike-slip faults due to a lack of exposure of potential offset markers in map view. However, the faults in this study are a subset of a larger dataset of faults that were selected on the basis of fault-zone dimensions in an effort to focus on the detailed structural analysis of faults with small (<5 m) displacements (see Chapter 3). Accordingly, the four faults described in this chapter have comparable total fault-zone widths (including fault damage zones) of ~6m, average fault core widths of ~4 cm, and are inferred to have accommodated approximately equivalent average shear strains (see Section 3.6.3) (Figure 4.4).

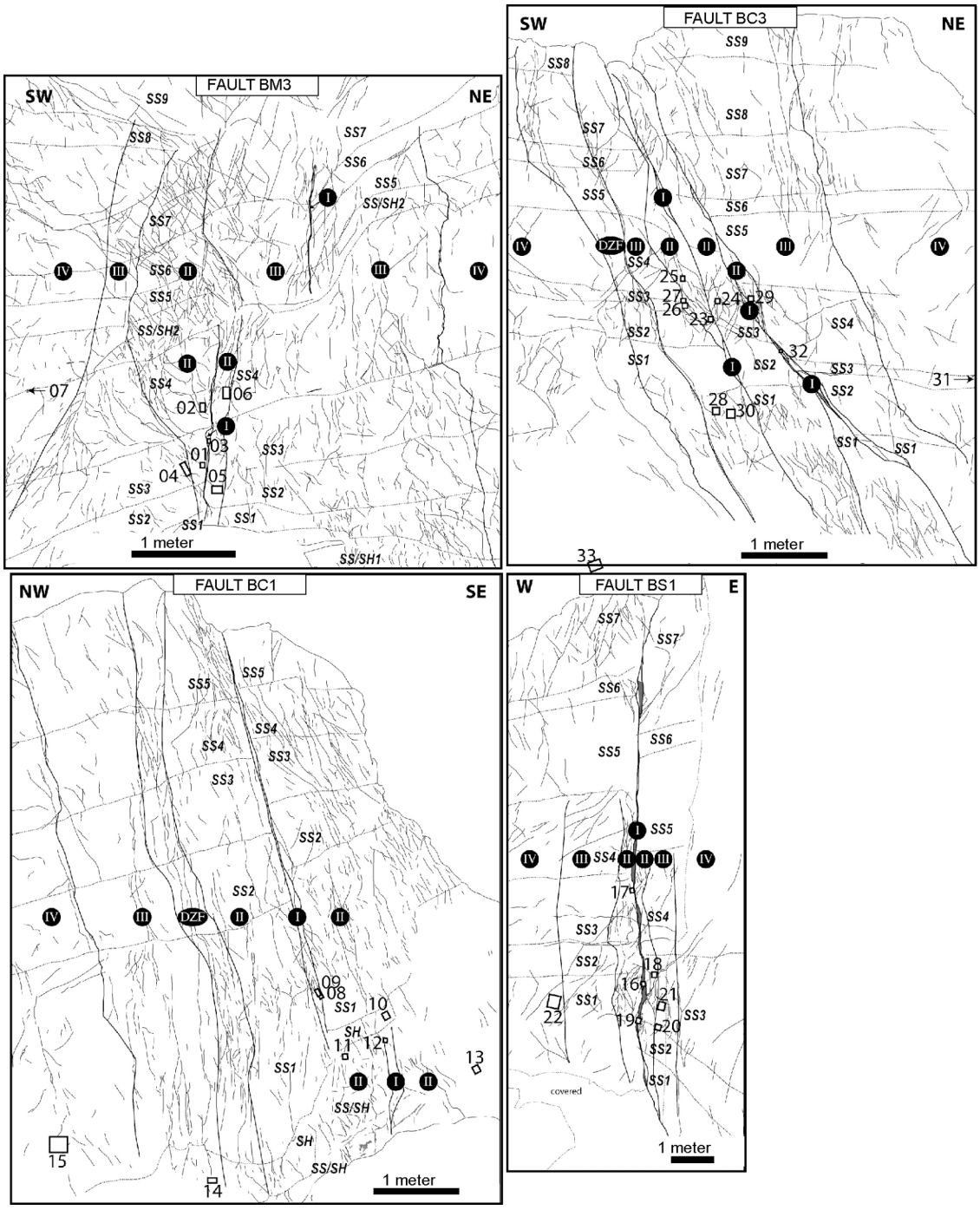

Figure 4.4. Cross-sectional outcrop maps showing fault-related deformation (black solid lines indicate faults, veins and fractures; gray fill is used to represent veins that are >0.5 cm wide), fault-zone domains (thicker fault-parallel lines mark the boundaries between domains; Roman numerals indicate different domains), stratigraphy (dashed black lines mark the stratigraphic boundaries; *SS#* indicate different stratigraphic units, *SS*, sandstone, *SH*, shale, *SS/SH*, interbedded sandstone and shale), and the distribution of samples collected for petrophysical analysis.

4.4 Fault Zone Elements

The major components of a fault zone are the fault core and the damage zone (Figure 4.5) (Chester and Logan, 1986; Caine et al., 1996).

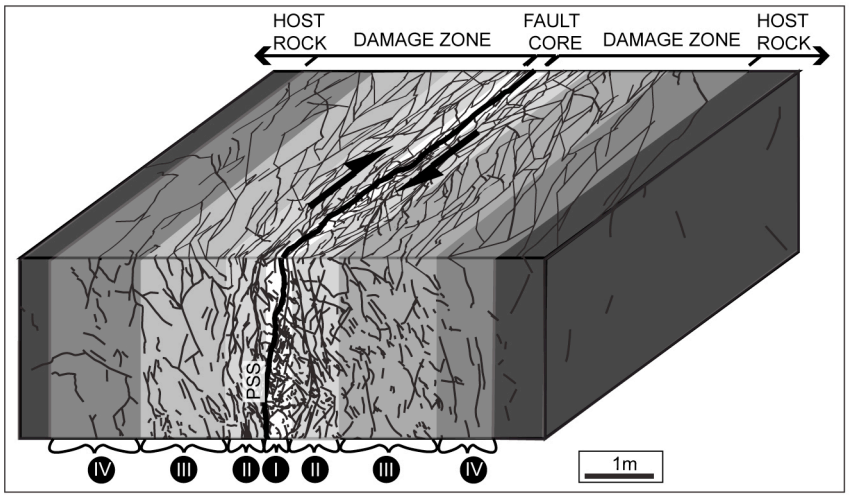

Figure 4.5. Generalized illustration of the fault zones at Borrego Mountain includes a fault core surrounded by a symmetrical damage zone that is organized into distinct domains (represented with different shades of gray and indicated with Roman numerals); *PSS*, principal slip surface. Note the discontinuous nature of damage elements in cross-section. The geometry of deformation in map view is not well constrained due to exposure limitations, but is inferred to be more continuous, with common intersections parallel to the σ_2 direction (vertical), as described in the structural mesh model (Sibson, 1996).

Fault displacement is mostly accommodated in the fault core, the innermost fault-zone domain (domain I), which includes the principal slip surface(s) of the fault. Fault damage zones are characterized by mesoscopic and microscopic deformation that accrues in the volume surrounding the fault core as a result of slip on the fault. The density of deformation within the damage zone is elevated relative to the average background level of deformation in the surrounding host rock (Chester, 1995). Many damage zones are zoned, with fault-parallel domains that may have distinct structural, geochemical, petrophysical, and geophysical properties (Schulz and Evans, 2000; Li and Vernon, 2001; Sayed, 2001; Spudich and Olsen, 2001; Wilson et al., 2003). Based on detailed outcrop mapping, microstructural data, and fracture analysis, the damage zones of faults in this study have been subdivided into fault-parallel domains that are marked by distinct levels of fracture density (see Section 3.6.2). The domains are

numbered with increasing distance from the fault core: domain II (adjacent to the fault core), domain III, etc. (Figures 4.4 and 4.5). Fault-zone domains I, II, III, IV are referred to in this study with prefixes FC, DZ, HR to denote fault core, damage zone, and host rocks, respectively.

4.4.1 Deformation Elements

Deformation features within the fault zones include cataclastic fault rocks, laumontite-, calcite-, and gypsum-cemented fractures, and open fractures; these features tend to be spatially coincident (Figure 4.6).

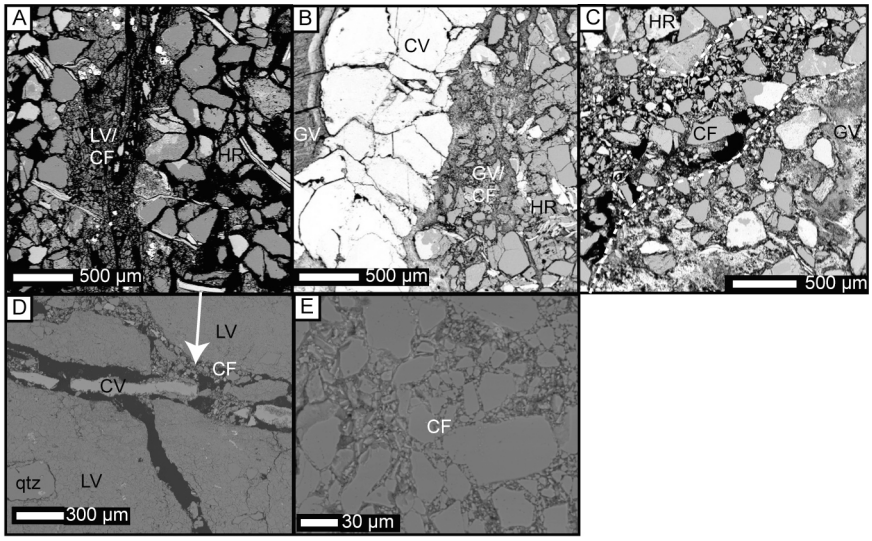

Figure 4.6. Photomicrographs of deformation features observed within the fault zones, *CF*, cataclastic fault rock; *CV*, calcite vein; *GV*, gypsum vein; *HR*, host rock; *LV*, laumontite vein; *qtz*, detrital quartz grain. (A) Faulted laumontite vein from fault BC1 is porous and highly fractured. Adjacent host rock is porous and fractured. (B) Parallel calcite vein, gypsum vein, and gypsum-cemented cataclastic fault rock from fault BC1. Out of the frame of view a calcite cement fragment is entrained in the gypsum vein and provides evidence that calcite cementation predates gypsum cementation. Cataclasis predates at least one generation of gypsum cementation. Note the fractures within the veins. (C) Parallel gypsum vein (contains entrained detrital grains) and uncemented, porous cataclastic fault rock from fault BC1. (D) Late-stage dilational fracture in a laumontite vein from fault BS1 is partially filled with calcite cement (arrows); cataclastic fault rock in the fracture postdates the laumontite vein and predates the calcite vein. (E) Low-porosity, uncemented cataclastic fault rock from fault BS1.

Microstructural observations provide evidence of alternating cycles of dilation, cementation, and cataclasis throughout the history of fault evolution (see Chapter 3). Field observations and fracture analysis indicate that the density of deformation features within the fault zones generally decreases with increasing distance from the

fault core in a domainal fashion, with mesoscopic variation in fracture density between the different fault-zone domains (see Section 3.6.2) (Figure 4.4). Background deformation levels are observed within domain IV in the four fault zones described in this study, therefore this domain is generally referred to as the host rock (HR) domain. The HR domain includes relatively sparse open and cemented fractures. Domain III is characterized by more intense deformation than in the HR, but significantly less than in domain II. Domain II includes an abundance of deformation elements adjacent to the fault core (Figure 4.4). Substantial microstructural variation in the dimensions and density of deformation features is evident in samples from the different domains (Figure 4.7). At fault BS1, sparse deformation elements occur within undeformed host rocks in domain III, whereas abundant thin open and cemented dilational fractures occur within domain II (Figure 4.7). The fault core (domain I) at BS1 is primarily composed of vein material and cataclastic fault rock (Figure 4.7).

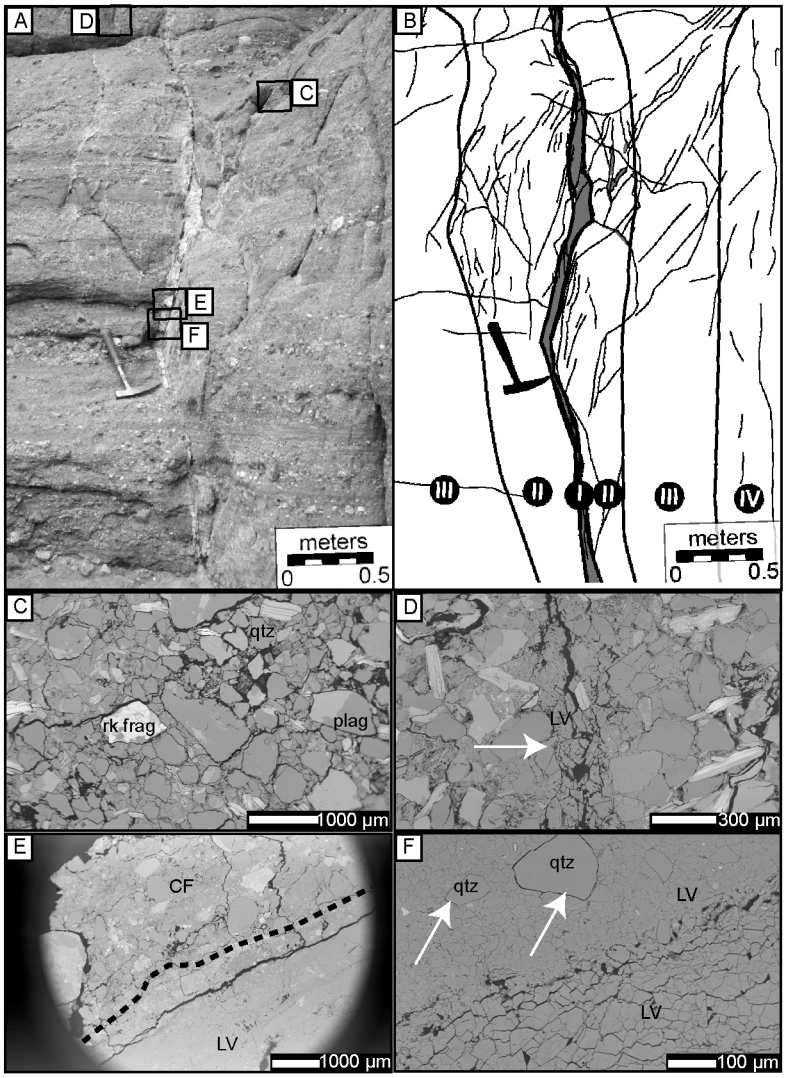

Figure 4.7. (A) Outcrop photo and (B) line drawing showing detail of the fault core (I) and adjacent damage-zone domains (II, III, IV) at BS1 near the base of the outcrop. (C–F) BSE micrographs of the West Butte Conglomerate showing mineralogical and textural variation between the fault-zone domains; *CF*, cataclastic fault rock; *LV*, laumontite vein; *plag*, plagioclase; *qtz*, quartz; *rk frag*, rock fragment. (C) Undeformed host rocks from DIII. (D) A thin (<300 µm) laumontite-cemented dilational fracture (white arrow) from DII. Note the late-stage fracture within the vein. (E) Cataclastic fault rock from the fault core (DI); a laumontite-cemented vein was formed along this fault. (F) A thick laumontite-cemented dilational fracture within the fault core (DI). Note the different textures of laumontite and the inclusion of detrital grains (white arrows).

4.5 Methodology

Petrophysical analysis was performed on thirty-two samples of the West Butte Conglomerate from faults BM3, BC1, BC3, and BS1, including seven to eleven samples from each fault zone. Samples were collected from the fault core (FC) and

three fault-parallel domains (DZII, DZIII, and HR) along transects across the fault zones. Sample locations are shown in Figure 4.4. Analytical tests include x-ray diffractometer (XRD) analysis, porosity and permeability measurements under low confining stress and increasing hydrostatic confining stress, laser particle size analysis (LPSA), and mercury injection capillary pressure (MICP) tests. Tables 4.1, 4.2, and 4.3 list the closest distance from each sample to the nearest principal slip surface within the respective fault zone. Because the damage zone is defined as the region around the fault that contains an elevated abundance of discrete deformation elements, a particular sample from within the damage zone may or may not contain one of these damage elements, and in the latter case may be classified as a "host rock" sample despite its location within the damage zone. As a result of this classification scheme, some "host rock" samples may occur closer to the fault core than some "damage zone" samples.

Hand samples were removed from the outcrops using a chisel; extreme care was taken in sample removal because zeolite-cemented host rocks tend to disintegrate easily and can be difficult to sample (Vincent and Ehlig, 1988). In preparation for the XRD analysis, samples were ground to a fine powder using a McCrone mill. A Philips XRD instrument was used to determine the bulk weight abundance of mineral phases and the total clay abundance. To further analyze clay mineralogy, a subset of these samples was further disaggregated using an ultrasonic probe and centrifuged to isolate the clay fraction (<4 μm). Diffractograms of sample scans were analyzed with Philips APD and Profit software to determine the types and abundances of the clay species. Grain size analysis was conducted using a Beckman Coulter LS200 LPSA instrument; the samples were dried and gently disaggregated in preparation for these tests.

Core plugs (1 in. diameter and 0.75–1.875 in. long) were extracted in the laboratory from the thickest, most consolidated parts of the samples using liquid nitrogen vent gas as the bit coolant and lubricant. Due to the difficulty in retrieving sufficiently large samples of intact fault core, plugs of fault core samples were not obtained for faults BM3 and BC3. Methanol was used as the extracting solvent in a soxhlet extractor to

remove water and salts from the samples. The samples were dried in a convection oven at 180˚F, and then allowed to cool to room temperature in airtight containers. Core plugs of fault core and damage zone samples are oriented both perpendicular and parallel to the principal slip surface of the fault zone. Core plugs of host rock samples are oriented both perpendicular and parallel to bedding. Suffixes '-perp' and '-para' are used in conjunction with the sample number to denote perpendicular and parallel plugs, respectively.

Porosity of the core plug samples was measured in a small volume helium porosimeter in a rubber-sleeved, hydrostatically loaded (5 MPa) overburden cell using Boyles' Law principle of gas expansion with helium gas. Permeability data were collected in a steady-state Hassler-sleeve air permeameter under a confining pressure of 5 MPa. Permeability data are corrected for Klinkenberg gas slippage effects (Klinkenberg, 1941; Tanikawa and Shimamoto, 2006); this correction amounts to less than a 10% change in the permeability for all samples except for the lowest permeability sample (<0.2 mD), which has a 27% correction factor.

Conventional high-pressure (0–60,000 psi) MICP experiments were conducted on the core plugs using a Micromeritics AutoPore 9500 instrument. Results from backscattered electron (BSE) image analysis of 3–6 samples from each fault zone using a scanning electron microscope (SEM) and an electron microprobe in conjunction with energy dispersive x-ray analysis (EDAX) are reported in Chapter 3. Microstructural data were used to determine host rock, fault rock, and cement mineralogy, deformation mechanisms, and the relative ages of microstructures (see Chapter 3). Some of these results are presented in this chapter as a complement to the petrophysical, LPSA and XRD data introduced herein; complete microstructural results are detailed in Appendix C. Data presented in Figures 4.8, 4.9, 4.10, 4.11, 4.12, 4.16, and 4.17 are organized by fault zone (symbol type) and by fault-zone domain (color).

4.6 Mineralogy

To determine the bulk weight abundance of various mineral phases and the total clay abundance, XRD analysis was performed on representative portions of fourteen fault core, damage zone and host rock samples from faults BM3, BC1 and BC3 (Table 4.1; Figure 4.8).

Table 4.1. Mineralogy from XRD analysis of selected samples; *Qtz*, quartz; *Plag*, plagioclase; *K-spar*, k-feldspar, *Lau*, laumontite; *S*, smectite; *I/S*, illite-smectite; *I*, illite; *K*, kaolinite; *C*, chlorite; *C/S*, chlorite-smectite; *Tr*, trace amount.

Fault	Sample Number	Domain	Distance to PSS (cm)	Qtz (%)	Plag (%)	K-spar (%)	Lau (%)	Clay Minerals (%)							Total Carbonate Minerals
								Total	*S*	*I/S*	*I*	*K*	*C*	*C/S*	
BM3	3	FC	0	32	11	11	0	42	4	6	10	4	7	11	4
BM3	5	DZII	26	35	29	9	9	13							5
BM3	6	DZII	23	36	26	8	11	15							4
BM3	7	HR	280	34	24	8	13	14	0	1	2	1	5	5	4
BC1	9	FC	0	37	10	4	19	25	Tr	1	6	1	6	11	5
BC1	10	DZII	13	43	19	7	0	26							4
BC1	12	FC	0	55	13	12	4	14	Tr	2	5	1	3	3	2
BC1	13	DZIII	60	50	11	8	3	24	15	2	4	Tr	3	0	1
BC1	14	HR	170	43	16	13	0	23							5
BC3	23	DZII	1	53	12	9	11	13	2	1	3	1	2	4	2
BC3	29	DZII	5	46	14	12	11	14							3
BC3	30	DZIII	40	45	12	6	12	16							9
BC3	31	HR	289	39	10	3	18	25	0	2	7	2	6	8	5
BC3	32	FC	0	36	26	6	13	14	2	2	2	Tr	3	5	5

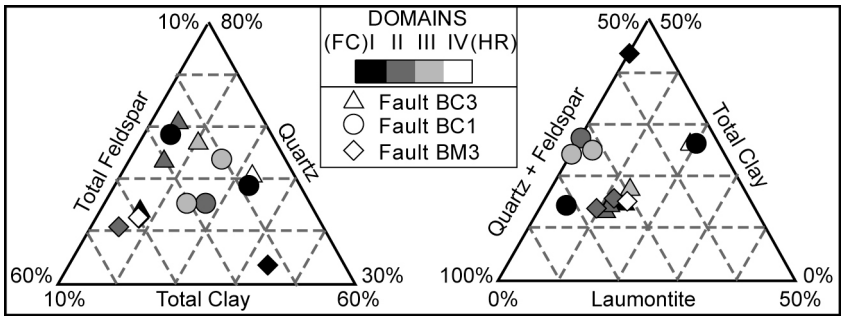

Figure 4.8. Ternary plots of whole rock XRD data from faults BM3, BC1, BC3. Symbols are organized by fault zone; color corresponds to the fault-zone domain. The plots display a limited range of 50% for each phase. Left: Quartz-total clay-total feldspar plot; right: Total clay-quartz + feldspar-laumontite plot.

Subsets of two or three samples from each fault zone were further analyzed to determine the types and abundances of the clay species. The average bulk mineralogy of the samples consists of 42% quartz, 20% clay minerals, 17% plagioclase, 11% laumontite, and 8% k-feldspar (Table 4.1; Figures 4.2 and 4.7C). Laumontite, the most

abundant authigenic phase, occurs as patchy intergranular cement and vein fill. Other mineral phases present in lesser amounts include an average of 4% carbonates, including calcite, dolomite and siderite. Trace amounts of pyrite were also measured in most of the samples. The average clay mineralogy of the eight samples selected for quantitative clay analysis consists of 7% chlorite-smectite, 6% smectite, 5% illite, 4% chlorite, 2% illite-smectite, and 2% kaolinite (Table 4.1). All of the clay minerals occur in both fault core and host rock samples. SEM images reveal that most of the clay is detrital, and clay minerals generally do not occur as host rock cement.

Samples from fault BM3 generally have lower quartz content than samples from faults BC1 and BC3 (Figure 4.8, left). Fault rock samples from faults BM3 and BC1 have higher abundances of clay than samples from the damage zones of these faults; in contrast, a host rock sample from fault BC3 has higher clay content than the fault core and damage zone samples from BC3 (Figure 4.8); this particular host rock sample was extracted from a finer grained bed. The observed variability in quartz content between deformed and undeformed samples is unremarkable relative to the overall mineralogical variability observed in samples from each fault zone.

SEM image analysis and XRD results indicate that the abundance of laumontite as both intergranular cement and vein fill is variable within each fault zone and between the different fault zones (Figures 4.2 and 4.8, right). All fault core and damage zone samples from BC3 have high laumontite content (11–13%) and a host rock sample has a particularly high abundance of laumontite (18%) (Figure 4.8, right). The laumontite in samples from fault BC3 primarily occurs as intergranular cement because fault BC3 has fewer cemented fractures than the other fault zones (see Section 3.7.5). At fault BC1, one fault core sample has a high abundance (19%) of laumontite, whereas another fault core sample has only 4% laumontite. The presence of laumontite in the fault cores is predominantly in the form of cemented fractures and is highly variable. Samples of the damage zone and host rock of BC1 have low (0–3%) laumontite content. In contrast, at fault BM3, host rock and damage zone samples have a high

abundance of laumontite (9–13%) whereas the clay-rich fault core sample contains no laumontite. From these data, it is not possible to infer a systematic relationship between the abundance of laumontite and proximity to the fault core at the scale of the core plugs. Whereas the laumontite veins are expected to be more abundant closer to the fault cores, the intergranular laumontite cement with similar composition complicates the signature. The high minus-cement porosity indicates that the intergranular laumontite cement formed during an early stage of burial and likely predates the faults in this study.

4.7 Grain Size Analysis

Grain size analysis was performed on representative portions of four to six samples from faults BM3, BC1, BC3, and BS1 using a LPSA instrument with a range of measurement from 0.375–2000 μm. Grain-size distributions for samples from each fault zone are shown in Figure 4.9; grain-size statistics are summarized in Table 4.2.

Table 4.2. Grain size statistical data from laser particle size analysis (LPSA) of selected samples.

Fault	Sample Number	Domain	Distance to PSS (cm)	Median (mm)	Sorting (Folk-Ward)	Skewness (Folk-Ward)	Kurtosis (Folk-Ward)
BM3	3	FC	0	0.02	1.87	0.13	0.90
BM3	4	DZIII	32	0.68	1.59	0.54	1.72
BM3	6	DZII	23	0.04	2.21	0.35	0.86
BM3	7	HR	280	0.15	1.91	0.26	1.15
BC1	9	FC	0	0.09	2.91	0.15	0.75
BC1	12	FC	0	0.12	2.82	0.23	0.81
BC1	14	HR	170	0.25	2.12	0.29	1.28
BC1	15	HR	335	0.73	1.36	0.45	1.16
BS1	17	DZII	0	0.67	1.71	0.55	1.57
BS1	18	DZII	20	0.63	1.71	0.51	1.49
BS1	20	DZIII	10	0.64	1.78	0.55	1.55
BS1	21	DZIII	9	0.75	1.61	0.57	1.78
BS1	22	HR	177	0.68	1.80	0.58	1.76
BC3	23	DZII	1	0.65	1.34	0.47	1.33
BC3	25	DZII	8	0.45	1.88	0.46	1.02
BC3	29	DZII	5	0.53	1.36	0.37	1.32
BC3	31	HR	289	0.09	2.85	0.21	0.75
BC3	32	FC	0	0.30	1.51	0.35	1.14
BC3	33	HR	240	0.49	1.45	0.36	1.14

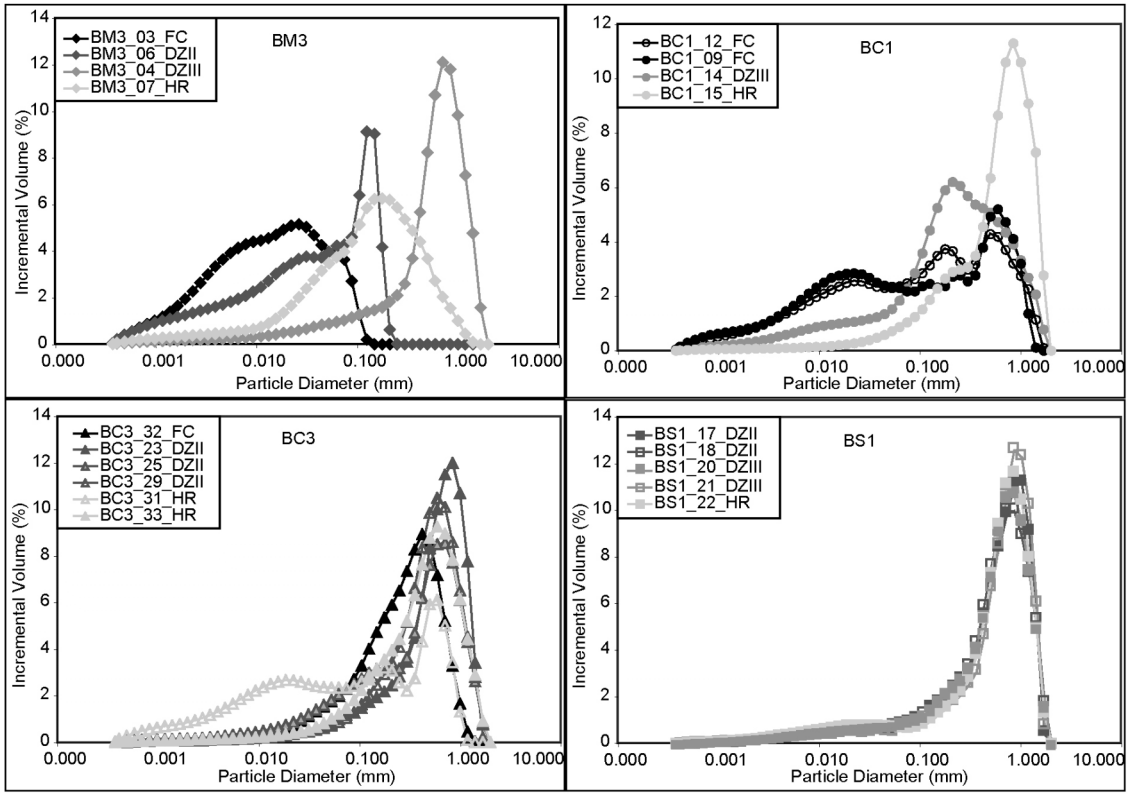

Figure 4.9. Grain size distribution expressed as incremental volume as a function of particle size for samples from faults BM3, BC1, BC3, and BS1. Color corresponds to the fault-zone domain; progressively lighter colors correspond to domains at a greater distance from the fault core.

Measured grain sizes from all samples range from 3.75×10^{-4}–2.0 mm; all grain sizes within that range can be found within each sample with the exception of FC and DZII samples from fault BM3 (Figure 4.9). For each fault-zone domain, the inclusive graphic standard deviation value (Folk and Ward, 1957) has a minimum between 1.34–1.51 and a maximum between 2.12–2.91, which corresponds with poorly sorted to very poorly sorted. Median grain sizes range from 0.095–1.451 mm for host rock samples, 0.245–0.746 mm for DZIII samples, 0.044–0.668 mm for DZII samples, and 0.015–0.305 mm for fault core samples. The maximum value of median grain size within each domain decreases systematically with increasing proximity to the fault core. Fault rock samples have the lowest median grain sizes and the narrowest range of median grain size values. In contrast, host rock samples exhibit the widest range of median grain size values.

Samples from each fault-zone domain, including host rocks and fault core samples, are coarse skewed (Figure 4.9). All samples have kurtosis values that range from 0.75 (platykurtic-more rounded peak) to 1.78 (very leptokurtic-sharper peak). Platykurtic to very leptokurtic values are observed in host rock and DZII samples, whereas DZIII and fault core samples exhibit a narrower range of values, from 1.28–1.78 for DZIII (leptokurtic to very leptokurtic-sharper peaks) and from 0.75–1.14 for fault core samples (platykurtic to leptokurtic-more rounded peaks).

For fault BM3, the most frequent particle size systematically decreases with increasing proximity to the fault core with the exception of the HR sample (#7), which was extracted from a finer-grained bed (Figure 4.9). For fault BC1, a similar trend is observed with HR sample #15 and DZIII sample #14 (Figure 4.9). FC samples from faults BM3 and BC1 are distinctly multimodal (Figure 4.9); these samples have higher abundances of clay than samples from the damage zones of these faults (Figure 4.9). For fault BC3, HR sample #31 is from a fine-grained bed; the other samples have unimodal distributions that do not show a relationship between the most frequent particle size and distance from the fault core (Figure 4.9). For fault BS1, the particle size curves are all very leptokurtic (sharper peaks), although as with fault BC3 there is no apparent relationship between the most frequent particle size and position within the fault zone (Figure 4.9). The samples from BS1 exhibit better sorting (all are poorly sorted, none are very poorly sorted) than samples from the other faults.

4.8 Petrophysical Characteristics

4.8.1 Porosity and Permeability at Low Confining Pressure

The porosity and permeability of twenty-four oriented core plug samples of fault core, damage zone and host rock from faults BM3, BC1, BC3, and BS1 were measured to determine how these parameters vary within each fault-zone domain and among the different domains. Porosity and permeability data under low effective stress (5 MPa) are organized by fault-zone domain in Figure 4.10 and Table 4.3.

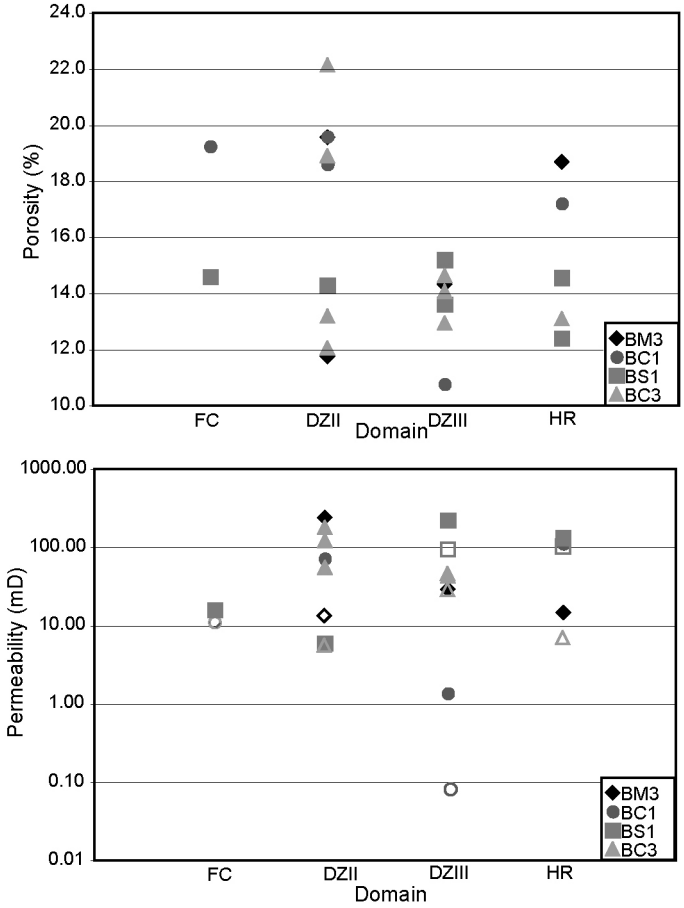

Figure 4.10. Results of porosity and permeability analysis at 5 MPa confining pressure as a function of fault-zone domain. In the permeability plot, open symbols are used to denote parallel samples and filled symbols represent perpendicular samples.

Table 4.3. Porosity and permeability of core plug samples at 5 MPa confining stress.

Fault	Sample Number	Domain	Distance to PSS (cm)	Porosity (%)	Klinkenberg Permeability (mD)
BM3	4-perp	DZIII	32	14.33	29.23
BM3	6-perp	DZII	23	19.57	241.41
BM3	6-para	DZII	23	11.76	13.37
BM3	7-perp	HR	280	18.70	14.70
BC1	9-para	FC	0	19.25	11.09
BC1	10-perp	DZII	13	18.61	71.91
BC1	11-para	DZII	9	19.60	193.55
BC1	13-perp	DZIII	60	15.16	1.36
BC1	13-para	DZIII	60	10.77	0.08
BC1	15-perp	HR	335	17.21	111.28
BS1	19-perp	FC	0	14.59	15.81
BS1	20-para	DZIII	10	13.62	95.20
BS1	21-perp	DZIII	9	15.20	221.85
BS1	22-perp	HR	177	14.56	132.74
BS1	22-para	HR	177	12.40	103.41
BS1	17-perp	DZII	0	14.30	5.98
BC3	23-perp	DZII	1	13.19	179.15
BC3	28-para	DZIII	50	14.64	46.08
BC3	26-perp	DZII	19	22.14	122.10
BC3	27-perp	DZII	19	18.91	55.09
BC3	29-para	DZII	5	12.06	5.62
BC3	30-perp	DZIII	40	12.94	43.26
BC3	30-para	DZIII	40	14.07	29.22
BC3	33-para	HR	240	13.10	6.99

4.8.1.1 Porosity

Fault core (FC) porosities at low effective stress range from 14.6–19.3%. Samples from DZII, near the fault core, have the widest range of porosity values, from 11.8–22.1% (σ=3.9), and the highest porosity values measured in this study (Figure 4.10). In contrast, samples from DZIII, at a greater distance from the fault core, have the narrowest range of porosity values at 10.8–15.2%, and the lowest porosity values measured in this study (Figure 4.10). Host rock (HR) sample porosities range from 12.4–18.7%.

For fault BM3, a decrease is observed from the porosity of the HR sample (the highest of all HR samples, 18.7%), to the porosity of the DZIII sample (14.3%) (Figure 4.10). The DZII cores, extracted from the same sample (#6-perp and #6-para), have widely variable porosities (19.6% and 11.8%). The high variability in porosity from two different cores from the same sample reflects the pronounced local variability in

porosity, probably due to patchy intergranular cement and fractures within the fault zone.

For fault BC1, there is an overall increase in porosity closer to the fault core, with the exception of the DZIII samples that have a particularly low porosity (Figure 4.10). The FC sample is derived from the material in the HR sample (#15), and has an 11.9% higher porosity than that HR sample. The average porosity of BC1 DZII samples (#10 and #11) is 19.1%; this average value represents a 47.3% increase in porosity over the average porosity of BC1 DZIII samples (#13-perp and #13-para). Note that samples #10 and #11 are both adjacent to the bedding-parallel segment of fault BC1 (Figure 4.4), see Chapter 5 or Nemser and Cowan (2009, *in press*) for a detailed description of the geometry of the BC1 fault zone. A slight increase in porosity from the HR sample #33 (13.1%) to the damage zone samples is also observed for fault BC3, although DZIII samples #28 and #30 also have low porosities (12.9% and 14.6%), and DZII porosities are highly variable. DZII samples #23 and #29 both have relatively low porosities (13.2% and 12.0%) whereas the other DZII samples #26 and #27 have high porosities (22.1% and 18.9%).

Samples from throughout the BS1 fault zone demonstrate less variability in porosity than is observed in the other fault zones (Figure 4.10). The DZIII sample from BS1 has a porosity of 15.2%, the highest of all samples from BS1, and the DZIII sample (#20) has a porosity of 13.6%, intermediate between the HR values. FC sample #19 exhibits nearly the same porosity as DZII sample #17 and HR sample #22-perp. As with fault BM3, the variability in porosity between two different cores from the same sample (HR cores #22-para and #22-perp, 12.4 and 14.6%, respectively) reflects the pronounced local variability in porosity.

4.8.1.2 Permeability

At low effective stress (5 MPa, corresponding to a depth of ~250 m), the samples tested in this study exhibit variability in permeability as a function of position within the fault zone (Figure 4.10). Fault core permeabilities are relatively low and range from

11.1–15.8 mD, although the range of permeabilities may be greater because only two fault core samples were analyzed. Samples from DZII have a wide range of permeabilities, between 5.6–241.4 mD (σ=89.1), and the highest permeability values measured in this study. Samples from DZIII have the widest range and include the lowest values of permeability, values range from 0.1–221.9 mD (σ=72.5). Permeabilities of HR samples range from 7.0–132.7 mD. At the scale of these core plugs, there is no observed anisotropy in permeability in samples from any of the fault-zone domains.

For fault BC1, the permeability of FC sample #9 (11 mD) is an order of magnitude lower than the HR sample #15 (111 mD) (Figure 4.10). DZII samples #10 and #11 have higher permeabilities (72 and 194 mD) than the DZIII samples #13-perp and #13-para, which have the lowest permeabilities of all of the samples (0.08 and 1.4 mD). For fault BM3, the samples show a steady increase in permeability with increasing proximity to the fault core with the exception of DZII sample #6-para, with a lower permeability of 13.4 mD (Figure 4.10). This trend is also observed in fault BC3, where the host rock sample has a low permeability (7 mD) and DZII samples have high permeabilities (up to 179 mD). The one outstanding data point is DZII sample #29, with an even lower permeability than that of the HR sample. For fault BS1, the permeability of FC sample #19, composed dominantly of zeolite cement, is also an order of magnitude lower (16 mD) than the HR samples; the permeability of DZII sample #17 is even lower, at 6 mD. The permeability of the DZIII and HR samples are comparable, in the range from 95–132 mD, with the exception of a high value in DZIII sample #21.

4.8.2 Porosity and Permeability Vs. Confining Pressure

Data on porosity and permeability under increasing hydrostatic confining stress (at 5, 10, 15, 20, 30, 40, and 60 MPa) were collected for eleven samples from faults BM3, BC1, BC3, and BS1 to assess how porosity and permeability might vary with depth of burial (Figure 4.11; Table 4.4).

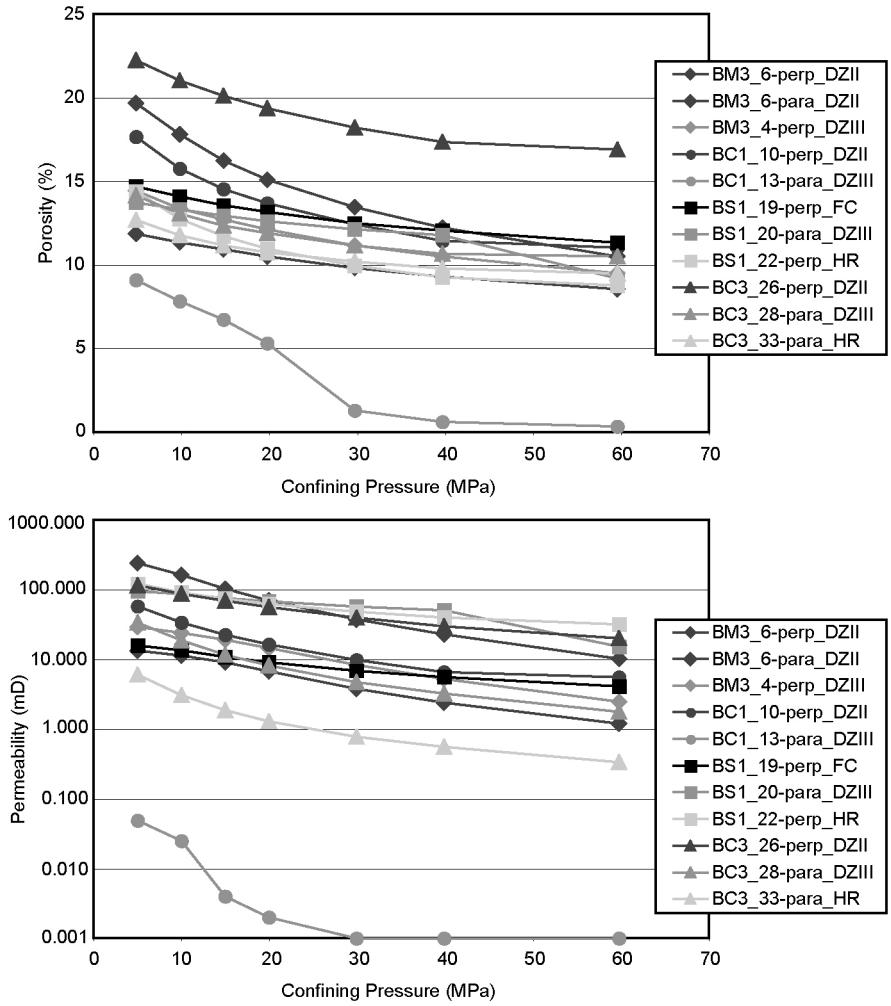

Figure 4.11. Results of porosity and permeability tests under varying confining pressure. Data are organized by fault (symbol type) and by fault-zone domain: progressively lighter colors correspond to domains at a greater distance from the fault core.

The range of confining pressures used in these experiments simulates burial depths up to ~3.0 km. The majority of porosity and permeability reduction in all samples occurs over the first 20 MPa (corresponding to ~1 km burial depth). Total net porosity reductions between 5 and 60 MPa range from 3.2% to 9.2%, corresponding to a 23–97% decrease, with a trend of a greater change in samples with increasing distance from the fault core. Over the range of confining stress, the decrease in permeability varies from 74% to 98%; the average permeability reduction is 88%. In general, as with porosity, a greater percentage change is observed in samples with greater distance

from the fault core. The DZIII sample #13-para from fault BC1 appears to have failed around 45 MPa based on the pronounced change in slope.

Table 4.4. Porosity and permeability of core plug samples at 5 MPa–60 MPa confining stress.

Fault	Sample Number	Domain	Net Confining Stress (Mpa)	Poro. (%)	Perm. (mD)
BM3	4-perp	DZIII	5	14.33	29.23
			10	13.26	24.02
			15	12.61	19.15
			20	12.01	14.58
			30	11.06	8.35
			40	10.40	5.24
			60	9.40	2.48
BM3	6-perp	DZII	5	19.57	241.41
			10	17.70	163.32
			15	16.14	102.68
			20	14.99	69.99
			30	13.35	37.45
			40	12.12	22.89
			60	10.40	10.24
BM3	6-para	DZII	5	11.76	13.37
			10	11.24	11.37
			15	10.83	9.11
			20	10.40	6.77
			30	9.71	3.80
			40	9.19	2.40
			60	8.45	1.20
BS1	19-perp	FC	5	14.59	15.81
			10	13.99	13.51
			15	13.47	10.87
			20	13.06	9.11
			30	12.39	6.88
			40	11.95	5.59
			60	11.23	4.11
BS1	20-para	DZIII	5	13.62	95.20
			10	13.22	86.63
			15	12.84	75.88
			20	12.50	68.05
			30	12.03	57.27
			40	11.68	50.77
			60	9.09	15.30
BS1	22-perp	HR	5	14.30	121.86
			10	12.64	91.36
			15	11.61	73.62
			20	10.86	62.57
			30	9.85	48.22
			40	9.16	40.00
			60	8.66	31.78
BC3	26-perp	DZII	5	22.13	115.66
			10	20.91	87.58
			15	20.00	69.36
			20	19.25	56.32
			30	18.10	39.65
			40	17.24	29.86
			60	16.79	20.07
BC3	28-para	DZIII	5	14.05	33.80
			10	12.95	18.78
			15	12.24	11.63
			20	11.80	8.18
			30	11.06	4.72
			40	10.56	3.25
			60	10.40	1.78
BC3	33-para	HR	5	12.58	6.06
			10	11.66	3.08
			15	11.06	1.87
			20	10.65	1.30
			30	10.09	0.78
			40	9.69	0.56
			60	9.39	0.34
BC1	10-perp	DZII	5	17.55	57.92
			10	15.66	33.95
			15	14.43	22.55
			20	13.58	16.47
			30	12.32	9.85
			40	11.34	6.57
			60	10.93	5.58
BC1	13-para	DZIII	5	8.99	0.05
			10	7.73	0.03
			15	6.63	0.00
			20	5.21	0.00
			30	1.20	0.00
			40	0.52	0.00
			60	0.24	0.00

4.8.3 Capillary Pressure

Mercury injection methods are commonly used to obtain capillary pressure data, an indicator of seal potential (Jennings, 1987; Pittman, 1992; Varva et al., 1992).

Conventional high-pressure (0–60,000 psi) mercury injection capillary pressure (MICP) tests were conducted on thirteen selected core plugs from faults BM3, BC3 and BS1 in order to measure pore throat apertures and total porosity. The first slope break in the mercury-air capillary pressure curve at low pressure is interpreted to represent the "entry pressure", the pressure at which the mercury enters the largest pore radius size available (Robinson, 1966). This value reflects the diameter of the pore apertures that control fluid flow through the sample. Injection curves that show the percentage of pore volume saturated by mercury as a function of increasing mercury injection pressure are presented in Figure 4.12. Entry pressures range from 4.06–7.06 and show no apparent correlation with distance from the fault core.

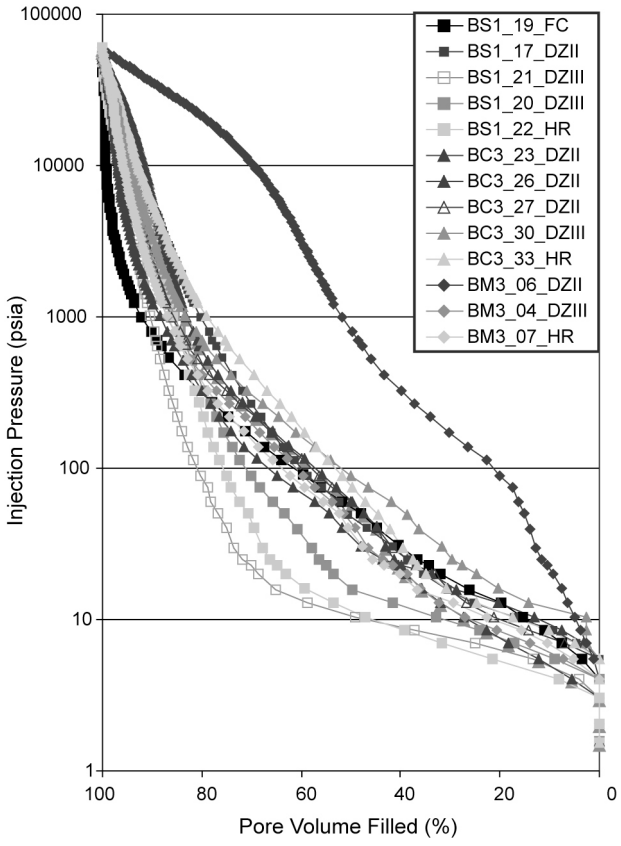

Figure 4.12. Mercury injection capillary pressure data for samples from faults BM3, BC3, and BS1. Data are organized by fault (symbol type) and by fault-zone domain: progressively lighter colors correspond to domains at a greater distance from the fault core.

The lowest pressure at which the mercury develops a throughgoing pathway through the sample is defined as the "threshold pressure" (the terms "displacement pressure" and "breakthrough pressure" are also used); this pressure is used to describe the strength of a rock (Schowalter, 1979; Katz and Thompson, 1987; Sneider et al., 1997). Different methods are used to estimate the threshold pressure from injection curves, including choosing the inflection point on the curves and choosing the capillary pressure at 7.5% (Sneider et al., 1997) or 10% (Schowalter, 1979) cumulative intruded mercury. Following Flodin et al. (2005), the pressures at 7.5% and 10% were adopted as end-member values that define a range of threshold pressures for each sample (Table 4.5).

Table 4.5. Threshold pressures from mercury injection capillary pressure (MICP) analysis of selected samples.

Fault	Sample Number	Domain	Threshold Pressure (psia) at 7.5%	Threshold Pressure (psia) at 10%
BM3	4-para	DZIII	5.6	6.2
BM3	6-perp	DZII	15.6	21.6
BM3	7-perp	HR	6.2	6.9
BS1	17-perp	DZII	7.9	8.7
BS1	19-perp	FC	7.1	8.1
BS1	20-para	DZIII	5.3	5.8
BS1	21-perp	DZIII	4.6	5.0
BS1	22-perp	HR	4.0	4.3
BC3	23-perp	DZII	4.5	5.1
BC3	26-perp	DZII	8.5	9.4
BC3	27-perp	DZII	7.2	7.6
BC3	30-para	DZIII	11.6	12.1
BC3	33-para	HR	7.8	8.5

Threshold pressures range between 4–8.5 psi for HR samples, and between 4.6–12.1 psi for samples from DZIII. The widest range was observed in samples from DZII (4.5–21.6 psi), and the one FC sample (from fault BS1) has a narrow range from 7.1–8.1 psi. The injection pressure curves for the FC and DZII samples show similar shapes, with the exception of DZII sample #6 from fault BM3 (Figure 4.12). This sample has the highest threshold pressures measured in this study, from 15.6 (at 7.5%) to 21.6 (at 10%). The curve for this sample is characterized by a relatively slow increase in saturation such that only 20% of the sample was filled at 100 psi and only 52% was filled at 1000 psi (in contrast, the other samples were at least 50% filled at

100 psi and at least 78% filled at 1000 psi). The injection pressure curves for DZIII and HR samples from fault BS1 also have a distinct character from the rest of the samples (Figure 4.12). At low injection pressures of 16 psi or less, 50% of the pore volume in these three samples was filled, in contrast with the other samples which were not 50% filled until pressures of ≥36 psi.

4.9 Discussion

4.9.1 Petrophysical Implications of Laumontite Cement

Laumontite cement impacts the petrophysical properties of these fault zones in several significant ways. Laumontite cements in sandstones can substantially reduce porosity, creating seals and diminishing reservoir capacity (Crossey et al., 1984). Laumontite also has the property of being very fragile and easily cracks along cleavage planes (Figure 4.7D) (Jove and Hacker, 1997). Secondary porosity can develop after laumontite is altered to kaolinite and calcite in the presence of CO_2 or H^+ according to reactions that lead to volume decreases of 10% and 28% respectively (Frost et al., 1982; Crossey et al., 1984). Kaolinite and calcite occur in these samples (calcite is more abundant) and there is evidence that the calcite postdates the laumontite (see Chapter 3). However, the relative abundance of these minerals is not sufficient to have a significant impact on porosity.

Laumontization may form directly by the *in-situ* alteration of plagioclase, or in two steps, with albitization followed by laumontization (Boles and Coombs, 1977; Boles, 1982; Blenkinsop and Sibson, 1992). The direct reaction (equation 1) is described in Boles and Coombs (1977):

(1) $NaAlSi_3O_8 \bullet CaAl_2Si_2O_8 + 2\ SiO_2 + 4\ H_2O$

(plagioclase)

$= NaAlSi_3O_8 + CaAl_2Si_4O_{12} \bullet 4H_2O$

(albite) (laumontite)

The separate albitization and laumontization reactions (equations 2 and 3) are described in Boles (1982). First, the differential dissolution of Ca-rich (anorthic) plagioclase results in secondary microporosity:

(2) $Na^{+} + H_4SiO_4 + NaAlSi_3O_8 \bullet CaAl_2Si_2O_8$

(plagioclase)

$= NaAlSi_3O_8 + Al^{+3} + Ca^{+2} + 4OH^{-}$

(albite)

Laumontite may then precipitate in pore space from hydrothermal fluid enriched in $Ca^{+}2$:

(3) $2Al^{+3} + Ca^{+2} + 8OH^{-} + 4\ SiO_2$

$= CaAl_2Si_4O_{12} \bullet 4H_2O$

(laumontite)

Albitization can occur over a broad temperature range, and within the albitization zone it is common to find a spectrum of plagioclase alteration, from unaltered to completely albitized (Ramseyer et al., 1992). Some dissolved feldspar grains contain substantial secondary microporosity as a result of the differential dissolution of Ca-rich (anorthic) plagioclase (Figure 4.13A); there is also evidence of some authigenic laumontite precipitation from hydrothermal fluid enriched in $Ca^{+}2$ within the secondary pores (Figure 4.13A). The preferential albitization of plagioclase is enhanced in grains with an anorthic chemical composition, when more grain surface area is in contact with pore fluid, and with a higher degree of grain fracturing (Ramseyer et al., 1992). Plagioclase dissolution appears to be concentrated along tabular zones; these may be relict fluid pathways (Figure 4.13B).

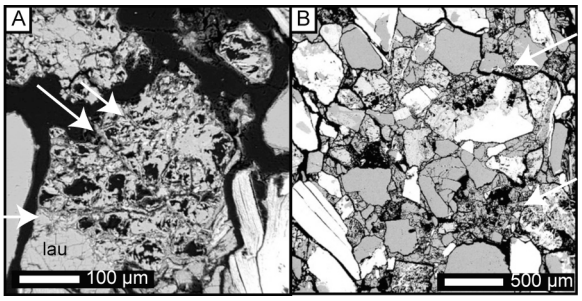

Figure 4.13. Photomicrographs of dissolved feldspars from damage-zone domain III of fault BC3. (A) Dissolved feldspar with preserved dissolution pathways; some secondary microporosity has been filled by authigenic laumontite (*lau*). (B) Plagioclase dissolution is concentrated along tabular zones (white arrows).

The variation in the degree of albitization within these samples gives rise to a heterogeneous spatial distribution of inter- and intragranular laumontite cement and secondary microporosity within dissolved plagioclase grains. The inconsistent distribution of intergranular laumontite cement in host rock samples is observed with the SEM (Figure 4.2) and in the variable abundance of laumontite in the XRD data (Figure 4.8). No systematic relationship between the abundance of intergranular laumontite and proximity to the fault core is evident at the scale of the core plugs. This result is consistent with the inference that the intergranular laumontite precipitated during the early diagenetic stage of shallow burial and predates faulting (see Chapter 3). Previous studies of well-cemented sandstones suggest that sandstones with >10% intergranular cement do not adhere to statistical relationships between permeability and porosity that are appropriate for uncemented or weakly cemented sandstones (Bloch and Helmold, 1995).

4.9.2 Petrophysical Implications of Deformation Features

Cataclastic fault rocks and laumontite-, calcite-, and gypsum-cemented fractures are typically spatially coincident within the fault cores of these fault zones (Figures 4.6 and 4.7E). Variable textures within veins of homogeneous composition indicate multiple generations of cementation events that exploited the same fractures (Figure 4.7F); in one particularly complex vein, >10 cementation events are observed (see Section 3.6.4). Some cemented features predate cataclasis; in these cases the cataclastic fault

rock is predominantly composed of authigenic cement material (Figure 4.6A). Other cemented features postdate cataclasis and are localized within or parallel to cataclastic fault rocks; where cemented fractures postdate cataclasis, the porosity of fault rocks may be substantially decreased (Figures 4.6B and 4.7E). Veins that predate and postdate cataclasis provide evidence of temporal alternation between dilation, cataclasis, and fluid flow events. Regardless of the relative timing of cementation and cataclasis, fault rock porosity and permeability may be increased when dilation postdates cementation and cataclasis (Figures 4.6A and 4.6D).

The principal deformation features in damage-zone domains II and III are cemented and open fractures; both the density and dimensions of these features generally decrease with increasing distance from the fault core. The presence of open fractures throughout the fault zone suggests that the most recent deformation event was dilatant. Open fractures tend to occur along preexisting veins and indicate some reactivation post-cementation (Figure 4.7D). Heterogeneous petrophysical properties within the fault cores arise as a result of the localized and variable spatial extents of cemented fractures that decrease the porosity and permeability relative to the host rock, and open fractures that locally act as conduits for fluid flow. Because of the extensive and episodic cementation history, the conduit/barrier system is both temporally and spatially variable.

4.9.3 Petrophysical Implications of Host Rock Variability

The variability in host rock and damage zone permeabilities is in part due to the lack of sorting and compositional heterogeneity within the petrologically immature West Butte Conglomerate, independent of the proportion and distribution of intergranular laumontite cement and deformation features. In faults BM3 and BC3, where the grain sizes of the host rock samples are more heterogeneous and include more fines, host rock samples have low permeabilities (Figures 4.9, 4.2A, and 4.2B) and there is a clear trend throughout the damage zone of increasing permeability with proximity to the fault core (Figure 4.10). In faults BC1 and BS1, where the host rock samples are more

coarse-grained and well-sorted, host rock samples have high permeabilities (Figures 4.2C and 4.7C), and there is a wide range of variability in permeability within DZII and DZIII. For fault BC1, there is a pronounced increase in permeability adjacent to the fault core in DZII, and a particularly low permeability observed in samples from DZIII (Figure 4.10). In contrast, for fault BS1, samples from DZIII have high permeabilities, whereas samples from DZII have low permeabilities (Figure 4.10). This suggests that although DZII and DZIII have pronounced differences in the density of deformation at the mesoscopic scale, at the scale of the core plugs, the substantial variability within each respective domain has a more pronounced signature than variation between the domains.

4.9.4 Porosity and Permeability of Fault Rocks at Low Confining Pressure

Given the increasing abundance of cemented fractures closer to the fault core at the mesoscopic scale, one might expect a general decrease in porosity approaching the fault core. However, in the two fault zones for which fault core samples were analyzed (faults BC1 and BS1), there is no evidence for porosity reduction in the fault core relative to the host rock and damage zone at the scale of the core plugs. This result represents a pronounced contrast with reported porosity reductions in fault rocks from deformation bands in sandstones (Antonellini and Aydin, 1994; Shipton et al., 2002) and shows some similarity with relatively smaller observed porosity reductions (and some porosity increases) in fault rocks derived from uncemented sandstones deformed by the shearing of joints (Flodin et al., 2005). An important finding from the latter study, demonstrated on the basis of petrophysical data, grain size data and SEM image analysis, is that fault rocks along sheared joints are characterized by increased microporosity relative to the host rocks (Flodin et al., 2005). In fault BC1, there is an 11.9% increase in porosity in the fault core sample relative to the host rock sample; in the fault core sample from fault BS1 there is an 8.2% increase in porosity over the average porosity measured in the host rocks. Enhanced microporosity within fault core samples occurs within cataclastic fault rocks (Figure 4.6) and dissolved feldspars

(Figure 4.13). The observed increase in the porosity of material in the fault core may also be related to dilational effects manifested as a higher concentration of both intragranular fractures within detrital grains and open intergranular fractures within and adjacent to the fault core (see Chapter 3).

The increase in porosity from host rock to fault core along faults BC1 and BS1 is accompanied by a reduction in permeability of up to one order of magnitude. This estimate falls on the low end of the ranges in permeability reduction values reported in other experiments within faulted sandstones that are deformed by the sheared joints mechanism (10^1–10^3) (Flodin et al., 2005), deformation band faulted sandstones (10^1–10^4) (Antonellini and Aydin, 1994), and faulted granitic rocks (10^1–10^3) (Evans et al., 1997). Given the limited number of fault core samples tested in this study, it is possible that the reduction in permeability from host rock to fault core exceeds one order of magnitude within one or more of these fault zones. Of the faults in this study, samples from fault BS1 demonstrate the best sorting and the least variability in measured porosity throughout the fault zone. Field and microstructural observations indicate that the fault core from BS1 is primarily composed of laumontite-cemented dilational fractures with tabular localized zones of cataclasite (Figures 4.7E, 4.7F, 4.6D, and 4.6E). The lack of grain size reduction within the fault core samples (Figure 4.9) is consistent with the observation that cataclasis is highly localized. The high porosity and low permeability within the fault core likely reflects microporosity within the laumontite vein and cataclastic fault rocks.

4.9.5 Porosity and Permeability at Low Confining Pressure Throughout the Fault Zone

There is substantial scatter in a plot of normalized permeability vs. normalized porosity at low confining pressure (Figure 4.14); values in this plot are normalized relative to the calculated mean host rock values for permeability (62.7 mD) and porosity (15.6%) at low confining pressure. No discernible trend relates normalized porosity or permeability to position within the fault zone. The lack of a systematic change in

permeability and porosity with distance from the fault core is interpreted as a result of the variability in host rock properties and the heterogeneous distribution of intergranular cement, cemented fractures, and open fractures throughout the fault zone.

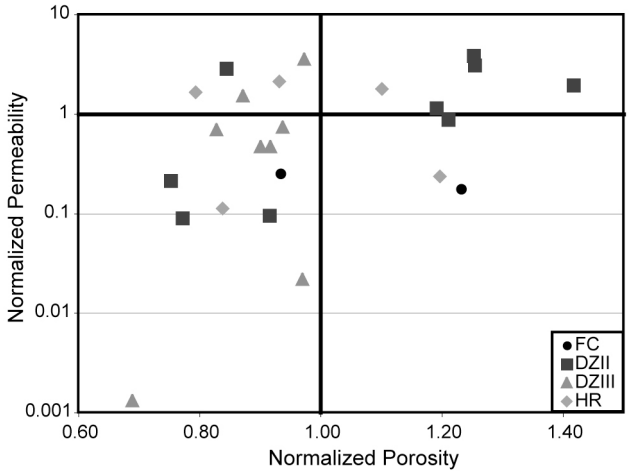

Figure 4.14. Plot of normalized permeability vs. normalized porosity at low confining pressure highlights the relative values of these parameters as a function of position within the fault zone. Values are normalized relative to the calculated mean host rock value for permeability (62.7 mD) and porosity (15.6%) at low confining pressure.

4.9.6 Porosity and Permeability as a Function of Grain Size

Results from the particle size analysis indicate an overall decrease in grain size with increasing proximity to the fault core in fault zones BC1 and BM3; no significant grain size reduction is observed along faults BC3 and BS1 (Figure 4.9). It is not possible to infer a lower limit of grain-size reduction based on the distribution of fault core grain sizes sampled in this study. A plot of permeability and porosity vs. mean grain size demonstrates that whereas there is an increase in both parameters with increasing grain size above 0.4 mm, the fine-grained samples (which include a HR sample, a FC sample and two DZII samples) tend to have relatively high porosities and low permeabilities (Figure 4.15).

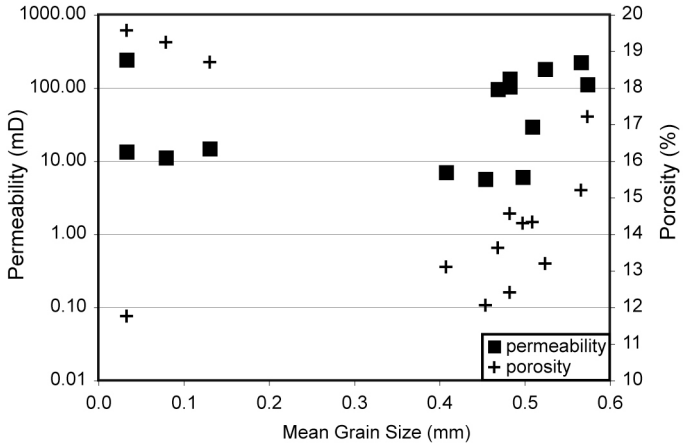

Figure 4.15. Permeability and porosity data at low confining pressure as a function of mean grain size for the data presented in Figure 4.9.

Among the fine-grained samples, the two outliers are the BM3 DZII cores extracted from the same sample: #6-perp (with a relatively high permeability) and #6-para (with a relatively low porosity). The absence of data in the middle of Figure 4.15 underscores the result that the particle size data are generally coarse-skewed, and relatively fine-grained host rock samples and fault rocks and DZII samples with multimodal size distributions are the exceptions.

Figure 4.16 shows the cumulative volume percentage as a function of grain size for all of the data from Figure 4.9. Four of the five curves at the fine-grained end of this plot correspond to FC or DZII samples from fault zones BC1 and BM3. Permeability and porosity data were only acquired for two of these five samples due to the challenge of obtaining large enough samples for core plugs. These two samples plot on the left side of Figure 4.15, with relatively high porosities and low permeabilities. All of the other samples represented on Figure 4.16 for which there is also permeability and porosity data plot on the right side of Figure 4.15, with relatively low porosities and high permeabilities. Therefore it is reasonable to infer that smaller mean grain size leads to lower permeability and enhanced porosity, probably due to microporosity (Flodin et al., 2005).

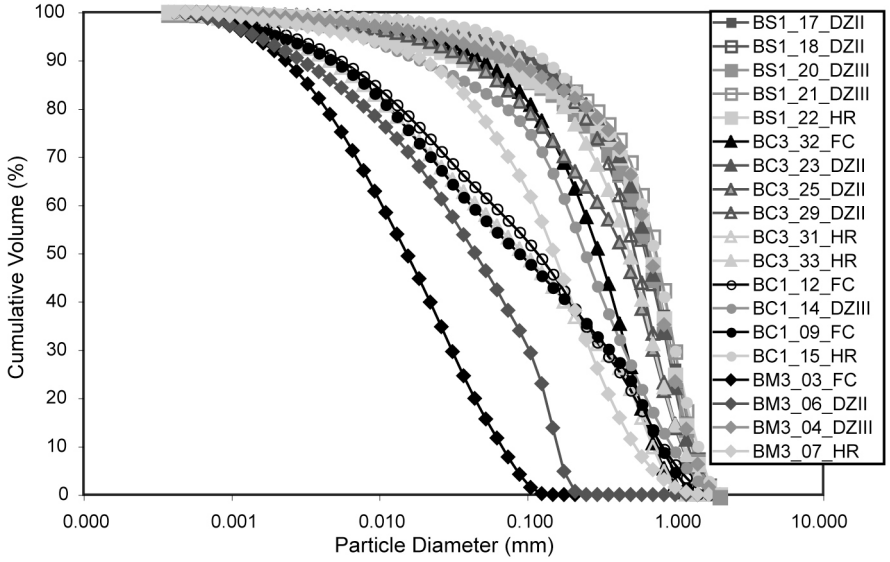

Figure 4.16. Cumulative volume percent as a function of particle diameter for the data presented in Figure 4.9.

4.9.7 Porosity and Permeability as a Function of Confining Pressure

Experiments at changing confining pressure reveal that between 5 and 60 MPa, greater net porosity and permeability reductions occur in samples with increasing distance from the fault core (Figure 4.11; Table 4.4). Because the degree of mechanical compaction does not vary across the fault zone (bedding is gently dipping and the fault zones are steeply dipping), and the abundance of open fractures and microfractures is higher closer to the fault core, this trend suggests that an increase in cementation towards the fault core limits total porosity and permeability reductions, even at high confining stress.

A plot of normalized permeability vs. confining pressure illustrates how the samples from different fault-zone domains respond differently to the changes in effective stress (Figure 4.17). DZII samples tend to show sharper declines in permeability within the first few increments of increasing confining pressure (5 MPa to 15 MPa); HR sample #22-perp from fault BS1 also has an initially steep decline in permeability. These data are interpreted as an indication that the DZII samples (that tend to have the highest initial permeabilities of all fault-zone domains) have more open cracks at low effective stress that are prone to collapse at effective stresses in the range of 5–15 MPa, similar

to the interpretations of Evans et al. (1997) in the damage zones of faulted granitic rocks.

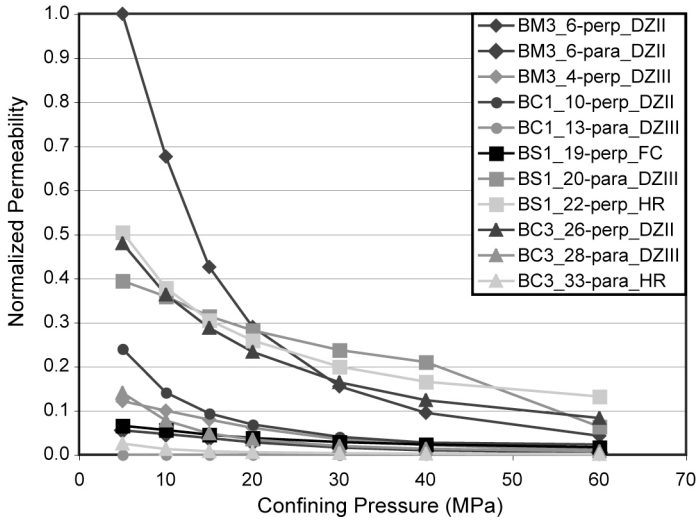

Figure 4.17. Normalized permeability as a function of confining pressure; values are normalized relative to the mean host rock permeability (62.7 mD).

4.10 Conclusions

Analytical data from four small displacement strike-slip fault zones provide evidence for high spatial variability in the petrophysical properties of faulted cemented sandstones. Variability is observed at the scale of each fault zone, at the scale of distinct fault-zone domains, at the scale of individual hand samples (from which different core plugs may have distinct petrophysical properties), and at the microscale. The pronounced variability is interpreted as a result of multiple factors: (1) the lack of sorting and petrological immaturity of the West Butte Conglomerate; (2) the inconsistent distribution of abundant (>10%) intergranular laumontite cement (and the lack of a systematic relationship between the abundance of laumontite and proximity to the fault core); (3) the properties of the laumontite cement; and (4) the occurrence and spatial distribution of open and cemented deformation features throughout the fault zone.

Relative to the other fault-zone domains, samples from the damage-zone domain closest to the fault core with the highest abundance of deformation features (i.e. DZII in this study) are characterized by: (1) the widest range of measured porosity values; (2) the highest porosity and permeability values at low effective stress; (3) the widest range in threshold pressures; (4) the highest threshold pressures; and (5) the steepest declines in permeability with increasing confining pressure (to 15 MPa). In contrast, samples from the damage-zone domain at a greater distance from the fault core and with fewer deformation features (i.e. DZIII) have the narrowest range of measured porosity values, and the lowest porosity and permeability values from this study. This contrast highlights the heterogeneity at the scale of the fault-zone domains. The relatively variable petrophysical properties of samples from the inner damage zone reflects the variability within each domain and is a function of the high concentration of cemented and open fractures close to the fault core. Differing petrophysical properties of parallel and perpendicular cores extracted from the same sample illustrate the variability at the scale of the hand samples. Finally, SEM images document localized zones of dilation, cementation, and cataclasis, exemplifying the petrophysical heterogeneity at the microscale.

The faults with relatively heterogeneous host rocks that include finer grained beds have low permeabilities. In these fault zones (faults BM3 and BC3), the samples show a clear trend throughout the damage zone of increasing permeability with proximity to the fault core; fault core samples were not tested. In contrast, faults with relatively coarse-grained host rocks have high permeabilities, and there is a particularly wide range of variability in permeability within the fault damage zone. In these fault zones (faults BC1 and BS1), there is an overall increase in the porosity of samples closer to the fault core, and an order of magnitude decrease in the permeability of fault rock relative to host rock. The increased porosity of fault rocks is interpreted as a result of dilational effects and the microporosity of the fault rocks and cemented fractures.

Results from this study indicate that the petrophysical properties of laumontite-cemented faulted sandstones differ from those observed in poorly cemented to uncemented sandstones deformed by the same mechanism of shearing across joints. Analog studies of faulted sandstone reservoirs with minimal cementation are therefore not sufficient for predicting the fluid-flow behavior within cemented reservoirs that contain faults that are either resolvable using geophysical techniques or subseismic in scale.

Chapter 5: Downdip Segmentation of Strike-Slip Fault Zones in the Brittle Crust

5.1 Summary

Outcrop-scale field evidence from the southern San Jacinto fault zone in southern California indicates that bedding-parallel slip may be an important mechanism for transferring and accommodating slip within strike-slip fault zones that cut across heterogeneous stratigraphy. Steeply dipping strike-slip fault segments exposed in conglomeratic sandstones abruptly terminate at weaker shale layers where slip occurs on bedding-parallel planes. Cross-sections of fault-related seismicity within the southern San Jacinto fault zone reveal that events generally cluster within tabular, steeply dipping fault-parallel streaks that are limited in extent in the downdip direction. The depths of the downdip terminations of shallow streaks tend to be roughly coincident with the depths of the updip terminations of deeper streaks; these configurations define stepover geometries that range in character from sharp to diffuse. The examples described herein provide evidence that downdip segmentation within strike-slip fault zones may be common over a wide range of scales.

5.2 Introduction

Many authors have documented the evolution of faults by segment linkage (Peacock and Sanderson, 1991, and references therein), and the role of segment boundaries in the earthquake rupture process (e.g., Sibson, 1985). The majority of these studies address along-strike segmentation, although some investigations address downdip segmentation of normal faults (Childs et al., 1996; Mansfield and Cartwright, 1996) and thrust faults (Nicol et al., 2002). In particular, linkage of vertically restricted discontinuities along bedding-parallel planes gives rise to a stepover geometry that has been observed along normal faults (Wilkins and Gross, 2002), along fractures (Cooke and Underwood, 2001), and in the classic ramp-flat geometry observed in thrust systems. Whereas many studies investigate the growth of strike-slip faults by along-strike segment linkage (e.g., Kelly et al., 1998), there are no published examples of

strike-slip faults with downdip segmentation. The purpose of this chapter is to describe an outcrop-scale example of downdip segmentation in a strike-slip fault zone, and to propose that a similar geometry can be inferred on a larger scale from the distribution of earthquake hypocenters.

Downdip segmentation in strike-slip fault zones has been postulated on a regional scale in southern California. Earthquake focal mechanisms (Webb and Kanamori, 1985), seismic reflection data (Fuis et al., 2003), and gravity data (Li et al., 1992) along strike-slip faults have been interpreted as evidence of a regional décollement. However, Huang et al. (1996) demonstrated that low-angle fault planes at different depths, and with variable slip directions and slip senses, are distributed throughout the middle and upper crust, unassociated with a regional décollement. The kinematic relationship between these low-angle faults and the steeply dipping faults in southern California remains a subject of debate (Huang et al., 1996). Shallow local décollements (in the upper 5 km) have been invoked to account for offsets between seismic streaks and the surface geology along the Clark fault within the San Jacinto fault zone (Belgarde and Janecke, 2007). Whereas regional décollements and inferred local décollements are driven by different mechanisms (regional stresses and local stresses, respectively), they both represent geometric complexity in strike-slip fault zones at depth. On the basis of field observations and patterns defined by seismicity data, downdip segmentation may be present within strike-slip fault zones at a variety of scales and crustal levels, possibly including, but not limited to, the basement-cover contact.

5.3 Downdip Segmentation of Strike-Slip Faults

5.3.1 Outcrop-Scale Field Evidence

The Borrego Mountain area in the western Salton Trough region contains exceptional exposures of extensive deformation associated with slip along the Coyote Creek fault of the highly segmented southern San Jacinto fault zone (Figure 5.1).

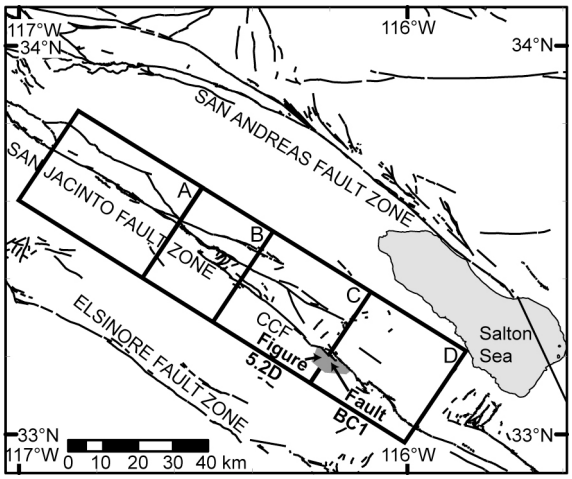

Figure 5.1. Regional map of the Salton Trough shows surface traces of major Quaternary fault zones (Bryant, 2005) and locations of sections A–D along the southern San Jacinto fault zone. Borrego Mountain area is shaded gray. *CCF*, Coyote Creek fault. Locations of fault Butte Canyon 1 (BC1) and the outcrop shown in Figure 5.2D indicated with arrows.

Strike-slip faulting at Borrego Mountain may be related to the restraining bend in the Coyote Creek fault to the northwest (Steely, 2006). Ongoing transpressive deformation along the Coyote Creek fault probably commenced at ca. 0.6 Ma at the latitude of Borrego Mountain as the fault propagated southeast (Lutz et al., 2006; Kirby et al., 2007); this estimate provides a maximum age for the subsidiary faulting. Fault 'Butte Canyon 1' (BC1) in Butte Canyon Wash at Borrego Mountain (574,888 m E, 3,672,085 m N) (Figure 5.1) belongs to a population of steeply dipping, NE-striking strike-slip faults exposed throughout Borrego Mountain within the Pliocene West Butte Conglomerate (Steely, 2006). Based on measurements of stratigraphic thicknesses (e.g., Dorsey et al., 2004; Steely, 2006), the maximum depth of burial of fault BC1 was ~3 km at the inception of faulting. Fault BC1 has accommodated <5 m of displacement, and is ~1 km southwest of the mapped surface trace of the main Coyote Creek fault and ~12 m from a major NE-striking fault along Butte Canyon.

At the site of fault BC1, the West Butte Conglomerate can be divided into three major units based on the mechanical stratigraphy: (1) conglomeratic sandstone (SS), (2) shale with sandstone lenses (SH), and (3) interbedded sands and shales (SS/SH) (Figure 5.2A). The SS-SH contact is the most prominent stratigraphic and mechanical

boundary within this sedimentary sequence. Two subvertical planar strike-slip fault segments are exposed within fault BC1: segments BC1A and BC1B (Figure 5.2A). It is possible that out of the plane of inspection, these fault segments coalesce into a continuous structure (Nicol et al., 2002). However, in this exposure, segment BC1A terminates abruptly at the SS-SH contact, and bedding is intact directly below this termination (Figures 5.2A and 5.2B).

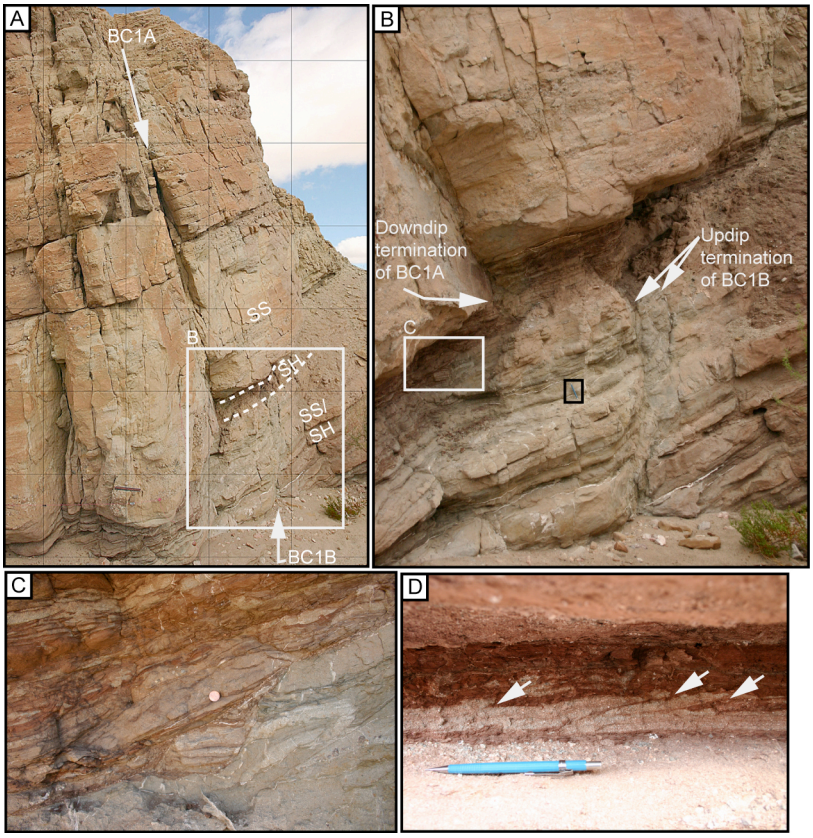

Figure 5.2. A: Fault BC1. *SS*, conglomeratic sandstone; *SH*, shale; *SS/SH*, interbedded sands and shales. Dashed lines indicate intact bedding beyond the segment terminations; 1 m grid. B: Detail highlights the stratigraphic correspondence between the downdip termination of BC1A and the updip termination of BC1B, which includes two subparallel strands (pencil for scale in black box). C: Detail of bedding-plane deformation within SH (penny for scale). D: Imbricate thrusting (arrows) within a sandy bed adjacent to a clay-rich layer in an outcrop from Borrego Mountain Wash (see Figure 5.1 for location).

Approximately one meter to the east of the downdip termination of fault BC1A, the updip termination of segment BC1B is also coincident with the SS-SH contact; bedding is intact directly above this termination (Figures 5.2A and 5.2B). Bedding-

parallel slip surfaces and recumbent folding are indicative of bedding-parallel slip in a zone within SH (Figure 5.2C). Additional examples of bedding-parallel deformation within the Borrego Mountain area (including the small imbricate thrusts pictured in Figure 5.2D) show that bedding-parallel shear is an important mechanism of strain accommodation within this predominantly strike-slip environment.

Segments BC1A and BC1B are inferred to have developed as discrete structures and become linked during failure in a sharp stepover geometry (Figure 5.3A). Geometrical and space constraints require that if the two steeply dipping segments were not continuous when they slipped to accommodate strike-slip motion, the décollement zone within SH must have failed contemporaneously. The following section explores the possibility that seismicity can also be explained by coeval deformation along discontinuous, steeply dipping fault segments, but on a much larger scale.

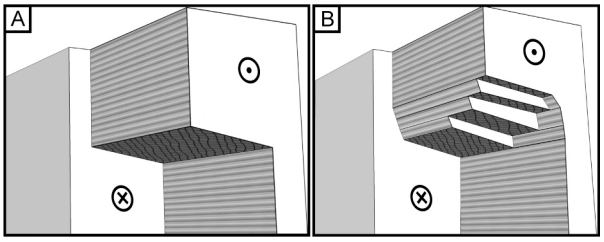

Figure 5.3. Block diagrams illustrate (A) sharp and (B) diffuse stepover geometries within dextral strike-slip faults. Steep slip surfaces are striped; low-angle slip surfaces are hatched.

5.3.2 Seismological Evidence

Seismicity data (1981–2005) along the southern San Jacinto fault zone was analyzed using an earthquake catalog for southern California in which events have been relocated using waveform cross-correlation techniques (Lin et al., 2007) (Figure 5.4); zones of seismicity along major fault zones collapse into tabular streaks that are unlikely to be an artifact of the relocation method (Shearer, 2002). The seismicity is considered within four sections (A–D from northwest to southeast); section boundaries are defined based on rupture history, along-strike segmentation of the mapped fault trace, and gaps in seismicity.

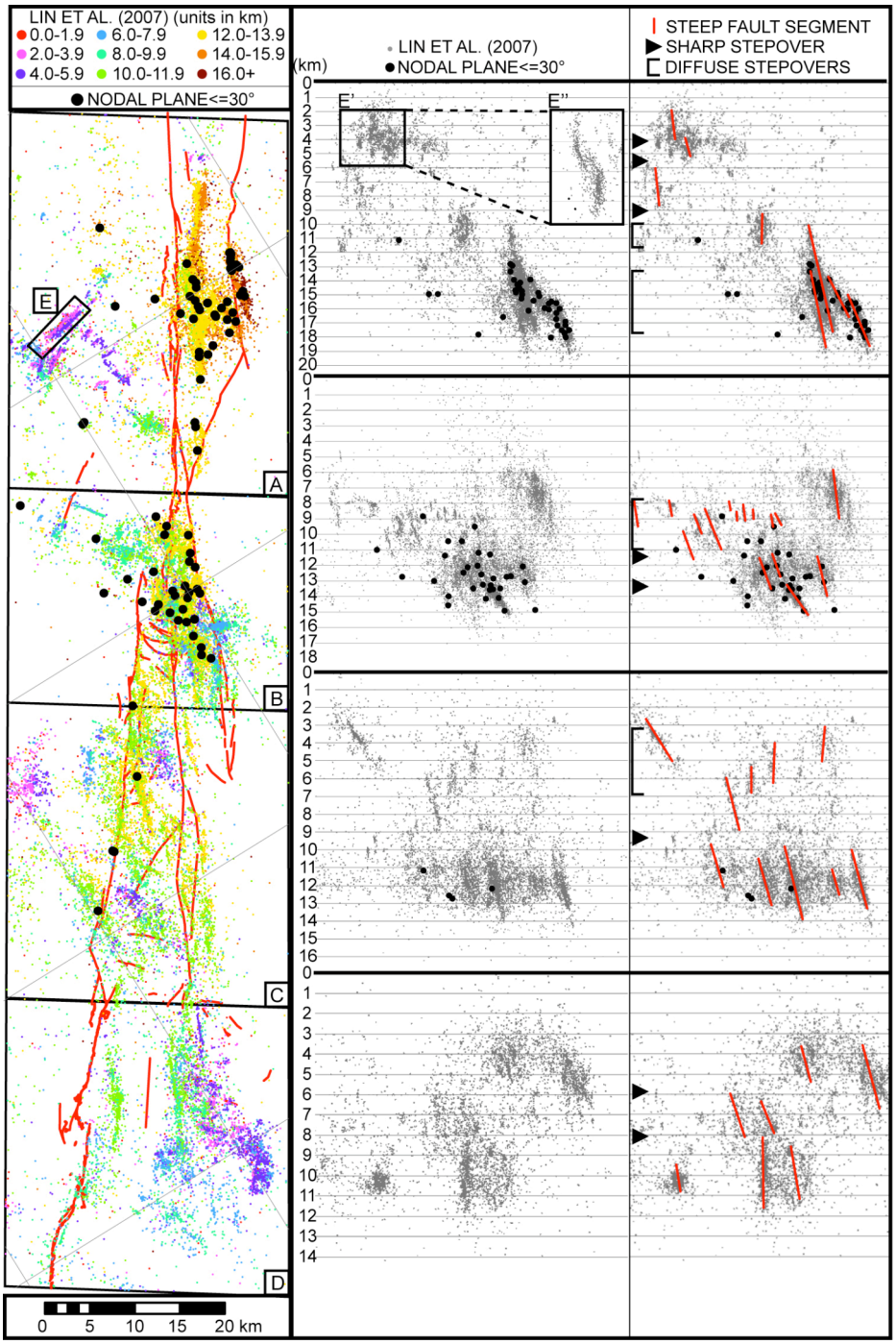

Figure 5.4. Seismicity (1981–2005) (Lin et al., 2007) in sections A–D along the southern San Jacinto fault zone. Larger black circles indicate events with at least one low-angle (≤30°) nodal plane. Left: Map view. Earthquakes are color-coded by depth (2 km bins). Center: Cross-sections show seismicity from sections A–D collapsed onto planes that are perpendicular to the dominant structural trend of each section (depth in km; 2X vertical exaggeration). Seismicity within section E is shown in two cross-sections: E' is perpendicular to the dominant trend of structure within section A, whereas E" (shown at 4X vertical exaggeration to highlight a stepover) is perpendicular to the structure in section E. Right: Interpreted cross-sections show steep fault segments and depths of inferred stepovers.

Sections A–C encompass the ~110 km long Anza/Clark segment that extends southeast from the Hemet releasing stepover, and the parallel 40 km long Coyote Creek fault. Section D corresponds with the Borrego Mountain segment, defined by the extent of surface rupturing during the 1968 M_w 6.5 Borrego Mountain earthquake that ruptured ~33 km of the Coyote Creek fault (Clark, 1972; Dawson et al., 2008). The base of the seismicity within sections A–D is at 20 km, 18 km, 16 km, and 14 km respectively; this southeastward shallowing corresponds with an increase in heat flow as the fault nears the Salton Trough (Nazareth and Hauksson, 2004).

5.3.2.1 Vertically Restricted Seismicity Streaks

When seismicity data are color-coded by depth, vertically restricted fault segments are apparent throughout all sections as monochromatic streaks (Figure 5.4, left). Corresponding cross-sections (Figure 5.4, center) are drawn perpendicular to the dominant structural trend of each section to optimize the collapse of the majority of individual events into narrow streaks. The cross-sections highlight the presence of vertically restricted fault segments throughout the fault zone. Regions where seismicity appears more diffuse in a cross-section (e.g., E', Figure 5.4, center) generally represent fault segments with strikes that differ from the dominant trend within the section (e.g., E, Figure 5.4, left); these segments collapse into tabular streaks along strike-perpendicular cross-sections (E", Figure 5.4, center).

On the basis of the cross-sections, it emerges that the sharp stepover observed at fault BC1 represents one end-member style of stepover where there is limited vertical overlap between steep segments (Figure 5.3A). Diffuse stepovers where there is substantial (≥1 km) vertical overlap between steep segments are also observed (Figure 5.3B); both styles of stepover are independent of the lateral stepover distance. Sharp stepovers are apparent in each of the sections, and regions of diffuse stepovers are present in sections A–C (Figure 5.4, right). The lack of correspondence between the stepover depths within adjacent sections suggests that if these depths correlate with low-angle décollements, the décollements are limited in spatial extent.

5.3.2.2 Slip on Low-Angle Fault Planes

On the basis of field evidence at fault BC1 for bedding-parallel slip at the terminations of steeply dipping fault segments, it is important to examine the possibility that earthquakes on low-angle fault planes might correspond with depths where vertically restricted seismicity streaks terminate. To test this hypothesis, events within the study area with nodal planes that dip ≤30° were identified using a focal mechanism catalog (1984–2003) for southern California computed from P-wave polarity and S/P amplitude ratios (Hardebeck and Shearer, 2003). Since the listed fault plane in this catalog is chosen arbitrarily, relations in Ben-Menahem and Singh (1981) were used to determine the other nodal plane parameters. For each event the nodal plane with the lower dip is assumed to be the fault plane, following the methodology of Huang et al. (1996). Only focal mechanisms with quality ratings A, B, and C (average fault plane uncertainties of ≤25°, ≤35°, and ≤45°, respectively) are included in this analysis (Hardebeck and Shearer, 2003).

Of the 2729 events in this catalog that lie within sections A–D, events with both one nodal plane that dips ≤30° and the A–C quality rating constitute a small minority (86 events, or 3%) (Figure 5.4). There is no apparent spatial correspondence between events with low-angle fault planes and the terminations of steep fault segments within this region (Figure 5.4). Therefore, if décollements occur at the stepover depths, these structures are weak and unlikely to host seismic slip. In the context of the regional stress field, slip is unlikely to initiate on low-angle faults; rather these may slip passively, driven by slip on the steep fault segments. As a consequence of this kinematic model, low-angle faults may not generate temporally distinct seismic events.

5.4 Discussion

5.4.1 Influence of Mechanical Stratigraphy on Downdip Fault Segmentation

The agreement between the geometrical configuration observed at the outcrop scale and that inferred at multiple scales in the seismicity data suggests that downdip

segmentation occurs over a wide range of scales (Kattenhorn and Pollard, 2001). In the outcrop example of fault BC1, the relatively weak shales appear to have restricted fault propagation. Steep fault segments at the kilometer scale may also be vertically restricted by shallowly inclined mechanical boundaries (stratigraphic contacts and/or structural fabrics). In the western Salton Trough, >6 km of upper Miocene to Pleistocene strata rest on the Late Cretaceous Peninsular Ranges Batholith and older metasedimentary rocks (Dibblee, 1954). The basin fill includes some shales that may easily accommodate bedding-parallel slip, whereas the lithology of the underlying basement rocks likely inhibits a throughgoing décollement. However, the basement includes low-angle tectonic fabrics associated with the Cretaceous reverse-sense eastern Peninsular Ranges mylonite zone (Sharp et al., 1979), and the late Miocene–Pliocene oblique-normal West Salton detachment zone (Axen and Fletcher, 1998). The seismicity reveals sharp and diffuse stepovers throughout the brittle crust, and therefore décollements may be present within the sedimentary cover, possibly at the cover-basement contact, and within the basement rocks.

5.4.2 Implications for Permeability and Fluid Flow

Faults can form conduits or barriers to fluid flow, and in low-permeability rocks, fault and fracture geometry may exert a primary control on fluid flow. Downdip segmentation may impact fault seal capacity in two contrasting ways. Segment linkage sites often give rise to enhanced permeability (Sibson, 1996) and may compromise the sealing capacity of a fault system as sites of leakage (Kattenhorn and Pollard, 2001). However, stepover geometries commonly occur along clay-rich beds, and may promote clay smear and therefore reduce cross-fault permeability and enhance fault seal capacity (Childs et al., 1996; Kattenhorn and Pollard, 2001).

5.4.3 Implications for Seismic Hazard

The recognition of previously undocumented stepover geometries throughout the brittle crust within active strike-slip fault zones has several important implications for seismic

hazard analysis. First, downdip segmentation can cause seismic sources to be laterally shifted at depth with respect to the surface traces of these structures (Belgarde and Janecke, 2007). Significant uncertainty in seismic hazard assessments may result when surface traces of faults do not provide adequate information about fault geometry and location at depth. Second, according to the results of this study, low-angle events do not correspond spatially with the terminations of steeply dipping segments. The inferred décollements are unlikely to generate significant seismicity independent of events on adjacent steep fault segments. Finally, downdip segmentation may also affect the rupture behavior of segmented fault zones. Rupture scenarios in seismic hazard analyses of segmented fault zones should also consider possible downdip segmentation.

5.5 Conclusions

Downdip segmentation has been described as an important geometrical and evolutionary characteristic of normal and thrust faults; downdip segmentation has been postulated for strike-slip faults though never before documented in the literature, likely due to sampling bias (Walsh et al., 1999). The stepover geometries described in this paper are present within an active strike-slip fault zone at various scales throughout the upper crust. Slip is inferred to be accommodated at stepover depths along low-angle décollements localized along stratigraphic and/or structural mechanical boundaries. These décollements appear to be limited in spatial extent and mechanically weak, and therefore unlikely to generate seismic energy.

Conclusions

Chapter 1 of this dissertation presents a summary of published studies that describe the regional tectonic and stratigraphic history of the western Salton Trough region of southern California. Chapter 2 provides a review of the structural and stratigraphic development of Borrego Mountain. These introductory chapters establish a geological context for the detailed studies of fault-zone architecture that follow in Chapters 3–5. Chapter 3 of this dissertation presents mesoscopic and microstructural observations of deformation within small displacement strike-slip fault zones that occur in laumontite-cemented sandstones at Borrego Mountain. The data are interpreted in the context of the paleo-damage zone model, a new conceptual model for the evolution of damage-zone architecture that provides a framework for the analysis of spatio-temporal relationships between different generations of deformation. The paleo-damage zone model offers an explanation for the observed fault-parallel damage-zone domains: the domain boundaries represent the outer extents of actively deforming zones ('paleo-damage zones') associated with individual slip events; the domains are a relict of the superimposition of paleo-damage zones with variable widths. Damage-zone domains are defined based on field observations of spatial variations in deformation density and refined using profile plots of fracture density derived from two-dimensional line maps using the image analysis software ImageJ64. The apparent domainal character of damage-zone deformation is confirmed by significant jumps in fracture index values at domain boundaries.

Two distinct categories of faulting mechanisms have been documented in sandstones: deformation band faulting and shearing along fractures (Aydin et al., 2006, and references therein). The faults described in this study have extensive evidence for dilatant fracturing and no deformation bands are observed, so these faults are best described as sheared joints. However, the geometry of deformation within the selected fault zones at Borrego Mountain does not conform to either the published conceptual model for the evolution of sheared joints (Myers and Aydin, 2004) or the classic Riedel

shear model that predicts characteristic orientations and a specific chronology for the development of subsidiary deformation within brittle fault zones (Riedel, 1929). The small displacement fault zones at Borrego Mountain instead resemble a structural mesh of faults and extensional fractures, like those described by Hill (1977) and Sibson (1996). Cemented dilational fractures and alteration products from fluid-rock interactions provide extensive evidence of fault-related fluid flow. Mutually cross-cutting relationships between cemented fractures and tabular regions of cataclasis indicate that the evolution of these fault zones has been dominated by repeating cycles of dilation, fluid flow, and cataclasis. Polymodal extensional fracture sets are interpreted to result from heterogeneous stress distributions due to local variability in stresses or fluid-driven deformation, as described in the structural mesh model. On the basis of the proximity of Borrego Mountain to the San Jacinto fault zone and by analogy with evidence of episodic faulting and fluid flow in other regions with high heat flow, it is reasonable to infer that the deformation observed at Borrego Mountain was associated with seismic activity, possibly earthquake swarms.

The number of earthquakes hosted on each fault exceeds the number of observed damage-zone domains. The abundant evidence for fracture reactivation suggests that the damage-zone architecture was established during the early stages of fault development, and preserved during subsequent events. Preservation of early damage-zone architecture is consistent with later events primarily reactivating existing fractures rather than breaking fresh rock in the damage zone. The observation of episodically reactivated fractures in the damage zones provides an indication that the slip-localization model is not appropriate for these faults. The spatial extents of fractures and veins are not coincident with domain boundaries and therefore information about the relative timing of these features cannot be used to resolve the relative ages of the variably sized paleo-damage zones. However, if the younger paleo-damage zones were sequentially larger, the observations would be consistent with predictions from the process-zone model. It is also possible that once established, the damage-zone

architecture was accentuated during repeating characteristic-type events that have similarly sized paleo-damage zones.

Chapter 4 describes the petrophysical evolution of the small displacement fault zones exposed within the West Butte Conglomerate at Borrego Mountain. These fault zones are characterized by pervasive intergranular laumontite cement and abundant cemented dilational fractures that give rise to heterogeneous and complex flow properties. Analytical tests include x-ray diffractometer (XRD) analysis, laser particle size analysis (LPSA), mercury injection capillary pressure (MICP) tests, and measurements of porosity and permeability under constant and variable confining stress. High spatial variability in petrophysical properties is observed within each fault zone at multiple scales: between distinct fault-zone domains, within each fault-zone domain, in individual hand samples, and at the microscale. Variability in petrophysical properties is attributed to the following factors: (1) poor sorting and heterogeneous petrology of the host rocks; (2) inconsistent distribution of abundant (>10%) intergranular laumontite cement; (3) petrophysical properties of the laumontite cement; and (4) the occurrence and spatial distribution of cemented and open dilatant fractures throughout the fault zone. Damage-zone domain II, directly adjacent to the fault core, is more petrophysically heterogeneous than the rest of the fault zone due to the high concentration of cemented and open fractures close to the fault core. The petrophysical properties of well-cemented faulted sandstones deformed by shearing across joints are unpredictable and differ substantially from the properties of fault zones in poorly cemented to uncemented sandstones.

Chapter 5 presents field evidence that small displacement strike-slip faults in heterogeneous stratigraphy tend to form discontinuous steeply dipping fault segments that are linked along nearly horizontal fault segments. Stepover geometries range in character from sharp to diffuse. Steeply dipping fault segments may be vertically restricted by shallowly inclined mechanical boundaries in the form of stratigraphic contacts and/or structural fabrics. Bedding-parallel slip accommodates strike-slip

motion along the shallowly dipping fault segments. Similar geometries are defined by well-located seismicity data suggesting that strike-slip faults may be segmented in the downdip orientation at a wide range of scales.

These results have numerous implications in a broader context: (1) As a result of downdip segmentation, surface traces of faults may not provide adequate information about the geometry and location of strike-slip fault zones at depth, introducing significant uncertainty into seismic hazard assessments. (2) Low-angle nodal planes—which do occur in strike-slip fault zones—do not correspond spatially with the depths of inferred bedding-parallel slip. Therefore, if décollements occur at the stepover depths, these structures are weak and unlikely to host seismic slip. Bedding-parallel slip on shallowly inclined fault segments in strike-slip fault zones may occur aseismically. (3) Downdip segmentation may be important in terms of the rupture behavior of segmented fault zones. Seismic hazard analyses of active segmented fault zones generally only consider along-strike segmentation; individual segment and multi-segment rupture scenarios should also account for downdip segmentation. (4) Downdip segmentation may impact fault seal capacity in two contrasting ways. Segment linkage sites often give rise to enhanced permeability (Sibson, 1996) and may compromise the sealing capacity of a fault system as sites of leakage (Kattenhorn and Pollard, 2001). However, stepover geometries commonly occur along clay-rich beds, and may promote clay smear and therefore reduce cross-fault permeability and enhance fault seal capacity (Childs et al., 1996; Kattenhorn and Pollard, 2001).

REFERENCES

Allen, C.R., Grantz, A., Brune, J.N., Clark, M.M., Sharp, R.V., Theodore, T.G., Wolfe, E.W., and Wyss, M., 1968, The Borrego Mountain earthquake, April 8, 1968 (April 9, GCT): Bulletin of the Seismological Society of America, v. 58, p. 1,183–1,186.

Allen, C.R., and Nordquist, J.M., 1972, Foreshock, main shock, and larger aftershocks of the Borrego Mountain earthquake, *in* Sharp, R.V., ed., The Borrego Mountain Earthquake of April 9, 1968, US Geological Survey Professional Paper 787, p. 16–23.

Allmendinger, R.W., 2002, Stereonet for Macintosh, v. 6.3.3; Shareware software. Department of Geological Sciences, Cornell University, Ithaca.

Anders, M.H., and Wiltschko, D.V., 1994, Microfracturing, paleostress and the growth of faults: Journal of Structural Geology, v. 16, p. 795–815.

Anderson, J.L., Osborne, R.H., and Palmer, D.F., 1980, Petrogenesis of cataclastic rocks within the San Andreas fault zone of southern California, U.S.A: Tectonophysics, v. 67, p. 221–249.

Antonelis, K., Johnson, D.J., Miller, M.M., and Palmer, R., 1999, GPS determination of current Pacific-North American Plate motion: Geology, v. 27, p. 299–302.

Antonellini, M., and Aydin, A., 1994, Effect of faulting on fluid flow in porous sandstones: petrophysical properties: AAPG Bulletin, v. 78, p. 355–377.

Antonellini, M., Aydin, A., and Pollard, D.D., 1994, Microstructure of deformation bands in porous sandstones at Arches National Park, Utah: Journal of Structural Geology, v. 16, p. 941–959.

Atwater, T., 1970, Implications of plate tectonics for the Cenozoic tectonic evolution of western North America: Geological Society of America Bulletin, v. 81, p. 3,513–3,535.

—, 1989, Plate tectonic history of the northeast Pacific and western North America, *in* Winterer, E.L., Hussong, D.M., and Decker, R.W., eds., The eastern Pacific Ocean and Hawaii, The geology of North America: Denver, Geological Society of America, p. 21–70.

Atwater, T., and Stock, J., 1998, Neogene plate tectonic history of southwestern United States; an update: International Geological Review, v. 40, p. 375–402.

Axen, G., Kairouz, M., Steely, A.N., Janecke, S.U., and Dorsey, R.J., 2004, Structural expression of low-angle normal faults developed in wrench settings; an example from the West Salton detachment system: Abstracts with Programs - Geological Society of America, v. 36, p. 548–549.

Axen, G.J., and Fletcher, J.M., 1998, Late Miocene-Pleistocene extensional faulting, northern Gulf of California, Mexico and Salton Trough, California: International Geology Review, v. 40, p. 217–244.

Aydin, A., Borja, R.I., and Eichhubl, P., 2006, Geological and mathematical framework for failure modes in granular rock: Journal of Structural Geology, v. 28, p. 83–98.

Bartholomew, M.J., 1968, Geology of the northern portion of Seventeen Palms and Font's Point quadrangles, Imperial and San Diego Counties, California [M.S. thesis]: Los Angeles, University of Southern California, 60 p.

—, 1970, San Jacinto fault zone in the northern Imperial Valley, California: Geological Society of America Bulletin, v. 81, p. 3,161–3,166.

Beach, A., Welbon, A.I., Brockbank, P.J., and McCallum, J.E., 1999, Reservoir damage around faults: outcrop examples form the Suez rift: Petroleum Geoscience, v. 5, p. 109–116.

Belgarde, B.E., and Janecke, S.U., 2007, A "hidden" fault? Structural geology of three segments of the Clark fault, San Jacinto Fault zone, California: Abstracts with Programs - Geological Society of America, v. 39, p. 375.

Ben-Menahem, A., and Singh, S.J., 1981, Seismic waves and sources: New York, Springer-Verlag, 1108 p.

Ben-Zion, Y., and Lyakhovsky, V., 2006, Analysis of aftershocks in a lithospheric model with seismogenic zone governed by damage rheology: Geophysical Journal International, v. 165, p. 197–210.

Ben-Zion, Y., Peng, Z., Okaya, D., Seeber, L., Armbruster, J.G., Ozer, N., Michael, A.J., Baris, S., and Aktar, M., 2003, A shallow fault zone structure illuminated

by trapped waves in the Karadere-Duzce branch of the north Anatolian Fault, Western Turkey: Geophysical Journal International, v. 152, p. 699–717.

Ben-Zion, Y., and Sammis, C.G., 2003, Characterization of fault zones: Pure and Applied Geophysics, v. 160, p. 677–715.

Bennett, R.A., Rodi, W., and Reilinger, R.E., 1996, Global Positioning System constraints on fault slip rates in southern California and northern Baja, Mexico: Journal of Geophysical Research, v. 101, p. 21,943–21,960.

Bernet, M., Gaupp, R., and Wilhelm, S., 1997, Zeolite-cementation induced by basalt intrusions in Permotriassic sandstones of the Beacon Supergroup (Victoria Land, Antarctica): Gaea Heidelbergensis, v. 3, p. 73.

Biegel, R.L., and Sammis, C.G., 2004, Relating fault mechanics to fault zone structure: Advances in Geophysics, v. 47, p. 66–113.

Billi, A., Salvini, F., and Storti, F., 2003, The damage zone-fault core transition in carbonate rocks: implications for fault growth, structure and permeability: Journal of Structural Geology, v. 25, p. 1,779–1,794.

Blenkinsop, T.G., 2008, Relationships between faults, extension fractures and veins, and stress: Journal of Structural Geology, v. 30, p. 622–632.

Blenkinsop, T.G., and Sibson, R.H., 1992, Aseismic fracturing and cataclasis involving reaction softening within core material from the Cajon Pass drill hole: Journal of Geophysical Research, v. 97, p. 5,135–5,144.

Bloch, S., and Helmold, K.P., 1995, Predicting reservoir quality in sandstones: AAPG Bulletin, v. 79, p. 97–115.

Boles, J.R., 1982, Active albitization of plagioclase, Gulf Coast Tertiary: American Journal of Science, v. 282, p. 165–180.

Boles, J.R., and Coombs, D.S., 1977, Zeolite facies alteration of sandstones in the Southland Syncline, New Zealand: American Journal of Science, v. 277, p. 982–1,012.

Bryant, W.A. (compiler), 2005, Digital database of Quaternary and younger faults from the fault activity map of California, version 2.0: California Geological Survey

Web Page, <http://www.consrv.ca.gov/CGS/information/publications/QuarternaryFaults_ver2.htm>; downloaded 3/2008.

Burdick, L.J., and Mellman, G.R., 1976, Inversion of body waves from Borrego Mountain earthquake to the source mechanism: Bulletin of the Seismological Society of America, v. 66, p. 1,485–1,499.

Burford, R.O., 1972, Continued slip on the Coyote Creek Fault after the Borrego Mountain earthquake, *in* Sharp, R.V., ed., The Borrego Mountain Earthquake of April 9, 1968, US Geological Survey Professional Paper 787, p. 105–111.

Byerlee, J., 1993, Model for episodic flow of high-pressure water in fault zones before earthquakes: Geology, v. 21, p. 303–306.

Caine, J.S., Evans, J.P., and Forster, C.P., 1996, Fault zone architecture and permeability structure: Geology, v. 24, p. 1,025–1,028.

Chester, F.M., 1995, Geologic studies of deeply exhumed faults of the San Andreas system, southern California: collaborative research with Saint Louis University and Utah State University: NEHRP Annual Project Summary, Award No. 94G2457, v. 37.

Chester, F.M., and Chester, J.S., 1998, Ultracataclasite structure and friction processes of the Punchbowl fault, San Andreas system, California: Tectonophysics, v. 295, p. 199–221.

—, 2000, Stress and deformation along wavy frictional faults: Journal of Geophysical Research, v. 105, p. 23,421–23,430.

Chester, F.M., Evans, J.P., and Biegel, R.L., 1993, Internal structure and weakening mechanisms of the San Andreas fault: Journal of Geophysical Research, v. 98, p. 771–786.

Chester, F.M., and Logan, J.M., 1986, Composite planar fabric of gouge from the Punchbowl fault, California: Journal of Structural Geology v. 9, p. 621–634.

Chester, J.S., Chester, F.M., and Kronenberg, A.K., 2005, Fracture surface energy of the Punchbowl Fault, San Andreas system: Nature, v. 437, p. 133–136.

Chester, J.S., and Fletcher, R., 1997, Stress distribution and failure in anisotropic rock near a bend on a weak fault: Journal of Geophysical Research, v. 102, p. 673–708.

Childs, C., Nichol, A., Walsh, J.J., and Watterson, J., 1996, Growth of vertically segmented normal faults: Journal of Structural Geology, v. 18, p. 1,389–1,397.

Christie-Blick, N., and Biddle, K.T., 1985, Deformation and basin formation along strike-slip faults: Special Publication - Society of Economic Paleontologists and Mineralogists, v. 37, p. 1–34.

Clark, M.M., 1972, Surface rupture along the Coyote Creek Fault, *in* Sharp, R.V., ed., The Borrego Mountain Earthquake of April 9, 1968, US Geological Survey Professional Paper 787, p. 55–86.

Clauser, C., and Huenges, E., 1995, Thermal conductivity of rocks and minerals: AGU Reference Shelf, v. 3, p. 105–126.

Cooke, M.L., and Underwood, C.A., 2001, Fracture termination and step-over at bedding interfaces due to frictional slip and interface opening: Journal of Structural Geology, v. 23, p. 223–238.

Cowie, P.A., and Scholz, C.H., 1992a, Displacement-length scaling relationship for faults: data synthesis and discussion: Journal of Structural Geology, v. 14, p. 1149–1156.

—, 1992b, Physical explanation for the displacement-length relationship of faults using a post-yield fracture mechanics model: Journal of Structural Geology, v. 14, p. 1,133–1,148.

Crider, J.G., and Peacock, D.C.P., 2004, Initiation of brittle faults in the upper crust: a review of field observations: Journal of Structural Geology, v. 26, p. 691–707.

Crossey, L.J., Frost, R.B., and Surdam, R.C., 1984, Secondary porosity in laumontite-bearing sandstones, *in* McDonald, D.A., and Surdam, R.C., eds., Clastic diagenesis: AAPG Memoir 37, p. 225–237.

Cruikshank, K.M., and Aydin, A., 1995, Unweaving the joints in Entrada Sandstone, Arches National Park, Utah, U.S.A: Journal of Structural Geology, v. 17, p. 409–421.

Das, S., and Scholz, C., H., 1981, Off-fault aftershock clusters caused by shear stress increase?: Bulletin of the Seismological Society of America, v. 71, p. 1,669–1,675.

Davatzes, N.C., and Aydin, A., 2003, Overprinting mechanisms in high porosity sandstones of SE Utah: Journal of Structural Geology, v. 25, p. 1,795–1,813.

Davatzes, N.C., Eichhubl, P., and Aydin, A., 2005, Structural evolution of fault zones in sandstone by multiple deformation mechanisms: Moab fault, southeast Utah: GSA Bulletin, v. 117, p. 135–148.

Dawson, T.E., Rockwell, T.K., Weldon, R.J., II, and Wills, C.J., 2008, Summary of geologic data and development of *a priori* rupture models for the Elsinore, San Jacinto, and Garlock faults, *Appendix F in* The Uniform California Earthquake Rupture Forecast, version 2 (UCERF 2): U.S. Geological Survey Open-File Report 2007-1437F, 23 p.

Dean, M.A., 1988, Genesis, mineralogy, and stratigraphy of the Neogene Fish Creek Gypsum, southwestern Salton Trough, California [M.S. thesis], San Diego State University, 150 p.

Dean, M.A., Zoback, M.L., and Rowland, S.M., 1990, The Neogene Fish Creek Gypsum; forerunner to the incursion of the Gulf of California into the western Salton Trough: Abstracts with Programs - Geological Society of America, v. 22, p. 18.

DeMets, C., Gordon, R.G., Argus, D.F., and Stein, S., 1994, Effect of recent revisions to the geomagnetic reversal time scale on estimates of current plate motions: Geophysical Research Letters, v. 21, p. 2,191–2,194.

Dibblee, T.W., Jr., 1954, Geology of the Imperial Valley region, California, geology of southern California: California Division of Mines Bulletin, v. 170, p. 21–28.

—, 1984, Stratigraphy and tectonics of the San Felipe Hills, Borrego Badlands, Superstition Hills and vicinity, *in* Rigsby, C.A., ed., Field Trip Guidebook - Pacific Section, Society of Economic Paleontologists and Mineralogists, Volume 40, p. 31–44.

—, 1996, Stratigraphy and tectonics of the Vallecito-Fish Creek Mountains, Vallecito Badlands, Coyote Mountain, and Yuha Desert, southwestern Imperial basin, *in* Abbott, P.L., and Seymour, D.C., eds., Sturtzstrums and Detachment Faults,

Anza-Borrego Desert State Park, California, Volume 24, South Coast Geological Society Annual Field Trip Guide Book, p. 59–79.

Dieterich, J.H., 1979, Modeling of rock friction, 1, Experimental results and constituitive equations: Journal of Geophysical Research, v. 84, p. 2,161–2,168.

Dorsey, R.J., 2002, Stratigraphic record of Pleistocene initiation and slip on the Coyote Creek fault, Lower Coyote Creek, southern California: Contributions to crustal evolution of the southwestern United States, v. 365, p. 251–269.

—, 2005, Stratigraphy, tectonics, and basin evolution in the Anza-Borrego Desert region, *in* Jefferson, G.T., and Lindsay, L.E., eds., Fossil Treasures of Anza-Borrego Desert: San Diego, CA, Sunbelt Publications, p. 89–104.

Dorsey, R.J., Fluette, A., McDougall, K., Housen, B.A., Janecke, S.U., Axen, G.J., and Shirvell, C.R., 2007, Chronology of Miocene-Pliocene deposits at Split Mountain Gorge, Southern California; a record of regional tectonics and Colorado River evolution: Geology, v. 35, p. 57–60.

Dorsey, R.J., and Janecke, S.U., 2002, Late Miocene to Pleistocene West Salton detachment fault system and basin evolution, southern California: new insights: Abstracts with Programs - Geological Society of America, v. 34, p. 248.

Dorsey, R.J., Janecke, S.U., Kirby, S.M., Axen, G.J., and Steely, A.N., 2004, Pliocene lacustrine transgression in the western Salton Trough, Southern California; implications for regional tectonics and evolution of the Colorado River delta: Abstracts with Programs - Geological Society of America, v. 36, p. 317.

Dorsey, R.J., Janecke, S.U., Kirby, S.M., McDougall, K.A., and Steely, A.N., 2005, Pliocene evolution of the lower Colorado River in the Salton Trough; tectonic controls on paleogeography and the regional Borrego Lake, *in* Reheis, M.C., ed., U.S. Geological Survey Open-File Report OF 2005-1404, p. 13.

Dorsey, R.J., and Roering, J.J., 2006, Quaternary landscape evolution in the San Jacinto fault zone, Peninsular Ranges of Southern California; transient response to strike-slip fault initiation: Geomorphology, v. 73, p. 16–32.

Doser, D.I., and Kanamori, H., 1986, Depth of seismicity in the Imperial Valley region (1977-1983) and its relationship to heat flow, crustal structure, and the October 15, 1979, earthquake: Journal of Geophysical Research, v. 91, p. 675–688.

Dott, R.H., Jr., 1964, Wacke, graywacke and matrix; what approach to immature sandstone classification?: Journal of Sedimentary Petrology, v. 34, p. 625–632.

Dugdale, D.S., 1960, Yielding of steel sheets containing slits: Journal of Mechanics and Physics of Solids, v. 8, p. 100–104.

Engel, A.E.J., and Schultejann, P.A.A., 1984, Late Mesozoic and Cenozoic tectonic history of south central California: Tectonics, v. 3, p. 659–675.

Engelder, J.T., 1974, Cataclasis and the generation of fault gouge: Geological Society of America Bulletin, v. 85, p. 865–886.

Engelder, T., Gross, M.R., and Pinkerton, P., 1997, Joint development in clastic rocks of the Elk Basin anticline, Montana, Wyoming, *in* Hoak, T., Klawitter, A., and Blomquist, P., eds., An analysis of fracture spacing versus bed thickness in a basement-involved Laramide structure: Denver, Rocky Mountain Association of Geologists.

Erskine, B.G., and Wenk, H.R., 1985, Evidence for Late Cretaceous crustal thinning in the Santa Rosa mylonite zone, Southern California: Geology, v. 13, p. 274–277.

Escuder Viruete, J., Carbonell, R., Jurado, M.J., Marti, D., and Perez-Estaun, A., 2001, Two-dimensional geostatistical modeling and prediction of the fracture system in the Albala Granitic Pluton, SW Iberian Massif, Spain: Journal of Structural Geology, v. 23, p. 2,011–2,023.

Evans, J.P., and Chester, F.M., 1995, Fluid-rock interaction in faults of the San-Andreas system: Inferences from San Gabriel fault rock geochemistry and microstructures: Journal of Geophysical Research, v. 100, p. 13,007–13,020.

Evans, J.P., Forster, C.B., and Goddard, J.V., 1997, Permeability of fault-related rocks, and implications for hydraulic structure of fault zones: Journal of Structural Geology, v. 19, p. 1,393–1,404.

Faulkner, D.R., Lewis, A.C., and Rutter, E.H., 2003, On the internal structure and mechanics of large strike-slip fault zones: field observations of the Carboneras fault in southeastern Spain: Tectonophysics, v. 367, p. 235–251.

Faulkner, D.R., Mitchell, T.M., Healy, D., and Heap, M.J., 2006, Slip on 'weak' faults by the rotation of regional stress in the fracture damage zone: Nature, v. 444, p. 922–925.

Fialko, Y., Sandwell, D., Simons, M., and Rosen, P., 2005, Three-dimensional deformation caused by the Bam, Iran, earthquake and the origin of shallow slip deficit: Nature, v. 435, p. 295–299.

Fisher, Q.J., and Knipe, R.J., 1998, Fault sealing processes in siliciclastic sediments: Geological Society Special Publications, v. 147, p. 117–134.

Flodin, E.A., and Aydin, A., 2004, Evolution of a strike-slip fault network, Valley of Fire State Park, southern Nevada: Geological Society of America Bulletin, v. 116, p. 42–59.

Flodin, E.A., Gerdes, M., Aydin, A., and Wiggins, W.D., 2005, Petrophysical properties and sealing capacity of fault rock, Aztec Sandstone, Nevada, *in* Sorkhabi, R., and Tsuji, Y., eds., Faults, fluid flow, and petroleum traps: AAPG Memoir, v. 85, p. 197–217.

Folk, R.L., and Ward, W.C., 1957, Brazos River bar, a study in the significance of grain-size parameters: Journal of Sedimentary Petrology, v. 27, p. 3–27.

Fossen, H., and Hesthammer, J., 2000, Possible absence of small faults in the Gullfaks Field, northern North Sea: implications for downscaling of faults in some porous sandstones: Journal of Structural Geology, v. 22, p. 851–863.

Frost, R.B., Surdam, R.C., and Crossey, L.J., 1982, Secondary porosity in laumontite-bearing sandstones: AAPG Abstracts with Programs, v. 66, p. 569–570.

Fuis, G.S., Clayton, R.W., Davis, P.M., Ryberg, T., Lutter, J, W., Okaya, D.A., Hauksson, E., Prodehl, C., Murphy, M, J., Benthien, M.L., Baher, S.A., Kohler, M.D., Thygesen, K., Simila, G., and Keller, G.R., 2003, Fault systems of the 1971 San Fernando and 1994 Northridge earthquakes, southern California: Relocated aftershocks and seismic images from LARSE II: Geology, v. 31, p. 171–174.

George, P.G., and Dokka, R.K., 1994, Major Late Cretaceous cooling events in the eastern Peninsular Ranges, California, and their implications for Cordilleran tectonics: Geological Society of America Bulletin, v. 106, p. 903–914.

Ghent, E.D., 1979, Problems in zeolite facies geothermometry, geobarometry and fluid compositions: Special Publication - Society of Economic Paleontologists and Mineralogists, p. 81–87.

Gurrola, L.D., and Rockwell, T.K., 1996, Timing and slip for prehistoric earthquakes on the Superstition Mountain Fault, Imperial Valley, southern California: Journal of Geophysical Research, v. 101, p. 5,977–5,985.

Hardebeck, J.L., and Shearer, P.M., 2003, Using S/P amplitude ratios to constrain the focal mechanisms of small earthquakes: Bulletin of the Seismological Society of America, v. 93, p. 2,434–2,444.

Hay, R.L., and Sheppard, R.A., 2001, Occurrence of zeolites in sedimentary rocks; an overview: Reviews in Mineralogy and Geochemistry, v. 45, p. 217–234.

Heath, A.E., Walsh, J.J., and Watterson, J., 1994, Estimation of the effects of sub-seismic sealing faults on effective permeabilities in sandstone reservoirs, *in* Aasen, J.O., Berg, E., Buller, A.T., Hjelmeland, O., Holt, R.N., Kleppe, J., and Torsaeter, O., eds., North Sea Oil and Gas Reservoirs III, Kluwer Academic Publishers, p. 173–183.

Herzig, C., Carrasco, A., Schar, T., Murray, G., Rightmer, D., Lawerence, J., Milton, Q., and Wirths, T., 1995, Neogene stratigraphy of the Borrego Mountain area, Anza-Borrego Desert State Park, California, *in* Remeika, P., and Sturz, A., eds., Paleontology and geology of the western Salton Trough detachment, Anza-Borrego Desert State Park, California; Field trip guidebook and volume for the 1995 San Diego Association of Geologists field trip to Anza-Borrego Desert State Park, p. 133–136.

Hill, D.P., 1977, A model for earthquake swarms: Journal of Geophysical Research, v. 82, p. 1,347–1,352.

Hill, D.P., Mowinckel, P., and Peake, L.G., 1975, Earthquakes, active faults, and geothermal areas in the Imperial Valley, California: Science, v. 188, p. 1,306–1,308.

Hill, R.I., 1984, Petrology and petrogenesis of batholithic rocks, San Jacinto Mountains, southern California [Ph.D. thesis]: Pasadena, California Institute of Technology, 731 p.

Hoover, R.A., 1965, Areal geology and physical stratigraphy of a portion of the northern Santa Rosa Mountains, San Diego County, California [M.A. thesis]: Riverside, University of California, 81 p.

Housen, B.A., Dorsey, R.J., Janecke, S.U., and Axen, G.J., 2005, Rotation of Plio-Pleistocene sedimentary rocks in the Fish Creek Vallecito Basin, western Salton Trough, CA: Eos, Transactions, American Geophysical Union, v. 86, p. 39.

Huang, W., Silver, L.T., and Kanamori, H., 1996, Evidence for possible horizontal faulting in southern California from earthquake mechanisms: Geology, v. 24, p. 123–126.

Hudnut, K.W., and Clark, M.M., 1989, New slip along parts of the 1968 Coyote Creek Fault rupture, California: Bulletin of the Seismological Society of America, v. 79, p. 451–465.

Hudnut, K.W., and Sieh, K.E., 1989, Behavior of the Superstition Hills Fault during the past 330 years: Bulletin of the Seismological Society of America, v. 79, p. 304–329.

Hutton, L.K., Jones, L.M., Hauksson, E., and Given, D.D., 1991, Seismotectonics of southern California, *in* Slemmons, D.B., Engdahl, E.R., Blackwell, D.D., and Schwartz, D., eds., Neotectonics of North America, The geology of North America: Denver, Geological Society of America, p. 133–152.

James, E.W., and Silver, L.T., 1988, Implications of zeolites and their zonation in the Cajon Pass deep drillhole: Geophysical Research Letters, v. 15, p. 973–976.

Janecke, S.U., Kirby, S., Langenheim, V., Steely, A.N., Dorsey, R.J., Housen, B., and Lutz, A., 2005, High geologic slip rates on the San Jacinto fault zone in the SW Salton Trough, and possible near-surface slip deficit in sedimentary basins: Abstracts with Programs - Geological Society of America, v. 37, p. 275.

Janecke, S.U., Kirby, S.M., Langenheim, V.E., Housen, B.A., Dorsey, R.J., Crippen, R.E., and Blom, R.G., 2004, Kinematics and evolution of the San Jacinto fault zone in the Salton Trough; progress report from the San Felipe Hills area: Abstracts with Programs - Geological Society of America, v. 36, p. 317.

Janssen, C., Wagner, F.C., Zang, A., and Dresen, G., 2001, Fracture process zone in granite- a microstructural analysis: International Journal of Earth Sciences, v. 90, p. 46–59.

Jefferson, G., and Peterson, D., 1998, Hydrothermal origin of the Fish Creek Gypsum, Imperial County, southern California, *in* Lindsay, L., and Hample, W.G., eds., Geology and geothermal resources of the Imperial and Mexicali Valleys: San Diego, San Diego Association of Geologists, p. 40–51.

Jennings, J.J., 1987, Capillary pressure techniques: application to exploration and development geology: AAPG Bulletin, v. 71, p. 1,196–1,209.

Jourde, H., Flodin, E.A., Aydin, A., Durlofsky, L.J., and Wen, X.-H., 2002, Computing permeability of fault zones in eolian sandstone from outcrop measurements: AAPG Bulletin, v. 86, p. 1,187–1,200.

Jove, C., and Hacker, B., 1997, Experimental investigation of laumontite--> wairakite + H_2O: A model diagenetic reaction: American Mineralogist, v. 82, p. 781–789.

Kairouz, M.E., 2005, Geology of the Whale Peak region of the Vallecito Mountains: emphasis on the kinematics and timing of the West Salton Detachment fault, southern California [M.S. thesis]: Los Angeles, University of California, 156 p.

Kanamori, H., 2004, The diversity of the physics of earthquakes: Proceedings of the Japan Academy, Series B, v. 80, p. 297–316.

Kattenhorn, A.S., and Pollard, D.D., 2001, Integrating 3-D seismic data, field analogs, and mechanical models in the analysis of segmented normal faults in the Wytch Farm oil field, southern England, United Kingdom: AAPG Bulletin, v. 85, p. 1,183–1,210.

Katz, A.J., and Thompson, A.H., 1987, Prediction of rock electrical conductivity from mercury injection measurements: Journal of Geophysical Research, v. 92, p. 599–607.

Katz, Y., Weinberger, R., and Aydin, A., 2004, Geometry and kinematic evolution of Riedel shear structures, Capitol Reef National Park, Utah: Journal of Structural Geology, v. 26, p. 491–501.

Kelly, P.G., Sanderson, D.J., and Peacock, D.C.P., 1998, Linkage and evolution of conjugate strike-slip fault zones in limestones of Somerset and Northumbria: Journal of Structural Geology, v. 20, p. 1,477–1,493.

Kendrick, K., McFadden, L., and Morton, D., 1994, Soils and slip rates along the northern San Jacinto Fault: Abstracts with Programs - Geological Society of America, v. 27, p. 146–151.

Kendrick, K.J., Morton, D.M., Wells, S.G., and Simpson, R.W., 2002, Spatial and temporal deformation along the northern San Jacinto Fault, southern California; implications for slip rates: Bulletin of the Seismological Society of America, v. 92, p. 2,782–2,802.

Kerr, D.R., and Kidwell, S.M., 1991, Late Cenozoic sedimentation and tectonics, western Salton Trough, California, *in* Walawender, M.J., and Hanan, B.B., eds., Geological excursions in southern California, Volume Guidebook 1991 Annual Meeting Geological Society of America: San Diego, San Diego State University, p. 397–416.

Kim, Y.-S., Peacock, D.C.P., and Sanderson, D.J., 2004, Fault damage zones: Journal of Structural Geology, v. 26, p. 503–517.

Kirby, S.M., Janecke, S.U., Dorsey, R.J., Housen, B., and McDougall, K.A., 2005, A 1.07 Ma change from persistent lakes to intermittent flooding and desiccation in the San Felipe Hills, Salton Trough, Southern California, *in* Reheis, M.C., ed., U.S. Geological Survey Open-File Report OF 2005-1404, p. 18.

Kirby, S.M., Janecke, S.U., Dorsey, R.J., Housen, B.A., Langenheim, V.E., McDougall, K.A., and Steely, A.N., 2007, Pleistocene Brawley and Ocotillo Formations; evidence for initial strike-slip deformation along the San Felipe and San Jacinto fault zones, Southern California: Journal of Geology, v. 115, p. 43–62.

Kirby, S.R., 2005, The Quaternary tectonic and structural evolution of the San Felipe Hills, California [M.S. thesis]: Logan, Utah State University, 182 p.

Klinkenberg, L.J., 1941, The permeability of porous media to liquids and gases, Drilling and Production Practices: New York, American Petroleum Institute, p. 200–213.

Knopoff, L., and Lee, M.W., 1998, The self-organization of aftershocks: 1st ACES Workshop Proceedings, v. Session 4.2, p. 463–466.

Lachenbruch, A.H., Sass, J.H., and Galanis, S.P., Jr., 1985, Heat flow in southernmost California and the origin of the Salton Trough: Journal of Geophysical Research, v. 90, p. 6,709–6,736.

Langenheim, V.E., Jachens, R.C., Morton, D.M., Kistler, R.W., and Matti, J.C., 2004, Geophysical and isotopic mapping of preexisting crustal structures that influenced the location and development of the San Jacinto fault zone, southern California: Geological Society of America Bulletin, v. 116, p. 1,143–1,157.

LaPointe, P.R., and Hudson, J.A., 1985, Characterization and interpretation of rock mass joint patterns: Geological Society of America Special Paper 199, 37 p.

Li, Y.-G., Henyey, T., and Silver, T.L., 1992, Aspects of the crustal structure of the western Mojave Desert, California, from seismic reflection and gravity data: Journal of Geophysical Research, v. 97, p. 8,805–8,816.

Li, Y.-G., and Vernon, F.L., 2001, Characterization of the San Jacinto fault zone near Anza, California, by fault zone trapped waves: Journal of Geophysical Research, v. 106, p. 30,671–30,688.

Lin, G., Shearer, P.M., and Hauksson, E., 2007, Applying a 3D velocity model, waveform cross-correlation, and cluster analysis to locate southern California seismicity from 1981 to 2005: Journal of Geophysical Research, v. 112, p. doi:10.1029/2007JB004986.

Logan, J.M., Friedman, M., Higgs, N., Dengo, C., Shimamoto, T., Speed, R.C., Sharp, R.V., and Evernden, J.F., 1979, Experimental studies of simulated gouge and their application to studies of natural fault zones, U.S. Geological Survey Open-File Report OF 79-1239, p. 305–343.

Lohman, R.B., and McGuire, J.J., 2007, Earthquake swarms driven by aseimic creep in the Salton Trough: Journal of Geophysical Research, v. 112, p. doi: 10.1029/2006JB004596.

Lonsdale, P., 1991, Structural patterns of the Pacific floor offshore of Peninsular California, *in* Dauphin, J.P., and Simoneit, B.T., eds., The Gulf and peninsular provinces of the Californias, Volume 47: Tulsa, American Association Petroleum Geologists Memoir, p. 87–125.

Lunn, R.J., Willson, J.P., Shipton, Z.K., and Moir, H., 2008, Simulating brittle fault growth from linkage of preexisting structures: Journal of Geophysical Research, v. 113, p. doi:10.1029/2007JB005388.

Lutz, A.T., 2005, Tectonic controls on Pleistocene basin evolution in the central San Jacinto fault zone, southern California [M.S. thesis]: Eugene, University of Oregon, 136 p.

Lutz, A.T., and Dorsey, R.J., 2003, Stratigraphy of the Pleistocene Ocotillo Formation, Borrego Badlands, Southern California; basinal response to evolution of the San Jacinto fault zone: Abstracts with Programs - Geological Society of America, v. 35, p. 580.

Lutz, A.T., Dorsey, R.J., Housen, B.A., and Janecke, S.U., 2006, Stratigraphic record of Pleistocene faulting and basin evolution in the Borrego Badlands, San Jacinto fault zone, Southern California: Geological Society of America Bulletin, v. 118, p. 1,377–1,397.

Magistrale, H., 2002, The relation of the southern San Jacinto fault zone to the Imperial and Cerro Prieto faults: Special Paper - Geological Society of America, v. 365, p. 271–278.

Main, I.G., Kwon, O.K., Ngwenya, B.T., and Elphick, S.C., 2000, Fault sealing during deformation band growth experiments in porous sandstone: Geology, v. 22, p. 183–186.

Mansfield, C.S., and Cartwright, J.A., 1996, High resolution fault displacement mapping from three-dimensional seismic data: evidence for dip linkage during fault growth: Journal of Structural Geology, v. 18, p. 249–263.

Martel, S.J., Pollard, D.D., and Segall, P., 1988, Development of simple fault zones in granitic rock, Mount Abbot Quadrangle, Sierra Nevada, California: Geological Society of America Bulletin, v. 100, p. 1,451–1,465.

McClay, K., and Bonora, M., 2001, Analog models of restraining stepovers in strike-slip fault systems: AAPG Bulletin, v. 85, p. 233–260.

McCulloh, T.H., and Stewart, R.J., 1982, Laumontite in the western Transverse Ranges, California; mark of Neogene hydrothermal alteration coincident with transcurrent faults: Abstracts with Programs - Geological Society of America, v. 14, p. 213–214.

Moore, D.E., Hickman, S.H., Lockner, D.A., and Dobson, P.F., 2001, Hydrothermal minerals and microstructures in the Silangkitang geothermal field along the Great Sumatran fault zone, Sumatra, Indonesia: Geological Society of America Bulletin, v. 113, p. 1,179–1,192.

Morley, E.R., Jr., 1963, Geology of the Borrego Mountain Quadrangle and the western portion of the Shell Reef Quadrangle, San Diego County, California [M.S. thesis]: Los Angeles, University of Southern California, 138 p.

Morrow, C.A., and Byerlee, J.D., 1991, A note on the frictional strength of laumontite from Cajon Pass, California: Geophysical Research Letters, v. 18, p. 211–214.

Morton, D.M., and Matti, J.C., 1993, Extension and contraction within an evolving divergent strike-slip fault complex; the San Andreas and San Jacinto fault zones at their convergence in southern California, *in* Powell, R.E., Weldon, R.J., and Matti, J.C., eds., The San Andreas fault system: displacement, palinspastic reconstruction, and geologic evolution: Boulder, Geological Society of America Memoir 178, p. 217–230.

Myers, R., and Aydin, A., 2004, The evolution of faults formed by shearing across joint zones in sandstone: Journal of Structural Geology, v. 26, p. 947–966.

Myers, R.D., 1999, Structure and hydraulics of brittle faults in sandstone [Ph.D. thesis]: Stanford, California, Stanford University, 176 p.

Narr, W., and Suppe, J., 1991, Joint spacing in sedimentary rocks: Journal of Structural Geology, v. 13, p. 1,037–1,048.

Nazareth, J.J., and Hauksson, E., 2004, The seismogenic thickness of the southern California crust: Bulletin of the Seismological Society of America, v. 94, p. 940–960.

Nemser, E.S., and Cowan, D.S., 2009 *in press*, Downdip segmentation of strike-slip fault zones in the brittle crust: Geology, v. 37, p. 419–422.

Neuhoff, P.S., Fridriksson, T., and Bird, D.K., 2000, Zeolite parageneses in the North Atlantic igneous province; implications for geotectonics and groundwater quality of basaltic crust: International Geology Review, v. 42, p. 15–44.

Nicol, A., Gillespie, P.A., Childs, C., and Walsh, J.J., 2002, Relay zones between mesoscopic thrust faults in layered sedimentary sequences: Journal of Structural Geology, v. 24, p. 709–727.

Orange, D.L., Geddes, D.S., and Moore, J.C., 1993, Structural and fluid evolution of a young accretionary complex; the Hoh rock assemblage of the western Olympic Peninsula, Washington: Geological Society of America Bulletin, v. 105, p. 1,053–1,075.

Orgil, A., Rockwell, T.K., Weigand, P.W., and Shellebarger, J., 2001, Three dimensional paleoseismic investigation on the south break of the Coyote Creek Fault, southern California: Abstracts with Programs - Geological Society of America, v. 33, p. 58.

Oskin, M., and Stock, J., 2003a, Cenozoic volcanism and tectonics of the continental margins of the upper Delfin Basin, northeastern Baja California and western Sonora: Special Paper - Geological Society of America, v. 374, p. 421–438.

—, 2003b, Marine incursion synchronous with plate-boundary localization in the Gulf of California: Geology, v. 31, p. 23–26.

Oskin, M., Stock, J., and Martin-Barajas, A., 2001, Rapid localization of Pacific-North America plate motion in the Gulf of California: Geology, v. 29, p. 459–462.

Peacock, D.C.P., and Sanderson, D.J., 1991, Displacements, segment linkage and relay ramps in normal fault zones: Journal of Structural Geology, v. 13, p. 721–733.

Petersen, M.D., Seeber, L., Sykes, L.R., Nabelek, J.L., Armbruster, J.G., Paceco, J., and Hudnut, K.W., 1991, Seismicity and fault interaction, southern San Jacinto fault zone and adjacent faults, southern California; implications for seismic hazard: Tectonics, v. 10, p. 1,187–1,203.

Petersen, M.D., and Wesnousky, S.G., 1994, Fault slip rates and earthquake histories for active faults in Southern California: Bulletin of the Seismological Society of America, v. 84, p. 1,608–1,649.

Petit, J.-P., Wibberley, C.A.J., and Ruiz, G., 1999, 'Crack-seal', slip: a new fault valve mechanism?: Journal of Structural Geology, v. 21, p. 1,199–1,207.

Pittman, E.D., 1992, Relationship of porosity and permeability to various parameters derived from mercury injection-capillary pressure curves for sandstone: AAPG Bulletin, v. 76, p. 191–198.

Poliakov, A.N.B., Dmowska, R., and Rice, J.R., 2002, Dynamic shear rupture interactions with fault bends and off-axis secondary faulting: Journal of Geophysical Research, v. 107, p. doi:10.1029/2001JB000572.

Pollard, W.J., and Rockwell, T.K., 1995, Late Holocene slip rate for the Coyote Creek Fault, Imperial County, California: Abstracts with Programs - Geological Society of America, v. 27, p. 72.

Priest, S.D., and Hudson, J.A., 1981, Estimation of discontinuity spacing and tracing length using scanline survey: International Journal of Rock Mechanics and Mining Sciences and Geomechanics Abstracts, v. 18, p. 183–197.

Prior, D.J., Marsaglia, K.M., Rochford, E.L., Agar, S.M., Coy, G., Lewis, S.D., Behrmann, J.H., Musgrave, R.J., Arqueros, R., Bangs, N., Boden, P., Brown, K.M., Collombat, H., Didenko, A.N., Didyk, B.M., Forsythe, R., Froelich, P.N., Golovchenko, X., Kurnosov, V.B., Kvenvolden, K.A., Lindsley-Griffin, N., Marsaglia, K., Osozawa, S., Prior, D.J., Sawyer, D.S., Scholl, D.C., Spiegler, D., Strad, K., Takahashi, K., Torres, M.E., Faundez, M.V., Vergara, H.P., Wasedal, A., and Musgrave, R.J., 1995, Textural evidence of diagenetic evolution of Site 863, Chile triple junction: Proceedings of the Ocean Drilling Program, Scientific Results, v. 141, p. 153–167.

Ragona, D., Rockwell, T.K., and Altangerel, O., 2003, Earthquake behavior across a fault segment boundary; a high resolution paleoseismic study in the southern San Jacinto fault zone, Imperial Valley, southern California: Abstracts with Programs - Geological Society of America, v. 35, p. 27.

Ragona, D., Rockwell, T.K., and Orgil, A., 2001, Fault segmentation and earthquake behavior: a high resolution paleoseismic study in the southern San Jacinto fault zone: Eos, Transactions, American Geophysical Union, v. 82, Abstract S52D-0668.

Ramseyer, K., Boles, J.R., and Lichtner, P.C., 1992, Mechanism of plagioclase alteration: Journal of Sedimentary Petrology, v. 62, p. 349–356.

Reed, R.M., Laubach, S.E., Clift, S., Hooker, J., and Makowitz, A., 2002, Macrofractures, microfractures, and fracture-cement relations in Permian

sandstones from the Val Verde Basin, West Texas: Abstracts with Programs - Geological Society of America, v. 34, p. 11.

Reitz, D.T., 1977, Geology of the western and central San Felipe Hills, northwestern Imperial County, California [M.S. thesis]: Los Angeles, University of Southern California, 155 p.

Remy, R.R., 1994, Porosity reduction and major controls on diagenesis of Cretaceous-Paleocene volcaniclastic and arkosic sandstone, Middle Park Basin, Colorado: Journal of Sedimentary Research, v. 64, p. 797–806.

Revenaugh, J., 1998, Seismic estimation of cumulative offset on the San Jacinto fault zone: Eos, Transactions, American Geophysical Union, v. 79, p. F–593.

Rice, J.R., 1992, Fault stress states, pore pressure distributions, and the weakness of the San Andreas fault, *in* Evans, B., and Wong, T.F., eds., Fault mechanics and transport properties in rocks: San Diego, Academic Press, p. 475–503.

Riedel, W., 1929, Zur mechanik geologischer brucherscheinungen: Centralblatt fur Mineralogie, Geologie, und Paleontologie, v. Ser. B, p. 354–568.

Rightmer, D.A., and Abbott, P.L., 1996, Lithologically similar domains in the Fish Creek sturzstrom, Anza-Borrego Desert State Park, California: Abstracts with Programs - Geological Society of America, v. 28, p. 105.

Robinson, R.B., 1966, Classification of reservoir rocks by surface texture: AAPG Bulletin, v. 50, p. 547–559.

Rockwell, T., Loughman, C., and Merifield, P., 1990a, Late Quaternary rate of slip along the San Jacinto fault zone near Anza, southern California: Journal of Geophysical Research, v. 95, p. 8,593–8,605.

Rockwell, T.K., Klinger, R., and Goodmacher, J., 1990b, Determination of slip rates and dating of earthquakes for the San Jacinto and Elsinore fault zones, *in* Kooser, M.A., and Reynolds, R.E., eds., Geology around the margins of the Eastern San Bernardino Mountains, Volume 1: Redlands, Inland Geological Society, p. 51–56.

Ruisaard, C.I., 1979, Stratigraphy of the Miocene Alverson Formation, Imperial County, California [M.S. thesis]: San Diego, San Diego State University, 125 p.

Sanders, C., and Magistrale, H., 1997, Segmentation of the northern San Jacinto fault zone, southern California: Journal of Geophysical Research, v. 102, p. 27,453–27,467.

Sanders, C.O., 1987, Seismotectonics of the San Jacinto fault zone and the Anza seismic gap [Ph.D. thesis]: Pasadena, California Institute of Technology, 143 p.

—, 1989, Fault segmentation and earthquake occurrence in the strike-slip San Jacinto fault zone, California, *in* Schwartz, D.P., and Sibson, R.H., eds., Proceedings of Conference XLV; a workshop on Fault segmentation and controls of rupture initiation and termination, Open-File Report - U. S. Geological Survey, Report: OF 89-0315, p. 324–349.

Saucier, F., Humphreys, E., and Weldon, R.J., 1992, Stress near geometrically complex strike-slip faults: application to the San Andreas fault at Cajon Pass, southern California: Journal of Geophysical Research, v. 97, p. 5,081–5,094.

Sayed, A.Y., 2001, In situ compressional wave velocity across an exposed brittle fault zone [M.S. thesis], Virginia Polytechnic Institute and State University, 40 p.

Schlische, R.W., Young, S.S., Ackermann, R.V., and Gupta, A., 1996, Geometry and scaling relations of a population of very small rift-related normal faults: Geology, v. 24, p. 683–686.

Scholz, C.H., Dawers, N.H., Yu, J.-Z., Anders, M.H., and Cowie, P.A., 1993, Fault growth and fault scaling laws: Preliminary results: Journal of Geophysical Research, v. 98, p. 951–961.

Scholz, C.H., Sykes, L.R., and Aggarwal, Y.P., 1973, Earthquake prediction: a physical basis: Science, v. 181, p. 803–810.

Schowalter, T.T., 1979, Mechanics of secondary hydrocarbon migration and entrapment: AAPG Bulletin, v. 63, p. 723–760.

Schulz, S.E., and Evans, J., 2000, Mesoscopic structure of the Punchbowl fault, southern California and the geologic and geophysical structure of active strike-slip faults: Journal of Structural Geology, v. 22, p. 913–930.

Schulz, S.E., and Evans, J.P., 1998, Spatial variability in microscopic deformation and composition of the Punchbowl fault, southern California: implications for

mechanisms, fluid-rock interaction, and fault morphology: Tectonophysics, p. 223–244.

Sharp, R.V., 1967, San Jacinto fault zone in the Peninsular Ranges of southern California: Geological Society of America Bulletin, v. 78, p. 705–729.

—, 1975, En echelon fault patterns of the San Jacinto Fault zone, *in* Crowell, J.C., ed., San Andreas Fault in southern California; a guide to San Andreas Fault from Mexico to Carrizo Plain: California Division of Mines and Geology Special Report 118, p. 147–152.

—, 1981, Variable rates of late Quaternary strike slip on the San Jacinto fault zone, southern California: Journal of Geophysical Research, v. 86, p. 1,754–1,762.

Sharp, R.V., and Clark, M.M., 1972, Geologic evidence of previous faulting near the 1968 rupture on the Coyote Creek Fault, *in* Sharp, R.V., ed., The Borrego Mountain Earthquake of April 9, 1968, US Geological Survey Professional Paper 787, p. 131–140.

Sharp, R.V., Speed, R.C., Sharp, R.V., and Evernden, J.F., 1979, Some characteristics of the eastern Peninsular Ranges mylonite zone, U.S. Geological Survey Open-File Report OF 79-1239, p. 258–267.

Shearer, P.M., 2002, Parallel fault strands at 9-km depth resolved on the Imperial fault, southern California: Geophysical Research Letters, v. 29, p. doi:10.1029/2002GL015302.

Shipton, Z.K., and Cowie, P.A., 2001, Damage zone and slip-surface evolution over micro- to kilometer scales in high-porosity Navajo sandstone, Utah: Journal of Structural Geology, v. 23, p. 1825–1844.

—, 2003, A conceptual model for the origin of fault damage structures in high-porosity sandstone: Journal of Structural Geology, v. 25, p. 333–344.

Shipton, Z.K., Cowie, P.A., and Vermilye, J., 1997, Fault displacement profiles and off-fault damage; interpreting the record of fault growth: Abstracts with Programs - Geological Society of America, v. 29, p. 199.

Shipton, Z.K., Evans, J.P., Robeson, K.R., Forster, C.B., and Snelgrove, S., 2002, Structural heterogeneity and permeability in faulted eolian sandstone:

Implications for subsurface modeling of faults: AAPG Bulletin, v. 86, p. 863–883.

Shirvell, C.R., Axen, G.J., and Stockli, D.F., 2005, Pliocene (U-Th)/He cooling ages from the West Salton detachment system (WSDS), Salton Trough [modified]: Abstracts with Programs - Geological Society of America, v. 37, p. 274.

Sibson, R.H., 1985, Stopping of earthquake ruptures at dilational fault jogs: Nature, v. 316, p. 248–251.

—, 1986, Brecciation processes in fault zones; inferences from earthquake rupturing: Pure and Applied Geophysics, v. 124, p. 159–175.

—, 1990, Conditions for fault-valve behaviour, *in* Knipe, R.J., and Rutter, E.H., eds., Deformation Mechanisms, Rheology and Tectonics, 54. Geological Society of London Special Publications, p. 15–28.

—, 1996, Structural permeability of fluid-driven fault-fracture meshes: Journal of Structural Geology, v. 18, p. 1,031–1,042.

—, 2003, Thickness of the seismic slip zone: Bulletin of the Seismological Society of America, v. 93, p. 1,169–1,178.

Sibson, R.H., Moore, J.M.M., and Rankin, A.H., 1975, Seismic pumping- a hydrothermal fluid transport mechanism: Journal of the Geological Society, v. 131, p. 653–659.

Simpson, C., 1984a, Borrego Springs-Santa Rosa mylonite zone; a Late Cretaceous west-directed thrust in southern California: Geology, v. 12, p. 8–11.

—, 1984b, Ductile deformation of feldspars in mylonitic granodiorite, Santa Rosa mylonite zone, CA: Abstracts with Programs - Geological Society of America, v. 16, p. 63.

Sneider, R.M., Sneider, J.S., Bolger, G.W., and Neasham, J.W., 1997, Comparison of seal capacity determinations: Conventional cores vs. cuttings, *in* Surdam, R.C., ed., Seals, traps, and the petroleum system, AAPG Memoir 67, p. 1–12.

Spencer, J.E., and Normark, W.R., 1989, Neogene plate-tectonic evolution of the Baja California Sur continental margin and the southern Gulf of California, Mexico,

in Winterer, E.L., Hussong, D.M., and Decker, R.W., eds., The eastern Pacific Ocean and Hawaii, The geology of North America: Denver, Geological Society of America, p. 489–497.

Spudich, P., and Olsen, K.B., 2001, Fault zone amplified waves as a possible seismic hazard along the Calaveras fault in central California: Geophysical Research Letters, v. 28, p. 2,533–2,536.

Steely, A.N., 2003, Structural geology and stratigraphy of the Borrego Mountain area, southern California: Implications for late Cenozoic tectonic evolution of the western Salton Trough [B.S. thesis]: Eugene, University of Oregon, 77 p.

—, 2006, Evolution and kinematics of the West Salton detachment fault and its deforming supradetachment basin and the younger cross-cutting San Felipe fault zone [M.S. thesis]: Logan, Utah State University, 239 p.

Steely, A.N., Janecke, S.U., Axen, G.J., and Dorsey, R.J., 2005a, Pleistocene (approximately 1 Ma) transition from West Salton detachment faulting to cross-cutting dextral strike-slip faults in the SW Salton Trough: Abstracts with Programs - Geological Society of America, v. 37, p. 274–275.

Steely, A.N., Janecke, S.U., and Dorsey, R.J., 2004a, Evidence for syn-depositional folding of Imperial-age synrift deposits above the West Salton detachment fault, Borrego Mountain area, Southern California: Abstracts with Programs - Geological Society of America, v. 36, p. 317.

Steely, A.N., Janecke, S.U., Dorsey, R.J., and Axen, G., 2004b, Evidence for late Miocene-Quaternary low-angle oblique strike-slip faulting on the West Salton detachment fault, Southern California: Abstracts with Programs - Geological Society of America, v. 36, p. 37.

Steely, A.N., Janecke, S.U., Long, S.P., Carney, S.M., Oaks, R.Q., Jr., Langenheim, V.E., and Link, P.K., 2005b, Evolution of a late Cenozoic supradetachment basin above a flat-on-flat detachment with a folded lateral ramp, SE Idaho: GSA Field Guide, v. 6, p. 169–198.

Streit, J.E., 1997, Low frictional strength of upper crustal faults: A model: Journal of Geophysical Research, v. 102, p. 24,619–24,626.

Surdam, R.C., and Boles, J.R., 1979, Diagenesis of volcanic sandstones: Special Publication - Society of Economic Paleontologists and Mineralogists, p. 227–242.

Tanikawa, W., and Shimamoto, T., 2006, Klinkenberg effect for gas permeability and its comparison to water permeability for porous sedimentary rocks: Hydrology and Earth System Sciences Discussions, v. 3, p. 1,315–1,338.

Tchalenko, J.S., 1970, Similarities between shear zones of different magnitudes: Geological Society of America Bulletin, v. 81, p. 1,625–1,639.

Terzaghi, R.D., 1965, Sources of errors in joint surveys: Geotechnique, v. 15, p. 287–304.

Todd, V.R., Erskine, B.G., and Morton, D.M., 1988, Metamorphic and tectonic evolution of the northern Peninsular Ranges Batholith, southern California, *in* Ernst, W.G., ed., Metamorphism and Crustal Evolution of the Western United States; Rubey Volume VII: Englewood Cliffs, Prentice Hall, p. 894–937.

Tullis, T.E., 1988, Rock friction constituitive behavior from laboratory experiments and its implications for an earthquake prediction field monitoring program: Pure and Applied Geophysics, v. 126, p. 555–588.

Twiss, R.J., and Moores, E.M., 1992, Structural Geology: New York, W.H. Freeman and Company, 736 p.

Varva, C.L., Kaldi, J.G., and Sneider, R.M., 1992, Geological applications of capillary pressure: a review: AAPG Bulletin, v. 76, p. 840–850.

Verdugo, D., Ragona, D.E., and Rockwell, T.K., 2005, Further resolution of past earthquake surface ruptures at the Carrizo Wash site, Superstition Mountain strand of the San Jacinto Fault, Imperial Valley, southern California: Eos, Transactions, American Geophysical Union.

Vermilye, J., 1996, The growth of natural fracture systems: A fracture mechanics approach [Ph.D thesis]: New York, Columbia University, 236 p.

Vermilye, J.M., and Scholz, C.H., 1998, The process zone: A microstructural view of fault growth: Journal of Geophysical Research, v. 103, p. 12,223–12,237.

—, 1999, Fault propagation and segmentation: insight from the microstructural examination of a small fault: Journal of Structural Geology, v. 21, p. 1,623–1,636.

Vincent, M.W., and Ehlig, P.L., 1988, Laumontite mineralization in rocks exposed of San Andreas Fault at Cajon Pass, southern California: Geophysical Research Letters, v. 15, p. 977–980.

Walsh, J.J., Watterson, J., Bailey, W.R., and Childs, C., 1999, Fault relays, bends and branch-lines: Journal of Structural Geology, v. 21, p. 1,019–1,026.

Webb, T.H., and Kanamori, H., 1985, Earthquake focal mechanisms in the eastern Transverse Ranges and San Emigdio Mountains, southern California and evidence for a regional decollement: Bulletin of the Seismological Society of America, v. 75, p. 737–757.

Wesnousky, S.G., Prentice, C.S., and Sieh, K.E., 1991, An offset Holocene stream channel and the rate of slip along the northern reach of the San Jacinto fault zone, San Bernardino Valley, California: Geological Society of America Bulletin, v. 103, p. 700–709.

Wibberley, C.A.J., and Shimamoto, T., 2003, Internal structure and permeability of major strike-slip fault zones: the Median Tectonic Line in Mie Prefecture, Southwest Japan: Journal of Structural Geology, v. 25, p. 59–78.

Wilkins, S.J., and Gross, M.R., 2002, Normal fault growth in layered rocks at Split Mountain, Utah: influence of mechanical stratigraphy on dip linkage, fault restriction and fault scaling: Journal of Structural Geology, v. 24, p. 1,413–1,429.

Wilkins, S.J., Gross, M.R., Wacker, M., Eyal, Y., and Engelder, T., 2001, Faulted joints: kinematics, displacement-length scaling relations and criteria for their identification: Journal of Structural Geology, v. 23, p. 315–327.

Wilson, J.E., Chester, J.S., and Chester, F.M., 2003, Microfracture analysis of fault growth and wear processes, Punchbowl Fault, San Andreas system, California: Journal of Structural Geology, v. 25, p. 1,855–1,873.

Winker, C.D., 1987, Neogene stratigraphy of the Fish Creek-Vallecito section, southern California: Implications for early history of the northern Gulf of California and the Colorado Delta [Ph.D. thesis], University of Arizona, 494 p.

Winker, C.D., and Kidwell, S.M., 1986, Paleocurrent evidence for lateral displacement of the Pliocene Colorado River delta by the San Andreas fault system, southeastern California: Geology, v. 14, p. 788–791.

—, 1996, Stratigraphy of a marine rift basin; Neogene of the western Salton Trough, California, *in* Abbott, P.L., and Cooper, J.D., eds., Field Trip Guidebook (American Association of Petroleum Geologists. Pacific Section), Volume 80, p. 295–336.

—, 2002, Stratigraphic evidence for ages of different extensional styles in the Salton Trough, southern California: Abstracts with Programs - Geological Society of America, v. 34, p. 83–84.

Woodard, G.D., 1963, The Cenozoic succession of the west Colorado Desert, San Diego and Imperial Counties, southern California [Ph.D. thesis]: Berkeley, University of California, 173 p.

Yanagimoto, Y., and Iijima, A., 2003, Hydrothermal laumontization and microfracture formation in reservoir rocks at the Yufutsu Field, Hokkaido, northern Japan: Journal of Petroleum Geology, v. 26, p. 351–372.

Zen, E., and Thompson, A.B., 1974, Low grade regional metamorphism; mineral equilibrium relations: Annual Review of Earth and Planetary Sciences, v. 2, p. 179–212.

Appendices

Appendix A Mesoscopic Observations of Selected Faults

A.1 Borrego Mountain Wash Faults (Listed From South to North): BM1, BM3, BM2

A.1.1 Fault BM1

Fault BM1 is a steeply dipping strike-slip fault zone with an orientation of 152/82˚W towards the bottom of the exposure and 161/78˚W towards the top of the exposure (Figure 3.9). To the south of fault BM1, a zone of deformation ~9 m away includes fractures and chemical alteration but lacks a throughgoing fault; the nearest fault to the north (fault BM3) is ~8 m away (Figure 3.6). On both sides of fault BM1, bedding is gently dipping, ~16–19˚ towards the southwest.

The fault core of fault BM1 ranges from 0.4 cm wide to ~1 m wide. The width of the fault core is strongly controlled by mechanical stratigraphy: the core is narrow through the more competent units SS4, SS3, and SS7–SS10, and widens into in a heavily fractured region within the more thinly bedded strata of units SS/SH2 and SS5. At the mesoscopic scale, gypsum veins, calcite veins, and open fractures can be observed within the fault core. The dominant principal slip surface of the fault zone is localized on the left (southwest) edge of the fault core. Purely strike-slip motion along fault BM1 can be inferred from horizontal striae on slip surfaces within the fault core and a substantial change in the thickness of unit SS/SH2 across the fault. However, it is difficult to determine the sense of motion or quantify the amount of displacement in the strike-parallel direction. The damage zone of fault BM1 contains calcite veins, gypsum veins, and open fractures.

A.1.2 Fault BM3

Fault BM3 is vertically segmented, with three discontinuous subparallel steeply dipping fault segments: segments BM3A and BM3B within the top half of the exposure and segment BM3C (with an orientation of 147˚/83˚) in the bottom half of the exposure

(Figure 3.9). Bedding-parallel slip within unit SS/SH2 accommodates displacement at the upper termination of segment BM3C and the lower terminations of segments BM3A and BM3B. The nearest fault to the south (fault BM1) is ~8 m away; the nearest fault to the north is a large fault ~15 m away (Figure 3.6).

The fault core (DI) of segment BM3C ranges from ~0.4–6 cm wide, and the dominant principal slip surface is on the right (northeast) side of the core. The stratigraphic section can be correlated across fault BM3 with minimal dip-slip separation, and it is likely that slip has been nearly pure strike-slip. Horizontal striae and grooves on a polished principal slip surface from the core of BM3C indicate purely strike-slip motion. However, it is difficult to quantify the amount of displacement in the strike-parallel direction.

A.1.3 Fault BM2

Fault BM2 is a vertical fault zone with a strike of 160˚ (Figure 3.9). The nearest fault to the west of fault BM2 is ~8 m away (Figure 3.6). To the east of fault BM2, the outcrop is truncated by a locally north-trending wash ~4 m from the fault core. Thick calcite veins on the ground in the wash likely represent deformation related to an eroded fault. Strike-slip displacement along fault BM2 can be inferred from the continuity of stratigraphy across the fault zone, the vertical orientation of the fault, and its structural context within a strike-slip fault zone. However, it is difficult to determine the sense of motion or quantify the amount of displacement in the strike-parallel direction.

Because the stratigraphy at fault BM2 is relatively isotropic, mechanical stratigraphy does not appear to play an important role in controlling deformation mechanisms that operate along the fault (for example, there are no clay smears exposed along the fault). A clay-rich bed from unit SS1 was sampled at the base of the outcrop on the east side of the fault, but due to the gentle westerly (10˚) dip of bedding, it is not possible to observe how this bed affects the mechanical behavior of this fault zone.

The fault core (DI) of BM2 ranges from ~10–30 cm wide, and is bounded by two main principal surfaces that extend throughout the exposure. These features have calcite and laumontite vein fill and range from 0.1–3 cm wide. At the top of the outcrop, the structure is more complex and the principal slip surfaces branch into >2 discrete slip planes. The majority of the fault slip has been accommodated along the principal slip surface that is located along the eastern edge of DI. Towards the base of the outcrop, the fault core is a ~20 cm wide zone of fault breccia with coherent clasts of host rock up to 3 cm long surrounded by a white, fine-grained matrix. The matrix of the fault breccia is friable and likely contains fine-grained host rock and ground calcite and laumontite vein material, although microstructural analysis has not been performed on the fault breccia because it is difficult to sample.

A series of *en-echelon* calcite veins in the upper part of the outcrop are oriented ~30^{o} counterclockwise from the principal slip surfaces of the fault zone. These veins are generally ~2–5 cm thick and ~10–20 cm in length and extend across most of the fault core. The orientation of the veins is consistent with a principal shortening direction parallel to the veins and shear along the fault resulting in west-side-down displacement. These inclined veins may be the result of local extension caused by the non-planar boundaries of the fault core. Additional discontinuities in the fault core are thin (<0.3 cm) fractures that contain some calcite, gypsum, or laumontite vein fill and are limited in extent (<1 m long).

On both sides of fault BM2, the boundary between DII and DIII is nearly coincident with the outer edge of a green alteration halo that surrounds the fault core and is likely due to the high concentration of laumontite that has precipitated from fluid flow in the fault core (DI) and into the surrounding area of DII. The discontinuities within DIII along the scanline are thin (<0.2 cm) fractures that contain some calcite or gypsum vein fill and are limited in extent (the majority of these features are <30 cm long). DIV is characterized by relatively coherent host rock and less color alteration than the more

deformed damage-zone domains closer to the fault core. DIV includes open fractures and gypsum (selenite) veins that are oriented perpendicular to bedding.

A.2 Butte Canyon Wash Faults (Listed From South to North): BC1, BC3

A.2.1 Fault BC1

Fault BC1 is vertically segmented and consists of two subvertical planar strike-slip fault segments: segments BC1A (024/81˚E) and BC1B (Figure 5.2). Segment BC1A terminates abruptly at the SS-SH contact, and bedding is intact directly below this termination (Figure 5.2). The SS-SH contact is the most prominent stratigraphic and mechanical boundary within this sedimentary sequence. Approximately one meter to the east of the downdip termination of fault BC1A, the updip termination of segment BC1B is also coincident with the SS-SH contact; bedding is intact directly above this termination (Figure 5.2). Bedding-parallel slip surfaces and recumbent folding are indicative of bedding-parallel slip within SH (Figure 5.2). The geometry and kinematics of faulting at BC1 is described in detail in Chapter 5. There is a zone of faulting and fracturing 12 m to the west of BC1A, with undeformed host rock in between. To the east, the exposure of fault BC1 is truncated by Butte Canyon Wash (Figure 5.2).

Horizontal striae on polished principal slip surfaces within the fault core of segment BC1A indicate purely strike-slip motion. The favored kinematic interpretation (see Chapter 5) is that segments BC1A and BC1B developed as discrete structures (the relatively weak shales appear to have restricted fault propagation) and were linked during failure in a sharp stepover geometry (Figure 5.3A). Geometrical and space constraints require that if the two steeply dipping segments were not continuous when they slipped to accommodate strike-slip motion, the detachment surface(s) within SH must have failed contemporaneously. However, it is difficult to determine the sense of motion or quantify the amount of displacement in the strike-parallel direction.

A.2.2 Fault BC3

Fault BC3 consists primarily of two nonplanar fault segments, BC3A (west) and BC3B (east), with average orientations of 331/88E (west) and 007/68E (east), respectively (Figure 3.9). The region of the fault zone between the fault cores of segments BC3A and BC3B is classified as DII. The fault zone is wider and more complex towards the bottom of the exposure, as BC3B branches into two distinct strands. In contrast, the fault zone is narrower towards the top of the exposure, where the segments appear to begin to coalesce. Clay-rich horizons within units SS1 and SS2 contribute to clay smears along the fault. There are no other faults within 10 m on either side of fault BC3 and therefore there is no deformation attributable to other structures that interferes with the record of damage-zone deformation associated with slip on fault BC3. Undeformed host rock strata are exposed beyond the damage zone on both sides of the fault zone.

Variably oriented striae on a principal slip surface within the fault zone include oblique slip lineations in multiple orientations in addition to purely strike-slip lineations. While it is difficult to determine the sense of motion or quantify the amount of displacement in the strike-parallel direction, the amount of dip-slip displacement is estimated from the stratigraphic correlations. Segment BC3A has accommodated east-side-down normal slip, with a dip separation of 50 cm at the base of unit SS2. Segment BC3B has accommodated east-side-down normal slip, with a dip separation of 41 cm at the base of unit SS3. A prominent fracture to the west of these segments, within DIII, has accommodated 2 cm of east-side-down normal slip, measured at the base of unit SS2. Another prominent fracture to the east of these segments, at the DIII/DIV boundary, has 8 cm of east-side-down normal slip, measured at the base of unit SS3. In total, 101 cm of east-side-down normal slip is observed across the fault zone.

A.3 Blow Sand Wash Faults (Listed From East to West): BS1, BS2

A.3.1 Fault BS1

Fault BS1 is a ~20 m long, oblique-slip, vertical fault zone with a strike of 005˚ (Figure 3.6). The nearest fault to the west (fault BS2) is ~4 m away (Figure 3.6). To the east, the outcrop changes orientation such that the exposure becomes nearly parallel to fault strike and does not allow for a characterization of fault deformation along a fault-perpendicular transect (Figure 3.9). Unit SS5 is coarse grained and poorly sorted and is a distinctive marker unit that can be traced across the faults. Bedding is subhorizontal with cross-bedded bedforms. There is significant variation in grain-size in this stratigraphic interval, but none of the exposed units are clay-rich and no clay smears occur along the fault.

The fault core (DI) of BS1 ranges from ~1–14 cm wide. There are two main, anastomosing principal slip surfaces in the fault core that extend throughout the exposure; the majority of the fault slip has been accommodated along the surface that is located along the eastern edge of DI. The fault core predominantly consists of a distinctive, thick laumontite vein. This vein varies in thickness from 0–7 cm and is mesoscopically varicolored and foliated, indicating multiple generations of laumontite cementation. It is difficult to differentiate between laumontite-cemented veins and cataclastic deformation bands based on field observations, although microstructural analysis shows that they occur in close spatial association. Variably oriented striae on a principal slip surface within the fault core of fault BS1 include both horizontal lineations that indicate purely strike-slip motion and oblique slip lineations. It is difficult to determine the sense of motion or quantify the amount of displacement in the strike-parallel direction of fault BS1. The dip-slip displacement is east-side-down, with a dip-slip separation at the base of unit SS5 of 1.4 m.

The damage zone of fault BS1 includes open fractures, laumontite veins, calcite veins, gypsum veins, and microfractures. DII is characterized by a high density of laumontite veins that have precipitated from fluid flow in the fault core (DI) and the surrounding

area of DII. These fractures range from 0.3–2 cm in width and 10 cm–2.5 m in length, are nonplanar, and tend to intersect each other, forming an interconnected network of laumontite veins that extend outside of the fault core. The boundary between DII and DIII is defined by an abrupt decrease in the density of laumontite veins with distance from the fault core. DIII is characterized by a significantly lower density of deformation than in adjacent DII, and contains open fractures and laumontite and calcite veins that range in thickness from 0.1–0.3 cm with a regular average spacing of ~50 cm. The veins in DIII are generally longer (>3 m) than in DII.

The boundary between DIII and DIV is defined by an abrupt decrease in the density of laumontite veins with distance from the fault core; DIV is characterized by relatively coherent host rock with fewer discontinuities per cm than is observed in adjacent DIII. The predominant deformation features in DIV are open fractures, although a few laumontite veins are also observed. Very thin gypsum (selenite) veins occur on the west side of the fault in all damage-zone domains. There are no exposed selenite veins on the east side of the fault, although the exposure on the east side of the fault is limited due to the change in orientation of the outcrop. It is difficult to determine whether the level of deformation in DIV approaches or is equivalent to background levels of deformation due to the change in orientation of the outcrop on the east side of the fault and the close proximity of fault BS1 on the west side of the fault.

A.3.2 Fault BS2

Fault BS2 is a steeply dipping fault zone (350˚/85˚E) (Figure 3.9). The nearest fault to the east (fault BS1) is ~4 m away (Figure 3.6). There are two main, anastomosing principal slip surfaces in the fault core that extend throughout the exposure; the core branches into two parts in the center of the outcrop. The fault core is filled with a thick laumontite vein, similar to the fault core of BS1. Variably oriented striae on a principal slip surface within the fault zone include horizontal lineations that resulted from purely strike-slip motion and oblique slip lineations. However, it is difficult to determine the sense of motion or quantify the amount of displacement in the strike-parallel direction.

The dip-slip displacement is east-side-down, with a dip-slip separation at the base of unit SS5 of 0.2 m. The damage zone of fault BS1 includes open fractures, laumontite veins, calcite veins, gypsum veins, and microfractures, similar to the deformation features observed in the fault core.

Appendix B Domain Characterizations

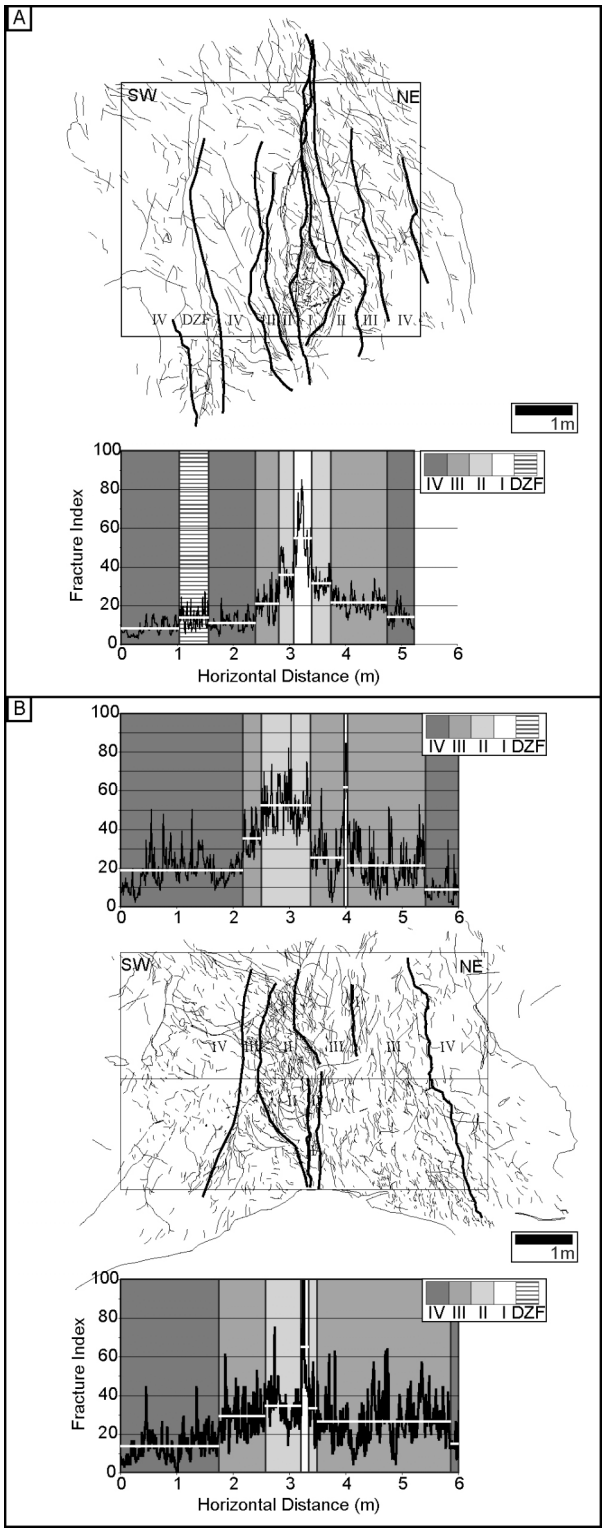

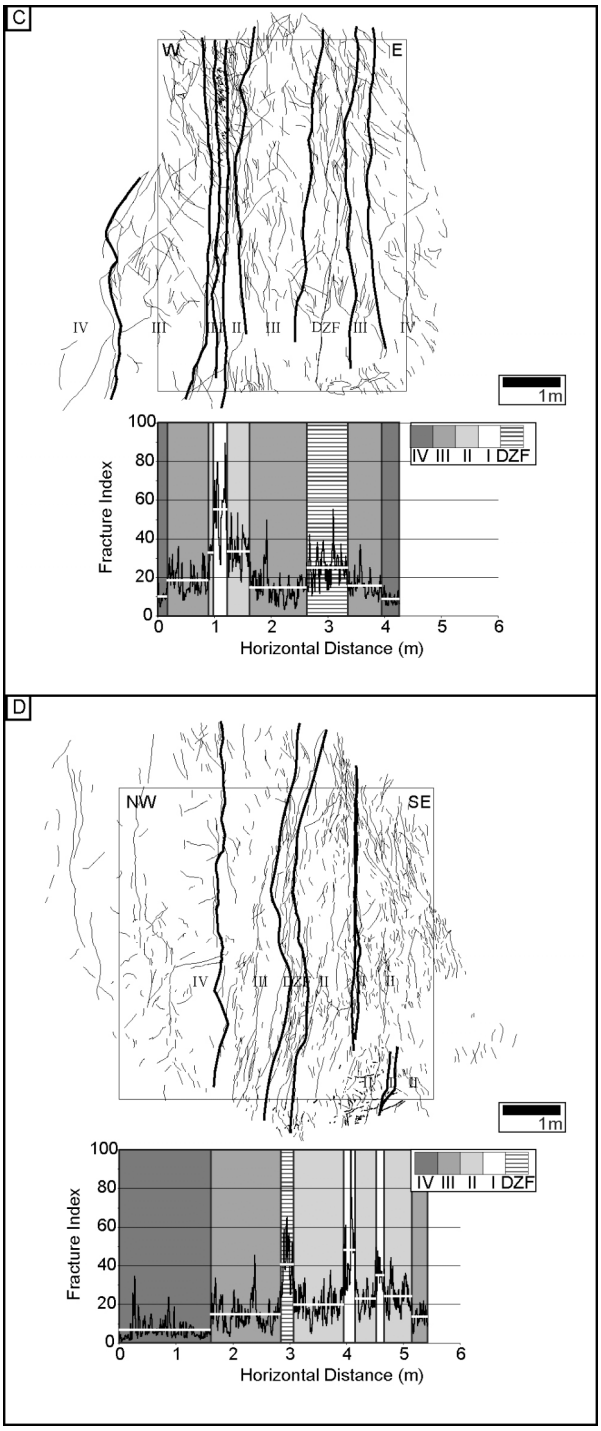
C
W
E
IV
III
II
III
DZF
III
IV
1m
IV III II I DZF
Fracture Index
100
80
60
40
20
0
0 1 2 3 4 5 6
Horizontal Distance (m)
D
NW
SE
IV
III
DZF
II
1m
IV III II I DZF
Fracture Index
100
80
60
40
20
0
0 1 2 3 4 5 6
Horizontal Distance (m)

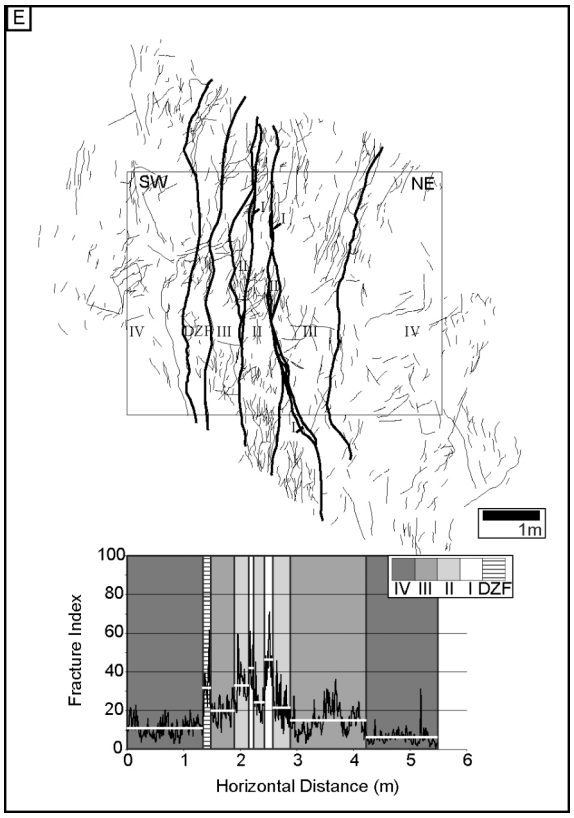
E
SW
NE
IV
DZF
III
II
I
1m
Fracture Index
100
80
60
40
20
0
0
1
2
3
4
5
6
Horizontal Distance (m)
IV III II I DZF

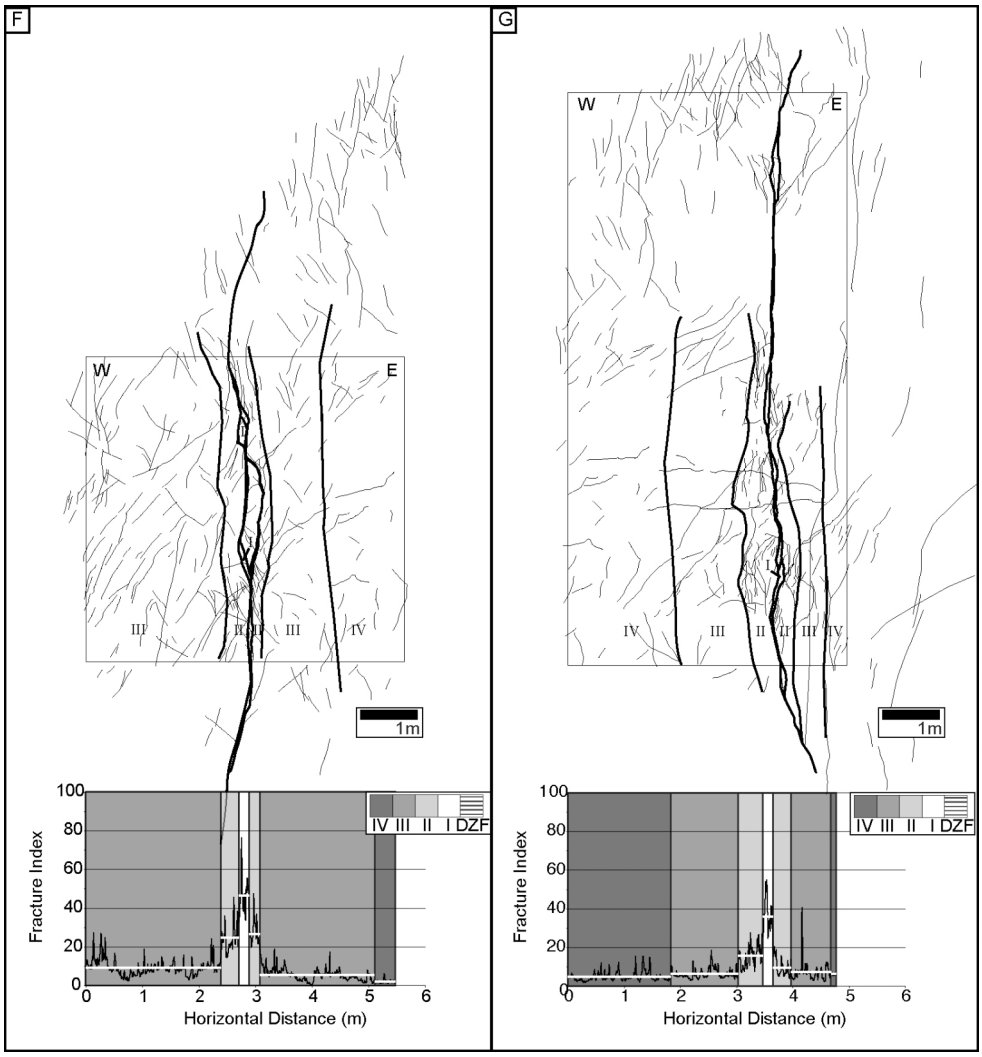

Figure B.1. Binary digitized deformation maps for faults (A) BM1, (B) BM3, (C) BM2, (D) BC1, (E) BC3, (F) BS1, and (G) BS2 are rotated such the principal slip surfaces are parallel to a vertical reference line. The average deformation density profile plots (black line graphs) were generated using the image analysis software ImageJ64. The x-axes represent the horizontal distance through the fault zones (m) and y-axes represent the vertically averaged pixel intensity (mean of all binary values) sampled in parallel 0.45 cm wide vertical columns across each fault zone. White horizontal bars indicate the mean fracture index value for each domain; domains are indicated with shades of gray.

Appendix C Microstructural Data From Selected Faults

C.1 Fault BM1 Microstructures

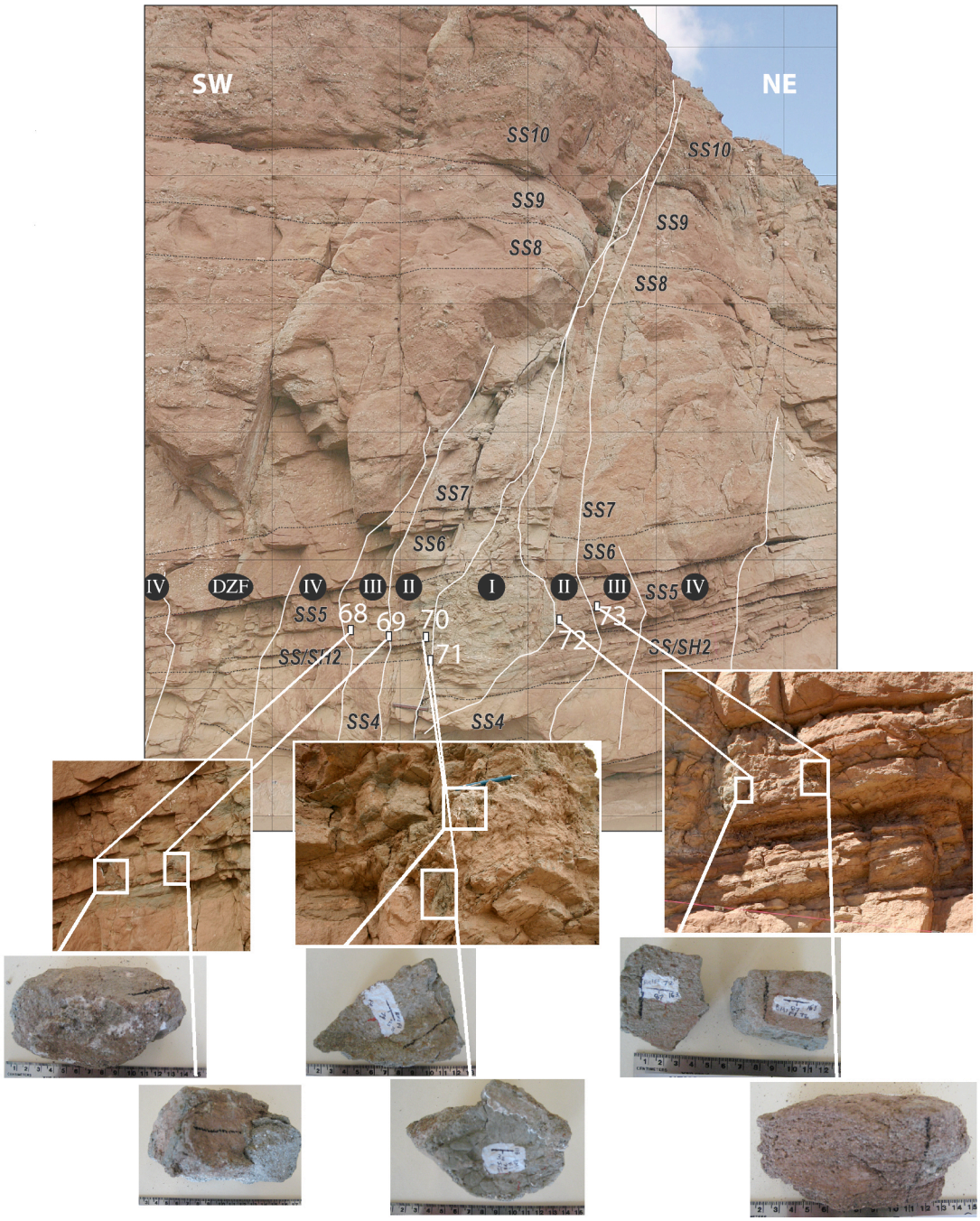

Figure C.1.1. Sample distribution for fault BM1.

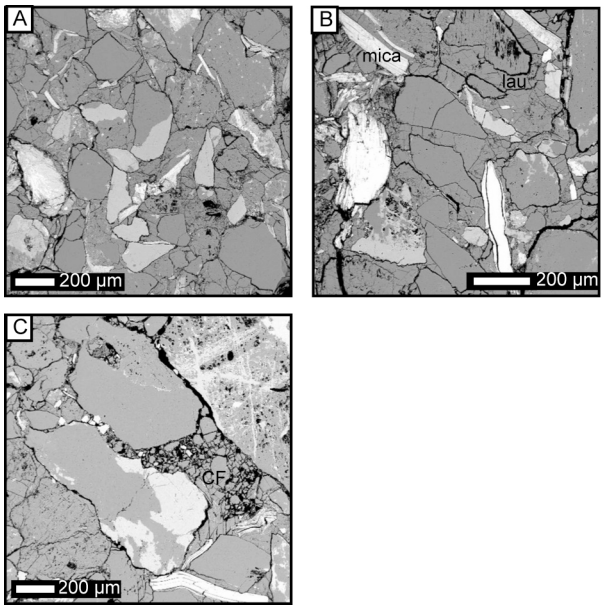

Figure C.1.2. Fault BM1, DIII, unit SS5, Sample #68. (A) Host rock contains laumontite cement and partially dissolved feldspars. (B) Detrital grains in host rock are rarely in contact due to pervasive laumontite cement (*lau*); some microfracturing of detrital grains; plagioclase dissolution is concentrated in Na-rich regions. (C) Cataclastic fault rock (*CF*) is confined to an isolated region.

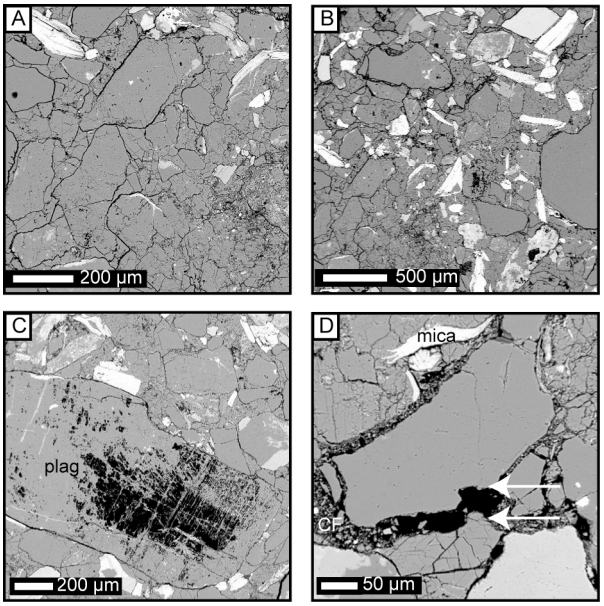

Figure C.1.3. Fault BM1, DIII, unit SS5, Sample #69. (A) Host rock contains pervasive laumontite cement, intact detrital grains, and partially dissolved feldspars. (B) Due to the high contrast in this image, micas in host rock appear as white. (C) Detail of partially dissolved feldspar (*plag*). (D) Laumontite cement and detrital grain, previously attached, have been separated (white arrows) and cataclastic fault rock (*CF*) has flowed in between.

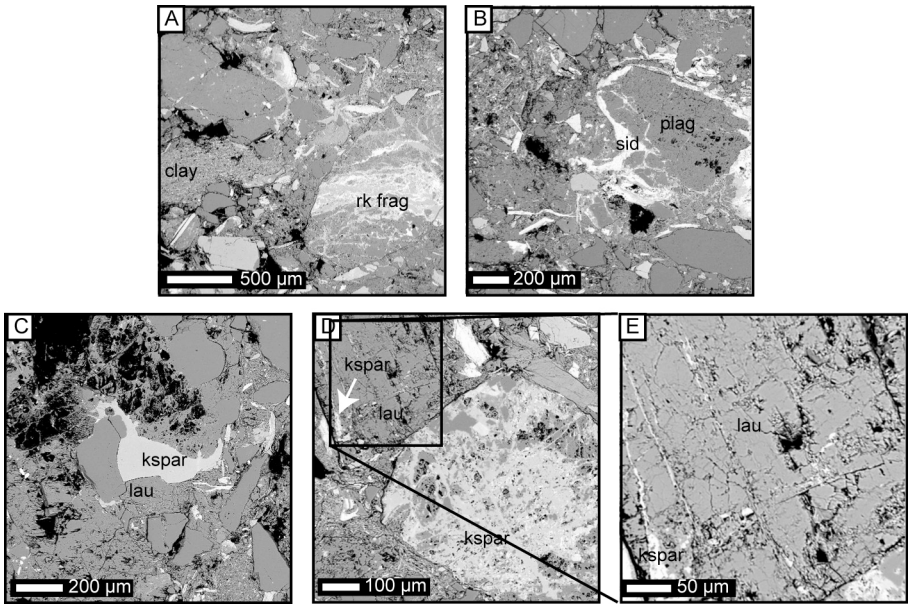

Figure C.1.4. Fault BM1, DII, unit SS5, Sample #70. (A) Host rock is poorly sorted, contains abundant rock fragments (*rk frag*) and detrital clay. (B) Dissolved feldspars (*plag*) and patchy siderite cement (*sid*). (C) Nearly complete dissolution of plagioclase with remnant dissolution pathways. (D) Dissolved feldspar filled with laumontite (*lau*), streaks of k-feldspar (*kspar*) remain; adjacent feldspar is dominantly k-feldspar and mostly undissolved. (E) Detail of laumontite within dissolved plagioclase; streaks of k-feldspar remain.

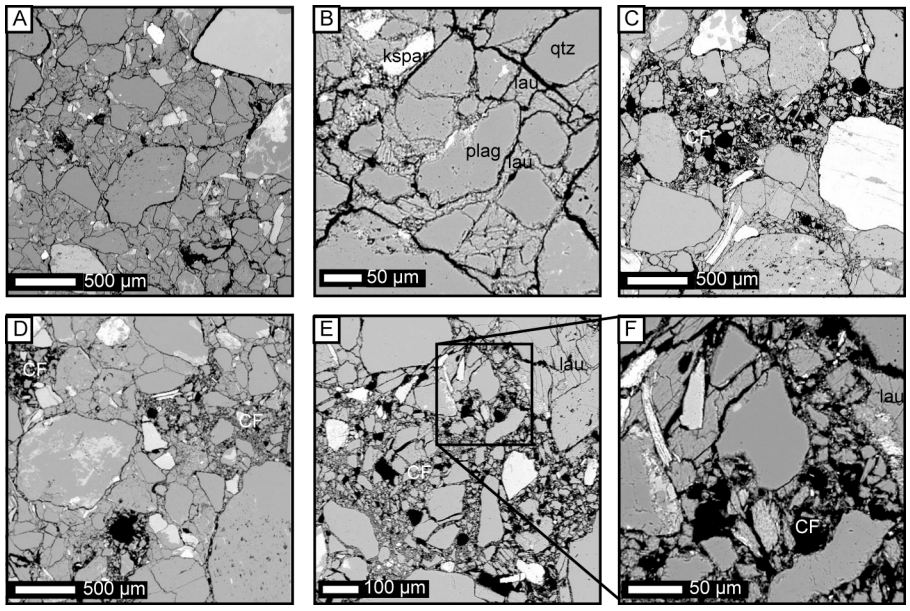

Figure C.1.5. Fault BM1, DI, units SS4+ SS/SH2, Sample #71. (A) Host rock contains laumontite cement (*lau*) and minor feldspar dissolution; *kspar*, k-feldspar; *plag*, plagioclase; *qtz*, quartz. (B) Detail of host rock. (C) Tabular region of cataclastic fault rock (*CF*). (D) Cataclastic fault rock occurs in spots, these may be tabular regions perpendicular to the image. Detail of high-porosity cataclastic fault rock. (F) Cataclastic fault rock contains fragmented laumontite and detrital grains.

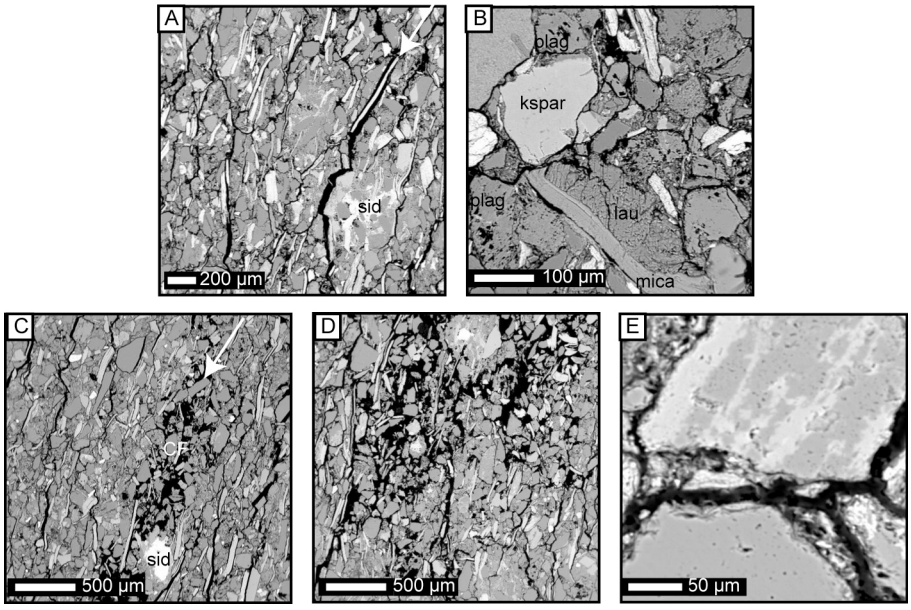

Figure C.1.6. Fault BM1, DII, unit SS5, Sample #72. (A) Host rock is particularly foliated with well-aligned micas, and contains laumontite and some siderite cement (*sid*); minor fracture (arrow) follows grain boundaries. (B) Detail of host rock with some plagioclase dissolution; *lau*, laumontite; *kspar*, k-feldspar; *plag*, plagioclase. (C) Tabular region of dilation and minor cataclasis (*CF*, arrow), this region of dilation is clearly different from the fracture in (A). (D) More evidence of dilation and minor cataclasis. (E) Flaking occurs at the edges of detrital grains.

C.2 Fault BM2 Microstructures

Figure C.2.1. Sample distribution for fault BM2.

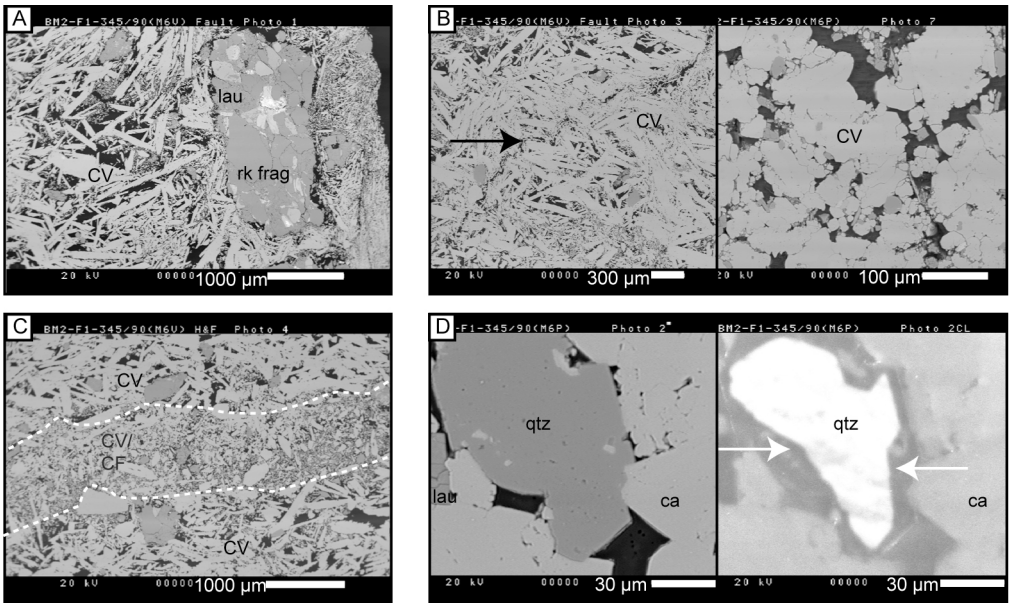

Figure C.2.2. Fault BM2, DI, unit SS5, Sample #53. (A) Thick (3 cm wide) calcite vein (*CV*) contains a laumontite (*lau*)-cemented fragment of host rock (*rk frag*). (B) Two distinct textures of authigenic calcite indicate multiple generations of calcite cementation; a late calcite-filled fracture occurs within the thick calcite vein (black arrow). (C) Cataclastic fault rock (*CF*) within the calcite vein postdates calcite cementation. (D) Quartz grain (*qtz*) surrounded by calcite cement (*ca*); CL image reveals that quartz overgrowth (white arrows) predates the calcite cementation.

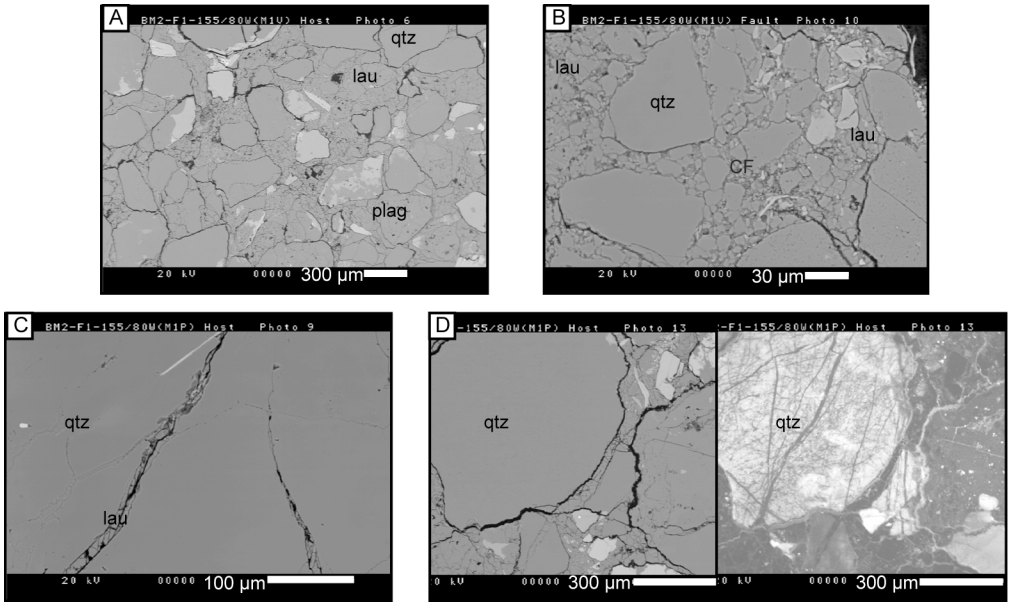

Figure C.2.3. Fault BM2, DI, unit SS6, Sample #54. (A) Poorly sorted host rock contains laumontite cement (*lau*), micas, quartz (*qtz*), abundant feldspars (*plag*), rock fragments, and detrital clay. (B) Cataclastic fault rock (*CF*) with moderate grain size reduction includes broken laumontite, indicates cataclasis postdates at least one phase of laumontite cementation. (C) A late fracture in a detrital quartz grain filled with laumontite. (D) Detrital quartz grain; CL image reveals extensive quartz overgrowth within the grain.

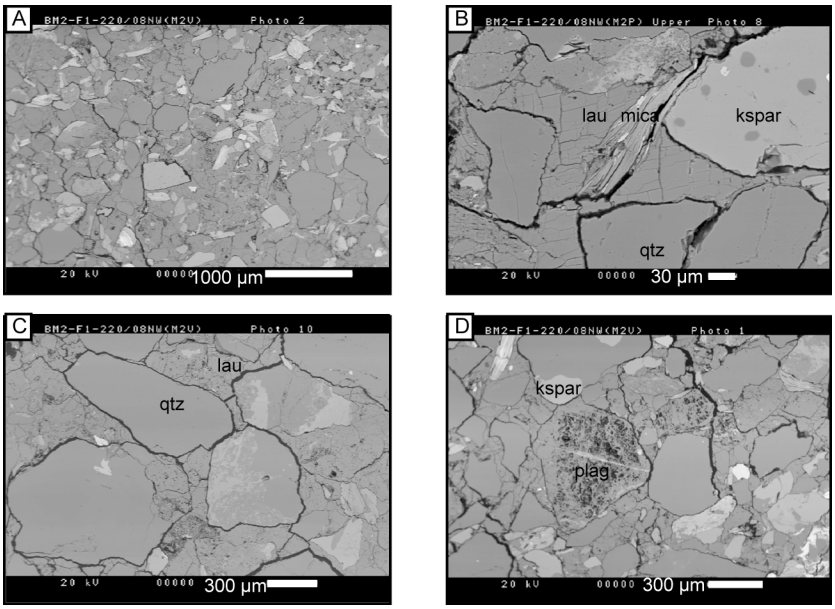

Figure C.2.4. Fault BM2, DIV, unit SS4, Sample #56. (A) Detrital grains in host rock are not in contact due to early stage laumontite cementation. (B), (C) Detail of host rock, detrital grains include quartz (*qtz*), k-feldspar (*kspar*) and mica, and are mostly intact; there is abundant laumontite (*lau*) cement. (D) Some plagioclase (*plag*) dissolution is evident in the host rock.

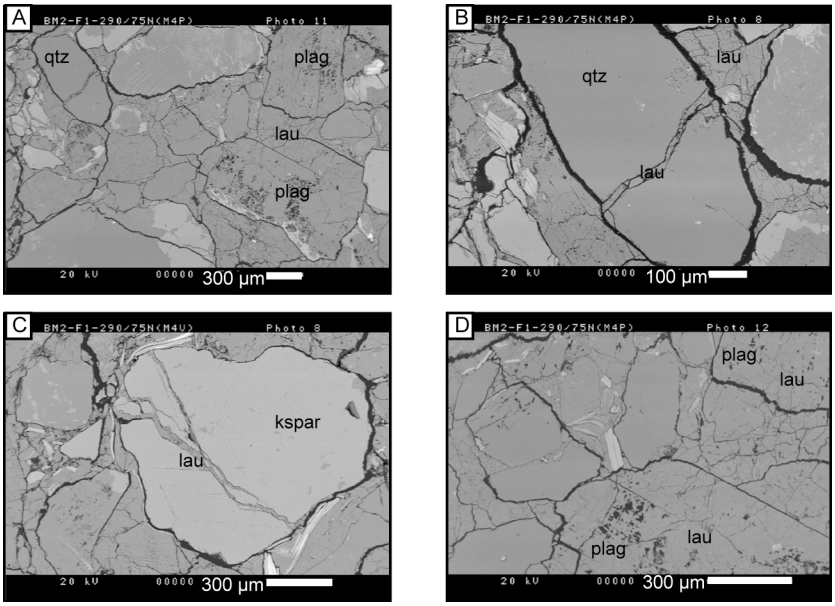

Figure C.2.5. Fault BM2, DIII, unit SS4, Sample #57. (A) Dissolved plagioclase (*plag*) grains retain unaltered primary shapes. (B), (C) Fractures in detrital quartz (*qtz*) and k-feldspar (*kspar*) grains are filled with laumontite (*lau*) cement; these veins were contemporaneous with pervasive intergranular laumontite cementation. (D) Laumontite cement occurs within plagioclase grains.

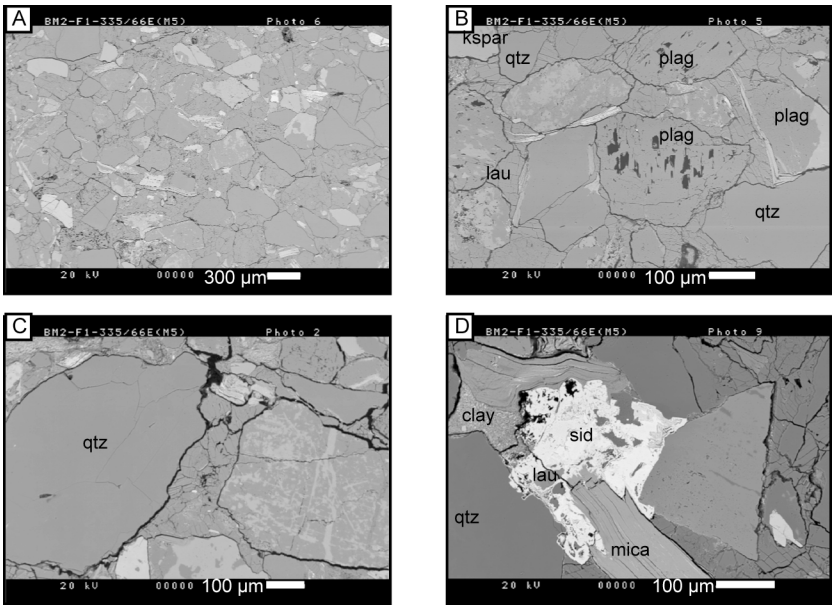

Figure C.2.6. Fault BM2, DIII, unit SS1, Sample #58. (A) Laumontite-cemented host rock. (B) Representative mineralogy includes k-feldspar (*kspar*), laumontite (*lau*), plagioclase (*plag*), and quartz (*qtz*). (C) Detail of host rock with microfractures in detrital grains. (D) Rare siderite cement (*sid*) surrounds laumontite grains and so postdates laumontite cementation.

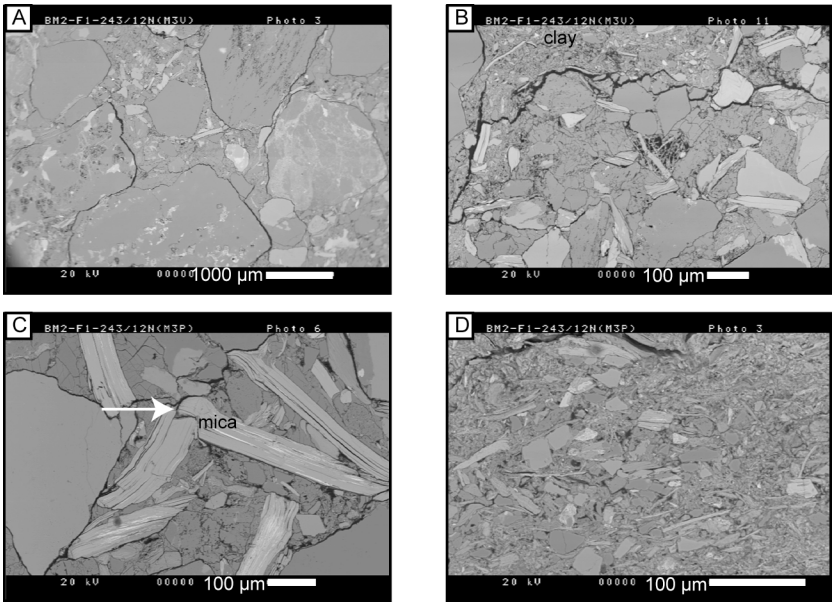

Figure C.2.7. Fault BM2, DZF, unit SS1, Sample #59. (A) Host rock is poorly sorted with grains >2 mm in diameter and a higher clay content than any other sample from this fault, contains dissolved feldspars. (B) Detrital clay within host rock. (C) Bent and broken mica grains (arrow) provide some evidence for mechanical compaction; evidence for compaction is limited due to early pervasive laumontite cementation. (D) The high clay content in this sample may account for the relatively lower proportion of laumontite cement.

C.3 Fault BM3 Microstructures

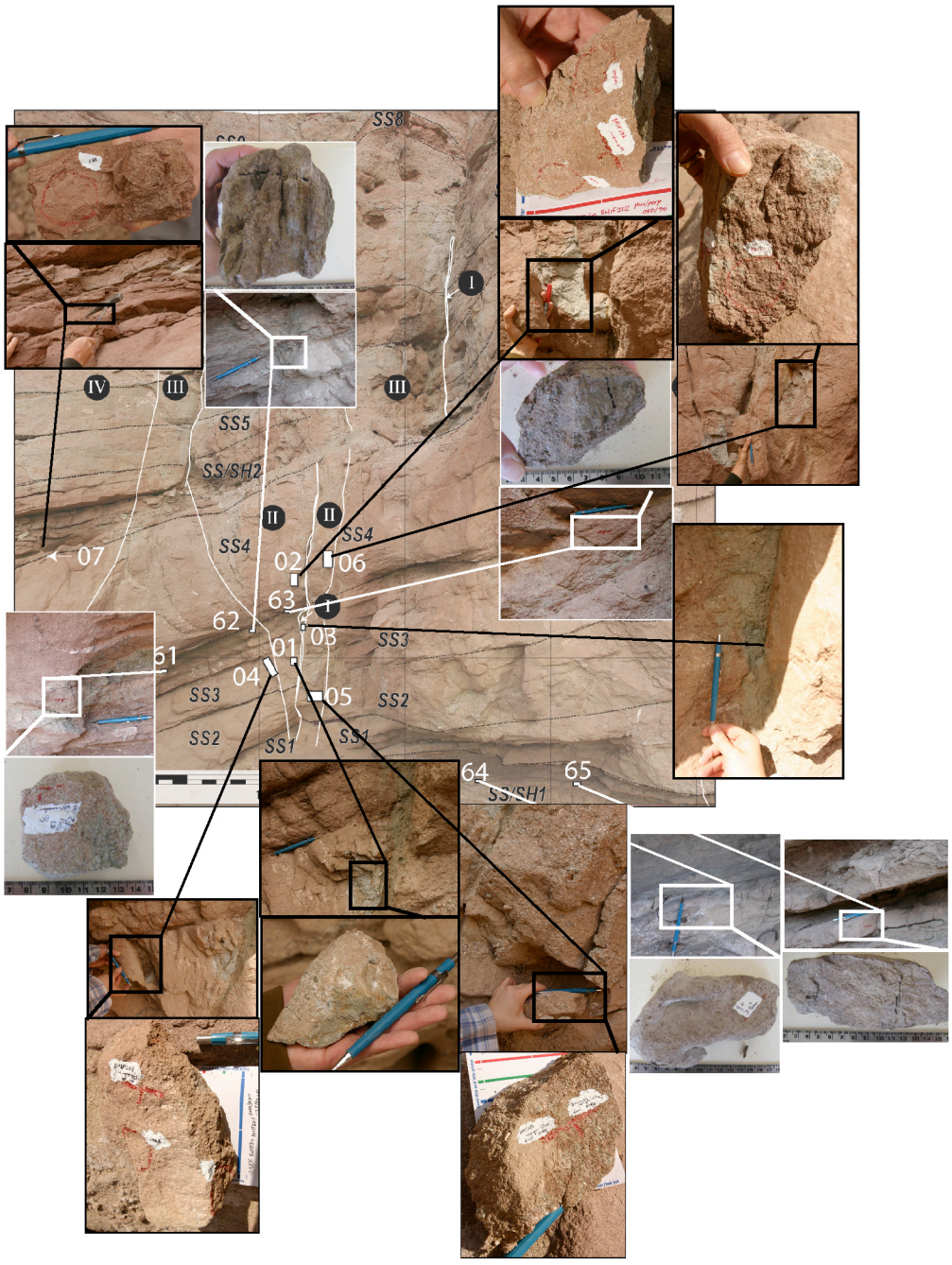

Figure C.3.1. Sample distribution for fault BM3.

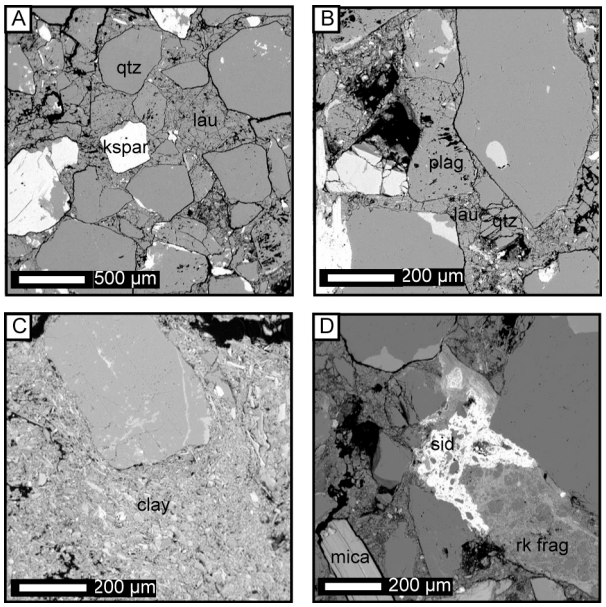

Figure C.3.2. Fault BM3, DIII, unit SS3, Sample #61. (A) Host rock is poorly sorted and contains k-feldspar (*kspar*), laumontite (*lau*) cement, and quartz (*qtz*). (B) Partial plagioclase (*plag*) dissolution and fragmented quartz creates some secondary porosity. (C) Host rock contains substantial detrital clay. (D) Siderite (*sid*) cement postdates laumontite cement as it contains a fragment of laumontite; also note the rock fragment (*rk frag*).

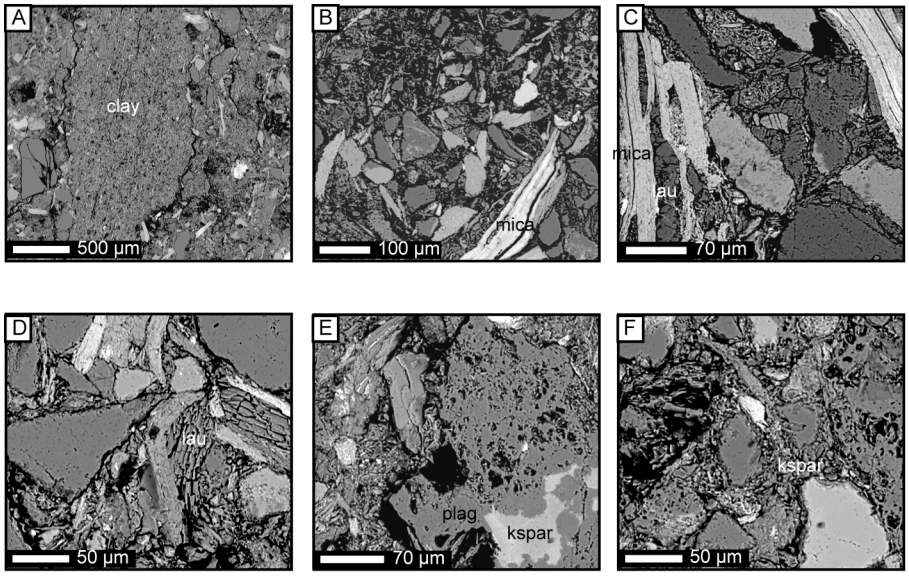

Figure C.3.3. Fault BM3, DIII, unit SS3, Sample #62. (A) Host rock contains detrital clay. (B) Secondary porosity due to feldspar dissolution and fragmentation of laumontite cement. (C) Laumontite (*lau*) cement exploits cleavage planes within a mica grain. (D) Laumontite has a fragmented morphology. (E) Feldspar grains are preferentially dissolved in Na-rich regions; *plag*, plagioclase; *kspar*, k-feldspar. (F) Fragmented laumontite and k-feldspar.

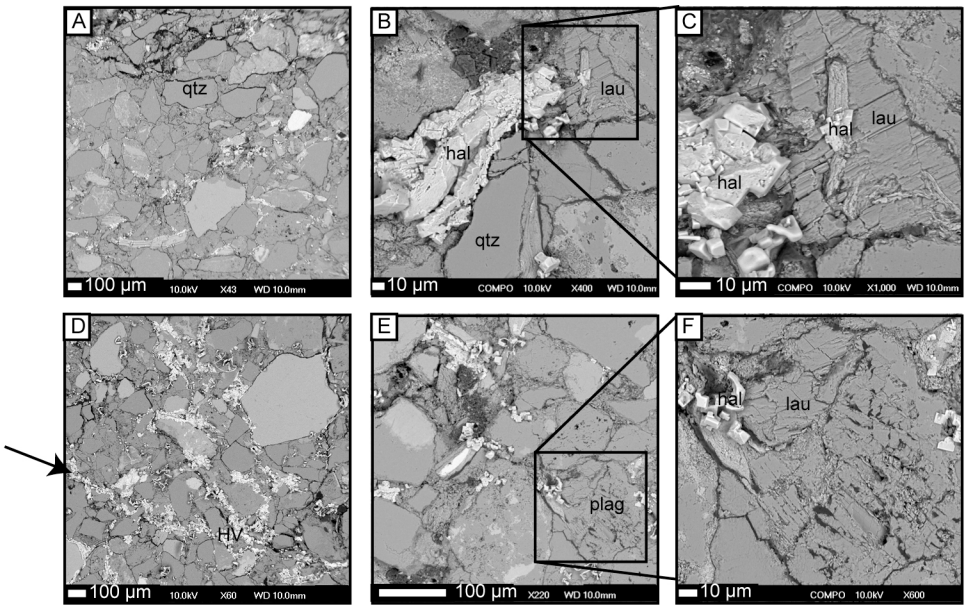

Figure C.3.4. Fault BM3, DII, unit SS3, Sample #63. (A) Host rock contains laumontite (*lau*) cement and halite. (B) Halite (*hal*) appears to grow on top of other minerals and be very late stage, also note fractured quartz (*qtz*). (C) Detail of halite vein (*HV*) and laumontite. (D) Representative image shows the distribution of halite; note the concentration parallel to the black arrow. (E) Plagioclase (*plag*) replaced by laumontite. (F) Detail of laumontite replacing plagioclase with halite growth superimposed.

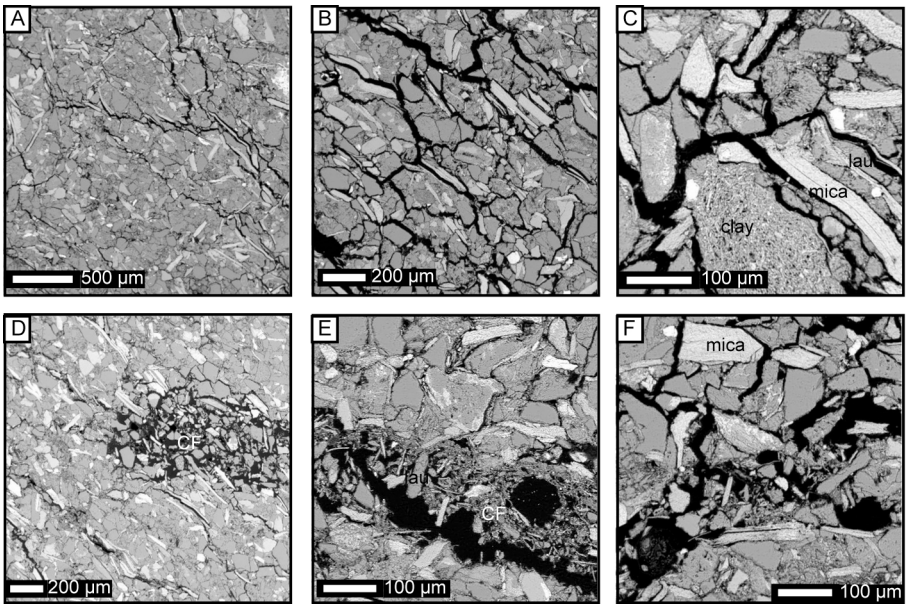

Figure C.3.5. Fault BM3, DIII, unit SS/SH1, Sample #64. (A) Host rock is foliated. (B) Fractures in host rock may be artificial, from sample preparation. (C) Detrital clay (*clay*) in host rock. (D) Epoxy-filled region of dilational cataclastic fault rock (*CF*) is different in character from fractures in A–C. (E) Cataclastic fault rock contains laumontite (*lau*) and is also dilatant. (F) High secondary porosity within cataclastic fault rock.

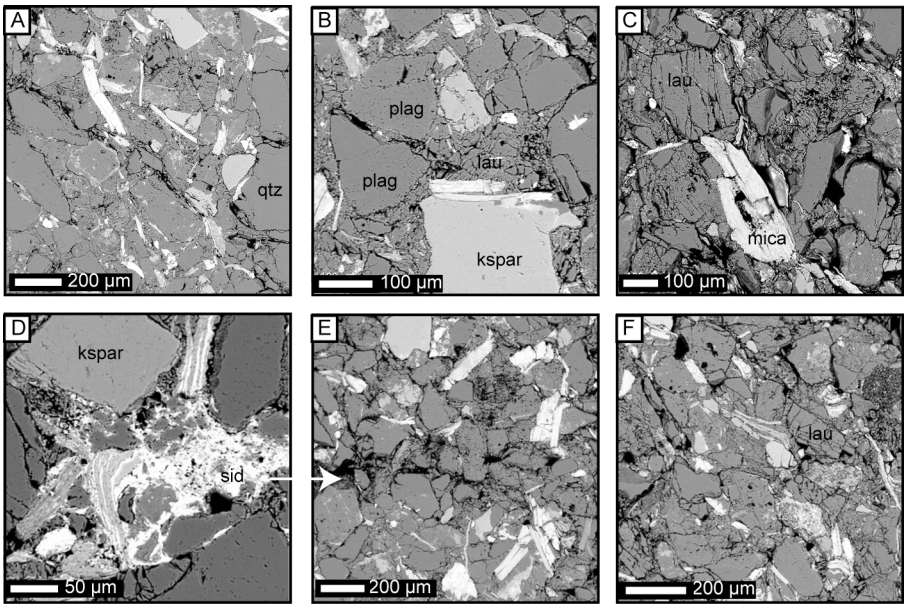

Figure C.3.6. Fault BM3, DIII, unit SS/SH1, Sample #65. (A) Host rock is foliated; *qtz*, quartz. (B) Minor plagioclase (*plag*) dissolution, extensive laumontite (*lau*) cement; *kspar*, k-feldspar. (C) Detrital plagioclase grain completely replaced by laumontite. (D) Patchy siderite (*sid*) cement. (E) Plagioclase dissolution is concentrated along tabular zones (arrow). (F) Fragmentation is common within regions of concentrated plagioclase dissolution.

C.4 Fault BC1 Microstructures

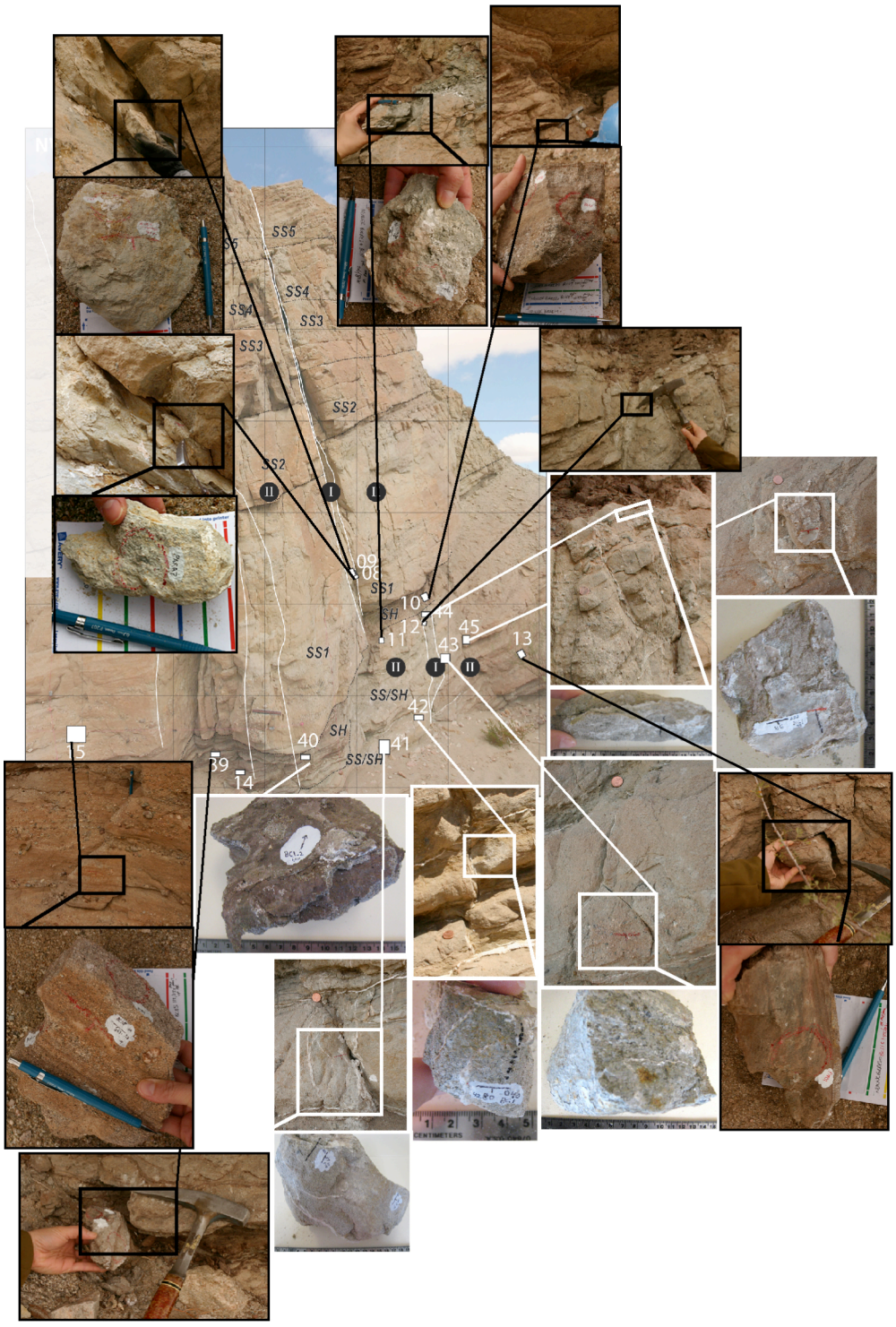

Figure C.4.1. Sample distribution for fault BC1.

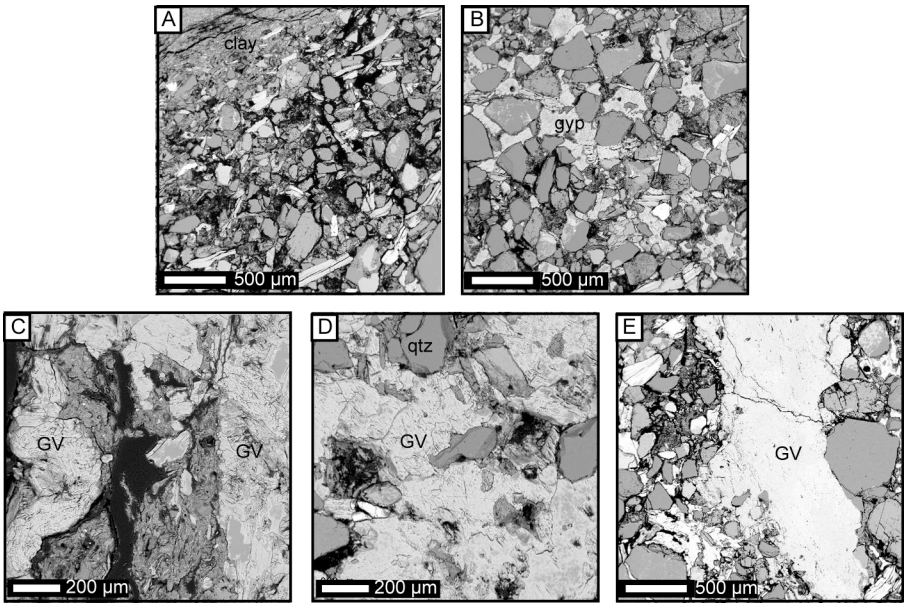

Figure C.4.2. Fault BC1, DII, unit SH, Sample #40. (A) Host rock contains clay-rich layers, many dissolved feldspars, minor laumontite cement. (B) Host rock with patchy gypsum (*gyp*) cement. (C) Multiple parallel gypsum veins (*GV*). (D) Detail of fractured detrital quartz (*qtz*) grains within gypsum vein. (E) Gypsum vein, parallel to cataclastic fault rock, seeps into adjacent host rock.

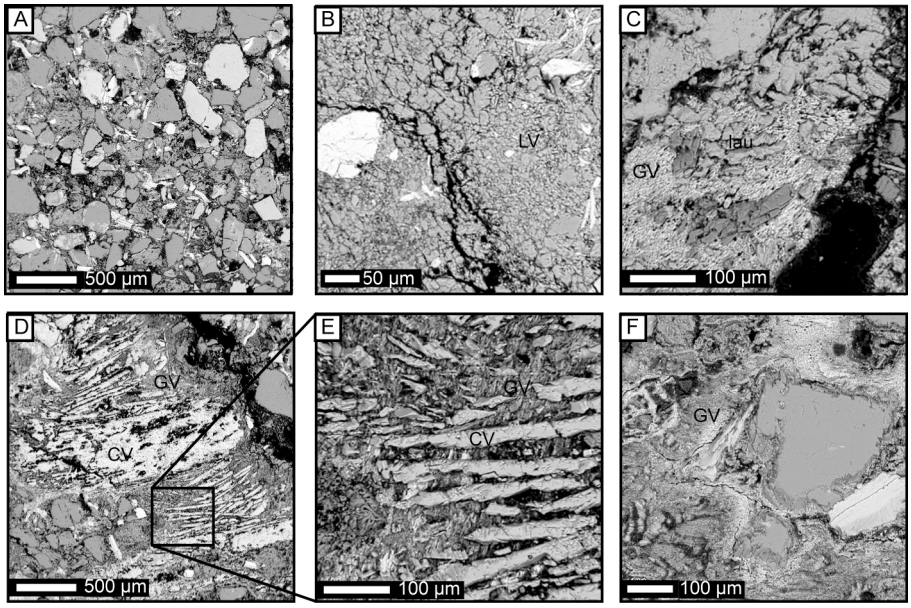

Figure C.4.3. Fault BC1, DII, unit SS/SH, Sample #41. (A) Host rock. (B) Laumontite vein (*LV*) contains a late fracture. (C) Laumontite (*lau*) fragments within gypsum vein (*GV*). (D) Prismatic calcite vein material (*CV*) within gypsum vein. (E) Detail of calcite entrained within gypsum. (F) Flow fabric preserved within gypsum vein.

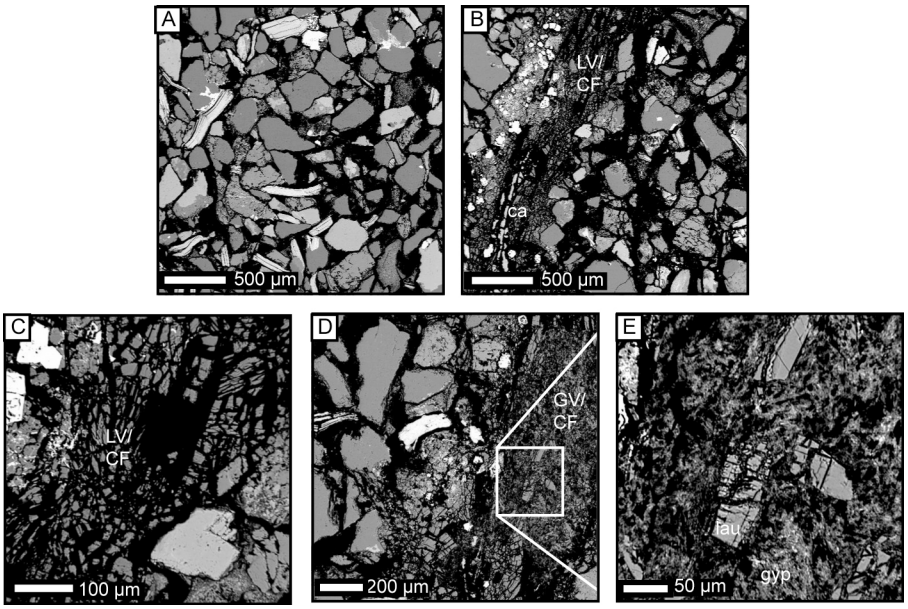

Figure C.4.4. Fault BC1, DII, unit SS/SH, Sample #42. (A) Host rock is porous with many dissolved feldspars. (B) Faulted laumontite (*LV/CF*) and calcite (*ca*) vein is porous and highly fractured. Adjacent host rock is porous and fractured. (C) Detail of faulted laumontite vein. (D) Faulted gypsum vein (*GV/CF*) and adjacent host rock. (E) Laumontite (*lau*) entrained in fault rock that contains gypsum (*gyp*).

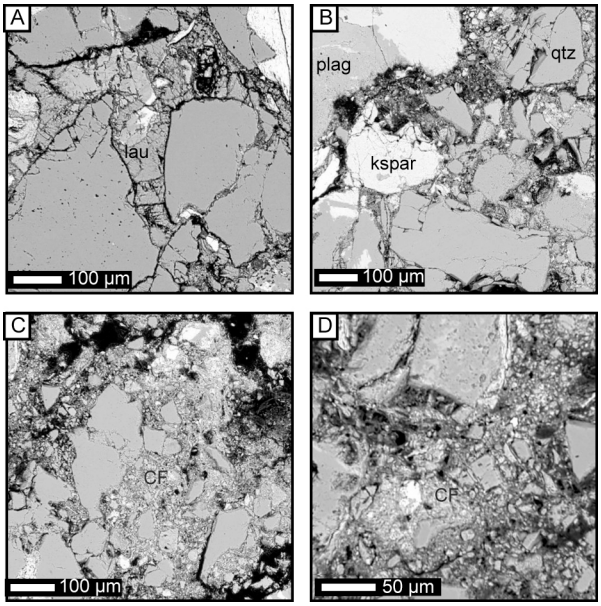

Figure C.4.5. Fault BC1, DII, unit SS/SH, Sample #43. (A) Host rock with intergranular laumontite (*lau*) cement. (B) Cataclastic fault rock with fractured detrital k-feldspar (*kspar*), plagioclase (*plag*), and quartz (*qtz*) grains. (C) Cataclastic fault rock (*CF*). (D) Detail of cataclastic fault rock.

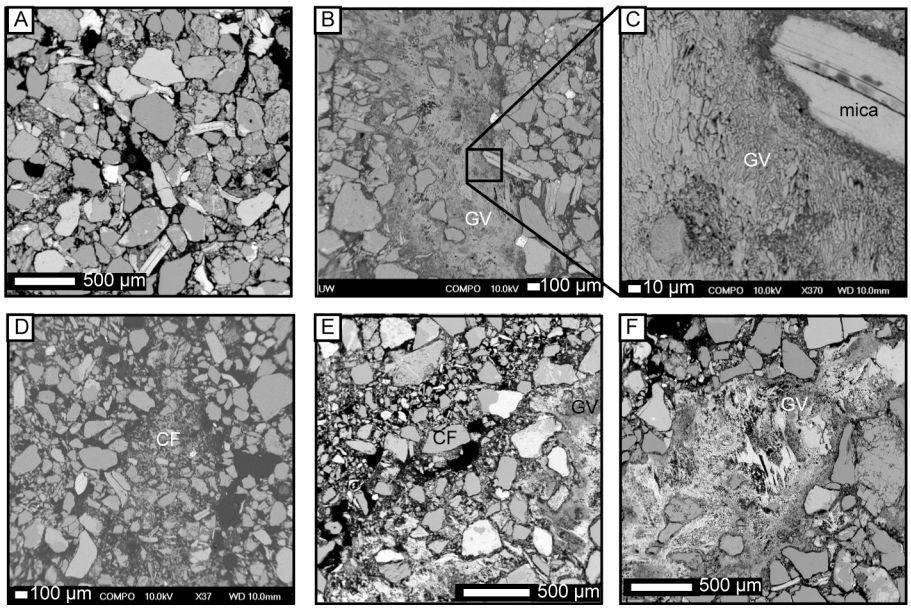

Figure C.4.6. Fault BC1, DI, unit SS/SH, Sample #44. (A) Host rock. (B) Gypsum vein (*GV*) with adjacent host rock. (C) Detail of gypsum vein. (D) Cataclastic fault rock (*CF*), adjacent host rock has increased porosity. (E) Gypsum vein is adjacent to cataclastic fault rock.

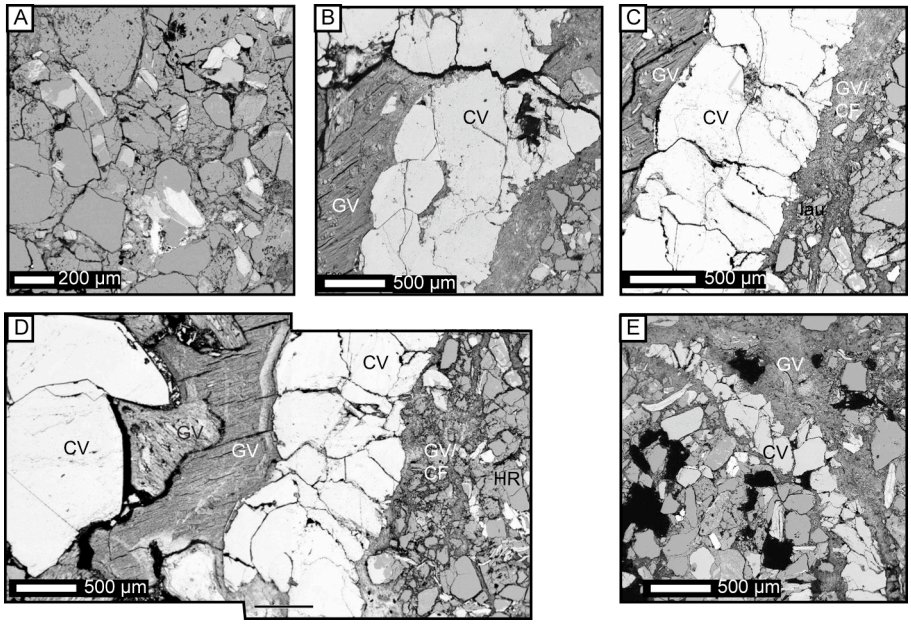

Figure C.4.7. Fault BC1, DII, unit SS/SH, Sample #45. (A) Host rock with pervasive laumontite cement. (B) Parallel calcite vein (*CV*), gypsum vein (*GV*) and faulted gypsum vein; calcite fragment is entrained in gypsum vein. (C) Laumontite (*lau*) is entrained within faulted gypsum vein (*GV/CF*). (D) Calcite veins, gypsum veins and faulted gypsum vein are parallel; host rock (*HR*) at far right. Different generations of gypsum cement recorded in variable growth textures. (E) Thin calcite vein parallel to gypsum vein.

C.5 Fault BC3 Microstructures

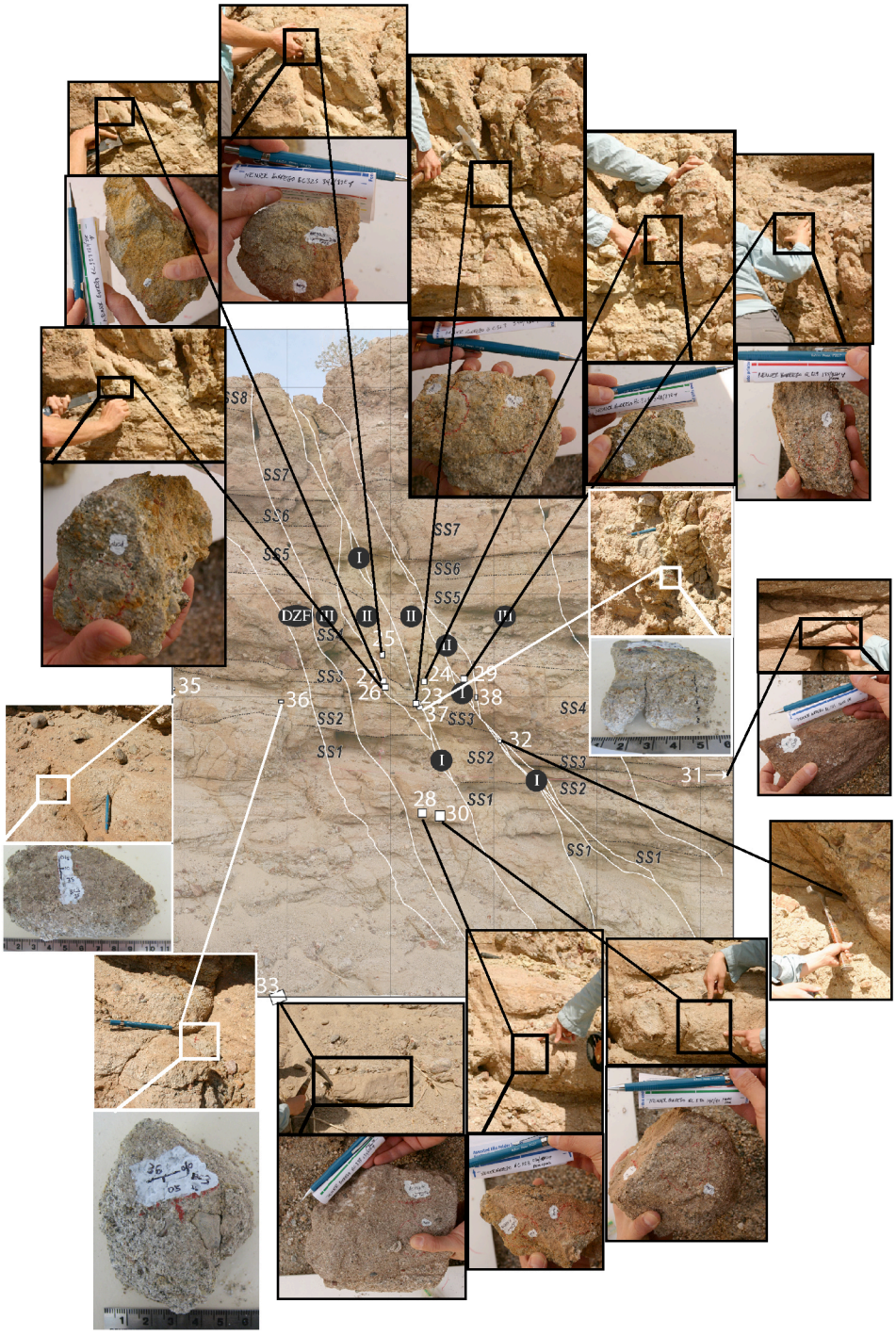

Figure C.5.1. Sample distribution for fault BC3.

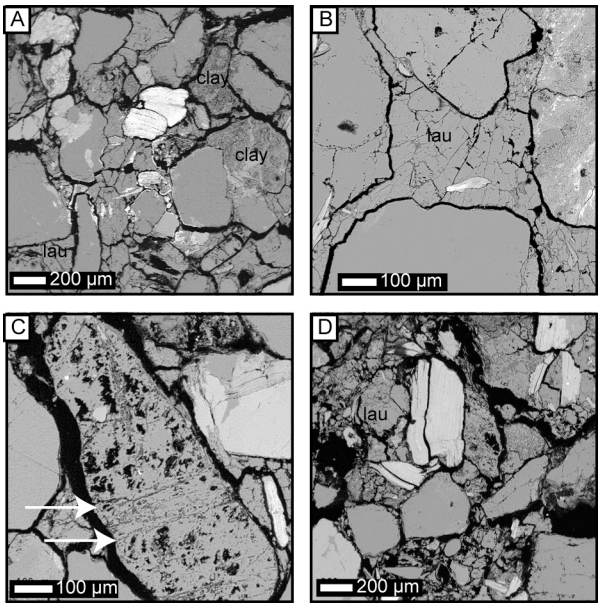

Figure C.5.2. Fault BC3, DIV, unit SS2, Sample #35. (A) Host rock contains laumontite (*lau*) cement and a high proportion of detrital clay. (B) Close-up of host rock with detail of laumontite cement and detrital grains, some with microfractures, others unfractured. (C) Dissolved feldspar with remnant dissolution pathways (white arrows). (D) A spatially limited region of cataclastic fault rock with higher porosity.

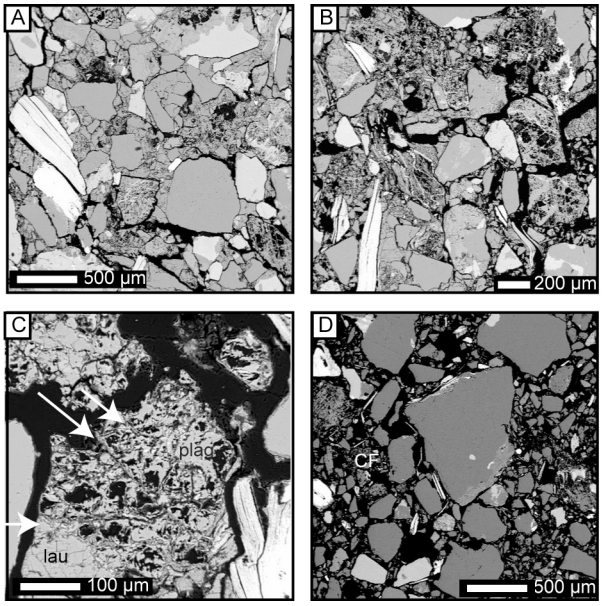

Figure C.5.3. Fault BC3, DIII, unit SS2, Sample #36. (A) Host rock contains laumontite cement, intact detrital grains, and dissolved feldspars. (B) An abundance of dissolved feldspars. (C) Laumontite (*lau*) in dissolved plagioclase (*plag*) with preserved dissolution pathways (white arrows). (D) Tabular regions of cataclastic fault rock (*CF*) with higher porosity.

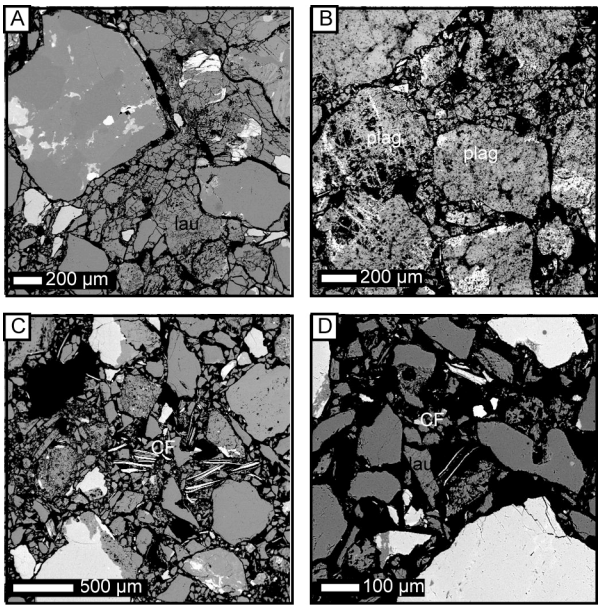

Figure C.5.4. Fault BC3, DII, unit SS3, Sample #37. (A) Relatively intact detrital grains surrounded by fractured laumontite (*lau*) cement and dissolved detrital feldspars. (B) Highly fractured laumontite cement and dissolved detrital plagioclase (*plag*) grains. (C) Higher-porosity cataclastic fault rock (*CF*) contains includes fragmented laumontite cement. (D) Close-up of fault rock.

C.6 Fault BS1 Microstructures

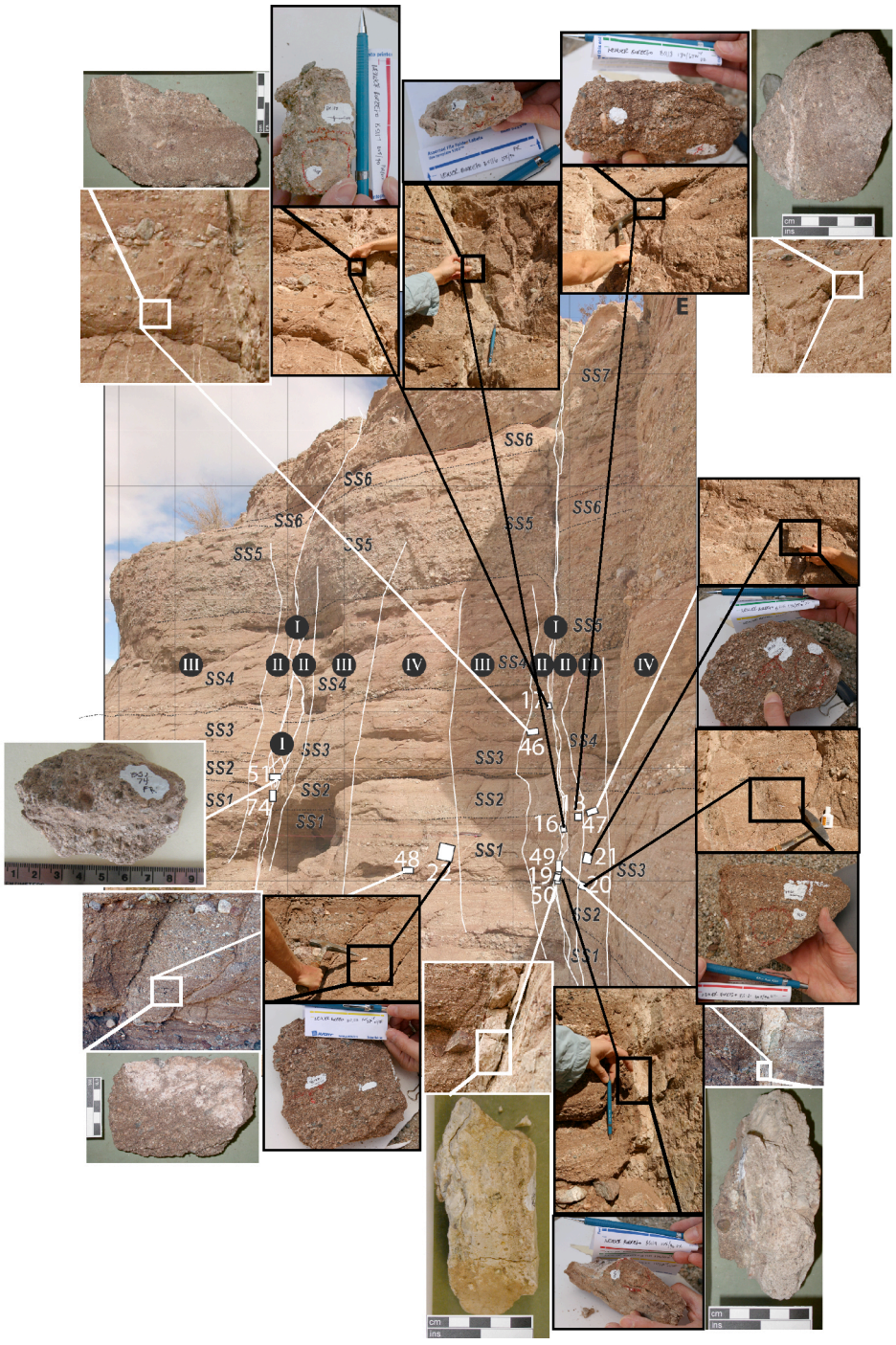

Figure C.6.1. Sample distribution for faults BS1 and BS2.

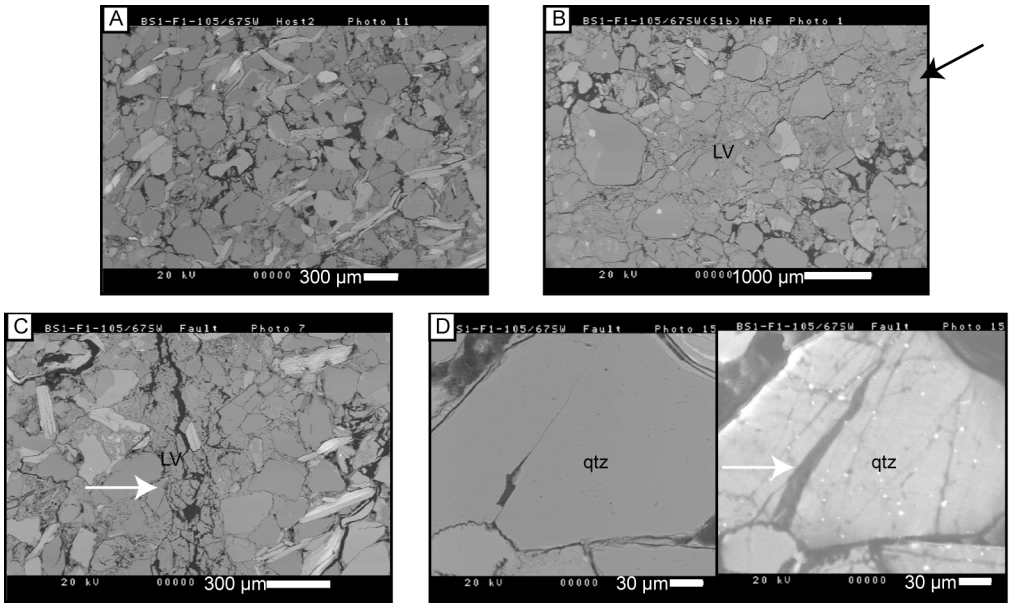

Figure C.6.2. Fault BS1, DII, unit SS3, Sample #46. (A) Aligned micas in the host rock indicate some mechanical compaction predated laumontite cementation. (B) Laumontite vein (*LV*, black arrow) surrounded by relatively porous host rock. (C) Small fractures within a narrow laumontite vein (arrow) indicate some reactivation post-cementation. (D) Quartz (*qtz*) grain with a clay rim and a late-stage partially open microfracture; CL image reveals more extensive fracturing within the quartz grain and quartz overgrowth development (white arrow).

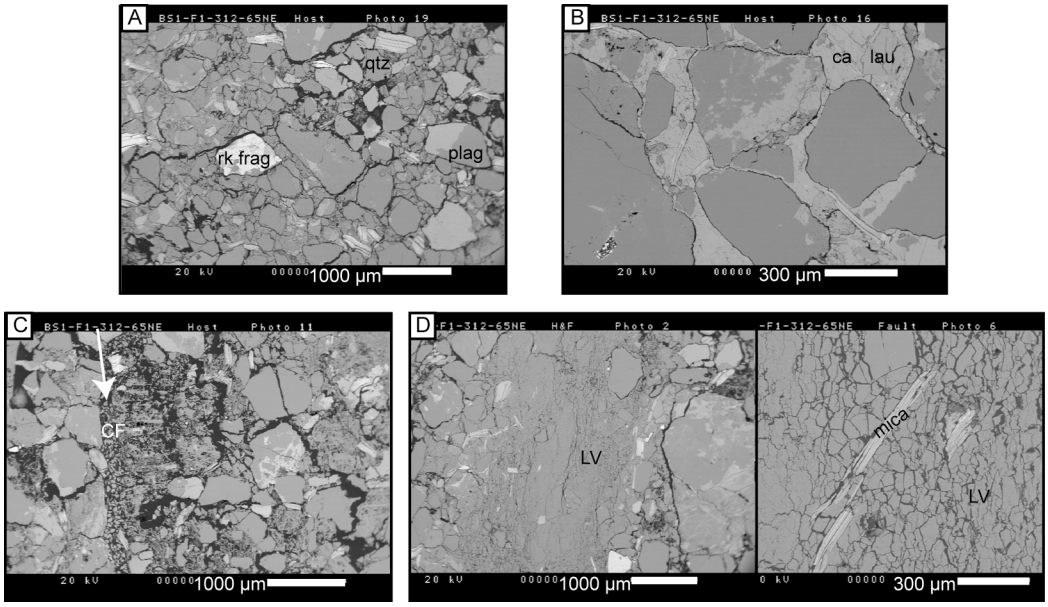

Figure C.6.3. Fault BS1, DIII, unit SS3, Sample #47. (A) Host rock contains plagioclase (*plag*), quartz (*qtz*), and rock fragments (*rk frag*). (B) Calcite (*ca*) cement contains laumontite (*lau*) fragment and postdates at least one phase of laumontite cementation. (C) Narrow band of cataclastic fault rock (*CF*, white arrow). (D) Thick (~2 mm) laumontite vein (*LV*) has a generally homogenous, blocky texture; close-up of detrital grains entrained in vein.

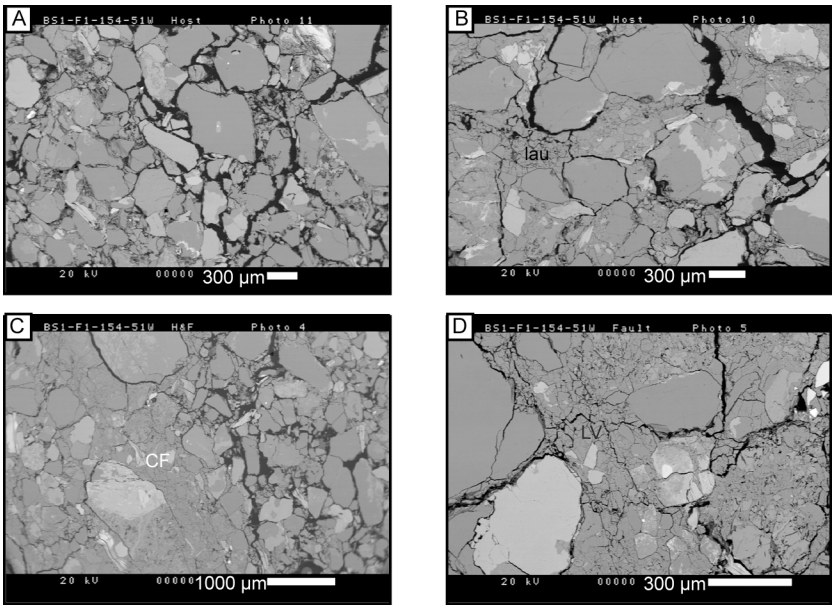

Figure C.6.4. Fault BS1, DIV, unit SS1, Sample #48. (A) Host rock with relatively little laumontite cement. (B) Host rock with higher proportion of laumontite (*lau*) cement. (C) Host rock adjacent to cataclastic fault rock (*CF*) is more porous than the rest of the host, indicating fault-related dilation. (D) Detail of fault rock.

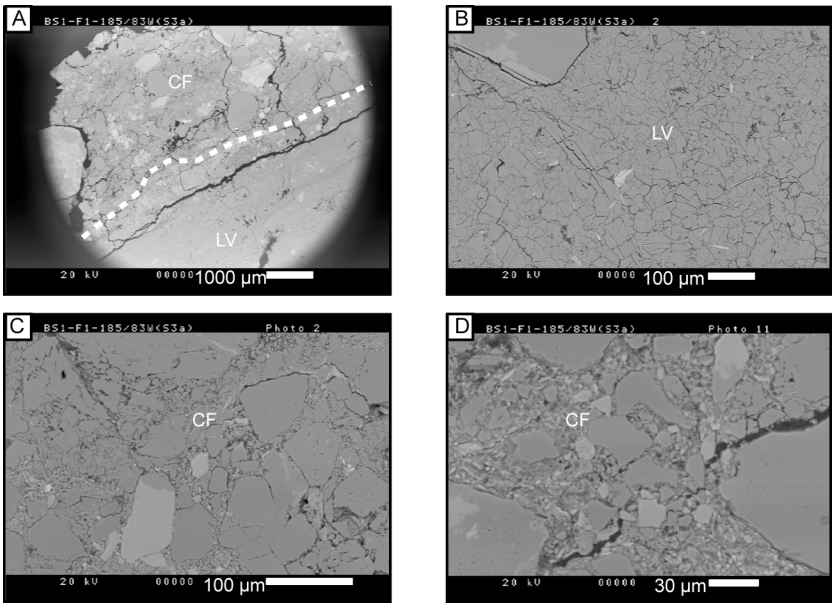

Figure C.6.5. Fault BS1, DI, Sample #49. (A) Cataclastic fault rock (*CF*) (>2.5 mm thick); a laumontite vein (*LV*) was formed along this fault and provides evidence of post-deformation dilation. A transitional zone where fragments of the fault rock have been incorporated into the vein separates the fault rock and laumontite vein. (B) Detail of laumontite vein; the crystal structure in the vein is intact, evidence that dilation and laumontite vein fill postdates the cataclasis. (C), (D) Detail of cataclastic fault rock.

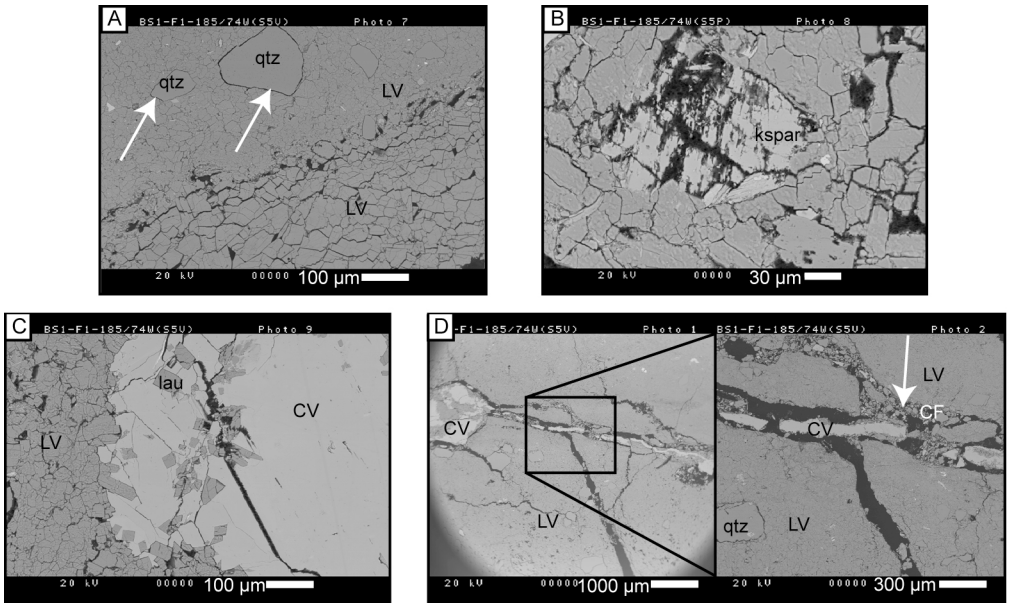

Figure C.6.6. Fault BS1, DI, Sample #50. (A) A thick laumontite vein (*LV*) has two distinct textures (indicating >1 cementation event) and entrained detrital quartz grains (*qtz*, white arrows). (B) Dissolved detrital feldspar surrounded by laumontite cement; k-feldspar (*kspar*) remains. (C) Fragments of laumontite (*lau*) within patchy calcite vein (*CV*) cement indicate calcite cementation postdates laumontite cement. (D) Late-stage fracture in laumontite vein is partially filled with calcite cement; cataclastic fault rock (*CF*, white arrow); in fracture postdates laumontite vein and predates calcite vein.

C.7 Fault BS2 Microstructures

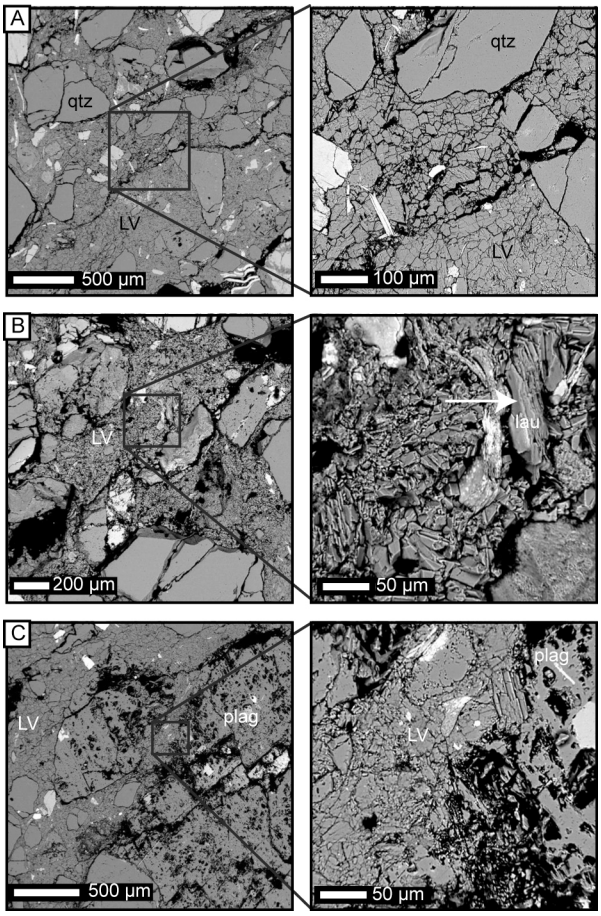

Figure C.7.1. Fault BS2, DI, unit SS1, Sample #74. (A) Thick laumontite vein (*LV*) with fractured detrital quartz (*qtz*) grains. A late fracture through the vein provides some evidence for dilation post-cementation. (B) Laumontite (*lau*, white arrow) from an older generation of cement is entrained within the laumontite vein; some cataclasis postdates cementation. (C) Plagioclase (*plag*) dissolution affects the grain edges to some extent, some laumontite growth within the plagioclase grain.

C.8 Summary of Microstructural Observations of Deformation Features

Table C.8.1 Summary of deformation features and relative timing between these features for each sample selected for microstructural analysis. *LV*, laumontite vein; *CV*, calcite vein; *GV*, gypsum vein; *HV*, halite vein; *CF*, cataclastic fault rock; *OF*, open fracture; '<' used to denote 'younger than'.

Fault	Sample Number	Fault Zone Domain	Distance to PSS (cm)	Deformation Features						Relative Timing
				LV	CV	GV	HV	CF	OF	
BM1	68	III	72					X	X	CF<OF
	69	III	41					X	X	CF<OF
	70	II	11						X	
	71	I	1					X	X	CF<OF
	72	II	90					X	X	OF<CF
BM3	61	III	130						X	
	62	III	49						X	
	63	II	25				X			
	64	III	163					X	X	CF<OF; OF<CF
	65	III	255						X	
BM2	53	I	0		X			X	X	CF<CV; OF<CV; 2+ gen CV
	54	I	0					X	X	OF<CF
	56	IV	184						X	
	57	III	120						X	
	58	II	38						X	
	59	DZF	147						X	
BC1	40	II	80			X			X	OF<GV
	41	II	60	X	X	X			X	GV<LV; GV<CV; OF<LV
	42	II	15	X	X	X		X	X	GV<LV; CF<LV; LV<CV; CF<GV; OF<ALL
	43	I	4					X	X	OF<CF
	44	I	0			X		X	X	CF<GV
	45	II	30		X	X		X	X	2+ gen GV; GV<CF; GV<CV; OF<ALL
BC3	35	IV	240					X	X	OF<CF
	36	III	140					X	X	OF<CF
	37	I	0					X	X	OF<CF
BS1	46	II	40	X					X	OF<LV
	47	III	40	X	X			X	X	OF<LV
	48	IV	250	X				X	X	OF<LV
	49	I	0	X				X	X	LV<CF; OF<ALL
	50	I	0	X	X				X	2+ gen LV; CV<LV; OF<LV; OF<CV; CF<LV; CV<CF
BS2	74	I	0	X				X	X	2+ gen LV; CF<LV; OF<ALL

VITA

Eliza Nemser was born in New York, New York. In 1998 she earned a Bachelor of Arts degree, *cum laude*, with honors in Geosciences from Williams College. In 2001 she was graduated with a Master of Science degree in Geology from the University of Washington. From 2002–2004 she worked as a Seismic Geologist for the Seismic Hazards Group in the Engineering Division of URS Corporation in Oakland, California. In 2006 she completed a three-month internship with the Structural Geology and New Ventures Teams at Chevron Corporation in San Ramon, California. In 2009 she earned a Doctor of Philosophy in Earth and Space Sciences from the University of Washington.